

**Molekulardynamik Simulationen
zum
Glasübergang in Makromolekularen
Filmen**

(Molecular Dynamics Simulations on the Glass Transition in Macromolecular Films)

Dissertation

zur Erlangung des Grades
“Doktor der Naturwissenschaften”
am Fachbereich Physik
der Johannes Gutenberg-Universität Mainz,
vorgelegt von

Fathollah Varnik

geboren in Bandar-Shah (Iran)

Mainz, November 2000

Datum der Prüfung: 20. Dezember 2000

Zusammenfassung

Untersucht wurde ein Polymermodell der Kettenlänge 10. Ein Lennard-Jones (LJ) Potential wirkte zwischen *allen* Teilchenpaaren. Außerdem sorgte ein sogenanntes FENE-Potential für die Bindung benachbarter Teilchen einer Kette. Die Filmgeometrie war realisiert durch das Anbringen zweier glatter z^{-9} -Wände an $z = -D/2$ und $z = D/2$ (z ist der Abstand von einer Wand und D die Filmdicke).

Als Vorbereitung für Simulationen unter konstantem Druck wurde zuerst der Drucktensor in inhomogenen Flüssigkeiten untersucht. Das zentrale Resultat dieser Studie war, daß eine in der Literatur häufig benutzte Formel (die so-genannte IK1-Formel) zu *unphysikalischen Oszillationen* der Normalkomponente, P_N , des Drucktensors führt. Man kann aber unter Benutzung der mechanischen Stabilität zeigen, daß $P_N(z)$ eine Konstante sein muss.

Der Einfluß der Wände zeigt sich unter anderem in Dichteoszillationen, welche mit der Temperatur immer ausgeprägter werden. In der Nähe der Wände dominiert die parallele Ausrichtung der Polymere und die Ketten werden flacher. Das sogenannte Korrelationsloch ist größer in der Nähe der Wände. Die statischen Orientierungseigenschaften des Systems konnten in guter Näherung mit einer selbstkonsistenten Feldtheorie beschrieben werden.

Es wurde eine Beschleunigung der Dynamik des Films verglichen zum "Bulk" (System ohne Wände) beobachtet. Eine Moden-Kopplungs(MC)-Analyse der Dynamik oberhalb des Glasübergangs ergab dann erwartungsgemäß eine starke Abhängigkeit der kritischen Temperatur T_c von der Filmdicke D . Im Vergleich zum Bulk ($D = \infty$) ändert sich T_c von 0.45 auf 0.41, 0.39 und 0.31 für Filmdicken $D=20$, 10 und 5 (alle Angaben sind in LJ-Einheiten).

Zudem wurden für eine Dichte im Volumen von $\rho_{\text{bulk}} = 0.99$ umfangreiche Nichtgleichgewichtssimulationen durchgeführt und es wurde die Temperaturabhängigkeit der Scherviskosität bestimmt. Die so erhaltene Scherviskosität konnte gut mit einem Vogel-Fulcher-Tammann-Fit beschrieben werden. Es konnte auch gezeigt werden, daß die Stokes-Einstein Beziehung im beobachteten Temperaturintervall nicht gilt.

Zudem konnten die gewonnenen Erkenntnisse zur korrekten Berechnung des Drucktensors mit Erfolg bei der Berechnung der lokalen Viskosität $\eta(z)$ angewendet werden.

Auch ein Verfahren zur Berechnung der Wärmeleitfähigkeit im gesamten Temperaturbereich ist erarbeitet worden.

Contents

1	Introduction	3
1.1	Motivation	3
1.2	A Short Introduction to the Glass Transition	4
1.3	Brief Outline of This Report	9
2	Model	11
2.1	A Complete Simulation Run	12
3	Pressure Tensor of Inhomogeneous Systems	15
3.1	Simpler Case: Pressure of Homogeneous Systems	15
3.2	Inhomogeneous Systems: The Method of Irving and Kirkwood	17
3.3	Planar Systems	19
3.3.1	Ambiguity in the Definition of P_T : Harasima's Approach	21
3.3.2	The Method of Planes	22
3.3.3	An Approximate Formula: IK1-method	23
3.3.4	Mechanical Stability Requires $\mathbf{P}_N = \text{const}$	24
3.4	Results	25
3.4.1	Profiles of $\mathbf{P}_N(\mathbf{z})$: IK1 versus (full) IK	25
3.4.2	Surface Tension and Surface of Tension	29
4	Molecular Dynamics Simulation Techniques	33
4.1	Microcanonical Ensemble Simulation	33
4.2	Extended Lagrangian Methods: NVT -Ensemble	35
4.2.1	Choice of the Parameter Q	40
4.3	NpT -Ensemble I: Homogeneous Systems	44
4.3.1	Choice of the Parameter M_η	48
4.4	NpT -Ensemble II: Planar Systems	50
4.4.1	Constants of Motion	53
4.4.2	Choice of $M_{\eta,\alpha}$ and Q_α	54
4.4.3	Integration of Equations of Motion	55
4.5	PBC and the Calculation of the Pressure	57
5	NP_NDT-Simulation of Thin Films	65
5.1	Iterative Calculation of the Surface Tension, γ , While Keeping both P_N and D Constant	66
5.2	Convergence of the Iterative Method	66
5.3	On the Choice of γ^0 and τ	68
5.4	An Improvement of the Iterative Method	70

5.5	Again on the Choice of τ	73
5.6	How Small the Allowed Relative Error ϵ Can Be?	75
6	<i>NVE</i> versus <i>NVT</i> and <i>NpT</i>	79
6.1	Ensemble Independence of Static Properties	79
6.2	<i>NpT</i> -Ensemble Simulation and the Dynamics	81
7	Statics	87
7.1	A Brief Remark on Finite Size Effects	87
7.2	Density Profiles	87
7.3	Wall Effects on the Packing Structure	88
7.4	MD versus Self-Consistent-Field Theory	91
7.5	Average Chain Shape	96
8	Dynamics	103
8.1	Finite Size Effects	103
8.2	High Temperatures	105
8.3	Low Temperatures	110
8.4	Scatter Plots	116
9	System under Shear Stress	121
9.1	The Pressure Tensor and the Shear Viscosity	121
9.2	Details of the Simulation	122
9.3	Thermostating the System Through the Walls	125
9.4	Thermostating a Flow via Nosé-Hoover	129
9.5	Bulk Viscosity	133
9.6	Local Viscosity	136
10	Conclusion	141
A		145
A.1	Properties of the Liouville operator \mathcal{L}	145
A.2	Hoover- <i>NpT</i> Equations versus Nosé-Andersen	146
	Literature	149

Chapter 1

Introduction

1.1 Motivation

Macromolecular science has had a major impact on the way we live. Just 50 years ago, materials we now take for granted were non-existent. With further advances in the understanding of polymers and with new applications being explored, it is reasonable to expect that this evolution will provide us with still more exotic materials and thus will enhance the importance of the polymer science for the modern technology.

Due to their structural complexity, polymers are generally not crystalline at low temperatures. Rather they exhibit an amorphous, glassy structure. The concept of the glass transition thus plays an important role in understanding the properties of polymer systems. Let us start at a (high) temperature where the system is in the liquid state. As temperature decreases the polymer melt exhibits strong viscoelasticity, i.e. it becomes rubber-like. However, as the temperature drops below the so called glass transition temperature, T_g , the melt freezes for the time scale of the experiment. For all practical purposes it can be considered, however, as a solid, which is amorphous and mechanically very brittle. Thus, the knowledge of T_g is essential in adapting materials to various applications. In general, values of T_g well below room temperature define the domain of the so called elastomers, i.e. polymers with strong elastic properties like rubber. Polymers with a T_g above the room temperature, on the contrary, are usually rigid and brittle.

As a particular class of polymeric materials, polymer films find applications in the stabilization of colloids or as protective coatings in microelectronics and thus play an increasingly important role in the industrial evolution. As mentioned above, polymers and thus these films exhibit a glassy structure at low temperatures. An important information for materials design is therefore how the glass transition is affected by the thin film geometry. This is one of the basic questions to be addressed in this work.

However, before elaborating on the glass transition, let me briefly compile some facts of the history of polymers. The very first synthetic polymer was discovered thousands of years ago. It was an artificially crosslinked form of the proteins found in animal-skin, the leather [1]. It is reported that in 1496 European discoverers found Indians using tree latex to make shoes, bottles and clothing [2]. In the first half of the nineteenth century, 1823 to be precise, Charles Goodyear discovered vulcanization, a tire making process, through an accident. The list of discoveries related to polymers is quite long, however, for those who like cinema, I finish the listing by mentioning the discovery of bakelite, a cellulose polymer used to make billiard balls and movie films [2].

1.2 A Short Introduction to the Glass Transition

A qualitative understanding of the glass transition can be achieved in the following way. Glassy materials are often formed by substances containing long chains, temporary or permanent networks of linked atoms or those that possess a complex molecular structure. When the system is rapidly cooled below the melting temperature, T_f , if crystallization is not already excluded by the complex structure, it will be avoided due to the slow dynamics, i.e. the molecular motion becomes too slow to take up a crystalline conformation. Therefore, the random arrangement characteristic of the liquid state persists down to temperatures below T_f [3].

Due to the similarity of the structure of a glassy system to that of a liquid, some static properties (like density, for example) behave smoothly at T_g . This is in contrast to a material which crystallizes at the melting temperature. This point is illustrated in panel (a) of Fig. 1.1 where the specific volume (volume per particle, $v = V/N$) is plotted schematically for a crystalline material (C) and for an amorphous system (G). At T_f , the crystalline material undergoes a sharp phase transition which is evidenced by the abrupt change of the specific volume. Such a transition, however, does not occur in the glassy system. In this case, v changes continuously. The rate of change of v (i.e. the slope dv/dT), however, is smaller in the glassy state than in the liquid state. This difference can be used to define T_g as the temperature at which the straight lines tangential to $v(T)$ in the liquid and glassy states intersect.

However, it must be emphasized that T_g depends on the cooling rate [3–5]. Thus, for a given substance, T_g is not a unique number. The dependence of T_g on the cooling rate can be understood as follows. Let $\tau(T)$ denote the typical relaxation time of a given system at temperature T . When the system is cooled down at an arbitrary, but constant rate, γ , it will spend $\Delta T \gamma^{-1}$ at each “visited” temperature, where ΔT is the distance between two adjacent temperatures. If the cooling process is started at a sufficiently high temperature so that $\tau(T) \ll \Delta T \gamma^{-1}$, the system will have enough time to “visit” a sufficiently large number of configurations typical of the actual value of temperature. This is what is usually meant by saying that the system is equilibrated at the given temperature. However, the dynamics of the system slows down at lower T and, consequently, the relaxation time, $\tau(T)$, increases. Therefore, there will be a temperature at which $\tau(T) \approx \Delta T \gamma^{-1}$. Further cooling will now drive the system “out of equilibrium”. This is the region in Fig. 1.1 where $v(T)$ leaves the straight line of the liquid phase. Obviously, a larger cooling rate will make the system to fall “out of equilibrium” already at a higher temperature. This idea is also depicted (again schematically) in panel (b) of Fig. 1.1. A larger cooling rate thus leads to a higher glass transition temperature, T_g . The above idea is qualitative in character. However, one can obtain a quantitative criterion by assuming the validity of the (empirical) Vogel-Fulcher-Tammann (VFT)-formula

$$\tau(T) = A \exp\left(\frac{B}{T - T_0}\right) \quad (1.1)$$

for temperatures close to T_g . Rewriting Eq. (1.1) for $T = T_g$ and setting $\tau(T_g) \approx \Delta T \gamma^{-1}$ yields [3–5]

$$T_g = T_0 - B / \log(A' \gamma) \quad (1.2)$$

where $A' = A/\Delta T$ and B are fit parameters.

Equation (1.2) has been used by Vollmayr *et al.* to fit $T_g(\gamma)$ obtained from computer simulations of a binary Lennard-Jones mixture and on SiO_2 [3–6]. The excellent agreement of the fit with the simulation results is depicted in Fig. 1.2.

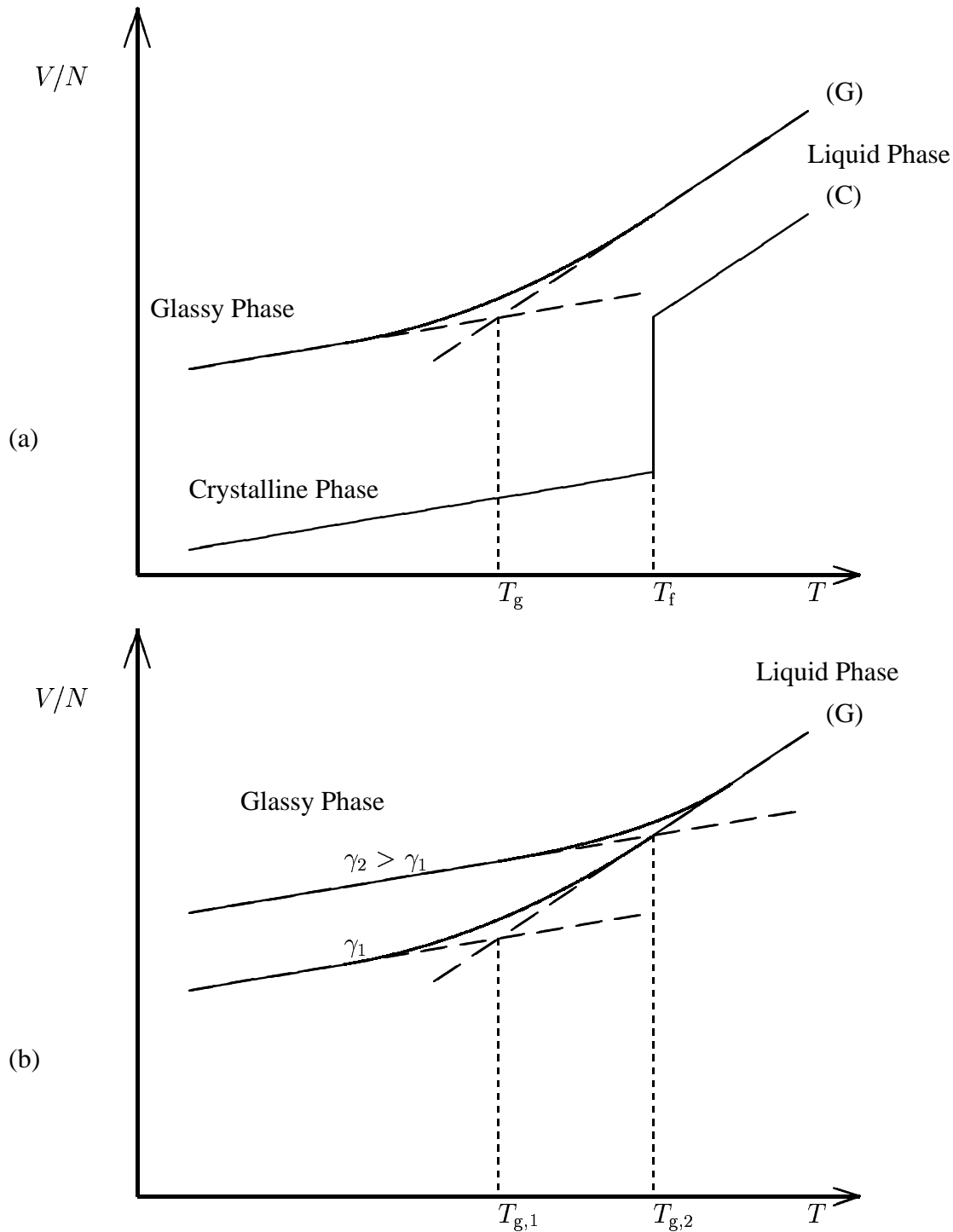


Figure 1.1: Panel (a): Schematic illustration of the temperature dependence of the specific volume, $v(T) = V/N$, for a crystalline material (C) and a glass forming material (G). There is a sharp change in $v(T)$ of the crystalline material at melting point, T_f , whereas $v(T)$ of the amorphous system varies smoothly, changing, however, slope when going from the liquid region to the glassy regime. The intersection of tangent lines defines the glass transition temperature T_g . Panel (b): Dependence of T_g on the cooling rate, γ . Higher cooling rates drive the system out of equilibrium at a higher temperature, thus leading to a larger T_g .

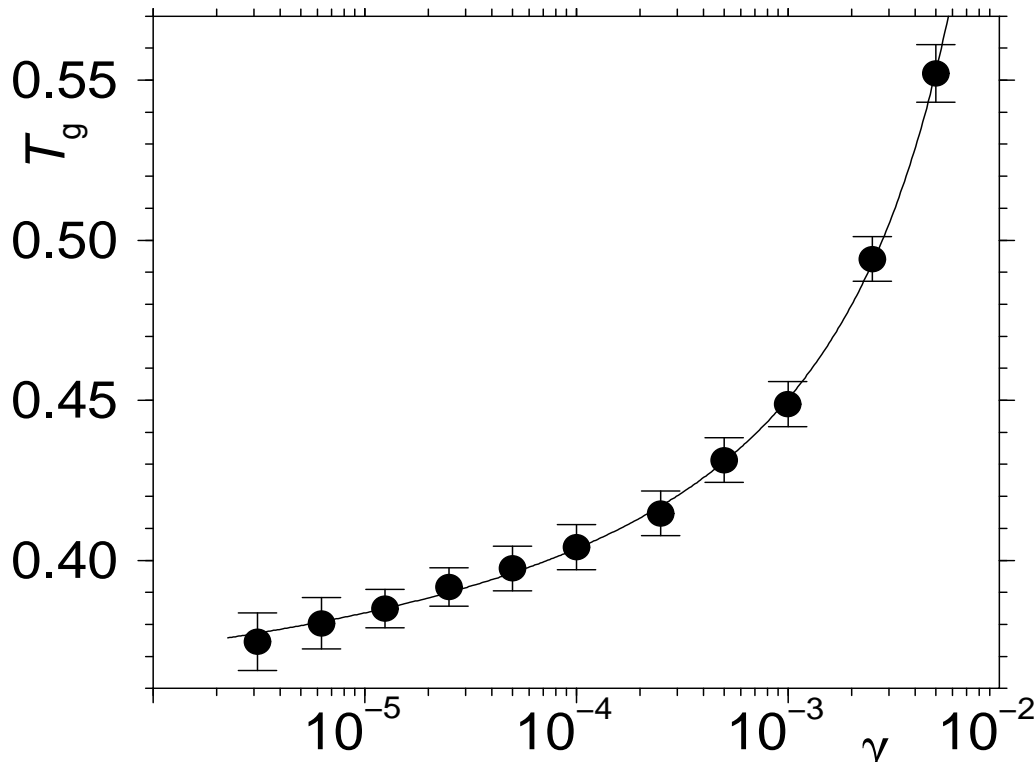


Figure 1.2: Glass transition temperature, T_g , of a binary Lennard-Jones system versus the cooling rate γ . The solid line is a fit with the function given by Eq. (1.2) [From Ref. [5] with permission].

Dependence of T_g on the cooling rate has also been observed in both real and computer experiments of other systems [7–10]. An important implication of the above picture is that, in principle, every material can be brought to an amorphous glassy state provided that the cooling rate is high enough. This expectation is supported by computer simulations on liquid argon [11–14].

Thus, a glassy state seems to be a “frozen” non-equilibrium configuration. The time needed for a transition towards equilibrium is much larger than the duration of a typical experiment. In fact, there is also a phenomenological definition of the glass transition temperature, T_g , based on this idea. One defines T_g as the temperature at which the relaxation times are of order $\approx 10^2$ up to $\approx 10^3$ seconds [9].

It has to be mentioned that the time scale for which the glass transition can be observed in a particular system can span over more than 12 decades, i.e. from microscopic times of order of about 10 ps to macroscopic time scales of a day or more [3]. The investigation of this phenomenon is therefore a great challenge from both the experimental and the theoretical point of view.

An intuitive and appealing picture is provided by the free volume theory of Cohen and Turnbull [15–17]. The main idea of this theory is that a tagged particle can leave its initial position only if it finds a “free volume” of size $v_f \geq v_c$ (v_c being some critical volume of the order of the size of a molecule) in its neighborhood. Let $\langle v_f \rangle$ be the average free volume per particle. Assuming statistical independence, one can show that the probability of finding a free volume, $v_f \geq v_c$, is proportional to $\exp(-v_c/\langle v_f \rangle)$ [9]. It follows then for the self diffusion

constant

$$D \propto \exp\left(-\frac{v_c}{\langle v_f \rangle}\right). \quad (1.3)$$

A temperature dependence for $\langle v_f \rangle$ is found in the following way. Let $v = V/N$ be the specific volume and let v_0 be the (average) volume of a particle. Obviously, there will be an average free volume per particle of $\langle v_f \rangle = v - v_0$. Note that v_0 is mainly determined by the interaction potential and thus can be regarded as independent of temperature. However, under the condition of constant pressure, which is usually the case in real experiments, v is a function of temperature. Therefore, $\langle v_f \rangle = \langle v_f \rangle(T) = v(T) - v_0$. Let now $v(T_0) = v_0$. Expanding $v(T)$ to first order in T immediately leads to $\langle v_f \rangle(T) = (T - T_0)\alpha v_0$, where the expansion coefficient α is defined through $v_0\alpha = \partial v / \partial T|_{T=T_0}$. Setting this result in Eq. (1.3) leads to the VFT-formula for the self diffusion constant

$$D \propto \exp\left(-\frac{B}{T - T_0}\right), \quad (1.4)$$

where $B = v_c / (v_0\alpha)$. Despite of this success, it must be noted that the free volume theory is phenomenological in nature as it does not provide a precise definition of the critical volume, v_c .

An alternative approach to the phenomenon of glass transition was proposed by Bengtzelius, Götze and Sjölander and, independently, Leutheusser [18, 19] who extended a mode-coupling approach originally proposed to describe the dynamics close to second order phase transitions and later further developed for the description of liquids at high temperatures to this field of the glass transition, whence the term mode-coupling theory (MCT). The central prediction of the simplest version of the theory, the so called “ideal MCT”, is the existence of a critical temperature $T_c > T_g$ below which the relaxation times diverge and, thus, the system becomes non-ergodic. For temperature above, but not too far from T_c the theory makes many interesting predictions. As an example we note here the prediction of a power law dependence of the self diffusion constant for T close to T_c

$$D(T) \propto |T - T_c|^\gamma, \quad (1.5)$$

where γ is a critical exponent. A complete description of the theory and its predictions can be found in review articles by Götze, Götze and Sjögren, Schilling and articles edited by Yip [20–23]. Due to the novelty of its predictions for the dynamics of *supercooled liquids*, i.e. liquids at sufficiently low temperatures close to but above T_c ($T > T_c > T_g$), mode-coupling theory has been applied by many groups to a wide range of systems either in real experiments or in computer simulations [24–31].

Another line of thinking concerning the glass transition is to ask if the slowing down of the dynamics when approaching T_g can be interpreted in terms of the critical slowing down of the dynamics near a second order phase transition [3]. A second order phase transition is usually characterized by the divergence of a length scale. However, the low temperature behavior of the pair distribution function $g(r)$ does not indicate the existence of such a length scale [see section 7.3, panels (a) and (b) of Fig. 7.2, for example]. It does, however, *not* mean that a diverging length scale can not be found in other quantities.

The idea of a diverging length scale related to the glass transition has given rise to the concept of “cooperative motion” empirically introduced by Adam and Gibbs [32]. According to Adam and Gibbs, near the glass transition, individual particle motion is frozen out. Thus, the only possibility for structural relaxation is that of the collective motion of many particles.

Note that, here, the focus is no longer on the static correlations, but on correlations between the *dynamics* of particles. The associated length scale is thus a dynamic one. Let $\xi(T)$ denote the typical size of a cluster of cooperatively moving particles. It is well-known that close to a second order phase transition the relaxation time of such a cluster scales like ξ^z , where $z > 0$ is the so called dynamic critical exponent [33]. The sharp rise of the relaxation times near T_g is then explained by assuming the divergence of ξ when lowering the temperature towards T_g .

The above reasoning, however, is based on an empirical assumption that $\xi(T)$ increases with decreasing temperature. A significant improvement was achieved by Edwards and Vilgis [34]. These authors introduced an exactly solvable model system exhibiting glassy behavior at low T and showed that the concept of cooperative motion alone was enough to give rise to a VFT-law [see Eq. (1.4)].

Recent computer experiments also support the idea of cooperative motion. For example, it was observed by Kob *et al.* [35, 36] that particles move mainly in string-like clusters. Benne-
mann *et al.* [37] report on a growing length scale for the dynamics of a polymer melt. Strong heterogeneity in the dynamics has also been observed in molecular dynamics simulations of bond breakage processes [38] and of binary mixture of soft spheres [39–41]. It is found that particles move preferably within mobile clusters thus leading to a heterogeneity in the dynamics.

Being easily detectable in a simulation, the regions of heterogeneous dynamics are unfortunately not as easily accessible to real experiments [42]. This results from the fact that dynamic heterogeneity is not necessarily strongly correlated to density fluctuations. The structures of these regions are therefore more or less identical. Thus, one cannot use scattering experiments to determine the length scale $\xi(T)$ [42]. Fortunately, there is an issue to this problem. Recall that the relaxation time of a cluster of strongly correlated particles such as that observed in cooperative motion scales like ξ^z , where $z > 0$. As the temperature decreases $\xi(T)$ becomes larger and eventually reaches the system size, $\xi(T) = L$. If this occurs, the relaxation time, τ , of the system will scale like $\tau \propto L^z$. In other words, the relaxation dynamics of the system will become size dependent. This size dependence is indeed observed in Monte Carlo studies of the so called bond-fluctuation model (BFM) in 2D [43]. In the mentioned reference, the system size was varied while maintaining the periodic boundary conditions (pbc). An acceleration of the dynamics of the smaller systems have been observed in accordance with $\tau \propto L^z$.

A simple way of changing the system size in a real experiment is, for example, to vary the thickness of a planar film. Applying the same arguments as given above to a thin film of thickness D we should expect finite-size effects on the dynamics for temperatures at which $\xi(T) \approx D$. Note that boundary conditions are no longer periodic, but can change from an absorbing one to an approximately neutral or a repulsive one.

Experiments on polymer systems reveal that if the interaction between the polymers and the substrate (the wall) is attractive, the glass transition temperature T_g of the films becomes larger than the bulk value for small film thicknesses [44], thus indicating a slower dynamics in the film compared to the bulk system.

On the other hand, experiments on freely standing polystyrene films (i.e., no solid substrate, but two polymer-air interfaces) [45] find a dramatic decrease of T_g by up to 20% if the film thickness becomes much smaller than the chain size. Obviously, this decrease becomes much weaker if one or even both of the free interfaces are replaced by a weakly interacting solid substrate.

Whereas the strong depression of T_g in the freely standing film could possibly be attributed to the significant release of geometric constraints at the air-polymer interface, the acceleration of the structural relaxation of a polymer melt between two (almost) neutral solid substrates

is less clear intuitively. The study of the present continuum model may help to improve our understanding of this phenomenon.

1.3 Brief Outline of This Report

The model investigated in this work will be introduced in the next chapter. Chapter 2 also contains a description of the main stages of a complete simulation run.

As real experiments on polymer films are usually done under the condition of a constant pressure normal to the surfaces, it is reasonable to carry out simulations under similar conditions. This leads to chapter 3 where the pressure tensor, $\mathbf{P}(\mathbf{r})$, of inhomogeneous systems and, in particular, that of a system with planar geometry is investigated. We will address some ambiguity which still exists in the definition of $\mathbf{P}(\mathbf{r})$. Furthermore, through a detailed analysis, we will stress the erroneous character of a formula for the pressure of a planar system, which, due to its simple and appealing form, is often used in the literature [see Eq. (3.38) and also subsection 3.3.4].

Chapter 4 is partly devoted to a review of the MD simulation techniques. There, we also give an extension of the so called Hoover-Melchionna equations of motion [see Eqs. (4.75)-(4.79)] to planar systems. In section 4.4.3 the integration scheme used to solve the extended motion equations is presented.

At the beginning of the present studies, we were faced with the following problem. On the one hand, as already mentioned, we were interested in simulations at a constant normal pressure. On the other hand, to separate the effects of the temperature from that of the film thickness, D , it was necessary to vary the temperature at a well defined value of D . However, a simulation at a constant normal pressure usually requires a fluctuating film thickness. Thus, there seems to be a conflict between the criteria of $D = \text{const.}$ and $P_N = \text{const.}$ We show in chapter 5 that this problem can be solved via an iterative calculation of the surface tension.

Chapter 6 compares the static and dynamic properties of the system with respect to simulations in NVE , NVT and NpT ensembles. Static properties of the system are investigated in chapter 7. In addition to a study of the density profiles and a brief discussion of the influence of walls on the packing structure, we also compare MD results on chain specific profiles with self-consistent field (SCF) calculations of M. Müller. The last section of chapter 7 contains an analysis of some quantities useful to characterize the average shape of a chain.

In chapter 8 we focus on dynamic properties, where we analyze both high and low temperatures. In particular, the mode-coupling critical temperature is calculated for some film thicknesses. Using (so called) “scatter plots” we visualize in the last section of this chapter the heterogeneity in the dynamics.

Finally, chapter 9 contains results of MD simulations of the present model system under a homogeneous shear stress. We show in this chapter how the knowledge of the local pressure tensor can be used to calculate the local viscosity, $\eta(z)$.

The derivation of some formula is given in appendix A.1.

Chapter 2

Model

We study a Lennard-Jones model for a polymer melt [46] embedded between two impenetrable walls. Two potentials are used for the interaction between particles. The first one is a truncated and shifted LJ-potential which acts between all pair of particles regardless of whether they are connected or not,

$$U_{\text{LJ-ts}}(r) = \begin{cases} U_{\text{LJ}}(r) - U_{\text{LJ}}(r_c) & \text{if } r < r_c, \\ 0 & \text{otherwise,} \end{cases} \quad (2.1)$$

where

$$U_{\text{LJ}}(r) = 4\epsilon \left[(r/\sigma)^{12} - (r/\sigma)^6 \right] \quad (2.2)$$

and $r_c = 2 \times 2^{1/6} \sigma$.

With the exception of the most part of this chapter, where we define the model, all simulation results will be given in Lennard-Jones (LJ) units in the following, i.e. $\sigma = 1$, $\epsilon = 1$, etc.

In addition to the Lennard-Jones potential a FENE-Potential [47]

$$U_{\text{FENE}}(r) = -\frac{k}{2} R_0^2 \ln \left[1 - \left(\frac{r}{R_0} \right)^2 \right], \quad (2.3)$$

acts between *adjacent* monomers of a chain thus ensuring the connectivity. Here $k = 30$ is the strength factor and $R_0 = 1.5$ the maximum allowed length of a bond. Thus, the unbonded monomers interact via the LJ-potential (2.1) only, whereas the bonded ones exert both LJ and FENE forces on one another.

The wall potential was chosen as

$$U_{\text{W}}(z) = \left(\frac{\sigma}{z} \right)^9, \quad (2.4)$$

where $z = |z_{\text{particle}} - z_{\text{wall}}|$ ($z_{\text{wall}} = \pm D/2$). This corresponds to an infinitely thick wall made of infinitely small particles which interact with inner particles via the potential $45(r/\sigma)^{-12}/(\pi \rho_{\text{wall}})$ where ρ_{wall} denotes the density of wall particles. The sum over the wall particles then yields $(\sigma/z)^9$.

Figure (2.1) compares the bond potential, i.e. the sum of LJ and FENE potentials with the LJ-potential. It is obvious from this figure that the bonded monomers prefer shorter distances than the unbonded ones. In other words, we have two intrinsic length scales in our system. If these length scales are chosen to be incompatible to fit into a crystalline structure, one could

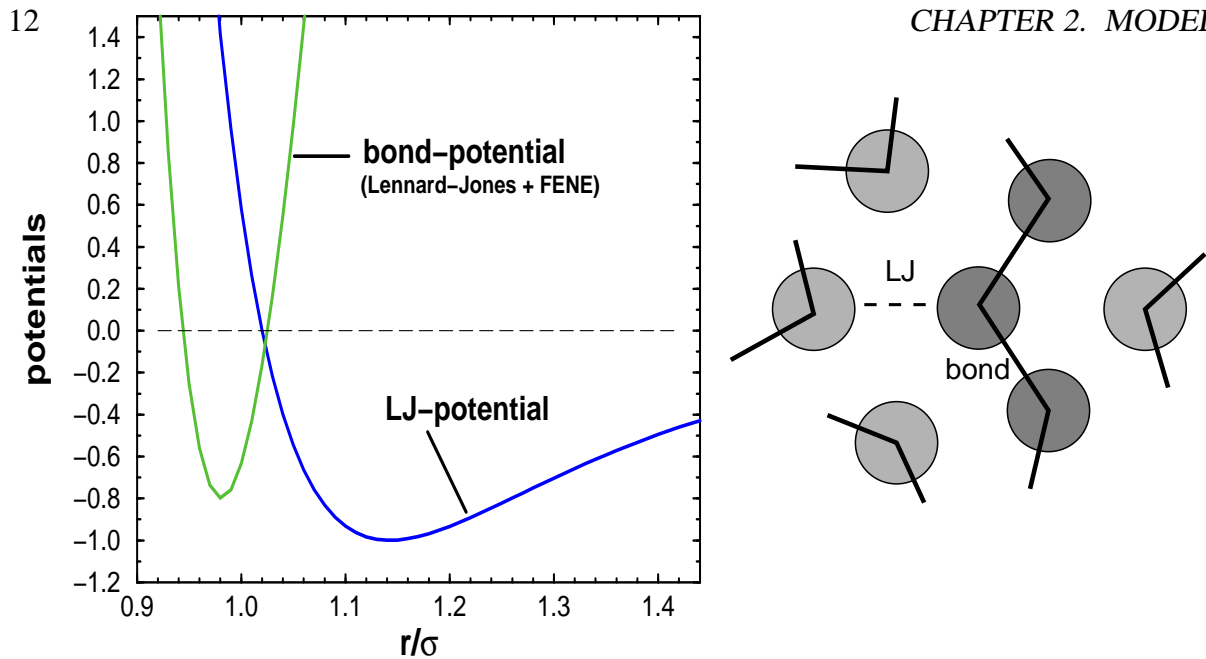


Figure 2.1: Left panel: Lennard-Jones potential (LJ) versus the bond potential, the sum of the LJ and FENE potentials. The minimum position of the bond-potential is smaller than that of the LJ-potential: The bond potential has its minimum at $r \simeq 0.96\sigma$ whereas that of a pure LJ-potential lies at $r = \sqrt[6]{2}\sigma$. This incompatibility prevents crystallization, which is confirmed by the behavior of $S(q)$ [see Fig. 2.2]. Right panel: “Visualization” of the same potentials.

expect that the system would not crystallize at low temperatures, but becomes amorphous. We are, of course, interested in such an amorphous behavior. We thus examine in Fig. (2.2) the structure factor of our system at various temperatures. As is seen from this figure, the structure of the system remains close to that of a liquid even at very low temperatures ($T_{c,\text{bulk}} = 0.45$, see below). The central peak of the structure factor becomes more pronounced as the temperature decreases, but there are no Bragg peaks which would be typical of a periodic structure. The static and dynamic properties of this model were studied in the bulk when gradually supercooling towards the glass transition [37,46,48–50]. The model begins to develop sluggish relaxation if the temperature drops below $T \approx 0.7$ and yields a critical temperature of mode-coupling theory of $T_{c,\text{bulk}} \simeq 0.45$ [48] upon further cooling. We quote this value for the sake of comparison with the film results to be discussed below. We will see in chapter 8 that the presence of smooth walls results in an enhancement of the mobility of particles. This in turn leads to a decrease of $T_{c,\text{film}}$ with respect to the bulk.

2.1 A Complete Simulation Run

In chapter 4 we will discuss some important techniques which allow for a simulation at a given temperature and/or external pressure. Therefore, we also postpone to this chapter the investigations concerning the choice of an appropriate set of equations of motion and their discretized integration. The purpose of the present section is a description of the main stages of a simulation run, i.e. generation of an initial configuration, equilibration and production.

With the exception of simulation runs under shear stress [see chapter 9] where the equilibration of the system was achieved at constant density, the system was equilibrated under the condition of constant external pressure, NpT -ensemble. However, it will be demonstrated in chapter 6 that the dynamics of the system is strongly affected if the volume of the simulation

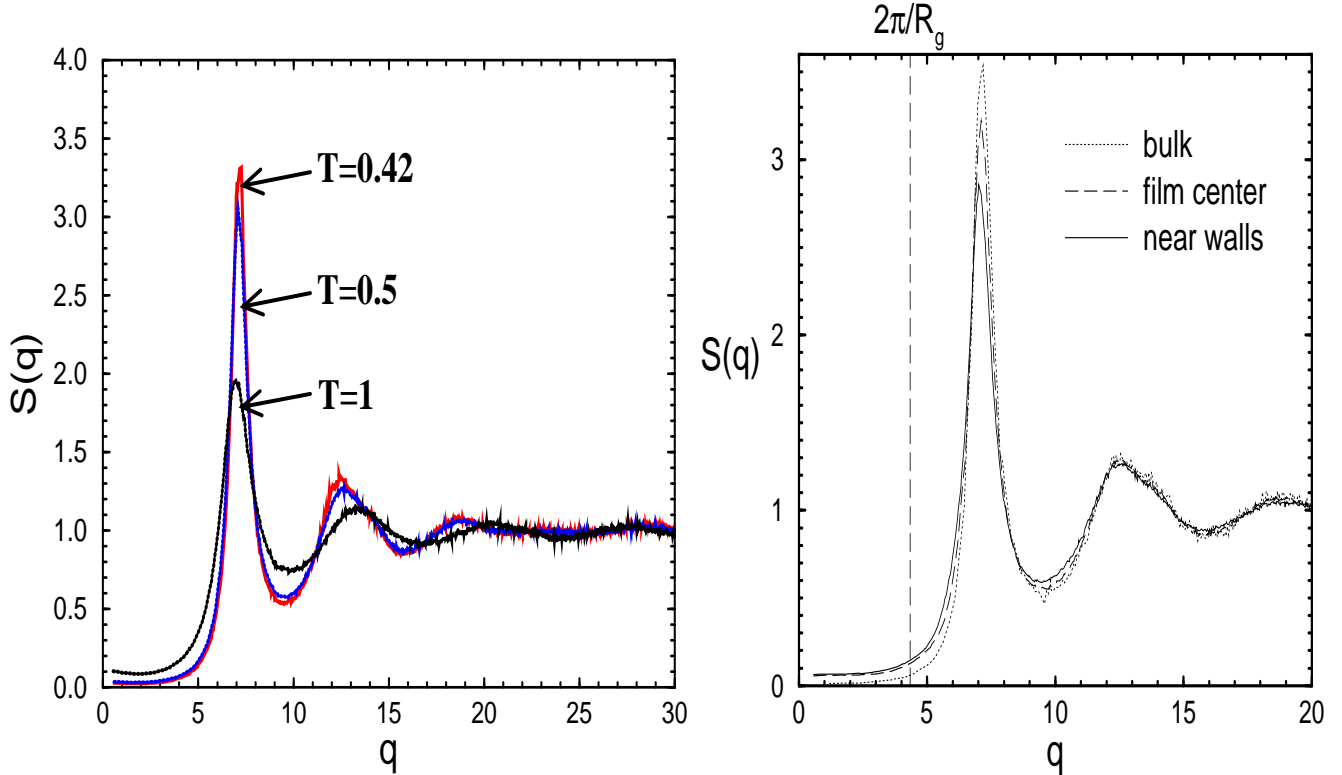


Figure 2.2: Left panel: Temperature dependence of the structure factor, $S(q)$, of a polymer film of thickness $D = 10$. Though the peaks of $S(q)$ become more pronounced at lower T 's, the Bragg peaks typical of a crystal are, however, absent. Right panel: Comparison of $S(q)$ for bulk, film center and the region close to the walls at $T = 0.46$. In both panels $q = 2\pi/R_g$ indicates the q -value corresponding to the bulk radius of gyration R_g

cell is allowed to vary, i.e. within a NpT -ensemble simulation. In contrast to that, it will also be demonstrated that, within the Nosé-Hoover approach, the coupling to a heat bath to perform simulations in a NVT -ensemble is less problematic. Therefore, all production runs were done at constant volume, or more precisely, in the NVT -ensemble.

At the beginning of the simulation the velocities of all particles were set to zero and NRRW- (Non-Reversal-Random-Walk-) chains were “synthesized”, i.e. only the average bond length and bond angle (known from previous bulk simulations) were used to build a chain of N ($= 10$) monomers. This initial state corresponds to very high energies (usually $E(t = 0) > 10^{10}$) due to the occurrence of extremely short distances between non-bonded monomers.

The surplus of energy must be removed to prevent numerical instabilities. For the bulk this can be done by replacing the full LJ-potential by a softer one. The LJ-potential is then switched on smoothly [47]. For our model, however, it was necessary to keep the (full) *wall* potential from the very beginning of the simulation to avoid penetration of the walls. We thus left the potentials unchanged, but used an adaptive time step: First, the maximum force \mathbf{F}_{\max} and the maximum velocity v_{\max} were determined. A time step Δ was then chosen so that the resulting displacement of a particle, which is subject to \mathbf{F}_{\max} and moves with initial velocity v_{\max} in direction of \mathbf{F}_{\max} , would be $dr_{\max} = 10^{-3}$. This (empirical) value is only applicable if \mathbf{F}_{\max} does not point in direction of a bond vector whose size b is closer to the maximum bond length R_0 (see U_{FENE}) than 10^{-3} , since a displacement of this size could break the bond. In such a situation we chose $dr_{\max} = (R_0 - b_{\max})/2$ instead of 10^{-3} to adjust the time step (b_{\max} denotes the largest measured bond length). The equations of motion were then integrated with this time step and the procedure was repeated.

After about 250 MD steps the velocities of all particles were renewed by drawing them from the Maxwell distribution, and the time derivative of the volume was set to zero. These steps are important to warrant the numerical stability of our procedure. Our criterion for the end of this stage was that the minimum distance between particles should not be smaller than a certain value, empirically 0.8, and that the normal pressure of the system should not be too far away from the external value, i.e., $|\bar{P}_N(t) - P_{N,\text{ext}}|/P_{N,\text{ext}} \leq 10^{-2}$, where $\bar{P}_N(t)$ was computed as an average over the last 20 samples preceding time t . The sample distance was empirically chosen to $10 \exp(1/T)$ MD steps to take into account stronger correlations at lower temperatures. Since we kept the film thickness D fixed, the simulation at constant pressure was realized by varying the area ($= A$) of the simulation box parallel to the walls. During this initial stage a high bath temperature, $T = 1$, was used.

After this initial stage (with a typical duration of 10^5 MD steps) the time step could be set to $\Delta = 0.003$. This value is close to that used in previous bulk simulations [46]. The system was then slowly cooled down to the desired temperature by gradually reducing temperature in a step-wise fashion: The bath temperature was set to the next smaller value and the system was propagated for a certain amount of time before the bath temperature was decreased again.

At the end of the cooling process the sampling of the mean-square displacement of the chain centers parallel to the walls, $g_{3||}(t)$, and of the volume was started. The system was propagated until $g_{3||} \geq 9R_{\text{ee||}}^2$ where $R_{\text{ee||}}$ denotes the component of the chain's end-to-end vector parallel to the walls. This criterion suffices to reach the free diffusive limit and to equilibrate the system completely. During this period the system volume was sampled once every 1000 time steps and the average volume of the system was calculated. The equilibrated configuration was then further propagated until the instantaneous volume reached the average value within a given relative accuracy, usually 10^{-5} . At this point the program fixed this volume and switched to a (pure) Nose-Hoover-Algorithm (NVT-Ensemble) for production runs in the canonical ensemble. During a production run sampling was done once every 1000 time steps.

Chapter 3

Pressure Tensor of Inhomogeneous Systems

Usual experiments on thin polymeric films are done under constant external pressure normal to the surface of the film, $P_{N,\text{ext}}$. It is therefore desirable to simulate in NpT -ensemble. The question is now how to characterize the pressure of inhomogeneous systems. For a homogeneous system, pressure, p , is a scalar quantity which is constant with respect to the position \mathbf{r} where it is determined: it is the well known hydrostatic pressure. But what about inhomogeneous systems? It is intuitively expected that the pressure of an inhomogeneous system is a function of the position \mathbf{r} . If one recalls that the pressure is equivalent to the force across an area one could further conclude that, due to the anisotropy of the system, the pressure should also depend on both the direction of the normal to the surface and that of the acting force. It is therefore not a scalar, but a tensor, $\mathbf{P}(\mathbf{r})$. An understanding of the properties of the pressure tensor of inhomogeneous systems is thus the first step in an attempt to simulate at constant external pressure. In this chapter we are going to address this problem.

3.1 Simpler Case: Pressure of Homogeneous Systems

In his famous “lectures on physics” R. P. Feynman said that one should always start with simpler problems before going on to more complicated ones [51]. It turns out that he was not very wrong. We thus start with a short overview of the pressure of homogeneous systems. Consider a system of N particles inside a container of volume V . We assume that the particles interact via pairwise forces only. Starting from the virial theorem of classical dynamics one can easily derive the following expression for the pressure, p , of the system (see for example [52])

$$p = \rho k_B T - \frac{1}{6V} \left\langle \sum_{i \neq j}^N \mathbf{r}_{ij} \cdot \mathbf{F}_{ij} \right\rangle. \quad (3.1)$$

Here, \mathbf{F}_{ij} denotes the force of particle j on i , $\mathbf{r}_{ij} := \mathbf{r}_j - \mathbf{r}_i$ the distance vector pointing from i to j and $\langle \dots \rangle$ stands for the statistical average. The first term in (3.1) arises from the average kinetic energy and the momentum transfer of the particles on the container walls, whereas the second term accounts for the contribution of the intermolecular forces. Obviously, the virial approach is based on the mechanical definition of the pressure as the time average of the force per unit area of particles on the container walls.

However, one can obtain the same expression (3.1) using a thermodynamic approach $p =$

$-(\partial F/\partial V)_T = 1/\beta (\partial \ln Z(\beta)/\partial V)_T$, where F denotes the free energy of the system, and

$$Z(\beta) = \frac{1}{\Lambda^{3N} N!} \int_{-\infty}^{+\infty} d\mathbf{r}^{3N} \exp(-\beta U(\mathbf{r}_1, \dots, \mathbf{r}_N)) \quad (3.2)$$

stands for the canonical partition function, $\beta = 1/k_B T$ the inverse temperature $\Lambda = \sqrt{2\pi \hbar^2 / m k_B T}$ the thermal de Broglie wavelength and finally U is the total potential function of the system. The quantities appearing in Λ are: $\hbar = h/2\pi$ (h being the Planck's fundamental constant), k_B the Boltzmann constant, T the temperature and m the mass of a particle.

The derivation we are going to demonstrate here is based on the rescaling of particle coordinates as described in ([53]). Let all particles be confined in a cube of side $L = V^{1/3}$, one corner of which is the origin of the coordinate system. Introducing rescaled coordinates $\mathbf{x}_i = V^{-1/3} \mathbf{r}_i$ one can write

$$p = \frac{1}{\beta} \frac{\partial \ln Z(\beta)}{\partial V} \quad (3.3)$$

$$= \frac{1}{\beta Z(\beta)} \frac{\partial}{\partial V} \int_0^{V^{1/3}} d\mathbf{r}^{3N} \exp(-\beta U^{\text{int}}(\mathbf{r}_1, \dots, \mathbf{r}_N)) \quad (3.4)$$

$$= \frac{1}{\beta Z(\beta)} \frac{\partial}{\partial V} \left\{ V^N \int_0^1 d\mathbf{x}^{3N} \exp(-\beta U^{\text{int}}(V^{1/3} \mathbf{x}_1, \dots, V^{1/3} \mathbf{x}_N)) \right\} \quad (3.5)$$

$$= \frac{N}{\beta V} - \frac{V^N}{3Z(\beta)V} \int_0^1 d\mathbf{x}^{3N} \left(\sum_{i=1}^N V^{1/3} \mathbf{x}_i \cdot \frac{\partial U^{\text{int}}}{\partial (V^{1/3} \mathbf{x}_i)} \right) \times \exp(-\beta U^{\text{int}}(V^{1/3} \mathbf{x}_1, \dots, V^{1/3} \mathbf{x}_N)) \quad (3.6)$$

$$= \frac{N}{\beta V} - \frac{1}{3V Z(\beta)} \int_0^{V^{1/3}} d\mathbf{r}^{3N} \left(\sum_{i=1}^N \mathbf{r}_i \cdot \frac{\partial U^{\text{int}}}{\partial \mathbf{r}_i} \right) \times \exp(-\beta U^{\text{int}}(\mathbf{r}_1, \dots, \mathbf{r}_N)) \quad (3.7)$$

$$= \rho k_B T + \frac{1}{3V} \left\langle \sum_{i=1}^N \mathbf{r}_i \cdot \mathbf{F}_i \right\rangle. \quad (3.8)$$

It is important to note that, in the above derivation, the potential U^{int} does *not* contain the external potentials arising from the container walls. The effect of these potentials is already taken into account in fixing the integration limits. This is best seen by splitting the total energy of the system in internal and external contributions, $U = U^{\text{int}} + U^{\text{ext}}$, and setting $U^{\text{ext}} = \sum_{i=1}^N V^{\text{ext}}(x_i) V^{\text{ext}}(y_i) V^{\text{ext}}(z_i)$, where $V^{\text{ext}}(x) = 0$ for $x \in [0, L]$ and $V^{\text{ext}}(x) = \infty$ otherwise. The force \mathbf{F}_i in (3.8) thus contains the contribution of the interparticle interactions only. We can therefore set $\mathbf{F}_i = \sum_{j(\neq i)}^N \mathbf{F}_{ij}$ in (3.8) and obtain, with a bit of elementary algebra and Newton's third law, equation (3.1).

Both the virial way and the thermodynamic approach given above assume that the particles are confined within a vessel of a given size. The validity of Eq. (3.1) could therefore be questionable for systems with periodic boundaries which is the typical case in molecular dynamics (MD) or Monte Carlo (MC) simulations. In such a situation there is no vessel to confine the system; the particles are thus allowed to move infinitely far from their initial positions. One thus needs an alternative derivation which does not make use of the assumption of confinement. Such a derivation does exist (see Appendix B of [54]). One finds the same expression for the pressure p as given in Eq. (3.1).

3.2 Inhomogeneous Systems: The Method of Irving and Kirkwood

In the derivations outlined in the previous section, we made use of the homogeneity and the isotropy of space and take p as a scalar. However, as mentioned earlier, in inhomogeneous systems, the pressure in general depends on both the spatial direction and the position. It is a *local* quantity as it depends on the position where the pressure is determined. It is a *tensor* as it depends on the directions of both the acting force and the unit vector normal to the infinitesimal surface. One thus needs a definition of the pressure tensor which takes into account both the inhomogeneity and the anisotropy of the system.

In their seminal paper “The Statistical Theory of Transport Processes” [55] Irving and Kirkwood (IK) gave statistical mechanical analogues of central equations of hydrodynamics: (mass) continuity equation, hydrodynamic equation of motion (or momentum continuity equation) and energy transport equation. As the divergence of the local stress tensor, $\nabla \cdot \boldsymbol{\sigma}(\mathbf{r})$, enters the second and third equations, they were necessarily led to a definition of $\boldsymbol{\sigma}(\mathbf{r})$ in terms of molecular positions and momenta. This approach demands quite a bit of algebra which we are not going to give here. As we are interested in a definition of the pressure tensor, we use $\mathbf{P}(\mathbf{r}) = -\boldsymbol{\sigma}(\mathbf{r})$ to write the final IK-expressions for the pressure tensor

$$\mathbf{P}(\mathbf{r}) = \mathbf{P}^K(\mathbf{r}) + \mathbf{P}^U(\mathbf{r}) \quad (3.9)$$

where

$$\mathbf{P}^K(\mathbf{r}) = \left\langle \sum_{i=1}^N m_i (\mathbf{v}_i - \mathbf{u})(\mathbf{v}_i - \mathbf{u}) \delta(\mathbf{r}_i - \mathbf{r}) \right\rangle \quad (3.10)$$

denotes the contribution of the momentum flux to the pressure tensor and

$$\begin{aligned} \mathbf{P}^U(\mathbf{r}) = & -\frac{1}{2} \left\langle \sum_{i \neq j}^N \frac{\mathbf{r}_{ij} \mathbf{r}_{ij}}{r_{ij}} U'(r_{ij}) \left\{ 1 - \frac{1}{2} \mathbf{r}_{ij} \cdot \nabla_{\mathbf{r}} + \dots \right. \right. \\ & \left. \left. + \frac{1}{n!} (-\mathbf{r}_{ij} \cdot \nabla_{\mathbf{r}})^{n-1} + \dots \right\} \delta(\mathbf{r}_i - \mathbf{r}) \right\rangle \end{aligned} \quad (3.11)$$

is the configurational part, which arises from the interaction between particles. We have adopted a notation in which the product between two vectors is dyadic (thus leading to a second rank tensor) unless there is an explicit dot “ \cdot ” denoting the contraction of two tensorial quantities. In Eqs. (3.10) and (3.11) \mathbf{v}_i is the velocity of i -th particle, m_i its mass, \mathbf{u} the streaming velocity; U stands for the pair potential and $U'(r) = dU/dr$.

Consider an infinitesimal surface $d\mathbf{S}$ moving with streaming velocity. $\mathbf{P}^K(\mathbf{r}) \cdot d\mathbf{S}$ is the momentum transferred per unit time across the area dS due to the thermal distribution of the single particle velocities about the mean fluid velocity \mathbf{u} . Obviously, $\mathbf{P} = \mathbf{P}^K$ when no interaction is present. The kinetic part of the pressure tensor thus corresponds to the contribution of an ideal gas. In a fluid however, due to the strong interactions, it is the configurational part of the pressure tensor, \mathbf{P}^U , which dominates. At first sight, the exact meaning of \mathbf{P}^U seems not to be very clear. It is nevertheless possible to find a satisfactory interpretation of the configurational part of the pressure tensor. Starting from a purely mechanical definition of the $\mathbf{P}^U(\mathbf{r})$, Irving and Kirkwood obtained an expression equivalent to that given in Eq. (3.11) (see Appendix

A in [55]). They defined $\mathbf{P}^U(\mathbf{r})$ as the infinitesimal force $d\mathbf{F}$ per unit area acting across an infinitesimal surface $d\mathbf{S}$ due to interaction of particles on opposite sides of $d\mathbf{S}$,

$$d\mathbf{F}(\mathbf{r}) = -\mathbf{P}^U(\mathbf{r}) \cdot d\mathbf{S} . \quad (3.12)$$

With this choice they obtained the following expression for the potential part of the pressure tensor

$$\mathbf{P}^U(\mathbf{r}) = -\frac{1}{2} \int \frac{\mathbf{R}\mathbf{R}}{R} U'(R) \left(\int_0^1 d\alpha \rho^{(2)}(\mathbf{r} - \alpha\mathbf{R}; \mathbf{r} + (1-\alpha)\mathbf{R}) \right) d^3\mathbf{R} , \quad (3.13)$$

where $\rho^{(2)}(\mathbf{r}; \mathbf{r}')$ denotes the two-particle density

$$\rho^{(2)}(\mathbf{r}; \mathbf{r}') = \left\langle \sum_{i \neq j}^N \delta(\mathbf{r}_i - \mathbf{r}) \delta(\mathbf{r}_j - \mathbf{r}') \right\rangle . \quad (3.14)$$

Equation (3.13) can be interpreted as follows: The term $-\mathbf{R}\mathbf{R}U'/R$ is a tensorial generalization of the virial $-RU'$ of the integrand in Eq. (3.1). It accounts for the force $\mathbf{R}U'/R$ that a particle at \mathbf{r}_1 experiences from another particle at \mathbf{r}_2 ($\mathbf{R} = \mathbf{r}_2 - \mathbf{r}_1$). The virial has to be multiplied by the probability of finding two particles at \mathbf{r}_1 and \mathbf{r}_2 . The probability is proportional to the density $\rho^{(2)}(\mathbf{r}_1; \mathbf{r}_2)$ which depends explicitly on both particle positions for inhomogeneous systems. Therefore, different values of $\rho^{(2)}(\mathbf{r}_1; \mathbf{r}_2)$ are obtained for fixed \mathbf{R} when shifting particle 1 or 2 to position \mathbf{r} , where the pressure shall be determined, i.e. for $\mathbf{r}_1 = \mathbf{r}$ ($\alpha = 0$) or $\mathbf{r}_2 = \mathbf{r}$ ($\alpha = 1$) (see Fig. 3.1). The integral over α takes all of these contributions into account. The outer integral finally sums over the possible vectors \mathbf{R} which pass through $d\mathbf{S}$. Using Eq. (3.14) one obtains from (3.13)

$$\mathbf{P}^U(\mathbf{r}) = -\frac{1}{2} \left\langle \sum_{i \neq j}^N \frac{\mathbf{r}_{ij}\mathbf{r}_{ij}}{r_{ij}} U'(r_{ij}) \int_0^1 d\alpha \delta(\mathbf{r}_i - \mathbf{r} + \alpha\mathbf{r}_{ij}) \right\rangle \quad (3.15)$$

$$= -\frac{1}{2} \left\langle \sum_{i \neq j}^N \mathbf{r}_{ij}\mathbf{F}_{ij} \int_0^1 d\alpha \delta(\mathbf{r}_i - \mathbf{r} + \alpha\mathbf{r}_{ij}) \right\rangle , \quad (3.16)$$

where $\mathbf{r}_{ij} = \mathbf{r}_j - \mathbf{r}_i$ ($r_{ij} = |\mathbf{r}_{ij}|$). It is now easy to verify the equivalence of Eqs. (3.15) and (3.11): the only thing to do is to apply, in Eq. (3.15), a Taylor expansion of $\delta(\mathbf{r}_i - \mathbf{r} + \alpha\mathbf{r}_{ij})$ at $\alpha = 0$ and carry out the integration over α . Finally, we note that for a homogeneous system, the second term on the left side of the Eq. (3.1) can be found by averaging the Eq. (3.15) over the entire volume, V , of the system and setting $p^U = (P_{xx}^U + P_{yy}^U + P_{zz}^U)/3$.

We recall that there is an arbitrariness in the definition of $\mathbf{P}(\mathbf{r})$ via hydrodynamic analogy. This is due to the fact that only $\nabla \cdot \mathbf{P}(\mathbf{r})$ enters the equations of hydrodynamics. These equations are thus invariant under the gauge transformation

$$\mathbf{P}(\mathbf{r}) \rightarrow \mathbf{P}(\mathbf{r}) + \nabla \times \boldsymbol{\chi}(\mathbf{r}) , \quad (3.17)$$

where $\boldsymbol{\chi}$ is a vector function of position [55–57]. The alternative route of a mechanical definition does not remove the ambiguity either. First, we address the ambiguity in the calculation of $\mathbf{P}^U(\mathbf{r})$ which contains the contribution of the interparticle forces to the pressure tensor at \mathbf{r} . Somehow the non-local two-particle force, \mathbf{F}_{ij} , has to be reduced to a local force $d\mathbf{F}(\mathbf{r})$ [58]. We can reformulate the question: Which pairs of particles should contribute to the force across

$d\mathbf{S}$ situated at \mathbf{r} ? This ambiguity was already pointed out in the seminal work of Irving and Kirkwood. They required that “all definitions must have this in common – that the stress between a pair of molecules be concentrated near the line of centers. When averaging over a domain large compared with the range of intermolecular force, these differences are washed out, and the ambiguity remaining in the macroscopic stress tensor is of negligible order” (footnote on p. 829 of [55]). The choice of Irving and Kirkwood was to say that only those pairs of particles should give rise to $d\mathbf{F}$ for which the line connecting their centers of mass passes through $d\mathbf{S}$. This is the most natural choice [53]. This convention was used by the derivation of Eq. (3.13) Although less problematic, there is also an ambiguity in the kinetic contribution to $\mathbf{P}(\mathbf{r})$. This ambiguity is closely related to the interpretation of $\mathbf{P}^K(\mathbf{r}) \cdot d\mathbf{S}$ as momentum flux across the infinitesimal surface $d\mathbf{S}$. One should therefore calculate the momentum flux across $d\mathbf{S}$ at a given time, and then take the time average. The question is how the point in time when the particle crosses $d\mathbf{S}$ is determined? Is it when the particle just touches the surface? Or is it when its center of mass coincides with the position of the surface? Obviously, there are infinitely many possible definitions of a crossover time. For point particles however, the center of mass \mathbf{R}_{cm} and the position vectors \mathbf{r} coincide and thus the ambiguity is removed.

3.3 Planar Systems

For systems with pair potential, equations (3.10) and (3.11) are valid regardless of the shape of the system. Furthermore, they are *not* restricted to states at thermal equilibrium. However, as we are interested in studying equilibrium properties of thin (polymer) films confined between two impenetrable walls, we are going to focus on the case of planar systems. First we introduce the assumption of planar symmetry. Let z denote the distance from a surface. Averaging Eq. (3.10) over directions parallel to the surface yields

$$\begin{aligned} \mathbf{P}^K(z) &= \frac{1}{A} \int dx dy \mathbf{P}^K(\mathbf{r}) \\ &= \frac{1}{A} \left\langle \sum_{i=1}^N m_i (\mathbf{v}_i - \mathbf{u})(\mathbf{v}_i - \mathbf{u}) \delta(z_i - z) \right\rangle, \end{aligned} \quad (3.18)$$

where A denotes the size of a surface. Similarly, one obtains from Eq. (3.15)

$$\begin{aligned} \mathbf{P}^U(z) &= \frac{1}{2A} \int dx dy \mathbf{P}^U(\mathbf{r}) \\ &= -\frac{1}{2A} \left\langle \sum_{i \neq j}^N \frac{\mathbf{r}_{ij} \mathbf{r}_{ij}}{r_{ij}} U'(r_{ij}) \int_0^1 d\alpha \delta(z_i - z + \alpha z_{ij}) \right\rangle \end{aligned} \quad (3.19)$$

$$= -\frac{1}{2A} \left\langle \sum_{i \neq j}^N \frac{\mathbf{r}_{ij} \mathbf{r}_{ij}}{r_{ij}} U'(r_{ij}) \frac{1}{|z_{ij}|} \Theta\left(\frac{z - z_i}{z_{ij}}\right) \Theta\left(\frac{z_j - z}{z_{ij}}\right) \right\rangle, \quad (3.20)$$

where we have used

$$\int_0^1 d\alpha \delta(z_i - z + \alpha z_{ij}) = \frac{1}{|z_{ij}|} \Theta\left(\frac{z - z_i}{z_{ij}}\right) \Theta\left(\frac{z_j - z}{z_{ij}}\right). \quad (3.21)$$

In Eq. (3.20) $\Theta(x)$ denotes the Heaviside step function ($\Theta(x) = 0$ if $x < 0$ and 1 for $x > 0$).

It must be emphasized that, heretofore, no use was made from the assumption of thermal equilibrium. Equations (3.18) and (3.20) can thus be used to calculate the pressure tensor of non-equilibrium planar systems, such as those under shear stress.

We now add the assumption of thermal equilibrium. It follows immediately that the streaming velocity must vanish: $\mathbf{u} = \mathbf{0}$. As positions and velocities are uncorrelated, one can use the equipartition theorem and simplify Eq. (3.18) to

$$P_{\alpha\beta}^K(z) = k_B T \rho(z) \delta_{\alpha\beta}, \quad (3.22)$$

where $\alpha, \beta \in \{x, y, z\}$. $\rho(z)$ denotes the density at z averaged over tangential coordinates x and y . The kinetic part of the pressure tensor is thus diagonal. It is worth noting that the diagonal character of \mathbf{P}^K is a general property of equilibrium states. It does not depend on the geometry of the system under consideration. On the other side, \mathbf{P} must be diagonal for planar systems at thermal equilibrium [53, 59, 60] (otherwise shear forces would exist). It is easy to see from the symmetry of the system that the pressure tensor has only two independent components, $P_N(z)$ and $P_T(z)$, which are respectively the normal and the tangential components [53, 59, 60]. The pressure tensor $\mathbf{P}(z)$ can thus be written as

$$\mathbf{P}(z) = (\mathbf{e}_x \mathbf{e}_x + \mathbf{e}_y \mathbf{e}_y) P_T(z) + \mathbf{e}_z \mathbf{e}_z P_N(z), \quad (3.23)$$

where $\mathbf{e}_x, \mathbf{e}_y, \mathbf{e}_z$ are orthogonal unit vectors and the lateral, $P_T(z)$, and normal component, $P_N(z)$, of $\mathbf{P}(z)$ are given by

$$P_{zz}(z) = P_N(z) \quad \text{and} \quad P_{xx}(z) = P_{yy}(z) = P_T(z). \quad (3.24)$$

Extracting the appropriate expressions from Eqs. (3.20) and (3.22) one obtains the following result for the lateral and normal components of the pressure tensor (IK-Method) [53, 60]

$$P_N^{\text{IK}}(z) = \rho(z) k_B T - \frac{1}{2A} \left\langle \sum_{i \neq j} \frac{|z_{ij}|}{r_{ij}} U'(r_{ij}) \Theta\left(\frac{z - z_i}{z_{ij}}\right) \Theta\left(\frac{z_j - z}{z_{ij}}\right) \right\rangle, \quad (3.25)$$

$$P_T^{\text{IK}}(z) = \rho(z) k_B T - \frac{1}{4A} \left\langle \sum_{i \neq j} \frac{x_{ij}^2 + y_{ij}^2}{r_{ij}} \frac{U'(r_{ij})}{|z_{ij}|} \Theta\left(\frac{z - z_i}{z_{ij}}\right) \Theta\left(\frac{z_j - z}{z_{ij}}\right) \right\rangle. \quad (3.26)$$

The reader may have noticed that, in the above formula, there is no expression containing the external fields. It is nevertheless possible to take into account any external field in the frame of IK-method. First, we note that the lateral component P_T of the pressure tensor remains unchanged under the presence of a potential acting via $f^{\text{ext}}(z)$, f^{ext} being an arbitrary, but differentiable function. To obtain the contribution of the walls acting via such an external field to P_N , one can consider each wall as an additional particle of infinite mass and use Eq. (3.25) for the extended system of $N + 2$ particles. Our system of interest contains two impenetrable opposite walls at z_{botwall} and z_{topwall} . Thus, we have $z_{\text{botwall}} < z_i < z_{\text{topwall}}$ for all (inner) particles (i.e. excluding the wall particles). As we are interested in pressure tensor *inside* the system, we consider planes with $z_{\text{botwall}} < z < z_{\text{topwall}}$ only. Along with the identity

$$\Theta(\alpha x) = \begin{cases} \Theta(x) & : \alpha > 0 \\ \Theta(-x) & : \alpha < 0 \end{cases} \quad (3.27)$$

one obtains from Eq. (3.25)

$$\begin{aligned} P_N^{\text{walls,IK}}(z) &= \frac{1}{A} \left\langle \sum_{i=1}^N F_W(z_i - z_{\text{botwall}}) \Theta(z_i - z) \right\rangle \\ &\quad - \frac{1}{A} \left\langle \sum_{i=1}^N F_W(z_{\text{topwall}} - z_i) \Theta(z - z_i) \right\rangle. \end{aligned} \quad (3.28)$$

In Eq. (3.28) $F_W(z) = -dU_W(z)/dz$, From Eq. (3.28) it follows that the force F_W of a wall on a particle contributes to the normal pressure on a given plane if the plane lies between the particle and the wall.

3.3.1 Ambiguity in the Definition of P_T : Harasima's Approach

We recall that Eqs. (3.25) and (3.26) are based on a specific choice of mapping pairwise forces which are non local to a given point \mathbf{r} in space (see section 3.2). As we have already mentioned in section 3.2, there is no unique way of defining which pairs of particles contribute to the force at \mathbf{r} . This ambiguity was clearly demonstrated by Harasima in 1958 [61]. He gave an alternative expression to the pressure tensor of planar systems based on a different choice of the contributing interactions (see Fig. 3.1): Harasima considered a prisma whose base is dA . The force $d\mathbf{F}(\mathbf{r})$ is thought to result from all interactions between particles in the prisma and those on the side of dA to which the vector $d\mathbf{A}$ points. This also includes particles whose center line does not pass through dA . Harasima's choice corresponds to a contour which goes parallel to the walls (or the planar surface) from \mathbf{r}_1 to (x_2, y_2, z_1) and then along the normal to \mathbf{r}_2 [53, 62]. Using this convention he obtained the same results for the normal component as Irving and Kirkwood [Eq. (3.25)],

$$P_N^H(z) = P_N^{IK}(z) , \quad (3.29)$$

but a different expression for the lateral component of the pressure tensor [53, 61]

$$P_T^H(z) = \rho(z)k_B T - \frac{1}{4A} \left\langle \sum_{i \neq j} \frac{x_{ij}^2 + y_{ij}^2}{r_{ij}} U'(r_{ij}) \delta(z_i - z) \right\rangle . \quad (3.30)$$

Thus, the *tangential component*, P_T , of the pressure tensor is not uniquely defined. Consequently, the *pressure anisotropy*, $P_N - P_T$, is ambiguous. This ambiguity is extensively discussed in the literature [53, 55, 56, 58–63]. However, the integral over z of Eq. (3.26) is identical to that of Eq. (3.30). This implies that both the IK and the H-methods yield the same results for any physical quantity which does not depend on the local profile of the pressure tensor. In particular, they lead to the same values of the surface tension γ (Kirkwood–Buff formula [53])

$$2\gamma = \int_{-D/2}^{+D/2} [P_N(z) - P_T(z)] dz \quad (3.31)$$

$$= \frac{1}{4A} \left\langle \sum_{i \neq j} \frac{r_{ij}^2 - 3z_{ij}^2}{r_{ij}} U'(r_{ij}) \right\rangle . \quad (3.32)$$

The factor 2 arises from the existence of two walls at $z = -D/2$ and $z = D/2$ in our simulation, D being the distance from one wall to the other (i.e. the film thickness). However, moments of $P_N - P_T$, such as the so called “surface of tension” z_s , i.e. the position where the surface tension acts,

$$z_s = \frac{1}{2\gamma} \int_{-D/2}^{+D/2} z [P_N(z) - P_T(z)] dz , \quad (3.33)$$

depends on the different choices made to determine \mathbf{P}^U . This was already pointed out by Harasima [61].

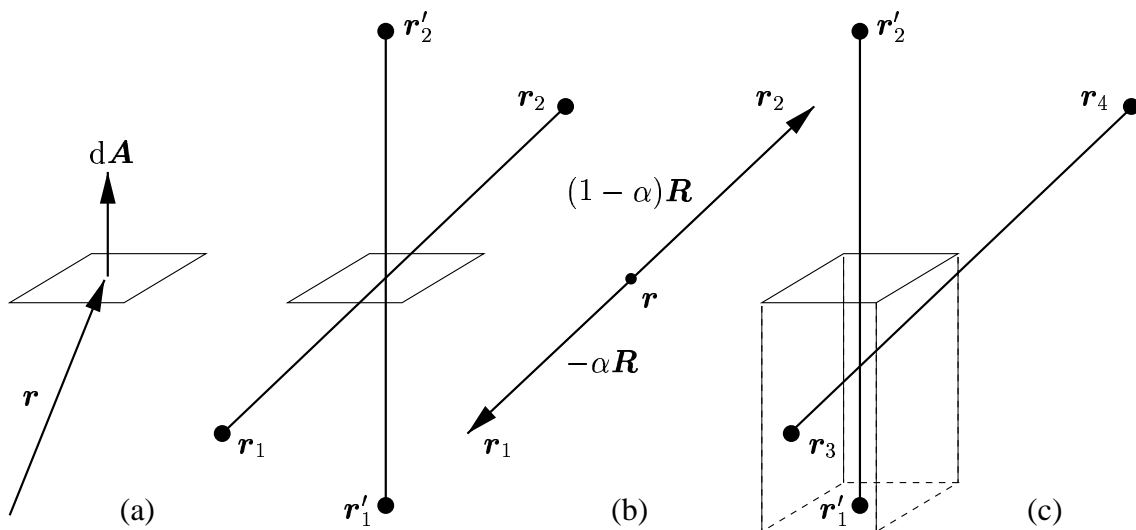


Figure 3.1: Schematic illustration of the different contributions to $\mathbf{P}^U(\mathbf{r})$ which are taken into account by Irving and Kirkwood (IK-method) and by Harasima (H-method). Let $d\mathbf{A}$ be an infinitesimal surface situated at position \mathbf{r} [panel (a)]. In the IK-method all particles whose center line passes through $d\mathbf{A}$ contribute to the force felt across the surface [panel (b)], whereas Harasima assumes that the interaction between the particles inside a prisma with base $d\mathbf{A}$ and those on the side to which $d\mathbf{A}$ is pointing causes the force at \mathbf{r} [panel (c)]. Panel (b) shows two possible contributions in the IK-method. If $\mathbf{R} = \mathbf{r}_2 - \mathbf{r}_1$, the position vectors of the particles can also be expressed as: $\mathbf{r}_1 = \mathbf{r} - \alpha \mathbf{R}$ and $\mathbf{r}_2 = \mathbf{r} + (1 - \alpha) \mathbf{R}$ ($0 \leq \alpha \leq 1$) [see Eq. (3.13)]. The interaction between \mathbf{r}'_1 and \mathbf{r}'_2 is also taken into account in the H-method, but not that between \mathbf{r}_1 and \mathbf{r}_2 . On the other hand, particles at \mathbf{r}_3 and $\mathbf{r}_4 (= \mathbf{r}_3 + \mathbf{R})$ contribute in Harasima's approach, whereas they don't in the IK-method.

In Sect. 3.4 we want to show for the polymer model considered that the differences in z_s obtained from the IK and H-expressions are small compared to the size σ of a particle, but not negligible. The ambiguous nature of z_s was discussed in detail in [53, 62]. In [62] a liquid-vapor interface is studied. Since there are no density oscillations near a free surface, which are characteristic of liquid-wall interfaces [64, 65] we expect the difference between the IK and H-expressions for $P_T(z)$ to be more pronounced for the thin films studied here.

3.3.2 The Method of Planes

Todd, Evans and Davis [56, 63] have introduced a variant of the original IK-derivation to determine the pressure tensor (termed “method of planes”) which avoids the ambiguity of defining a contour to relate two interacting particles. The problem is, however, not circumvented because one has to choose a gauge for both the pressure tensor and the momentum density [56]. The derivation starts from the continuity equations for the mass and momentum and leads to

$$P_{\alpha z}^U(z) = \frac{1}{2A} \left\langle \sum_{i=1}^M F_{\alpha i} \operatorname{sgn}(z_i - z) \right\rangle \quad (3.34)$$

$$= \frac{1}{2A} \left\langle \sum_{i \neq j} F_{\alpha ij} \left(\Theta(z_i - z) \Theta(z - z_j) - \Theta(z_j - z) \Theta(z - z_i) \right) \right\rangle \quad (3.35)$$

for the potential part of the pressure tensor and to

$$P_{\alpha z}^K(z) = \frac{1}{A} \left\langle \sum_{i=1}^M \frac{p_{\alpha i} p_{zi}}{m} \delta(z - z_i) \right\rangle \quad (3.36)$$

for the kinetic part ($\alpha = x, y, z$), where m is the mass of a particle. In Eq. (3.34) $\text{sgn}(x)$ is the sign function ($= 1$ if $x > 0$ and -1 for $x < 0$), $F_{\alpha i}$ is the α -component of the force exerted on particle i by all other particles and $p_{\alpha i}$ is the α -component of the peculiar momentum (i.e. $\mathbf{p}_i = m_i(\mathbf{v}_i - \mathbf{u})$) of particle i . Using the identity

$$|z_{ij}| \Theta\left(\frac{z - z_i}{z_{ij}}\right) \Theta\left(\frac{z_j - z}{z_{ij}}\right) = z_{ij} \left[\Theta(z - z_i) \Theta(z_j - z) - \Theta(z - z_j) \Theta(z_i - z) \right]. \quad (3.37)$$

one can verify that the diagonal components of the Eqs. (3.35) and (3.36) yield the IK-expression for the normal pressure [Eq. (3.25)]. Since Eq. (3.34) contains a single sum instead of the double sum of Eq. (3.25), it is computationally more convenient. Therefore, we used Eqs. (3.34) to calculate the configurational part of the normal pressure. Furthermore, we implemented Eq (3.36) for the calculation of the kinetic part of $P_{zx}(z)$, $P_{zy}(z)$ and $P_{zz}(z)$. However, Equations (3.35) and (3.36) are not sufficient for determining the surface tension γ , as they do not contain the diagonal components of the pressure tensor parallel to the walls, i.e. P_{xx} and P_{yy} . On the other hand, they provide a method for the calculation of the viscosity [56].

3.3.3 An Approximate Formula: IK1-method

In the literature (see [66, 67], for instance) there is still another formula for the pressure tensor, which is a kind of a “tensorized” version of the Harasima expression (3.30) (called “IK1” in [56])

$$\mathbf{P}^{\text{IK1}}(z) = \rho(z) k_B T \hat{\mathbf{1}} - \frac{1}{2A} \left\langle \sum_{i \neq j} \frac{\mathbf{r}_{ij} \mathbf{r}_{ij}}{r_{ij}} U'(r_{ij}) \delta(z_i - z) \right\rangle. \quad (3.38)$$

Todd, Evans and Daivis [56] noticed that Eq. (3.38) is equivalent to a zeroth-order approximation of the (full) IK-expression and that it leads to spurious unphysical oscillations of P_N . They thus concluded that this formula should not be used for inhomogeneous fluids. In the same reference, they gave a physical interpretation of the IK1-approximation in k -space (see Eq. (24) in [56]). One can also find a real-space interpretation in the following way. If one replaces the integral over α in Eq. (3.13) by the value of the integrand at the lower bound $\alpha = 0$ and follows the same argument which led to Eq. (3.15), one obtains

$$\mathbf{P}^U(\mathbf{r}) = -\frac{1}{2} \left\langle \sum_{i \neq j} \frac{\mathbf{r}_{ij} \mathbf{r}_{ij}}{r_{ij}} U'(r_{ij}) \delta(\mathbf{r}_i - \mathbf{r}) \right\rangle, \quad (3.39)$$

which gives the potential part of the IK1-expression (3.38) after averaging over the tangential coordinates.

Thus, the IK1-method corresponds to the assumption that the two-particle density $\rho^{(2)}(\mathbf{r}_1; \mathbf{r}_2)$ is unchanged upon translation of both arguments along the line $\mathbf{R} = \mathbf{r}_2 - \mathbf{r}_1$ which connects the points 1 and 2. However, the breaking of translational invariance is one of the basic characteristics of inhomogeneous systems. The more the system is inhomogeneous, the more the IK1-expression (3.38) for $P_N(z)$ should become inaccurate. On the other hand, integration over

z yields the same result as the IK- and H-approaches. Therefore, the IK1-method leads to the same surface tension γ , but to a different value for z_s compared to the other two methods.

In Sect. 3.4 we show that the IK1-result for z_s is too large to allow for an interpretation of z_s as the effective position of the interface, i.e. as the distance of closest approach of a particle to the wall. Furthermore, Eq. (3.38) leads to strong oscillations of P_N in contrast to the condition of mechanical stability which requires a constant profile for P_N (see section 3.3.4).

For the contribution of smooth walls within the IK1-approximation one finds the following expression in the literature [68]

$$\begin{aligned} P_N^{\text{walls,IK1}}(z) &= \frac{1}{A} \left\langle \sum_{i=1}^M F_W(z_i - z_{\text{botwall}}) \delta(z_i - z) \right\rangle \\ &- \frac{1}{A} \left\langle \sum_{i=1}^M F_W(z_{\text{topwall}} - z_i) \delta(z_i - z) \right\rangle, \end{aligned} \quad (3.40)$$

where the sum runs over inner particles only, as before. Since $F_W(z_i - z')\delta(z_i - z)$ is equivalent to $F_W(z - z')\delta(z_i - z)$, $P_N^{\text{walls,IK1}}(z)$ can be written as a product of the density profile and a contribution from the walls, i.e.

$$P_N^{\text{walls,IK1}}(z) = \left[F_W(z - z_{\text{botwall}}) - F_W(z_{\text{topwall}} - z) \right] \rho(z).$$

The formula (3.40) can be derived from Eq. (3.38) by somewhat ad-hoc replacing $1/2\{\delta(z - z_i) + \delta(z - z_{\text{wall}})\}$ by $\delta(z - z_i)$.

3.3.4 Mechanical Stability Requires $P_N = \text{const}$

In equilibrium, mechanical stability requires that the gradient of the pressure tensor vanishes [53, 57, 59, 60]

$$\nabla \cdot \mathbf{P} = \mathbf{0}, \quad (3.41)$$

where $\mathbf{0}$ denotes the nil vector. As argued in section 3.3 non-diagonal components of \mathbf{P} must vanish for a system with planar symmetry and the lateral components should be identical. So, we have

$$\frac{\partial P_{xx}}{\partial x} \mathbf{e}_x + \frac{\partial P_{yy}}{\partial y} \mathbf{e}_y + \frac{\partial P_{zz}}{\partial z} \mathbf{e}_z = \mathbf{0} \quad \text{and} \quad P_{xx}(\mathbf{r}) = P_{yy}(\mathbf{r}). \quad (3.42)$$

Since $\partial P_{xx}/\partial x = 0$, $\partial P_{yy}/\partial y = 0$ on the one hand, and $P_{xx} = P_{yy}$ on the other, the lateral components can be functions of z only. Furthermore, since $\partial P_{zz}/\partial z = 0$, the normal component of the pressure tensor is independent of the distance from the surfaces and must be identical to the external pressure $P_{N,\text{ext}}$. This gives

$$P_N(z) = P_{zz} = P_{N,\text{ext}} = \text{const} \quad \text{and} \quad P_T(z) = P_{xx}(z) = P_{yy}(z). \quad (3.43)$$

The argument presented here essentially follows the discussion of [53] (see p. 44 of [53]). We repeated it here to stress the erroneous character of expression (3.38). In Sect. 3.4 we will see that only the IK- (or H-) formula (3.25) satisfies condition (3.43). The independence of Eq. (3.25) on z was already proved analytically in the work of Harasima (see p. 224 of [61]). This important property helps us to set the pressure in the simulations for a given wall separation and temperature.

3.4 Results

3.4.1 Profiles of $P_N(z)$: IK1 versus (full) IK

In order to analyze the pressure profiles for our model we studied different film thicknesses ($D = 3, 5, 10, 20$) at various temperatures while always keeping $P_{N,\text{ext}} = 1$. For this external pressure many results for the bulk behavior are known [37, 46, 48–50]. Here, we want to discuss two representative cases: $D = 3$ ($\approx 2R_g$ where $R_g \simeq 1.45$ is the bulk radius of gyration) at $T = 1$, and $D = 10$ ($\approx 7R_g$) at $T = 0.42$. The temperature $T = 1$ corresponds to the high-temperature, (ordinary) liquid state of the melt, whereas $T = 0.42$ belongs to the supercooled temperature regime close to the critical temperature of mode-coupling theory ($T_c(D = 10) \approx 0.39$ [69]).

For a film of thickness $D = 3$ ten independent runs of 10^6 time steps were simulated at $T = 1$ and $P_{N,\text{ext}} = 1$. The total number of particles was 1000 corresponding to 100 chains of length $N = 10$ (this number of monomers per chain was always kept fixed in our simulations). For $D = 10$ five independent runs were done at $T = 0.42$. The length of a run was 4.4×10^7 time steps. Samples were taken every 1000 steps. The much longer simulation time in this case is necessary to allow for a detailed analysis of the dynamics of the system which is very slow at this temperature.

Figures 3.2 and 3.3 show the simulation results for the normal component of the pressure tensor, P_N , calculated according to the IK- and IK1-prescriptions, respectively [see Eq. (3.25) and Eq. (3.38)]. Furthermore, they resolve the different contributions stemming from the kinetic part, the virial (forces between inner particles, i.e. excluding the walls) and the walls. The striking difference between both prescriptions is that the IK1-method yields strong oscillations, whereas the pressure profile of the IK-method is constant throughout the film, in agreement with the condition of mechanical stability [see Sect. 3.3.4].

Since the kinetic contribution to P_N is proportional to the density profile $\rho(z)$, Fig. 3.2 shows that practically no particle is present in the vicinity of the walls. The excluded-volume interaction creates a depletion zone of about 0.8 between the wall ($z_{\text{wall}} = \pm 1.5$) and the monomer positions at this temperature. Any plane in this region separates all particles of the system, which lie on the side of the plane facing towards the inner part of the film, from the wall on the other side. There is no interparticle force across the plane and thus the virial contribution to the normal pressure vanishes. The behavior of $P_N(z)$ near the wall arises only from the wall-particle interaction. This interaction does not depend on the position of the plane as long as all the particles stay on the opposite side, i.e. as long as $\rho(z) \approx 0$. This explains why P_N is constant in the region close to the walls. With increasing distance from the wall the density starts to increase from zero. Then, the kinetic and virial parts begin to contribute, whereas the effect of the walls decreases. In this intermediate region none of the contributions is negligible, but their sum still remains constant, in accord with Eq. (3.43). Very far from the walls the contribution of the walls to P_N becomes negligible. There, one expects that the variations of the kinetic and virial terms must be opposite to each other. A first indication of this opposite behavior can be observed in Fig. 3.2. A better demonstration is, however, shown in Fig. 3.4 where the film thickness is large enough to exhibit an inner region with negligible wall contribution.

On the contrary, the various contributions of the IK1-methods are (almost) in phase. Figure 3.3 illustrates that the strong deviation of P_N^{IK1} from a constant is caused by the interaction of the wall with the monomers close to the maximum of $\rho(z)$ if $D = 3$. If the film thickness increases, Fig. 3.5 shows that the oscillations of P_N propagate through the whole film. Close to the wall, the dominant contribution still comes from the wall-monomer interaction, whereas

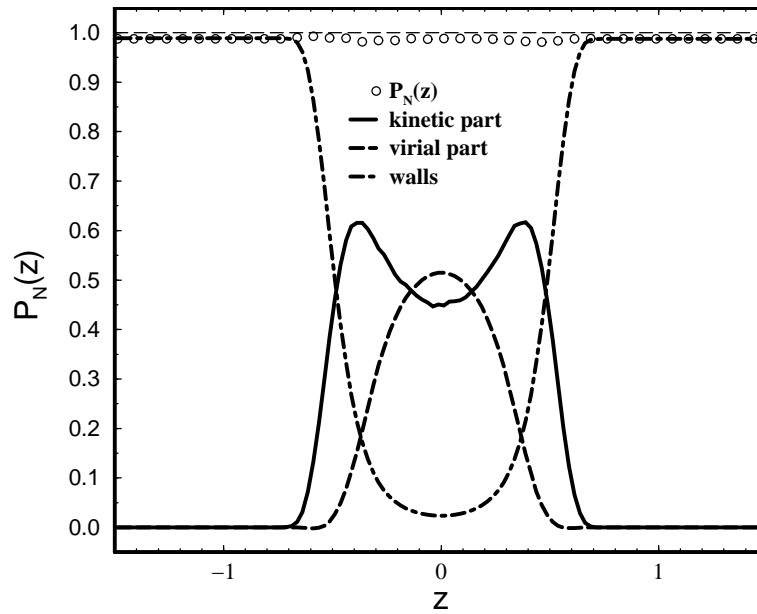


Figure 3.2: Different contributions to the normal pressure profile $P_N(z)$ for a film of thickness $D = 3$ ($\approx 2R_g$) at $T = 1$ (high-temperature liquid state) and $P_{N,\text{ext}} = 1$ according to the (full) IK-method [see Eq. (3.25)]. The H-method yields the same result [see Eq. (3.29)]. The various parts, kinetic (full line), virial (dashed line) and wall (dash-dotted), mutually balance one another to yield a constant profile $P_N(z) = P_{N,\text{ext}}$ (circles), as required by mechanical stability (see Sect. 3.3.4). The difference between $P_{N,\text{ext}} = 1$ (vertical dashed line) and $P_N(z)$ shows the accuracy to which we could fix $P_{N,\text{ext}}$ in the simulation for this film thickness. The difference is smaller than 2%.

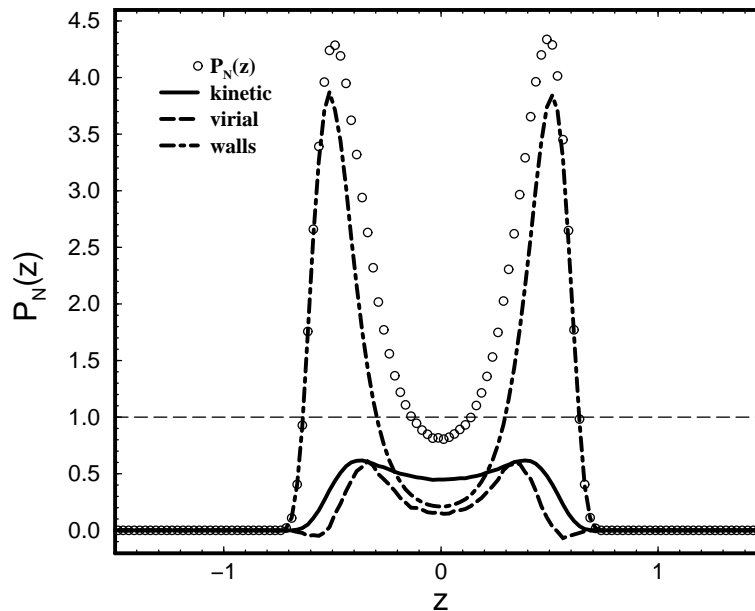


Figure 3.3: Different contributions to the normal pressure profile $P_N(z)$ for a film of thickness $D = 3$ ($\approx R_g$) at $T = 1$ (high-temperature liquid state) and $P_{N,\text{ext}} = 1$ (vertical dashed line) according to the IK1-method [see Eq. (3.38)]. Contrary to Fig. 3.2, the various parts, kinetic (full line), virial (dashed line) and wall (dash-dotted), do not balance, but amplify one another, resulting in a (non-physical) oscillatory structure of $P_N(z)$ (circles).

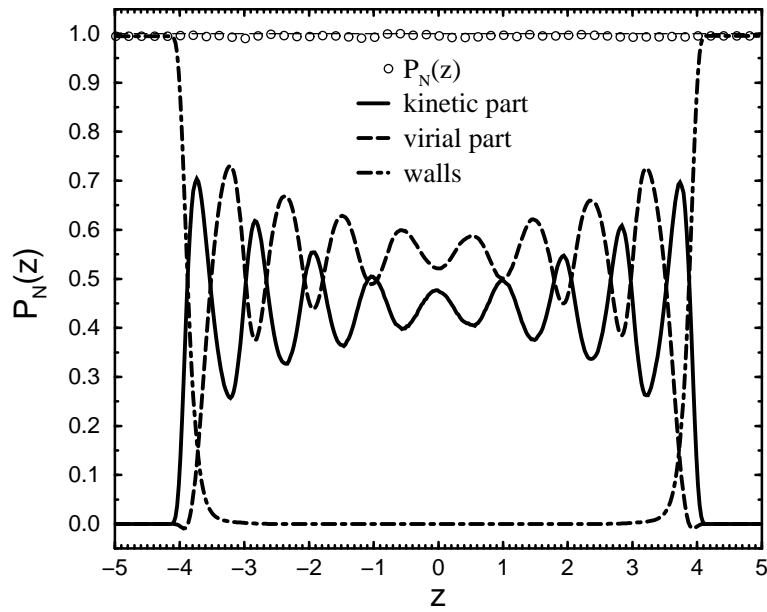


Figure 3.4: Different contributions to the normal pressure profile $P_N(z)$ for a film of thickness $D=10$ ($\approx 7R_g$) at $T=0.42$ (supercooled state close to $T_c \approx 0.39$ [69]) and $P_{N,\text{ext}}=1$ (vertical dashed line) according to the IK-method [see Eq. (3.25)]. The H-method gives the same result [see Eq. (3.29)]. As in Fig. 3.2, the various parts, kinetic (full line), virial (dashed line) and wall (dash-dotted), mutually balance one another and sum up to a constant profile $P_N(z) = P_{N,\text{ext}}$ (circles), in agreement with the condition of mechanical stability (see Sect. 3.3.4).

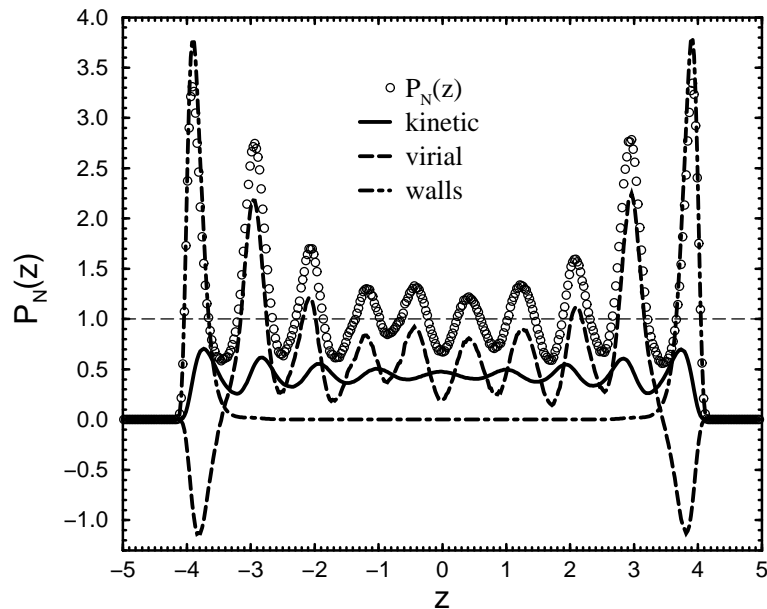


Figure 3.5: Different contributions to the normal pressure profile $P_N(z)$ for a film of thickness $D=10$ ($\approx 7R_g$) at $T=0.42$ (supercooled state close to $T_c \approx 0.39$ [69]) and $P_{N,\text{ext}}=1$ (vertical dashed line) according to the IK1-method [see Eq. (3.38)]. As in Fig. 3.3, the various parts, kinetic (full line), virial (dashed line) and wall (dash-dotted), give rise to a non-constant pressure profile (circles) contrary to the requirement of mechanical stability.

the oscillations in the inner part of the film are in phase with the virial. The contribution of the virial is negative close to the wall, reflecting a predominantly attractive interaction between the monomers. This dominance of the attractive interaction is also visible for the (correct) IK-method, but is much less pronounced in this case.

The situation becomes more complicated when studying the lateral component of the pressure tensor. Here, the two alternative formulas, Eqs. (3.26) and (3.30), can yield completely different profiles. Figures 3.6 and 3.7 compare the IK and the H-versions to calculate the lateral pressure $P_T(z)$ for $D = 3$, $T = 1$ and $D = 10$, $T = 0.42$, respectively. Whereas both methods oscillate in phase with one another for the thicker film, they are anti-correlated for $D = 3$. The lateral pressure of the IK-method is positive close to the walls, but negative in the middle of the film, whereas the behavior is just vice versa for the H-method. Due to the aforementioned ambiguity of $P_T(z)$ it is impossible to decide which method yields the physically more realistic result. If the film thickness increases, the qualitative difference between the IK- and H-methods (almost) vanishes and only quantitative differences remain. The oscillations of $P_T(z)$ clearly reflect the monomer profile. In the inner portion of the film they are much weaker for the H-method than for of the IK-method. This is related to the local nature of Eq. (3.30) due to the presence of delta-function. Density oscillations are thus incorporated not only in the kinetic term, but also also in the virial part of the Harasima formula. Both terms partially cancel each other. Although the profile generated by Eq. (3.30) is thus closer to $P_{N,\text{ext}}$ than that of Eq. (3.26), this should not be considered as an argument in favor of the H-method. A clear distinction between both methods would only be possible if one could find a quantity which specifically probes $P_T(z)$ and whose behavior is known *a priori*, as it was the case for $P_N(z)$.

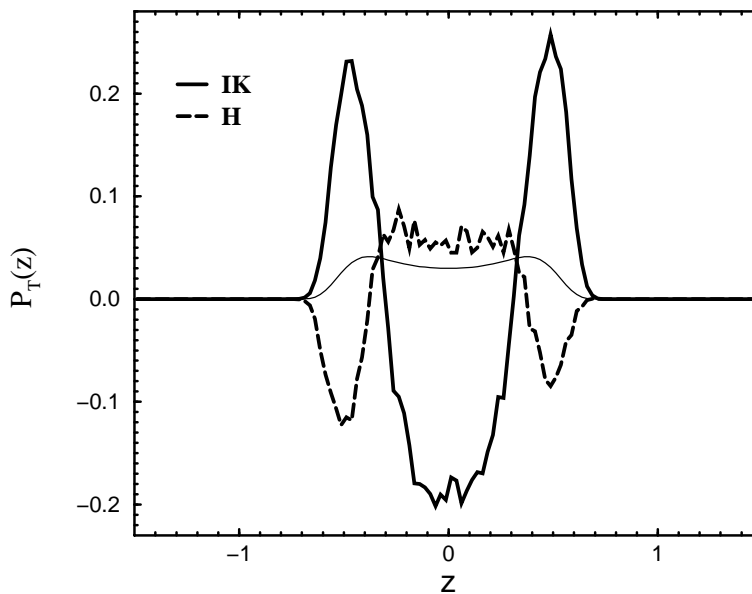


Figure 3.6: Tangential component $P_T(z)$ of the pressure tensor as obtained from the IK-formula [Eq. (3.26)] and from the H-formula [Eq. (3.30)] for $D = 3$ ($\approx 2R_g$), $T = 1$ (high-temperature liquid state) and $P_{N,\text{ext}} = 1$. The thin solid line shows the kinetic contribution $k_B T \rho(z)$ (divided by 15 to put it on the scale of the figure).

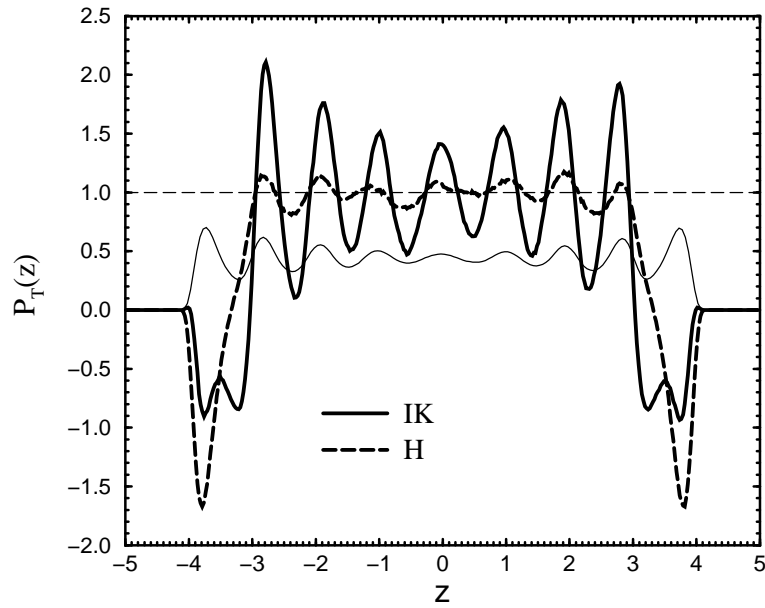


Figure 3.7: Tangential component $P_T(z)$ of the pressure tensor as obtained from the IK-formula [Eq. (3.26)] and from the H-formula [Eq. (3.30)] for $D = 10$ ($\approx 7R_g$), $T = 0.42$ (supercooled state close to $T_c \approx 0.39$ [69]) and $P_{N,\text{ext}} = 1$ (vertical dashed line). The thin solid line shows the kinetic contribution $k_B T \rho(z)$.

3.4.2 Surface Tension and Surface of Tension

As mentioned in Sect. 3.3.1, integration of the pressure profiles over z yields the same result for the IK-, H- and IK1-expressions. Therefore, all methods must lead to the same surface tension γ [i.e. Eq. (3.32)]. This expectation is nicely borne out by the simulation data for all film thicknesses and temperatures studied, where γ was calculated by Eq. (3.31). Figure 3.8 exemplifies this behavior for $D = 5$ ($\approx 3R_g$). With decreasing temperature the surface tension increases by about a factor of 1.5. Qualitatively, this temperature dependence is expected. The monomer density of a polymer melt close to a hard wall exhibits a profile that is large at the wall and decays towards the bulk value in an oscillatory fashion with increasing distance from the wall (see Fig. 3.11 as an example) [65]. Since the average density grows with decreasing temperature in a simulation at constant pressure, the maxima and minima of the profile become more pronounced. This means that there are more monomers in the highly populated layers at low than at high temperatures and that the oscillations of profile become more long-ranged. These effects tighten the film so that the free energy needed to move monomers out of the interface, i.e. the surface tension, should increase as temperature decreases. The same effect is expected when reducing the film thickness because the layering is more pronounced in thinner films. This expectation is borne out by the simulation data (see Fig. 3.9).

Contrary to γ , the discussion of Sect. 3.3.1 implies that the surface of tension, z_s , depends on the method applied. This fact is illustrated in Fig. 3.10 which shows the temperature dependence of z_s for the IK-, H- and IK1-methods. The difference between IK and the H-methods is rather small, whereas the IK1-result lies substantially above the values of the other two methods. Since z_s can be interpreted as the distance of closest approach of a monomer to the wall, i.e. as the effective position of the wall, the following simple argument rules out the IK1-result: At temperature T , a particle can only penetrate into a (soft) wall up to the point, z_w , where the wall

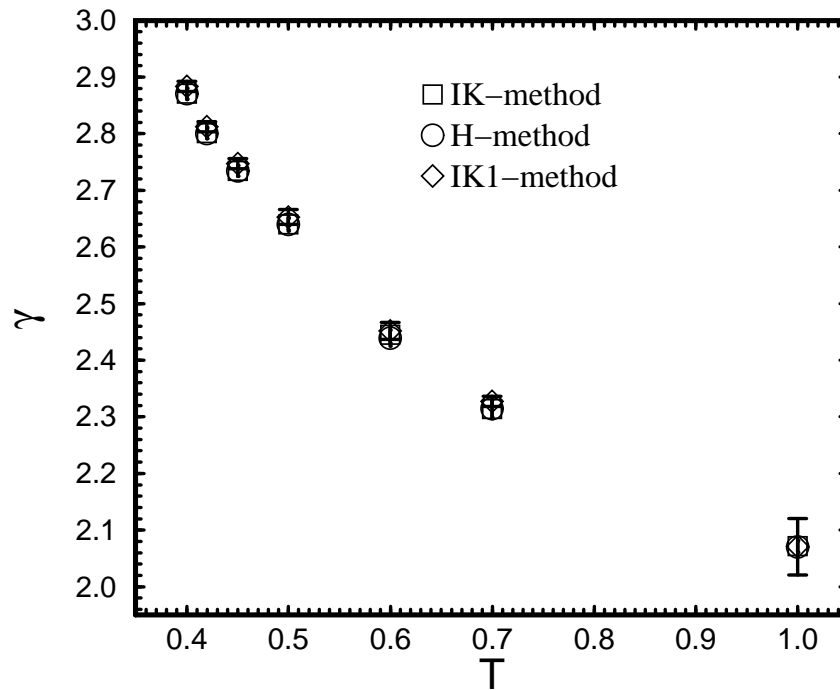


Figure 3.8: Temperature dependence of the surface tension, γ , calculated by Eq. (3.31), using the IK-, H- and IK1-methods for $D=5$ ($\approx 3R_g$) and $P_{N,\text{ext}}=1$. The temperatures shown range from the high-temperature, liquid state of the film to the supercooled state.

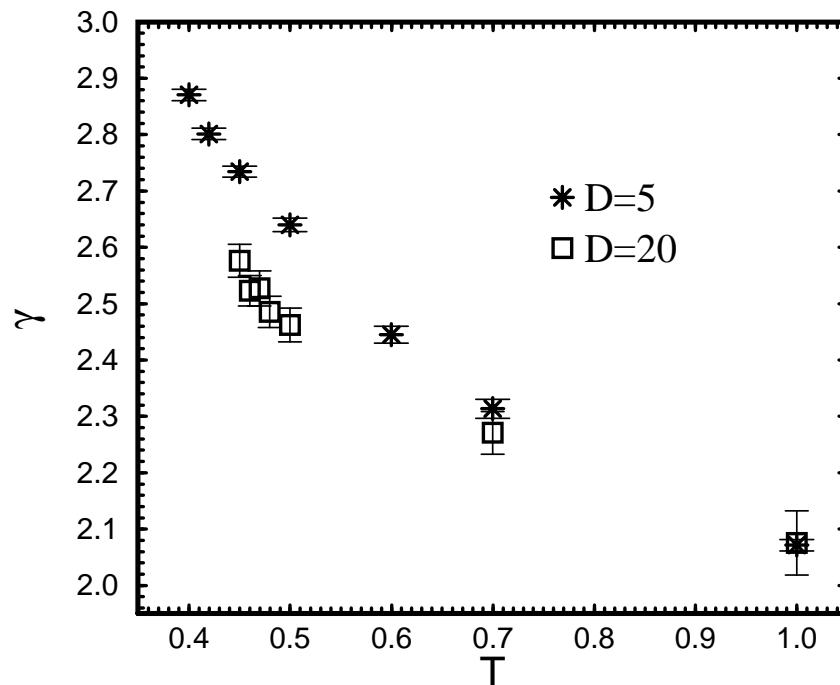


Figure 3.9: Comparison of the temperature dependence of the surface tension, γ , for $D=5$ ($\approx 3R_g$) and $D=20$ ($\approx 14R_g$). The results of the IK-method are shown only. The other methods (H- and IK1-methods) yield the same γ 's within the error bars, as exemplified in Fig. 3.8 for $D=5$. The external pressure is $P_{N,\text{ext}}=1$. The temperatures shown range from the high-temperature, liquid state of the film to the supercooled state.

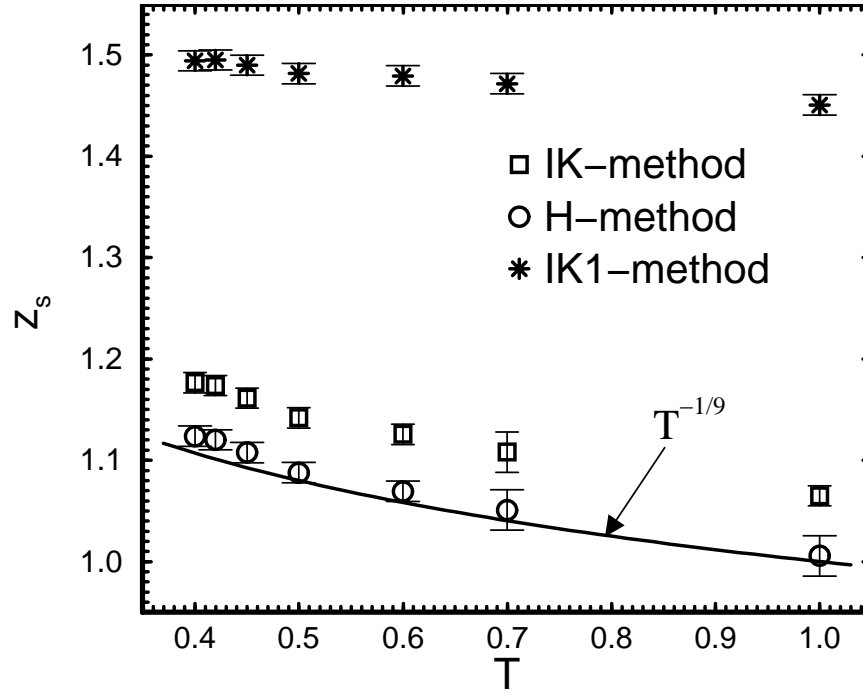


Figure 3.10: Temperature dependence of the surface of tension z_s [Eq. (3.33)] determined by the IK-, H- and IK1-methods for $D=5$ and $P_{N,\text{ext}}=1$. The solid line shows the simple estimate, $z_w = 1/T^{1/9}$ [Eq. (3.44)], for the position of the wall.

potential balances thermal energy of the particle, i.e. $U_w(z_w)/T=1$. Using Eq. (2.4) this gives

$$z_w = \left(\frac{1}{T}\right)^{1/9}. \quad (3.44)$$

Equation (3.44) is compatible with the IK- and H-predictions, but not with the IK1-result. Another way to illustrate this point is shown in Fig. 3.11 where we plotted the monomer density profile of a film of thickness $D=10$ at $T=0.42$. With increasing film thickness the IK- and H-values for z_w approach one another – for $D=20$ for example, they are indistinguishable within the error bars (not shown here) –, but the disparity to the IK1-result remains. The figure clearly shows that the IK1-method places the effective wall position deeply into the interior of the film, whereas it has to be situated in the region where the density profile approaches zero.

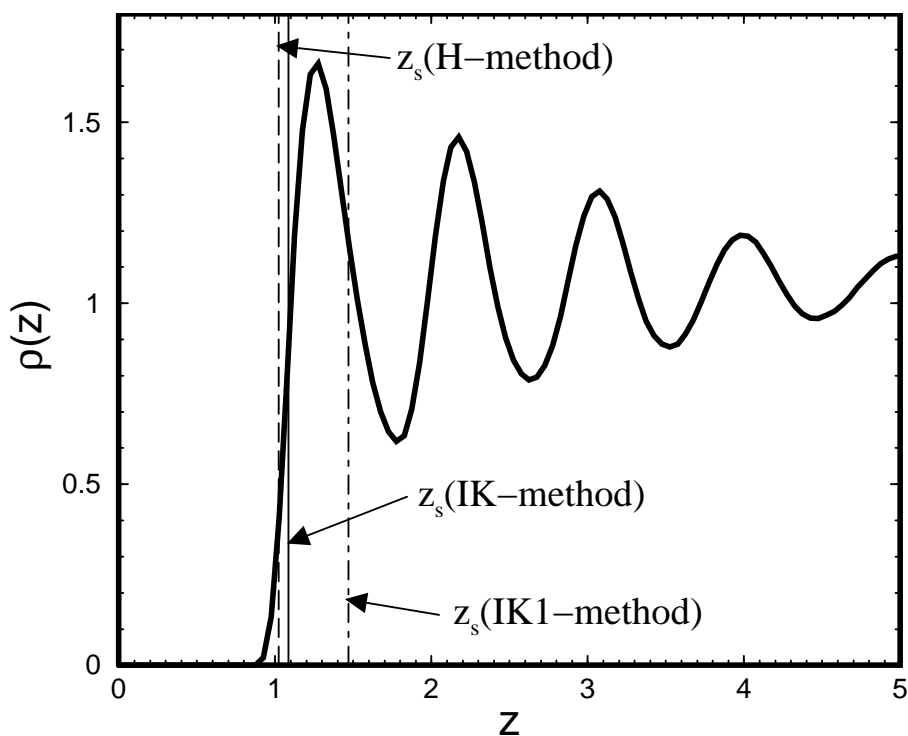


Figure 3.11: Monomer density profile of a film of thickness $D = 10$ ($\approx 7R_g$) at $T = 0.42$ ($> T_c \approx 0.39$ [69]) and $P_{N,\text{ext}} = 1$. Since the profile is symmetric around the middle of the film, the figure only shows one half of it. The scale of the abscissa was shifted so that the wall is placed at $z=0$. The vertical lines mark the values of z_s computed according to the IK-, H- and IK1-methods.

Chapter 4

Molecular Dynamics Simulation Techniques

The aim of a molecular dynamics (MD) simulation is to solve the Newtonian equation of motion

$$m_i \mathbf{r}_i = \mathbf{F}_i \quad (4.1)$$

for each particle i of a many body system of N particles. Here, \mathbf{F}_i is the force on particle i and \mathbf{r}_i its position. Obviously, this set of equations will conserve the total energy of the system, provided that the force \mathbf{F}_i can be derived from a potential $U(\mathbf{r}^N)$. Thus, for an ergodic system with conservative forces, such a simulation will drive the system through only that fraction of the phase space which corresponds to the initial energy E_0 of the system. In terms of statistical mechanics, one can say that the points of the phase space *visited* by the system belong to a microcanonical ensemble. It must be noted that Eq. (4.1), in principle, could also be used to simulate a system in thermal contact with a heat bath. One should then solve this equation for all particles including those of the heat bath. This approach is clearly fully unpracticable. Fortunately, techniques have successfully been developed to overcome this difficulty. In this chapter we will discuss some of them. However, if one is interested in analysing the properties of isolated systems, it is satisfactory to seek a solution of Eq. (4.1). This leads us to the following section, *Microcanonical Ensemble Simulation*.

4.1 Microcanonical Ensemble Simulation

We are going to derive here an elaborated algorithm to carry out a simulation at constant energy known as velocity-Verlet-algorithm. We follow a derivation given in [70, 71]. Let us denote a point in phase space as

$$\Gamma = (\mathbf{r}^N, \mathbf{p}^N) = (\mathbf{r}_1, \dots, \mathbf{r}_N; \mathbf{p}_1, \dots, \mathbf{p}_N)$$

and let $H = H(\Gamma)$ be the Hamiltonian of the system. The time evolution of a dynamical function $A(\Gamma(t))$ which does not explicitly depend on time, is given by

$$\begin{aligned} \frac{dA}{dt} &= \sum_i \left\{ \dot{\mathbf{r}}_i \cdot \frac{\partial}{\partial \mathbf{r}_i} + \dot{\mathbf{p}}_i \cdot \frac{\partial}{\partial \mathbf{p}_i} \right\} A \\ &= i\mathcal{L} A \end{aligned} \quad (4.2)$$

with the formal solution

$$A(\Gamma(t)) = \exp(i\mathcal{L}t)A(\Gamma(0)) . \quad (4.3)$$

The operator \mathcal{L} in Eq. (4.2) is called the Liouville operator of the system and, obviously, is defined as

$$i\mathcal{L} \equiv \sum_i \left\{ \dot{\mathbf{r}}_i \cdot \frac{\partial}{\partial \mathbf{r}_i} + \dot{\mathbf{p}}_i \cdot \frac{\partial}{\partial \mathbf{p}_i} \right\}. \quad (4.4)$$

It will be shown in appendix (A.1) that \mathcal{L} is Hermitian, i.e. $\mathcal{L} = \mathcal{L}^\dagger$. One of the consequences of the Hermitian property of \mathcal{L} is that the *propagator*

$$U(t) \equiv \exp(i\mathcal{L}t) \quad (4.5)$$

is unitary, i.e.

$$U^{-1}(t) = U^\dagger(t). \quad (4.6)$$

Using the unitary property of U , it is demonstrated in appendix (A.1) that the volume of a given region in phase space remains unchanged under the action of U , i.e. under time evolution within Hamiltonian dynamics. On the other hand, it follows directly from the definition (4.5) of U , that this operator is time reversible

$$U^{-1}(t) = U(-t). \quad (4.7)$$

An important implication of the time reversibility of $U(t)$ is that two distinct phase points $\Gamma(t_1)$ and $\Gamma'(t_1)$ remain distinct at all times t_2 before or after t_1 . For, if $\Gamma(t_2) = \Gamma'(t_2)$ for a given time t_2 , one can show $\Gamma(t_1) = U(t_1 - t_2)\Gamma(t_2) = U(t_1 - t_2)\Gamma'(t_2) = \Gamma'(t_1)$ which is in contradiction to the assumption of distinctness at t_1 .

Time reversibility and volume preserving properties make U an attractive candidate for the construction of numerically stable integration schemes [70, 71]. One tries to decompose $\exp(i\mathcal{L}t)$ so that the relation

$$\exp(\mathbf{c} \cdot \frac{\partial}{\partial \mathbf{q}}) f(\mathbf{q}) = f(\mathbf{q} + \mathbf{c}) \quad (4.8)$$

can be used to propagate the system's positions and momenta¹. For this purpose, one introduces \mathcal{L}_1 and \mathcal{L}_2 ($i\mathcal{L} = i\mathcal{L}_1 + i\mathcal{L}_2$)

$$i\mathcal{L}_1 \equiv \sum_i \dot{\mathbf{r}}_i \cdot \frac{\partial}{\partial \mathbf{r}_i} \quad (4.9)$$

$$i\mathcal{L}_2 \equiv \sum_i \dot{\mathbf{p}}_i \cdot \frac{\partial}{\partial \mathbf{p}_i}. \quad (4.10)$$

As the operators \mathcal{L}_1 and \mathcal{L}_2 do not commute, one applies the Trotter formula [72] to obtain an approximate decomposition

$$e^{i(\mathcal{L}_1 + \mathcal{L}_2)t} = [e^{i\mathcal{L}_1\Delta/2} e^{i\mathcal{L}_2\Delta} e^{i\mathcal{L}_1\Delta/2}]^P + \mathcal{O}(t\Delta^2) \quad (4.11)$$

where $\Delta = t/P$ is the time step of the resulting algorithm (see below) and must be chosen small enough to make the truncation error, which scales with Δ^2 , negligible. One could, of

¹The validity of Eq. (4.8) is easily seen in applying a Taylor expansion to $f(\mathbf{q} + \mathbf{c})$ which leads to the lhs of (4.8).

course, interchange \mathcal{L}_1 with \mathcal{L}_2 on the rhs of Eq. (4.11) and thus obtain another equally valid decomposition. Other choices of the Trotter decomposition are also possible, leading in general to different algorithms. We note that the discretization error is not only proportional to the square of the time step, Δ^2 , but also to the whole length of the simulation t . Thus, for a given time step, Δ , longer simulation runs will lead on average to greater errors. In other words, in order to maintain a constant discretization error, one should adapt the time step Δ to keep the product $t\Delta^2$ unchanged.

Neglecting the term $\mathcal{O}(t\Delta^2)$ in Eq. (4.11), the exact integration of the equations of motion (from $t = 0$) until time t can be approximated by P discrete integration steps each of length $\Delta = t/P$. A discrete integration step is thus defined through an application of the product

$$e^{i\mathcal{L}_1\Delta/2}e^{i\mathcal{L}_2\Delta}e^{i\mathcal{L}_1\Delta/2}.$$

Applying this product on the initial state $\Gamma(t) = (\mathbf{r}^N(t); \mathbf{p}^N(t))$ and using the relation (4.8) one obtains the following expressions for the position and momentum of a particle i of the system

$$\mathbf{r}_i(t + \Delta) = \mathbf{r}_i(t) + \frac{\mathbf{p}_i(t)}{m_i} \Delta + \mathbf{F}_i(t) \frac{\Delta^2}{2m_i} \quad (4.12)$$

$$\mathbf{p}_i(t + \Delta) = \mathbf{p}_i(t) + \frac{\Delta}{2m_i} [\mathbf{F}_i(t) + \mathbf{F}_i(t + \Delta)]. \quad (4.13)$$

This is the well-known velocity-Verlet-Algorithm. One of the important properties of this algorithm is that it preserves the phase space volume in each discrete step [70]. This can be easily seen by evaluating the Jacobian determinant of the transformation $\Gamma(t) \rightarrow \Gamma(t + \Delta)$, i.e. $|\partial\Gamma(t + \Delta)/\partial\Gamma(t)|$ which turns out to be unity. Also the time reversibility of the algorithm is valid on the discrete level. These are the main reasons for great stability and good accuracy of the Eqs. (4.12) and (4.13).

4.2 Extended Lagrangian Methods: *NVT*-Ensemble

As mentioned above, the simple integration of the Newtonian equations of motion Eq. (4.1) is only useful when studying isolated systems. In practice, one is often interested in studying physical properties at a given temperature and/or pressure. To simulate at constant T , one could in principle consider an extended system consisting of a heat bath plus the actual system of interest and apply Eq. (4.1) to that. However, this approach is not feasible. It is practically impossible to take into account a huge number of particles building up the heat bath. The situation does not improve if one also has to keep the external pressure at a given value.

Therefore, a lot of work has been done in this domain and several efficient techniques have been developed over the past 20 years to perform MD-simulation of a system under the condition of constant temperature and/or pressure [57, 73–87]. We are going to describe below a popular approach known as “extended Lagrangian method”. Within this approach a physical system is extended to a composite system consisting of the physical system and an external system. The conservation laws still hold for the extended system, but the total energy or the volume of the physical system is allowed to fluctuate [73, 88].

A pioneering work in this field was done by H. C. Andersen [73], who introduced an extended Lagrangian method for deriving isobaric equations of motion. He replaced the coordinates \mathbf{r}_i , $i = 1, \dots, N$, of the atoms by scaled coordinates

$$\boldsymbol{\rho}_i \equiv \mathbf{r}_i/V^{1/3}, \quad i = 1, \dots, N, \quad (4.14)$$

where V denotes the volume of the system. He then introduced a Lagrangian containing the system volume V as an additional degree of freedom

$$L_{\text{Andersen}} = V^{2/3} \sum_i \frac{m_i \dot{\boldsymbol{\rho}}_i^2}{2} - U(V^{1/3} \boldsymbol{\rho}^N) + \frac{M_V}{2} \dot{V}^2 - P_{\text{ext}} V, \quad (4.15)$$

where $\boldsymbol{\rho}^N \equiv (\boldsymbol{\rho}_1, \dots, \boldsymbol{\rho}_N)$ and U is the potential energy of the system and P_{ext} the external pressure. The parameter M_V plays the role of the mass for the volume motion. It can be interpreted as the mass of a movable piston and therefore is called ‘‘piston mass’’. Andersen could demonstrate that for an ergodic system, the equations of motion derived from the Lagrangian L_{Andersen} drive the system through the phase space due to the isoenthalpic-isobaric probability distribution [73]. In the same reference, Andersen mentioned that it might be possible to find an appropriate Lagrangian which allows energy fluctuations to generate the isothermal case. This Lagrangian was, however, unknown to him and therefore he resorted to the use of stochastic forces to change the kinetic energy of particles in order to keep the mean kinetic energy and thus the temperature constant.

The next great progress was achieved by Nosé [77–79] who introduced an extended Lagrangian, from which he derived equations of motion generating an isothermal probability density

$$L_{\text{Nosé}} = s^2 \sum_i \frac{m_i \dot{\mathbf{r}}_i^2}{2} - U(\mathbf{r}^N) + \frac{Q}{2} \dot{s}^2 - \frac{g}{\beta} \ln(s), \quad (4.16)$$

where $\beta = 1/(k_B T_{\text{ext}})$ is the inverse temperature. The additional parameter s serves as dynamical scaling of time.

The reader may now guess the form of the Lagrangian, from which one can derive equations of motion for the isothermal-isobaric case (NpT -ensemble),

$$\begin{aligned} L_{\text{NA}} &= s^2 V^{2/3} \sum_i \frac{m_i \dot{\boldsymbol{\rho}}_i^2}{2} - U(V^{1/3} \boldsymbol{\rho}^N) \\ &\quad + \frac{M_V}{2} \dot{V}^2 - P_{\text{ext}} V + \frac{Q}{2} \dot{s}^2 - \frac{g}{\beta} \ln(s). \end{aligned} \quad (4.17)$$

For the sake of simplicity, we will first derive equations of motion from the simpler Lagrangian $L_{\text{Nosé}}$ and demonstrate that it generates the NVT -probability distribution. The extension to the case of NpT -ensemble is then straightforward. To this end, we first apply the usual Lagrange formalism and calculate the appropriate expressions for the conjugate momenta

$$\boldsymbol{\pi}_i = \frac{\partial L_{\text{Nosé}}}{\partial \dot{\mathbf{r}}_i} = m_i s^2 \dot{\mathbf{r}}_i \quad (4.18)$$

$$\pi_s = \frac{\partial L_{\text{Nosé}}}{\partial \dot{s}} = Q \dot{s} \quad (4.19)$$

and thus construct the corresponding Hamiltonian

$$H_{\text{Nosé}} = \frac{1}{s^2} \sum_i \frac{\boldsymbol{\pi}_i^2}{2m_i} + U(\mathbf{r}^N) + \frac{1}{2Q} \pi_s^2 + \frac{g}{\beta} \ln(s). \quad (4.20)$$

The canonical equations of motion derived from $H_{\text{Nosé}}$ are

$$\dot{\mathbf{r}}_i = \frac{\boldsymbol{\pi}_i}{m_i s^2} \quad (4.21)$$

$$\dot{\boldsymbol{\pi}}_i = \mathbf{F}_i \quad (4.22)$$

$$\dot{s} = \frac{\pi_s}{Q} \quad (4.23)$$

$$\dot{\pi}_s = \frac{1}{s} \left\{ \sum_i \frac{\boldsymbol{\pi}_i^2}{m_i s^2} - g k_B T_{\text{ext}} \right\}. \quad (4.24)$$

Let H_0^* be the initial energy of the extended system with Hamiltonian $H_{\text{Nosé}}$. Let us suppose that the system is ergodic and that for sufficient long times the system is going to visit approximately all phase points lying on the hypersurface $H_{\text{Nosé}}(\mathbf{r}^N, \boldsymbol{\pi}^N, s, \pi_s) = H_0^*$ spending at each point equal amount of time. Time evolution will thus generate the microcanonical probability distribution

$$f_{\text{NVE}}(\mathbf{r}^N, \boldsymbol{\pi}^N, s, \pi_s; H_0^*) = \frac{1}{C(H_0^*)} \delta(H_{\text{Nosé}} - H_0^*) \quad (4.25)$$

where $C(H_0^*)$ is the microcanonical partition function which serves to normalize f_{NVE}

$$C(H_0^*) = \int ds d\pi_s \int d\mathbf{r}^{3N} d\boldsymbol{\pi}^{3N} \delta(H_{\text{Nosé}} - H_0^*). \quad (4.26)$$

The statistical average of a variable A can now be calculated

$$\begin{aligned} \langle A \rangle_{\text{NVE}} &= \int ds d\pi_s \int d\mathbf{r}^{3N} d\boldsymbol{\pi}^{3N} A f_{\text{NVE}}(\mathbf{r}^N, \boldsymbol{\pi}^N, s, \pi_s; H_0^*) \\ &= \frac{1}{C(H_0^*)} \int ds d\pi_s \int d\mathbf{r}^{3N} d\boldsymbol{\pi}^{3N} A \delta(H_{\text{Nosé}} - H_0^*). \end{aligned} \quad (4.27)$$

One now tries to make use of the following identity for integrals with delta functions [89]

$$\int dx \delta(h(x)) = \sum_{x_0} \delta(x - x_0) / |h'(x_0)| \quad (4.28)$$

where x_0 are simple roots of h and the derivative $h'(x_0) \neq 0$. One thus considers $h(s) \equiv H_{\text{Nosé}} - H_0^*$ as a function of s . It is easy to see that a unique exponential root could be found for $h(s)$, if one could eliminate the factor $1/s^2$ in front of the kinetic term in Eq. (4.20). This observation motivates the introduction of rescaled momenta $\mathbf{p}_i \equiv \boldsymbol{\pi}_i/s$. One now obtains

$$h(s) = \sum_i \frac{\mathbf{p}_i^2}{2m_i} + U(\mathbf{r}^N) + \frac{1}{2Q} \pi_s^2 + \frac{g}{\beta} \ln(s) - H_0^* \quad (4.29)$$

$$h'(s) = \frac{g}{\beta s} \quad (4.30)$$

$$s_0 = \exp \left(-\frac{\beta}{g} \left\{ \sum_i \frac{\mathbf{p}_i^2}{2m_i} + U(\mathbf{r}^N) + \frac{1}{2Q} \pi_s^2 - H_0^* \right\} \right). \quad (4.31)$$

In Eq. (4.31) s_0 is the unique root of h . The crucial role of the term $\ln(s)$ in $H_{\text{Nosé}}$ should now have become clear: It is necessary to obtain an *exponential* root for $h(s)$. Now, we can use the

identity (4.28) along with Eqs. (4.29), (4.30) and (4.31) to obtain from Eq. (4.27)

$$\begin{aligned}
\langle A \rangle_{\text{NVE}} &= \frac{\beta}{g C(H_0^*)} \int d\pi_s \int d\mathbf{r}^{3N} d\mathbf{p}^{3N} A s_0^{3N+1} \\
&= \frac{\beta}{g C(H_0^*)} \int d\pi_s \int d\mathbf{r}^{3N} d\mathbf{p}^{3N} A \\
&\quad \times \exp \left(-\frac{(3N+1)\beta}{g} \left\{ \sum_i \frac{\mathbf{p}_i^2}{2m_i} + U(\mathbf{r}^N) + \frac{1}{2Q} \pi_s^2 - H_0^* \right\} \right) \\
&= \frac{1}{C(H_0^*)} \sqrt{\left(\frac{2\pi Q\beta}{(3N+1)g} \right)} \exp \left(\frac{(3N+1)\beta H_0^*}{g} \right) \\
&\quad \times \int d\mathbf{r}^{3N} d\mathbf{p}^{3N} A \exp \left(-\frac{(3N+1)\beta}{g} \left\{ \sum_i \frac{\mathbf{p}_i^2}{2m_i} + U(\mathbf{r}^N) \right\} \right). \quad (4.32)
\end{aligned}$$

With the special choice of $g = 3N + 1$, it follows from Eq. (4.32)

$$\begin{aligned}
\langle A \rangle_{\text{NVE}} &= \text{const.} \int d\mathbf{r}^{3N} d\mathbf{p}^{3N} A \exp(-\beta \mathcal{H}^T(\mathbf{r}^N, \mathbf{p}^N)) \\
&= \langle A \rangle_{\text{NVT}}, \quad (4.33)
\end{aligned}$$

where $\langle \dots \rangle_{\text{NVT}}$ stands for canonical ensemble average and

$$\mathcal{H}^T(\mathbf{r}^N, \mathbf{p}^N) \equiv \sum_i \frac{\mathbf{p}_i^2}{2m_i} + U(\mathbf{r}^N). \quad (4.34)$$

From the above argument, it follows that the observable A can be a function of the positions \mathbf{r}^N and of the rescaled momenta $\mathbf{p}^N = \boldsymbol{\pi}^N/s$ only, so that the substitution $\mathbf{p}^N = \boldsymbol{\pi}^N/s$ would map $A(\mathbf{r}^N, \boldsymbol{\pi}^N/s)$ into $A(\mathbf{r}^N, \mathbf{p}^N)$. As the thermal averages of physical observables are expressed in terms of the rescaled variables rather than the original ones, the later are called “virtual” and the rescaled ones “real”. We note that \mathcal{H}^T is merely the energy function of the real system. It is obvious that a Hamiltonian of the form \mathcal{H}^T would only lead to (pure) Newtonian equations of motion without any thermostating mechanism. Therefore, it can *not* be used to derive the equations of motion of a thermostated system. Furthermore, in a thermostated system, \mathcal{H}^T is not a constant of motion. This is not surprising, for the system exchanges energy with heat bath. However, it is easy to see that the Hamiltonian of the extended system, i.e. $H_{\text{Nosé}}$, is a constant of the motion.

In his original paper [79] Nosé gave an interpretation of the variable s as a scaling factor for the time step Δ . He showed that only the ratio t/s has a real meaning and concluded that the length of the real time step, Δ' , must be given by Δ/s . He further argued that in a simulation with a constant time step Δ the length of the real time step Δ' will in general be a function of time. This is undesirable as one is usually interested in equidistant sampling in real time. This problem was solved by Hoover [83, 84] by rewriting Eqs. (4.21)-(4.24) in real time $dt' = dt/s$. Following Hoover, using

$$\frac{d}{dt} = \frac{1}{s} \frac{d}{dt'} \quad (4.35)$$

and some simple manipulations one obtains

$$\dot{\mathbf{r}}_i = \frac{\mathbf{p}_i}{m_i} \quad (4.36)$$

$$\dot{\mathbf{p}}_i = \mathbf{F}_i - \xi \mathbf{p}_i \quad (4.37)$$

$$\dot{s}/s = \xi \quad (4.38)$$

$$\dot{\xi} = \frac{1}{Q} \left\{ \sum_i \frac{\mathbf{p}_i^2}{m_i} - g k_B T_{\text{ext}} \right\}, \quad (4.39)$$

where $\xi \equiv \dot{s}/s$ and '·' stands for the time derivative with respect to real time. As all equations are expressed in real time, the equidistant sampling is ensured by choosing a constant integration time step Δ' . One of the further advantages of Hoover's formulation is that the scaling of time is no longer necessary. The presence of the heat bath is manifested by the friction variable ξ . However, contrary to the usual friction which always tends to decrease the kinetic energy of the system, ξ can take both positive and negative values and thus decrease or increase the velocity of particles. In fact, this is exactly what is needed to keep the mean kinetic energy constant. It is seen from Eq. (4.39) that at high/low mean kinetic energies ξ will increase/decrease and thus will slow down/accelerate particles [see Eq. (4.37)].

From $dH_{\text{Nosé}}/dt = 0$ it follows that $dH_{\text{Nosé}}/dt' = 1/s \, dH_{\text{Nosé}}/dt = 0$. Thus

$$H^* = \sum_i \frac{\mathbf{p}_i^2}{2m_i} + U(\mathbf{r}^N) + \frac{1}{2Q} \xi^2 + \frac{g}{\beta} \int \xi(t') dt' \quad (4.40)$$

is a constant of the motion. Here, we have used the notation H^* instead of $H_{\text{Nosé}}$ to stress the formal difference of the expressions (4.20) and (4.40): H^* is not a Hamiltonian and the Nosé-Hoover equations are not canonical. $H_{\text{Nosé}}$, on the contrary, is a Hamiltonian and generates the canonical equations (4.21)-(4.24). The constant property of H^* is useful for checking the program code. It can also serve to choose a suitable integration time step Δ : It should not be too small for reasons of efficiency, but not too large either in order to keep the H^* constant during the simulation. This motivates the use of the Eq. (4.38) which is actually redundant as far as the time evolution of the system is concerned. It is, however, necessary for the calculation of H^* .

We recall that the argument which led to the appropriate choice of $g = 3N + 1$ [see Eq. (4.33)] was based on virtual time averaging. Equations (4.36)-(4.39), however, are formulated in real time. We thus consider the relation between the virtual and real time averages. Let t and t' denote the virtual and real time, respectively. Following [70] the real time average of a dynamical quantity A can be written as

$$\begin{aligned} \langle A \rangle_{\text{real time}} &= \lim_{\tau' \rightarrow \infty} \frac{1}{\tau'} \int_0^{\tau'} dt' A(t') \\ &= \frac{\lim_{\tau \rightarrow \infty} \frac{1}{\tau} \int_0^\tau dt A(t)/s(t)}{\lim_{\tau \rightarrow \infty} \frac{1}{\tau} \int_0^\tau dt/s(t)} \\ &= \frac{\langle A/s \rangle_{\text{virtual time}}}{\langle 1/s \rangle_{\text{virtual time}}}. \end{aligned} \quad (4.41)$$

Using Eq. (4.41) and applying the same procedure which led to Eq. (4.32) yield

$$\begin{aligned}
\langle A \rangle_{\text{real time}} &= \frac{\int ds d\pi_s \int d\mathbf{r}^{3N} d\boldsymbol{\pi}^{3N} A/s \delta(H_{\text{Nosé}} - H_0^*)}{\int ds d\pi_s \int d\mathbf{r}^{3N} d\boldsymbol{\pi}^{3N} 1/s \delta(H_{\text{Nosé}} - H_0^*)} \\
&\vdots \\
&= \frac{\int d\mathbf{r}^{3N} d\mathbf{p}^{3N} A \exp(-\frac{3N}{g}\beta\mathcal{H}^T)}{\int d\mathbf{r}^{3N} d\mathbf{p}^{3N} \exp(-\frac{3N}{g}\beta\mathcal{H}^T)} \\
&= \langle A \rangle_{NVT} \text{ if } g = 3N.
\end{aligned} \tag{4.42}$$

Therefore, in real time sampling one must choose $g = 3N$. However, if Eqs. (4.36)-(4.39) are combined with a number r of constraints, one must set $g = 3N - r$. For example, if the center of mass momentum is kept constant explicitly, i.e. by means of subtracting \mathbf{P}_{cm} from the momentum of particles in each integration step, $g = 3N - 3$. Similarly, if r constraints are used in combination with Eqs. (4.21)-(4.24), $g = 3N + 1 - r$ is the appropriate choice.

4.2.1 Choice of the Parameter Q

Now we discuss the choice of the mass parameter Q appearing in Eq. (4.39). It is seen from Eq. (4.39) that the rate of change of ξ is proportional to the inverse of Q . Furthermore, $\langle Q\xi^2 \rangle = k_B T_{\text{ext}}$ which is a consequence of the equipartition principle. Thus the magnitude of ξ -oscillations varies with \sqrt{Q} [88]. Let now Q be chosen small enough so that ξ oscillates much faster than the typical time scale for energy fluctuations. As ξ enters directly the rate of change of the momenta [see Eq. (4.37)], the kinetic energy will mainly follow large magnitude oscillations of ξ . The configurational part of the energy, however, will vary much more slowly and thus be decoupled from ξ . This is the so called strong coupling limit.

On the other hand, remember that the limit $Q \rightarrow \infty$ corresponds to the microcanonical case. Thus, too large values of Q will lead to very slow energy exchange with the heat bath which is inefficient.

In [88] Nosé gave a criterion for an appropriate choice of Q . He linearized the equation of motion of the variable s and thus obtained a harmonic equation with frequency

$$\omega_s^2 = \frac{2d N k_B T_{\text{ext}}}{Q}, \tag{4.43}$$

where d is the dimension to which ξ couples. Of course $d = 3$ for a homogeneous system in three dimensional space. For an inhomogeneous system however, it can be convenient to introduce separate friction coefficients ξ_α , $\alpha = x, y, z$, where ξ_α couples to the α component of momenta only. This would lead to $d = 1$. Nosé argued further that the parameter Q should be chosen such that a resonance condition between the oscillations of s and some typical atomic frequency is obtained. We apply the same idea to Nosé-Hoover equations (4.36)-(4.39), differentiate $\dot{\xi}$ in (4.39) and obtain

$$\begin{aligned}
\ddot{\xi} &= \frac{2}{Q} \sum_i \frac{\mathbf{p}_i}{m_i} \cdot (\mathbf{F}_i - \xi \mathbf{p}_i) \\
&\approx -\frac{2}{Q} \sum_i \frac{\mathbf{p}_i^2}{m_i} \xi \\
&\approx -\frac{2}{Q} d N k_B T_{\text{ext}} \xi.
\end{aligned} \tag{4.44}$$

We now justify the neglect of $\sum_i \mathbf{p}_i \cdot \mathbf{F}_i/m_i$. The forces F_i do not depend on the *momenta*. They only depend on positions. As positions and momenta are not correlated at thermal equilibrium, the average value of $\sum_i \mathbf{p}_i \cdot \mathbf{F}_i/m_i$ must vanish. Furthermore, the higher derivatives of positions relax faster than the lower ones [90] what means that $\sum_i \mathbf{p}_i \cdot \mathbf{F}_i/m_i$ will vary in time faster than the instantaneous kinetic energy, $\sum_i \mathbf{p}_i^2/m_i$. The fast oscillations of the term containing the forces will thus lead to a noise like effect and can be ignored to the first approximation. Figure 4.1 displays time evolution of ξ , $\sum_i \mathbf{p}_i \cdot \mathbf{F}_i/m_i$ and $\sum_i \mathbf{p}_i^2/m_i$. It is seen from this figure that the term containing the forces oscillates rapidly around zero. The kinetic contribution to $\ddot{\xi}$, on the contrary, is almost constant with a value of approximately $Nk_B T_{\text{ext}}$. We thus expect Eq. (4.44) to be a good approximation close to the equilibrium, which means that the variable ξ obeys harmonic oscillations with the frequency

$$\omega_\xi^2 \approx \frac{2d Nk_B T_{\text{ext}}}{Q}. \quad (4.45)$$

To examine the validity of Eq. (4.45) we carried out simulations of films of thicknesses $D = 5$ and $D = 30$ at different values of Q while keeping all remaining parameters fixed. The temperatures and number of particles were $T = 0.55$, $N = 500$ in the case of thinner film and $T = 1$, $N = 3000$ for $D = 30$.

Note that the properties the thinner film ($D = 5$) are quite different from that of the bulk system [see chapters 7 and 8]. At $T = 1$ and $D = 30$, on the contrary, we do not observe much difference. In all cases, the external pressure normal to the interface was set to unity. After the

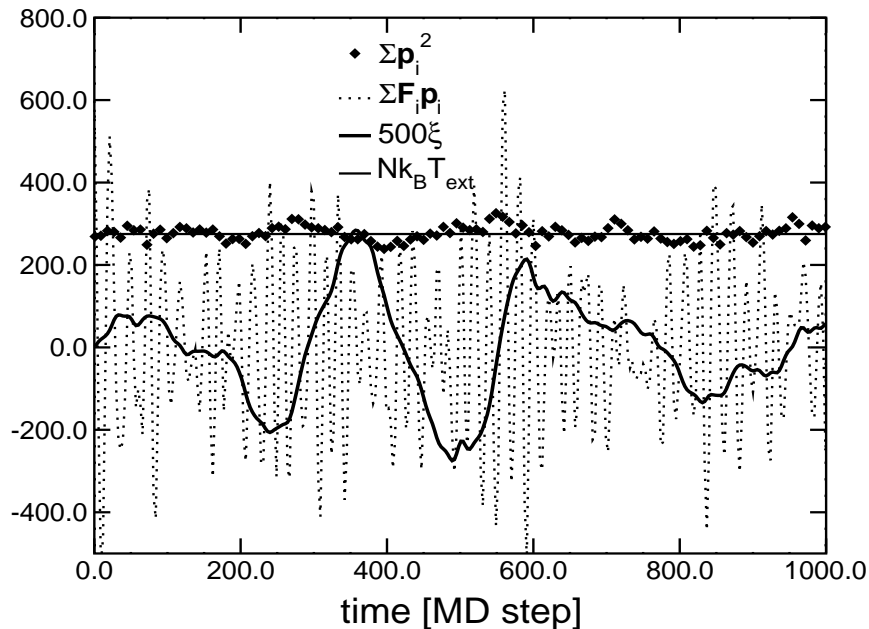


Figure 4.1: Time evolution of the friction parameter ξ and the contributions to $\ddot{\xi}$, namely $\sum_i \mathbf{p}_i \cdot \mathbf{F}_i/m_i$ and $\sum_i \mathbf{p}_i^2/m_i$. We have multiplied ξ by a factor of 500 to put it on the same scale as the other quantities. The term containing the force exhibits fast oscillations around zero, whereas the kinetic contribution is always positive and nearly constant.

simulation, we have computed the power spectrum densities of $\xi_Q(t)$, i.e.

$$P(\omega) \equiv \left| \int \exp(i\omega t) \xi(t) dt \right|^2 \quad (4.46)$$

for various values of the parameter Q . Figure (4.2) displays the frequencies $\omega_\xi(Q)$ for which the corresponding power spectrum is a maximum.

It is shown in Fig. 4.2, that both for the $D = 5$ and for $D = 30$ the oscillations frequency of the friction variable can be well described by the Eq. (4.39). The somewhat better agreement of the results in the case of $D = 5$ (see left panel) is due to smaller range of Q -values around the ‘‘optimum’’ choice, given by Eq. (4.39).

The reason of this good agreement for both the very thin film of three monomer layers² and the quasi-bulk system lies in the fact that the friction variable, ξ , couples to atomistic frequencies which are not very sensitive to the presence of the walls. This, in turn, can be explained by the fact that these frequencies are determined by strong interparticle forces.

Now that the validity of Eq. (4.44) is well examined also for the case of a confined system, we follow Nosé [88] and require $\omega_\xi = \omega_{\text{intrinsic}}$. This gives the following criterion for the ‘‘optimum choice’’ of Q

$$Q_{\text{opt}} \approx \frac{2d N k_B T_{\text{ext}}}{\omega_{\text{intrinsic}}^2}, \quad (4.47)$$

²note that D denotes the wall-to-wall separation. Therefore, the effective width of the region in the film with non-vanishing density is roughly $D-2$

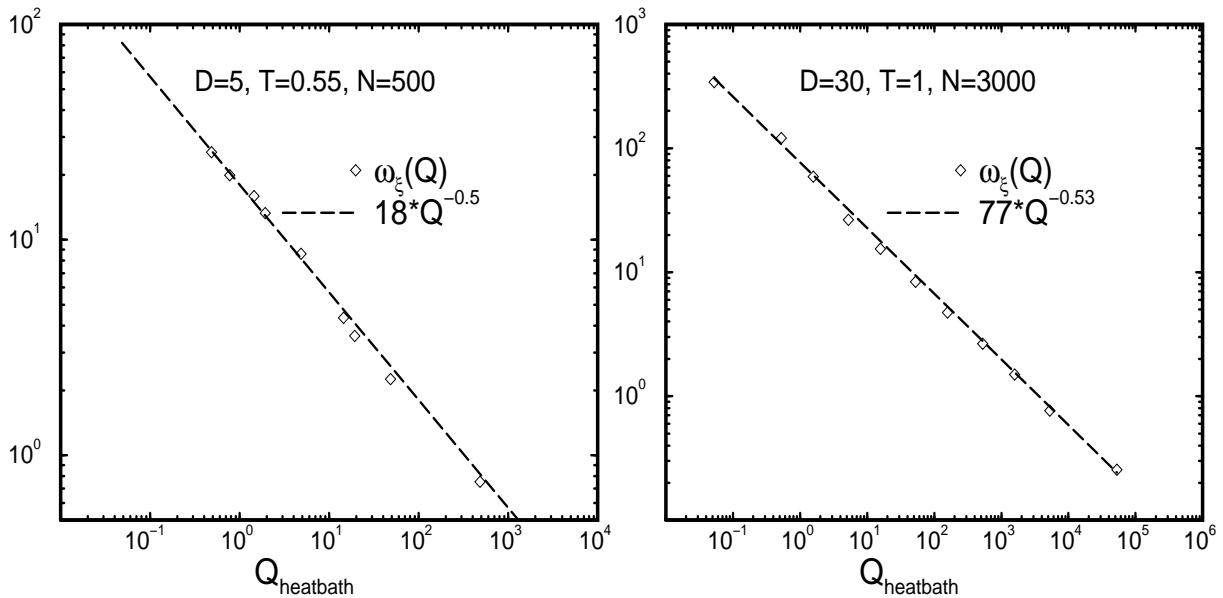


Figure 4.2: Q -dependence of the oscillation frequency of the friction coefficient $\xi(t)$ [see Eq. (4.39)]. Each of these frequencies is obtained from the maximum of the corresponding power spectrum of $\xi_Q(t)$. Left panel: A film of thickness $D = 30$ at a rather high temperature of $T = 1$ ($T_c(D = 20) = 0.41 < T_c(D = 30) < T_{c,c,bulk} = 0.45$) [see chapter 8]. Left panel: A film of thickness $D = 5$ at an intermediate temperature of $T = 0.55$ ($T_c(D = 5) = 0.31$) [see chapter 8]. Note that, in the later, a shorter Q -range is investigated which allows a better fit à la Eq. (4.39).

where $\omega_{\text{intrinsic}}^2$ is a typical intrinsic oscillation frequency of the system. For a system of particles interacting via pairwise Lennard-Jones potential, one can use the harmonic approximation of a fcc-lattice to obtain an estimate for the frequency $\omega_{\text{intrinsic}}$. We complete this discussion with a numeric example for typical values of Q . For a fcc-lattice of Lennard-Jones atoms one obtains

$$\omega_{\text{intrinsic}}^2 \approx \frac{2U''_{\text{LJ}}(r = \sqrt[3]{2}\sigma)}{m} \quad (4.48)$$

$$= 114.3 \frac{\epsilon}{m\sigma^2}, \quad (4.49)$$

where m is the mass of an atom and U''_{LJ} denotes the second derivative of the Lennard-Jones potential with respect to the distance r .

Untill now, we have only shown that one can understand the influence of the heat bath parameter, Q , on the time evolution of ξ . However, there is a further (and in fact more important) point to examine before using the Nosé-Hoover thermostat in a MD simulation: do Eqs. (4.36)-(4.39) always generate the same energy distribution regardless of the specific value of Q ? If this is the case, is the obtained energy distribution canonical?

For the present polymer model in bulk, these questions have been investigated in [91]. Assuming that the specific heat of the system only slightly differs from that predicted by the Dulong-Petit law, $c_V = 3Nk_B$, an affirmative answer to the above question was found. However, as the properties of a confined system are in some aspects strongly different from that of a bulk system, it is worth investigating the above question for thin films separately.

Recal that, in the canonical ensemble, the fluctuations of energy are directly related to the system's specific heat [64],

$$c_V = \frac{\langle E^2 \rangle - \langle E \rangle^2}{k_B T^2}. \quad (4.50)$$

The Dulong-Petit law, is based on a harmonic approximation to the interparticle potential [92,93]. This is a good approximation for solids at high but not too high temperatures. "Not too high" means that the temperature must still be well below the melting temperature. Close to the melting point, however, the amplitude of atomic oscillations becomes very large and, consequently, the harmonic approximation is inaccurate. Therefore, for liquids, one should expect deviations from the Dulong-Petit law.

If we knew the specific heat of the system, we could check for the canonical property of the energy distribution in examining the validity of Eq. (4.50). To our knowledge, there is unfortunately no general formula for the specific heat of a fluid system. Therefore, we cannot use Eq. (4.50) in examining the energy distribution. However, we can at least check the *independence* of the simulation results from the specific value of the heat bath parameter, Q . Furthermore, we can verify, if the obtained energy distribution is gaussian. This later condition, however, is satisfied by any random variable and therefore must be seen as a necessary but *not sufficient* condition. In addition, a comparison with the Dulong-Petit approximation, $\exp(-(E - \langle E \rangle)^2 / 2\Delta E^2)$, can also be helpful for it yields a sort of "order of magnitude test".

Once the reliability of the energy distribution is ensured, one can use Eq. (4.50) and calculate the constant volume heat capacity, c_V . So, in fact, we do not use Eq. (4.50) in verifying the canonical property. We actually proceed in the inverse direction, i.e. we compute c_V using the knowledge of the energy fluctuations.

Next, we examine the reliability of the energy distribution generated by the Nosé-Hoover motion equations (4.36)-Eq. (4.39). For this purpose, we carried out simulation runs at various values of Q , for both high and low temperatures, whereby the film thickness was also varied. We

report here two asymptotic cases: An extremely confined system at low T ($D = 5$, $T = 0.38$) and a quasi-bulk system at a relative high temperature $D = 30$, $T = 1$. Note that for the thinner film of $D = 5$, we find a mode-coupling critical temperature of $T_c(D = 5) = 0.31$. The corresponding T_c of the thicker film has not been computed. Nevertheless, we can estimate it to $T_c(D = 20) = 0.41 < T_c(D = 30) < T_{c\text{bulk}} = 0.45$. [see chapter 8].

The independence of the energy distribution from the “mass”, Q , of the heat bath, is demonstrated in both right and left panels of Fig. 4.3. The data shown in the left panel are extracted from 10 times shorter simulation runs than the results displayed in the right panel. Sampling was done once in 3 MD steps. Obviously, thermostating rate does not have much influence on the energy distribution. However, the case of $Q = 10^3$ in the left panel also shows that in the limit of very large Q , the coupling becomes inefficient and the energy distribution is no longer canonical.

Furthermore, it is shown in the right panel of Fig. 4.3 that the Dulong-Petit law no longer holds for $D = 5$ at $T = 0.38$. This implies that, for this film thickness and temperature, the configurational contribution to the specific heat cannot be replaced by a simple harmonic approximation. Using Eq. (4.50) we obtain

$$\frac{c_V(D = 5, T = 0.38)}{3Nk_B} = 1.32 \pm 0.03. \quad (4.51)$$

4.3 NpT -Ensemble I: Homogeneous Systems

It is straightforward to extend the procedure described above to the isobaric-isothermal case which is known as NpT -ensemble. One starts from the Lagrangian, L_{NA} , given in (4.17), derives the conjugate momenta, constructs the Hamiltonian and finally obtains the corresponding canonical equations of motion. If one goes a step further and introduces the real time and the derivatives with respect to it, one obtains [87]

$$\ddot{\mathbf{r}} = \frac{\mathbf{F}_i}{m_i} - \frac{\dot{s} \mathbf{p}_i}{s m_i} + \frac{\mathbf{r}_i}{Vd} \left(\ddot{V} - \frac{(d-1)\dot{V}^2}{dV} \right) \quad (4.52)$$

$$\ddot{s} = \frac{\dot{s}^2}{s} + \frac{1}{Q} \left\{ \sum_i \frac{\mathbf{p}_i^2}{2m_i} - gk_B T_{\text{ext}} \right\} \quad (4.53)$$

$$\ddot{V} = \frac{\dot{s}\dot{V}}{s} + \frac{s^2}{M_V} (P(t) - P_{\text{ext}}), \quad (4.54)$$

where $P(t)$ is the instantaneous pressure of the system

$$P(t) = \frac{1}{dV} \left(\sum_i \frac{\mathbf{p}_i^2}{m_i} + \sum_{i=1}^N \mathbf{r}_i \cdot \mathbf{F}_i \right). \quad (4.55)$$

It is important to note that the forces appearing in (4.55) are extracted from the Lagrangian L_{NA} via $\mathbf{F}_i = \partial L_{NA} / \partial \mathbf{r}_i$. For a system with periodic boundary conditions, one must therefore modify L_{NA} to take into account the presence of image particles. We postpone this problem to section 4.5, but just mention that in this case the correct expression for $P(t)$ is *not* obtained by just redefining the force \mathbf{F}_i on a particle i as the total force on i , i.e. by adding to \mathbf{F}_i the contribution of image particles in the formula (4.55). Similar to the case of NVT -ensemble in previous section, one can demonstrate that equations of motion derived from L_{NA} (see definition (4.17)) generate exactly the NpT -probability distribution, supposed that the system is

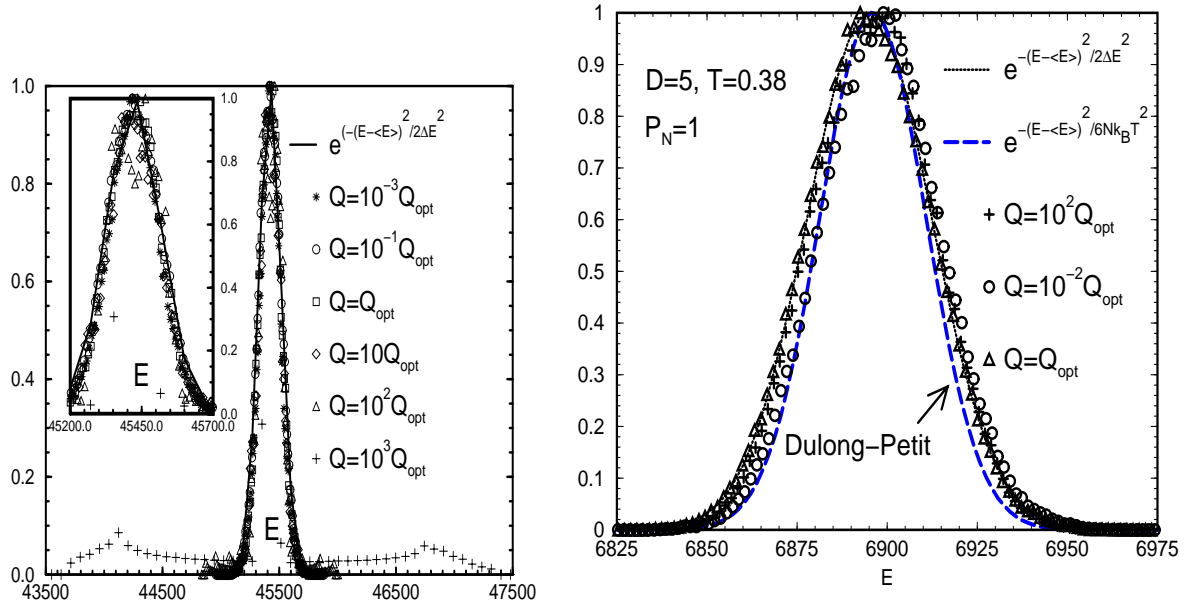


Figure 4.3: Independence of the energy distribution from the “mass”, Q , of the heat bath. Left panel: A film of thickness $D = 30$ at a rather high temperature of $T = 1$ ($T_c(D = 20) = 0.41 < T_c(D = 30) < T_{c\text{bulk}} = 0.45$) [see chapter 8]. Right panel: A film of thickness $D = 5$ at the lowest temperature simulated for this film thickness, $T = 0.38$ ($T_c(D = 5) = 0.31$) [see chapter 8]. The number of samples was $\approx 3 \times 10^4$ for the left panel and $\approx 3 \times 10^5$ for the right one. Sampling was done once in 3 MD steps. Both panels clearly demonstrate that the energy distribution is, in a wide range, independent of the parameter Q . For short simulation runs and extremely large values of Q (see $Q = 10^3 Q_{\text{opt}}$ in the left panel), however, the deviations from the correct distribution become important. The inner gaussian in the right panel indicates the expected energy distribution when harmonic approximation is applied, i.e. if the specific heat, c_V , obeys the Dulong-Petit law, $c_V = 3Nk_B T$.

ergodic. Furthermore, one can easily verify that these equations let L_{NA} unchanged. However, as Hoover was rather successful in simplifying the Nosé-motion equations 4.21-4.24, he introduced now the friction coefficient $\xi = \dot{s}/s$ along with the strain rate $\eta = \dot{V}/(dV)$ and proposed³

$$\dot{\mathbf{r}}_i = \frac{\mathbf{p}_i}{m_i} + \eta \mathbf{r}_i \quad (4.56)$$

$$\dot{\mathbf{p}}_i = \mathbf{F}_i - (\eta + \xi)\mathbf{p}_i \quad (4.57)$$

$$\dot{\xi} = \frac{1}{Q} \left\{ \sum_i \frac{\mathbf{p}_i^2}{m_i} - gk_B T_{\text{ext}} \right\} \quad (4.58)$$

$$\dot{\eta} = \frac{V}{M_\eta} (P(t) - P_{\text{ext}}) \quad (4.59)$$

$$\dot{V} = V\eta \quad (4.60)$$

We will show in appendix (A.2) that these equations are *not* fully equivalent to Eqs. (4.52)-(4.54) and that the discrepancy lies in the expression for $\dot{\eta}$. However, we will show that

³In fact, Hoover used a slightly different notation, namely $\dot{\epsilon} = \dot{V}/V$.

Eqs. (4.56)-(4.60) drive the system through the phase space according to the probability density

$$f(\mathbf{r}^N, \mathbf{p}^N, \xi, \eta, V) \propto \frac{1}{V} \exp(-\beta H(\mathbf{r}^N, \mathbf{p}^N, \xi, \eta, V)), \quad (4.61)$$

where the quantity H is given by

$$H = \sum_i \frac{\mathbf{p}_i^2}{2m_i} + U(\mathbf{r}^N) + \frac{1}{2}Q\xi^2 + \frac{1}{2}d M_\eta \eta^2 + P_{\text{ext}} V. \quad (4.62)$$

The proof makes use of the Liouville probability conservation theorem: Let $f(x) = f(x_1, \dots, x_N)$ denote the probability density for a set of variables $\{x_\mu\}_{\mu=1, \dots, N}$ (Note that, here, N is the total number of independent variables and not the particle number). It follows from the conservation of the total probability that f satisfies the continuity equation

$$\frac{\partial f}{\partial t} = - \sum_\mu \frac{\partial}{\partial x_\mu} (f \dot{x}_\mu). \quad (4.63)$$

The total derivative of f with respect to time can now be written

$$\frac{df}{dt} = \frac{\partial f}{\partial t} + \sum_\mu \frac{\partial f}{\partial x_\mu} \dot{x}_\mu \quad (4.64)$$

$$= -f \sum_\mu \frac{\partial \dot{x}_\mu}{\partial x_\mu}. \quad (4.65)$$

Equation (4.64) is the definition of total derivative of a function of many variables. Inserting the rhs of Eq. (4.63) for $\partial f / \partial t$ in Eq. (4.64) leads to Eq. (4.65). Note that no assumption was made about the canonical character of equations for $\{\dot{x}_\mu\}$. In fact, in canonical case $\sum_\mu \partial \dot{x}_\mu / \partial x_\mu = 0$ and thus $df/dt = 0$. This is the well-known Liouville theorem for Hamiltonian dynamics. Thus, given a set of independent variables $\{x_\mu\}$ and a set of (not necessarily canonical) equations for $\{\dot{x}_\mu\}$, the total time derivative of the corresponding probability density can be calculated using Eq. (4.65). With this background, verifying (4.61) becomes a matter of algebraic manipulations. Using Eqs. (4.56)-(4.60) the sum on the rhs of (4.65) becomes

$$\begin{aligned} \sum_\mu \frac{\partial \dot{x}_\mu}{\partial x_\mu} &= \sum_i \frac{\partial}{\partial \mathbf{r}_i} \cdot \dot{\mathbf{r}}_i + \sum_i \frac{\partial}{\partial \mathbf{p}_i} \cdot \dot{\mathbf{p}}_i + \frac{\partial \dot{\xi}}{\partial \xi} + \frac{\partial \dot{\eta}}{\partial \eta} + \frac{\partial \dot{V}}{\partial V} \\ &= \eta Nd - (\eta + \xi)Nd + \eta d \\ &= -\xi Nd + \eta d \quad \text{for Eqs. (4.56)-(4.60)}. \end{aligned} \quad (4.66)$$

Now calculate the rhs of (4.61)

$$\frac{d}{dt} \left(\frac{1}{V} \exp(-\beta H) \right) = - \left(\frac{\dot{V}}{V} + \beta \frac{dH}{dt} \right) \frac{1}{V} \exp(-\beta H). \quad (4.67)$$

Using the definition (4.62) of H along with Eqs. (4.56)-(4.60) yields

$$\begin{aligned}
\frac{dH}{dt} &= \sum_{\mu} \frac{\partial H}{\partial x_{\mu}} \dot{x}_{\mu} \\
&= \sum_i \left\{ -\mathbf{F}_i \cdot \dot{\mathbf{r}}_i + \frac{\mathbf{p}_i}{m_i} \cdot \dot{\mathbf{p}}_i \right\} + Q\xi \dot{\xi} + M_{\eta} \eta \dot{\eta} d + P_{\text{ext}} \dot{V} \\
&= \sum_i \left\{ -\mathbf{F}_i \cdot \left(\frac{\mathbf{p}_i}{m_i} + \eta \mathbf{r}_i \right) + \frac{\mathbf{p}_i}{m_i} \cdot (\mathbf{F}_i - (\eta + \xi) \mathbf{p}_i) \right\} \\
&\quad + \xi \left(\sum_i \frac{\mathbf{p}_i^2}{m_i} - k_{\text{B}} T_{\text{ext}} N d \right) + \eta V d (P(t) - P_{\text{ext}}) + P_{\text{ext}} V \eta d \\
&= -\eta \left(\sum_i \frac{\mathbf{p}_i^2}{m_i} + \sum_i \mathbf{F}_i \cdot \mathbf{r}_i \right) - \xi k_{\text{B}} T_{\text{ext}} N d + \eta V d P(t) \\
&= -\xi k_{\text{B}} T_{\text{ext}} N d.
\end{aligned} \tag{4.68}$$

where we also used the definition (4.55) of the instantaneous pressure $P(t)$. If we set Eqs. (4.60) and (4.68) in Eq. (4.67) we obtain

$$\begin{aligned}
\frac{d}{dt} \left(\frac{1}{V} \exp(-\beta H) \right) &= -(\eta d - \xi N d) \frac{1}{V} \exp(-\beta H) \\
&= - \left(\sum_{\mu} \frac{\partial \dot{x}_{\mu}}{\partial x_{\mu}} \right) \frac{1}{V} \exp(-\beta H),
\end{aligned} \tag{4.69}$$

where we made use of Eq. (4.66). Thus $1/V \exp(-\beta H)$ satisfies the necessary condition (4.65). For this condition to be sufficient we must suppose ergodicity. Thus, the NpT -equations (4.56)-(4.60) of Hoover generate a probability distribution which is not exactly equal, but very similar to the NpT -probability density $\exp(-\beta H)$.

An improvement of these equations was achieved by Melchionna *et al.* [87]. They noted that, if one replaced Eq. (4.56) by

$$\dot{\mathbf{r}}_i = \frac{\mathbf{p}_i}{m_i} + \eta (\mathbf{r}_i - \mathbf{R}_{\text{cm}}), \tag{4.70}$$

the modified set of equations (4.70) and (4.57)-(4.60) would generate the exact NpT -probability distribution, i.e. $f \propto \exp(-\beta H)$. This is easily checked by calculating the modification of Eq. (4.66) due to the new definition of $\dot{\mathbf{r}}_i$,

$$\begin{aligned}
\sum_i \frac{\partial}{\partial \mathbf{r}_i} \cdot \dot{\mathbf{r}}_i &= \sum_i \eta \left(\frac{\partial}{\partial \mathbf{r}_i} \dot{\mathbf{r}}_i - \frac{\partial}{\partial \mathbf{r}_i} \cdot \mathbf{R}_{\text{cm}} \right) \\
&= \eta N d - \eta \sum_i \frac{m_i d}{\sum_j m_j} \\
&= \eta N d - \eta d.
\end{aligned} \tag{4.71}$$

The first term in Eq. (4.71) is the result obtained from Eq. (4.56). The second term, on the contrary, is new. From the modified set of equations (4.70) and (4.57)-(4.60) we thus obtain [see Eq. (4.66)]

$$\sum_{\mu} \frac{\partial \dot{x}_{\mu}}{\partial x_{\mu}} = -\xi N d \text{ for Eqs. (4.70) and (4.57)-(4.60)}. \tag{4.72}$$

On the other hand, the corresponding change of dH/dt is $-\eta \mathbf{R}_{\text{cm}} \cdot \sum_i \mathbf{F}_i = 0$. Combining Eqs. (4.72), (4.68) and (4.65) yields

$$\frac{df}{dt} = -\frac{1}{k_B T_{\text{ext}}} \frac{dH}{dt} f(t) \quad (4.73)$$

with the well known solution

$$f(\mathbf{r}^N, \mathbf{p}^N, \xi, \eta, V) \propto \exp(-\beta H(\mathbf{r}^N, \mathbf{p}^N, \xi, \eta, V)). \quad (4.74)$$

To avoid possible confusion, we repeat the complete set of modified Hoover equations which generate the probability distribution (4.74)

$$\dot{\mathbf{r}}_i = \frac{\mathbf{p}_i}{m_i} + \eta(\mathbf{r}_i - \mathbf{R}_{\text{cm}}) \quad (4.75)$$

$$\dot{\mathbf{p}}_i = \mathbf{F}_i - (\eta + \xi)\mathbf{p}_i \quad (4.76)$$

$$\dot{\xi} = \frac{1}{Q} \left(\sum_i \frac{\mathbf{p}_i^2}{m_i} - N k_B T_{\text{ext}} d \right) \quad (4.77)$$

$$\dot{\eta} = \frac{V}{M_\eta} (P(t) - P_{\text{ext}}) \quad (4.78)$$

$$\dot{V} = V \eta d. \quad (4.79)$$

From now on, we will refer to Eqs. (4.75)-(4.79) as the Hoover-Melchionna equations of motion.

4.3.1 Choice of the Parameter M_η

Similar to the case of heat bath parameter Q we are faced with the problem of a reasonable choice for the parameter M_η which enters Eq. (4.78). In his pioneering work on simulation techniques [73], H. C. Andersen had already given a criterion for the choice of the mass variable M_V which he had introduced in extended Lagrangian L_{Andersen} . In the same reference, he noted that "for a small sample of fluid imbedded in a much larger sample of fluid, the volume of the sample will fluctuate in response to an imbalance between the internal and external pressure. The time scale for the fluctuations of the volume of a sample of fluid is approximately equal to the length of the sample divided by the speed of sound in the sample. Thus, it is desirable to choose the mass M_V so that the time scale for the fluctuations of V in the scaled system is approximately equal to $V^{1/3}$ divided by the speed of sound in the fluid." However, we find that it is often better to choose a somewhat larger value for M_η so that a sound wave could make a few round trips during a period of volume fluctuations. This allows a better response of the whole system to a given volume change.

Keeping all that in mind we look at the time evolution of volume fluctuations $\delta V(t) = V(t) - \langle V \rangle$. It follows immediately that $\delta \dot{V} = \dot{V} = \eta d V$. The fluctuation of the instantaneous

pressure is obviously given by $\delta P = P(t) - P_{\text{ext}}$. Hence we can write

$$\begin{aligned}\delta\ddot{V} &= \eta d\dot{V} + \dot{\eta} dV \\ &= \frac{dV^2}{M_\eta} \delta P + (d\eta)^2 V \\ &= \frac{dV^2}{M_\eta} \frac{\delta P}{\delta V} \delta V + \left(\frac{\delta\dot{V}}{V}\right)^2 V \\ &= -\frac{dV^2}{M_\eta \kappa_T} \frac{\delta V}{V} + \left(\frac{\delta\dot{V}}{V}\right)^2 V\end{aligned}\quad (4.80)$$

$$= -\frac{dV}{M_\eta \kappa_T} \delta V. \quad (4.81)$$

where we introduced in (4.80) the isothermal compressibility $\kappa_T = -1/V \delta V / \delta p|_T$. Supposing that $\delta\dot{V}$ and δV are of the same order of magnitude, we have neglected the second term on the rhs of (4.80), because, compared to the first one, it contains a factor of $\delta\dot{V}/V \ll 1$. Furthermore a linear approximation was used for δP which allows to express it in terms of compressibility. Thus, the volume fluctuations obey harmonic oscillations with a frequency

$$\omega_V^2 = \frac{dV}{M_\eta \kappa_T}. \quad (4.82)$$

Let n_{rt} be the number of round trips of a sound wave during a full period of volume fluctuations. Adopting a modified version of Andersen's criterion [73] we set

$$n_{\text{rt}} \omega_V = \omega_{\text{sound}} = \frac{2\pi}{2L/v_{\text{sound}}}, \quad (4.83)$$

where $L = V^{1/3}$, v_{sound} is the sound velocity and the factor 2 in the denominator comes from the motion of the sound wave through the simulation box and back ("round trip"). Combining Eqs. (4.82) and (4.83) yields the following equation for the parameter M_η

$$M_\eta = n_{\text{rt}}^2 \frac{dV}{\kappa_T} \frac{L^2}{\pi^2 v_{\text{sound}}^2}. \quad (4.84)$$

If we use the ideal gas approximation $v_{\text{sound}}^2 = 1/(\rho \kappa_S) = V/(N \kappa_S)$ for the sound velocity (κ_S being the adiabatic compressibility), we obtain from Eq. (4.84)

$$M_\eta = n_{\text{rt}}^2 dN \frac{\kappa_S}{\kappa_T} \left(\frac{L}{\pi}\right)^2. \quad (4.85)$$

Using $\kappa_S/\kappa_T = C_V/C_p$ we extract from Table 1.2 of [64] values of κ_S/κ_T for some typical simple monoatomic liquids: 0.455 for liquid argon, 0.909 for molecular liquid nitrogen and 0.625 for a simple liquid metal, sodium. Although certain properties of metals (for example heat capacity and thermal or electric conductivities) are in general very different from those of other systems, the ratio κ_S/κ_T seems to lie in the same range as for simple non-metallic liquids. Finally, recall that $\kappa_S/\kappa_T = 3/5 = 0.6$ for a monoatomic ideal gas and $\kappa_S/\kappa_T = 5/7 \approx 0.714$ for a gas of a diatomic molecules. This suggests that changes in κ_S/κ_T are rather slow with respect to material properties. Thus, we approximate this quantity by unity and obtain

from Eq. (4.85) an expression for M_η containing only those quantities which are known at the beginning of the simulation

$$M_\eta \approx n_{\text{rt}}^2 dN \left(\frac{L}{\pi} \right)^2. \quad (4.86)$$

We usually use $n_{\text{rt}} = 10$ which means that a sound wave makes 10 round trips through the system during a sole period of the volume fluctuations. This allows for a better response of the internal pressure to the volume changes. The choice of Andersen, however, corresponds to $n_{\text{rt}} = 1$.

4.4 NpT -Ensemble II: Planar Systems

So far, we have supposed that the system of study is homogeneous and isotropic. Only in this case the pressure is a scalar quantity and independent of the position. However, as extensively described in chapter (3), the pressure is a local tensor, $\mathbf{P}(\mathbf{r})$, in inhomogeneous systems. To simplify further discussions, we restrict ourselves to the case of planar systems confined between two walls. In this case the pressure tensor is diagonal at thermal equilibrium and has only two independent components, P_T and P_N in directions parallel and perpendicular to the surface respectively (in non equilibrium planar systems there are more than two independent components). The corresponding conjugated quantities are the area A of a surface and the distance D between the walls. Contrary to the case of a homogeneous system, the thermodynamic state of such a system is no longer uniquely determined by a choice of three independent parameters, say, N , p and T . As the main difference with respect to a homogeneous system is the presence of surfaces, it is natural to complete the set of variables NpT by the area A of a surface or by the surface tension γ . However, as just mentioned, the pressure of a planar system has two independent components at thermal equilibrium. Therefore, we must clarify the meaning of the pressure p : If p is associated with a change of volume while keeping the area, A , of the surfaces constant, it will correspond to the normal component of the pressure, P_N . However, if it is related to a volume change at fixed wall-to-wall distance D , it will be the lateral component, P_T , which would be the relevant quantity.

A satisfactory answer to this question is found by considering the energy change of the system due to a change of lateral and/or transversal dimensions of the system. First, we consider the energy change dE_N due to a change, dD , of film thickness (wall-to-wall separation). In this case, we use the fact that the normal pressure P_N (and thus the normal force) is constant overall in the film (see Eq. (3.43)) so that we can immediately write

$$dE_N = -F_N dD = -P_N A dD. \quad (4.87)$$

However, the lateral component P_T of the pressure tensor does depend on the distance z from a wall. To calculate the work dE_T against the lateral forces we thus divide the film in layers of thickness dz , calculate the energy change with respect to a change dA of the area of the surface and finally integrate over dz . This leads to

$$dE_T = - \int_{-D/2}^{+D/2} dz F_T(z) = -dA \int_{-D/2}^{+D/2} dz P_T(z) = -D dA \bar{P}_T, \quad (4.88)$$

where we have introduced the average lateral pressure

$$\bar{P}_T = \frac{1}{D} \int_{-D/2}^{+D/2} dz P_T(z). \quad (4.89)$$

The total energy change dE with respect to an arbitrary change of film thickness and/or surface area of a planar system is thus given by

$$\begin{aligned} dE &= dE_N + dE_T \\ &= -P_N A dD - \bar{P}_T D dA . \end{aligned} \quad (4.90)$$

The expression (4.90) for dE has a somewhat unusual form. However, using the definition (3.31) of the surface tension, and $dV = AdD + DdA$, it is a matter of simple algebra to obtain from Eq. (4.90)

$$dE = -P_N dV + \gamma dA . \quad (4.91)$$

So, when going from a homogeneous system to a system with planar geometry, the pair (p, V) of conjugate variables must be replaced by *two pairs* (P_N, V) and (γ, A) or, equivalently, by (AP_N, D) and (DP_T, A) . However, contrary to a homogeneous system, where a desired volume change is realized in a unique way by rescaling the system size, there are two distinct ways of changing the volume of a thin film: One can vary the surface area and/or the film thickness. Thus, the volume is not an appropriate variable for the molecular dynamics simulation of planar systems. It is more convenient to choose the second set of conjugate pairs. Note that within this choice, D is conjugate to AP_N and not only P_N . Similarly, A is conjugate to DP_T . In fact, once D and A are chosen as the thermodynamic variables of the system, the corresponding thermodynamic forces are obtained from a change of energy while keeping all other parameters constant. This gives, when using Eq. (4.90)

$$\tilde{P}_\perp \equiv - \left(\frac{\partial E}{\partial D} \right)_{S,A} = P_N A \quad (4.92)$$

$$\tilde{P}_\parallel \equiv - \left(\frac{\partial E}{\partial A} \right)_{S,D} = \bar{P}_T D . \quad (4.93)$$

Here, S stands for the system entropy. Thus, the fluctuations of the film thickness couple to $\tilde{P}_\perp = AP_N$ and those of A are related to $\tilde{P}_\parallel = D\bar{P}_T$. Consequently, the external forces corresponding to D and A are

$$\begin{aligned} \tilde{P}_{\perp,\text{ext}} &= P_{N,\text{ext}} A , \\ \tilde{P}_{\parallel,\text{ext}} &= P_{T,\text{ext}} D , \end{aligned} \quad (4.94)$$

respectively. It follows from this argument that, a priori, a formalism which makes use of the fluctuations of D and/or A , will allow for simulations at constant $\tilde{P}_{\perp,\text{ext}}$ and/or constant $\tilde{P}_{\parallel,\text{ext}}$ only. To obtain a simulation at constant normal pressure, $P_{N,\text{ext}}$, for example, one should add the condition of constant surface area. This means that a NpT -simulation at constant normal pressure does necessarily involve fluctuations of the film thickness while keeping the surface area constant. Similarly, a NpT -simulation at $\bar{P}_T = P_{T,\text{ext}}$ requires simultaneously both a fluctuating A and the condition of $\dot{D} = 0$.

As we want to formulate a generalization of the Hoover-Melchionna equations (4.75)-(4.79), we first define [see Eq. (4.62)]

$$\begin{aligned} H_{\text{film}} &= \sum_i \frac{\mathbf{p}_i^2}{2m_i} + U(\mathbf{r}^N) + \left(\frac{1}{2} Q_\parallel \xi_\parallel^2 + \frac{1}{2} Q_\perp \xi_\perp^2 \right) \\ &\quad \left(\frac{1}{2} M_{\eta,\parallel} d_\parallel \eta_\parallel^2 + \frac{1}{2} M_{\eta,\perp} d_\perp \eta_\perp^2 \right) + \tilde{P}_{\perp,\text{ext}} D + \tilde{P}_{\parallel,\text{ext}} A . \end{aligned} \quad (4.95)$$

Here, $d_{\parallel} = 2$ and $d_{\perp} = 1$ are the dimensions in directions parallel and perpendicular to the surface respectively. To simplify the notation, we further define the reduced volume of each subspace in directions parallel and perpendicular to the interface, respectively,

$$\begin{aligned} V_{\parallel} &\equiv A, \\ V_{\perp} &\equiv D. \end{aligned} \quad (4.96)$$

Obviously, $V = V_{\parallel}V_{\perp}$ is the volume of the system. Let $\alpha \in \{\parallel, \perp\}$. Using Eqs. (4.96) we can write H_{film} in a compact form

$$H_{\text{film}} = \sum_{\alpha} \left(\sum_i \frac{\mathbf{p}_{i,\alpha}^2}{2m_i} + \frac{1}{2}Q_{\alpha}\xi_{\alpha}^2 + \frac{1}{2}d_{\alpha}M_{\eta,\alpha}\eta_{\alpha}^2 + \tilde{P}_{\alpha}V_{\alpha} \right) + U(\mathbf{r}^N). \quad (4.97)$$

A comparison with (4.62) reveals the striking analogy between H_{film} and Hoover's H -function. Using this formal analogy it is therefore straightforward to generalize the Hoover-Melchionna equations (4.75)-(4.79) to the case of planar systems

$$\dot{\mathbf{r}}_{i,\alpha} = \frac{\mathbf{p}_{i,\alpha}}{m_i} + \eta_{\alpha}(\mathbf{r}_{i,\alpha} - \mathbf{R}_{\text{cm},\alpha}) \quad (4.98)$$

$$\dot{\mathbf{p}}_{i,\alpha} = \mathbf{F}_{i,\alpha} - (\eta_{\alpha} + \xi_{\alpha})\mathbf{p}_{i,\alpha} \quad (4.99)$$

$$\dot{\xi}_{\alpha} = \frac{1}{Q_{\alpha}} \left(\sum_i \frac{\mathbf{p}_{i,\alpha}^2}{m_i} - Nk_{\text{B}}T_{\text{ext}}d_{\alpha} \right) \quad (4.100)$$

$$\dot{\eta}_{\alpha} = \frac{V_{\alpha}}{M_{\eta,\alpha}} (\tilde{P}_{\alpha}(t) - \tilde{P}_{\alpha,\text{ext}}) \quad (4.101)$$

$$\dot{V}_{\alpha} = V_{\alpha}\eta_{\alpha}d_{\alpha}. \quad (4.102)$$

The explicit form of the probability distribution $f(\mathbf{r}^N, \mathbf{p}^N, \eta_{\alpha}, \xi_{\alpha}, V_{\alpha})$, generated by Eqs. (4.98)-(4.102) is found in a similar way as in section 4.3 where we demonstrated that Hoover-Melchionna equations (4.75)-(4.79) generate the probability distribution $\exp(-\beta H)$. For this purpose, we first calculate (see Eqs. (4.65) and (4.66))

$$\begin{aligned} \sum_{\mu} \frac{\partial \dot{x}_{\mu}}{\partial x_{\mu}} &= \sum_i (d_{\parallel}\eta_{\parallel} + d_{\perp}\eta_{\perp}) \left(1 - \frac{m_i}{\sum_i m_i}\right) \leftarrow \sum_{i,\alpha} \frac{\partial}{\partial \mathbf{r}_{i,\alpha}} \cdot \mathbf{r}_{i,\alpha} \\ &\quad - N(d_{\parallel}\eta_{\parallel} + d_{\perp}\eta_{\perp} + d_{\parallel}\xi_{\parallel} + d_{\perp}\xi_{\perp}) \leftarrow \sum_{i,\alpha} \frac{\partial}{\partial \mathbf{p}_{i,\alpha}} \cdot \mathbf{p}_{i,\alpha} \\ &\quad + d_{\parallel}\eta_{\parallel} + d_{\perp}\eta_{\perp} \leftarrow \sum_{\alpha} \frac{\partial \dot{V}_{\alpha}}{\partial V_{\alpha}} \\ &= -N(d_{\parallel}\xi_{\parallel} + d_{\perp}\xi_{\perp}). \end{aligned} \quad (4.103)$$

Using Eq. (4.65) this gives

$$\frac{df}{dt} = N(d_{\parallel}\xi_{\parallel} + d_{\perp}\xi_{\perp})f. \quad (4.104)$$

If we could show

$$\frac{dH_{\text{film}}}{dt} = -k_{\text{B}}T_{\text{ext}} N(d_{\parallel}\xi_{\parallel} + d_{\perp}\xi_{\perp}), \quad (4.105)$$

it would immediately follow from Eqs. (4.104) and (4.105) that

$$f \propto \exp(-\beta H_{\text{film}}). \quad (4.106)$$

As the calculation of dH_{film}/dt is indeed very similar to that leading to Eq. (4.68), we skip some intermediate steps to arrive at

$$\begin{aligned} \frac{dH_{\text{film}}}{dt} &= \sum_{\alpha} \eta_{\alpha} V_{\alpha} d_{\alpha} \left\{ -\frac{1}{d_{\alpha} V_{\alpha}} \left(\sum_i \frac{\mathbf{p}_{i,\alpha}^2}{m_i} + \sum_i \mathbf{F}_{i,\alpha} \cdot (\mathbf{r}_{i,\alpha} - \mathbf{R}_{\text{cm},\alpha}) \right) + \tilde{P}_{\alpha}(t) \right\} \\ &\quad - k_{\text{B}} T_{\text{ext}} N \sum_{\alpha} \xi_{\alpha} d_{\alpha}. \end{aligned} \quad (4.107)$$

The validity of Eq. (4.105) immediately follows from Eq. (4.107) if we set the first sum in Eq. (4.107) to zero. This amounts to the definition of $\tilde{P}_{\alpha}(t)$ as

$$\tilde{P}_{\alpha}(t) \equiv \frac{1}{d_{\alpha} V_{\alpha}} \left(\sum_i \frac{\mathbf{p}_{i,\alpha}^2}{m_i} + \sum_i \mathbf{F}_{i,\alpha} \cdot (\mathbf{r}_{i,\alpha} - \mathbf{R}_{\text{cm},\alpha}) \right). \quad (4.108)$$

It is important to note that the specific definition of $\tilde{P}_{\alpha}(t)$ is closely related to the requirement that the probability distribution f is proportional to $\exp(-\beta H_{\text{film}})$. However, it is a remarkable property of the Hoover-like construction of H_{film} and of Eqs. (4.98)-(4.102) that the definition (4.108) does indeed correspond to the definitions of the average lateral and normal components of the pressure tensor of a planar system. To see this, we set in Eq. (4.108) $\alpha = \parallel$ and $\alpha = \perp$. Using $d_{\parallel} = 2$, $d_{\perp} = 1$, $V_{\parallel} = A$ and finally $V_{\perp} = D$ one obtains

$$\tilde{P}_{\parallel}(t) = \frac{1}{2A} \left(\sum_i \frac{\mathbf{p}_{i,\parallel}^2}{m_i} + \sum_i \mathbf{F}_{i,\parallel} \cdot (\mathbf{r}_{i,\parallel} - \mathbf{R}_{\text{cm},\parallel}) \right) \quad (4.109)$$

$$\tilde{P}_{\perp}(t) = \frac{1}{D} \left(\sum_i \frac{\mathbf{p}_{i,\perp}^2}{m_i} + \sum_i \mathbf{F}_{i,\perp} \cdot (\mathbf{r}_{i,\perp} - \mathbf{R}_{\text{cm},\perp}) \right). \quad (4.110)$$

Using Eqs. (4.92) and (4.93), it follows from Eqs. (4.109) and (4.110)

$$P_{\text{T}}(t) = \frac{1}{2V} \left(\sum_i \frac{\mathbf{p}_{i,\parallel}^2}{m_i} + \sum_i \mathbf{F}_{i,\parallel} \cdot (\mathbf{r}_{i,\parallel} - \mathbf{R}_{\text{cm},\parallel}) \right) \quad (4.111)$$

$$P_{\text{N}}(t) = \frac{1}{V} \left(\sum_i \frac{\mathbf{p}_{i,\perp}^2}{m_i} + \sum_i \mathbf{F}_{i,\perp} \cdot (\mathbf{r}_{i,\perp} - \mathbf{R}_{\text{cm},\perp}) \right). \quad (4.112)$$

These are the well known expressions for the lateral and normal components of the instantaneous pressure tensor in a planar system when averaged over the whole system.

Similar to the expression (4.55) for the pressure of a homogeneous system, the validity of expressions (4.111) and (4.112) is also limited to systems *without* periodic boundaries. The case of a system with periodic boundaries will be investigated in section 4.5.

4.4.1 Constants of Motion

It is easy to see from Eqs. (4.97) and (4.105) that

$$\begin{aligned} G_{\text{film}} &= \sum_{\alpha} \left(\sum_i \frac{\mathbf{p}_{i,\alpha}^2}{2m_i} + \frac{1}{2} Q_{\alpha} \xi_{\alpha}^2 + \frac{1}{2} d_{\alpha} M_{\eta,\alpha} \eta_{\alpha}^2 + \tilde{P}_{\alpha} V_{\alpha} \right) + U(\mathbf{r}^N) \\ &\quad + N k_{\text{B}} T_{\text{ext}} \sum_{\alpha} d_{\alpha} \int \xi_{\alpha}(t') dt' \end{aligned} \quad (4.113)$$

is constant under the time evolution, i.e. $dG_{\text{film}}/dt = 0$. This quantity can therefore serve to check the accuracy of the integration.

Next, we examine the time evolution of the center of mass momentum

$$\begin{aligned}\dot{\mathbf{P}}_{\text{cm},\alpha}(t) &= \sum_i \dot{\mathbf{p}}_{i,\alpha} \\ &= \sum_i \mathbf{F}_{i,\alpha}(t) - (\xi_\alpha(t) + \eta_\alpha(t)) \sum_i \mathbf{p}_{i,\alpha}(t) \\ &= \sum_i \mathbf{F}_{i,\alpha}^{\text{ext}}(t) - (\xi_\alpha(t) + \eta_\alpha(t)) \mathbf{P}_{\text{cm},\alpha}(t),\end{aligned}\tag{4.114}$$

where $\mathbf{F}_{i,\alpha}^{\text{ext}}$ is the projection of the external force on particle i into the α -subspace. In deriving Eq. (4.114) we used the fact that the sum of internal forces is zero. It is important to note that, even in the absence of external forces, the center of mass momentum is *not* necessarily constant. In this case, one obtains from Eq. (4.114)

$$\dot{\mathbf{P}}_{\text{cm},\alpha}(t) = -(\xi_\alpha(t) + \eta_\alpha(t)) \mathbf{P}_{\text{cm},\alpha}(t).\tag{4.115}$$

The constancy of $\mathbf{P}_{\text{cm},\alpha}$ thus requires $\mathbf{P}_{\text{cm},\alpha}(0) = \mathbf{0}$. We will see in later chapters that for a given length of the discrete time step Δ , a NpT -ensemble simulation, i.e. a simulation allowing for the fluctuations of the system size, leads in general to much larger discretization errors than the NVE or NVT alternatives. If these errors give rise to an initial center of mass momentum, a further acceleration can follow depending on the sign of the rhs of Eq. (4.115). However, a non-vanishing center of mass momentum is not problematic as long as the system properties are computed in the center of mass coordinates. Indeed, the thermodynamic properties of the system are usually formulated in this coordinate system. The temperature, $k_B T$, for example, is given by $m \langle (v - \langle v \rangle)^2 \rangle$ and *not* by $m \langle v^2 \rangle$. Here $\langle v \rangle$ is the average velocity of particles and thus the center of mass velocity. This simple, but important distinction is usually ignored because $\mathbf{P}_{\text{cm}} = \mathbf{0}$ in most relevant cases.

It also follows from Eq. (4.114) that, when external forces are present, $\mathbf{P}_{\text{cm},\alpha}$ and thus the center of mass position, $\mathbf{R}_{\text{cm},\alpha}$, will vary with time. In particular, for a thin film embedded between two (identical) impenetrable repulsive walls $\mathbf{R}_{\text{cm},\perp}$ will move around the film center.

Finally, it is directly seen from Eq. (4.98), that the usual velocity-momentum relation is not valid within the presented formalism, i.e. $\dot{\mathbf{r}}_{i,\alpha} \neq \mathbf{p}_{i,\alpha}/m_i$. Nevertheless, this relation holds for the corresponding center of mass quantities, i.e.

$$\dot{\mathbf{R}}_{\text{cm},\alpha} = \left(\sum_i m_i \right)^{-1} \mathbf{P}_{\text{cm},\alpha}(t).\tag{4.116}$$

This can easily be seen by summing Eq. (4.98) over all particles and using the definition of the center of mass position, namely $\mathbf{R}_{\text{cm},\alpha} = \sum_i m_i \mathbf{r}_{i,\alpha} / \sum_i m_i$.

4.4.2 Choice of $M_{\eta,\alpha}$ and Q_α

As Eqs. (4.98)-(4.102) are formally identical to Hoover-Melchionna equations (4.75)-(4.79), the analysis of subsections 4.2.1 and 4.3.1 concerning the choice of Q and M_η can directly be adopted for Q_α and $M_{\eta,\alpha}$. Actually, the data used to test the theoretical discussion of subsection 4.2.1 was obtained from simulations of thin films and not from those of a bulk system. This

is justified by the formal analogy just mentioned. However, for the sake of completeness, we repeat the formula for the optimum choice of Q for planar systems

$$Q_\alpha \approx \frac{2d_\alpha N k_B T_{\text{ext}}}{\omega_{\text{intrinsic}}^2}. \quad (4.117)$$

In rewriting Eq. (4.47) we should have replaced $\omega_{\text{intrinsic}}^2$ by $\omega_{\text{intrinsic},\alpha}^2$ to take into account the anisotropy of the system with respect to the directions parallel ($\alpha = \parallel$) and perpendicular ($\alpha = \perp$) to the surface. However, as the atomic frequencies are in general rather insensitive to these anisotropies, we use the same $\omega_{\text{intrinsic}}^2$ for both parallel and perpendicular directions. The approximation (4.49) can also be used for an estimate of $\omega_{\text{intrinsic}}^2$.

In a similar way, we can translate the results obtained in subsection 4.3.1 for a reasonable choice of M_η to the case of planar systems. This reads

$$M_{\eta,\parallel} \approx 2n_{\text{rt}}^2 N \left(\frac{A^{1/2}}{\pi} \right)^2 \quad (4.118)$$

$$M_{\eta,\perp} \approx n_{\text{rt}}^2 N \left(\frac{D}{\pi} \right)^2, \quad (4.119)$$

where n_{rt} is the requested ratio of the round trip frequency of a sound wave to the typical frequency of the volume fluctuations.

4.4.3 Integration of Equations of Motion

In section 4.1 we derived the so called velocity-Verlet algorithm (4.13) for the integration of the Newtonian equation of motion (4.1). The major advantage of this algorithm is that it is time reversible and volume preserving. Unfortunately, this algorithm cannot be used by the integration of Eqs. (4.98)-(4.102). The reason lies in the coupling between $\dot{\mathbf{r}}_{i,\alpha}$ with $\mathbf{r}_{i,\alpha}$ in Eq. (4.98) and in the presence of the velocity dependent term in Eq. (4.99). So, a decomposition into a purely position-translating and a purely momentum translating term [see Eqs. (4.9) and (4.10)] is no longer possible.

Nevertheless, we will start from a symmetric ansatz and derive a propagation algorithm, which reduces to the velocity-Verlet algorithm (4.13) in the absence of coupling to the heat bath and at constant D and constant A .

Consider the following symmetric approximation to a function $f(t)$

$$f(t+h) = f(t) + \frac{h}{2} \left(\dot{f}(t) + \dot{f}(t+h) \right) + \mathcal{O}(h^3), \quad (4.120)$$

where $\dot{f} = df/dt$. To see that the above expansion is indeed of the order h^2 , we apply a first order Taylor expansion to $\dot{f}(t+h)$

$$\dot{f}(t+h) = \dot{f}(t) + h\ddot{f}(t) + \mathcal{O}(h^2). \quad (4.121)$$

Using Eq. (4.121), one obtains from Eq. (4.120)

$$f(t+h) = f(t) + h\dot{f}(t) + \frac{h^2}{2}\ddot{f}(t) + \frac{h}{2}\mathcal{O}(h^2). \quad (4.122)$$

Clearly, the last term in Eq. (4.122) is of order $\mathcal{O}(h^3)$.

Let us apply the expansion (4.120) to Eq. (4.98). This gives

$$\begin{aligned}
\mathbf{r}_{i,\alpha}(t+h) &= \mathbf{r}_{i,\alpha}(t) + \frac{h}{2} (\dot{\mathbf{r}}_{i,\alpha}(t) + \dot{\mathbf{r}}_{i,\alpha}(t+h)) \\
&= \mathbf{r}_{i,\alpha}(t) + \frac{h}{2} \left\{ \frac{\mathbf{p}_{i,\alpha}(t)}{m_i} + \eta_\alpha(t) (\mathbf{r}_{i,\alpha}(t) - \mathbf{R}_{\text{cm},\alpha}(t)) \right\} \\
&\quad + \frac{h}{2} \left\{ \frac{\mathbf{p}_{i,\alpha}(t+h)}{m_i} + \eta_\alpha(t+h) (\mathbf{r}_{i,\alpha}(t+h) - \mathbf{R}_{\text{cm},\alpha}(t+h)) \right\}.
\end{aligned} \tag{4.123}$$

The problem is now that some expressions on the rhs of Eq. (4.123) require the knowledge of the positions and other variables at the later time $t+h$. The simplest way of solving this problem is to apply a first order Taylor expansion to all those quantities on the rhs of (4.123) which have $t+h$ as argument

$$f(t+h) \approx f^e \equiv f(t) + hf'(t). \tag{4.124}$$

This is the well known *Euler method* which explains the origin of the superscript on f . Note that, although the error introduced by the Euler step (4.124) is of the order $\mathcal{O}(h^2)$, the corresponding error in $\mathbf{r}_{i,\alpha}(t+h)$ will be of the order $\mathcal{O}(h^3)$. This is due to the extra factor of h in front of $(t+h)$ -dependent quantities on the rhs of Eq. (4.123). The order of the approximation in Eq. (4.123) is therefore unchanged when the Euler step is used. With this approximation, Eq. (4.123) becomes

$$\begin{aligned}
\mathbf{r}_{i,\alpha}(t+h) &= \mathbf{r}_{i,\alpha}(t) + \frac{\mathbf{p}_{i,\alpha}(t)}{m_i} \left\{ h - \frac{h^2}{2} [\eta_\alpha(t) + \xi_\alpha(t)] + \frac{h^2}{2} \xi_\alpha^e \right\} \\
&\quad + \frac{h^2}{2m_i} \mathbf{F}_{i,\alpha}(t) \\
&\quad + (\mathbf{r}_{i,\alpha}(t) - \mathbf{R}_{\text{cm},\alpha}(t)) \left\{ \frac{h}{2} \eta_\alpha(t) + \frac{h^2}{2} \eta_\alpha^e \eta_\alpha(t) \right\} \\
&\quad + \frac{h^2}{2} \eta_\alpha^e (\mathbf{r}_{i,\alpha}(t) - \mathbf{R}_{\text{cm},\alpha}^e(t)).
\end{aligned} \tag{4.125}$$

Note that the calculation of $\mathbf{R}_{\text{cm},\alpha}^e$ does not require an extra loop over $\mathbf{r}_{i,\alpha}^e$. It can be directly calculated from the knowledge of $\mathbf{R}_{\text{cm},\alpha}$ and $\mathbf{P}_{\text{cm},\alpha}$ at the previous step. This is a consequence of Eq. (4.116).

One could proceed further in a similar way and derive the corresponding expression for $\mathbf{p}_{i,\alpha}(t+h)$. However, there is a better way in propagating the momenta. The information on the new coordinates $\mathbf{r}_{i,\alpha}(t+h)$ can be used to calculate the corresponding new forces, $\mathbf{F}_{i,\alpha}(t+h)$. This yields a better result than applying an Euler step to $\mathbf{F}_{i,\alpha}(t+h)$. In fact, using the Euler-approximation for forces is not only inaccurate, but also more complicated as it requires the knowledge of their time derivatives. Thus, we first calculate the new forces and then propagate the momenta. Within the force loops the contribution of forces to the system pressure should also be computed for the pressure enters the time evolution of η_α [see Eq. (4.101)].

Once the new forces are computed, one can obtain the new momenta by evaluating

$$\begin{aligned}
\mathbf{p}_{i,\alpha}(t+h) &= \mathbf{p}_{i,\alpha}(t) + \frac{h}{2} (\mathbf{F}_{i,\alpha}(t) + \mathbf{F}_{i,\alpha}(t+h)) \\
&\quad - \frac{h}{2} (\xi_\alpha(t) + \eta_\alpha(t) + \xi_\alpha^e(t) + \eta_\alpha^e(t)) \mathbf{p}_{i,\alpha}(t) \\
&\quad - \frac{h^2}{2} (\xi_\alpha^e(t) + \eta_\alpha^e(t)) \mathbf{F}_{i,\alpha}(t) \\
&\quad + \frac{h^2}{2} (\xi_\alpha^e(t) + \eta_\alpha^e(t)) (\xi_\alpha(t) + \eta_\alpha(t)) \mathbf{p}_{i,\alpha}(t).
\end{aligned} \tag{4.126}$$

During the calculation of the new momenta, one can also compute the new kinetic energy, so that at the end, the friction variables ξ_α can be propagated a step further [for ξ_α^e see Eq. (4.130)]

$$\xi_\alpha(t+h) = \frac{\xi(t) + \xi_\alpha^e}{2} + \frac{h}{2Q_\alpha} \left\{ \sum_i \frac{\mathbf{p}_{i,\alpha}^2(t+h)}{m_i} - d_\alpha k_B T_{\text{ext}} \right\}. \quad (4.127)$$

The propagation of η_α , however, requires the calculation of the pressure. As already mentioned, the contribution of forces to the internal pressure can be obtained during the force calculation. The new kinetic energy is also known at this stage of integration. Thus, the new generalized forces $\tilde{P}_\alpha(t+h)$ can be computed using Eq. (4.108). This allows the evaluation of $\eta_\alpha(t+h)$ via [see Eqs. (4.131) and (4.132)]

$$\eta_\alpha(t+h) = \frac{\eta_\alpha(t) + \eta_\alpha^e}{2} + \frac{hV_\alpha^e}{2M_{\eta,\alpha}} (\tilde{P}_\alpha(t+h) - \tilde{P}_{\alpha,\text{ext}}). \quad (4.128)$$

Finally, the new (reduced) volumes V_α are found to be

$$V_\alpha(t+h) = \frac{V_\alpha(t) + V_\alpha^e}{2} + \frac{h}{2} d_\alpha V_\alpha^e \eta_\alpha(t+h). \quad (4.129)$$

The intermediate quantities ξ_α^e , η_α^e and V_α^e are obtained from an Euler step

$$\xi_\alpha^e = \xi(t) + \frac{h}{Q_\alpha} \left\{ \sum_i \frac{\mathbf{p}_{i,\alpha}^2(t)}{m_i} - d_\alpha k_B T_{\text{ext}} \right\} \quad (4.130)$$

$$\eta_\alpha^e = \eta_\alpha(t) + \frac{hV_\alpha(t)}{M_{\eta,\alpha}} (\tilde{P}_\alpha(t) - \tilde{P}_{\alpha,\text{ext}}) \quad (4.131)$$

$$V_\alpha^e = V(t) + hV(t)\eta_\alpha(t)d_\alpha. \quad (4.132)$$

Next, we show that in the special case of the microcanonical-ensemble, the integration scheme just derived reduces to the velocity-Verlet algorithm. Within the presented formalism, a NVE -simulation is achieved by setting $Q_\alpha = M_{\eta,\alpha} = \infty$ as well as $\eta_\alpha(t=0) = 0$ and $\xi_\alpha(t=0) = 0$. It follows then immediately from Eqs. (4.130)-(4.132) that $\xi_\alpha^e = \eta_\alpha^e = 0$ and $V_\alpha^e = V_\alpha(0)$. Inserting these results in Eqs. (4.127)-(4.129) yields $\eta_\alpha(h) = 0$ and $\xi_\alpha(h) = 0$ and $V_\alpha(h) = V(0)$. Finally, Eqs. (4.125) and (4.126) simplify to

$$\mathbf{r}_{i,\alpha}(h) = \mathbf{r}_{i,\alpha}(0) + h \frac{\mathbf{p}_{i,\alpha}(0)}{m_i} + \frac{h^2}{2m_i} \mathbf{F}_{i,\alpha}(0) \quad (4.133)$$

$$\mathbf{p}_{i,\alpha}(h) = \mathbf{p}_{i,\alpha}(0) + \frac{h}{2} (\mathbf{F}_{i,\alpha}(0) + \mathbf{F}_{i,\alpha}(h)), \quad (4.134)$$

which are identical to the velocity-Verlet equations (4.12)-(4.13).

Recalling the comments on the generalized external forces $\tilde{P}_{\perp,\text{ext}}$ and $\tilde{P}_{\parallel,\text{ext}}$, we close this subsection emphasizing that, within the presented approach to the NpT -simulation of planar systems, one must set $M_{\eta,\parallel} = \infty$ and $\eta_{\parallel} = 0$, if one is interested in performing a simulation at constant normal pressure, $P_{N,\text{ext}}$. Similarly, for a simulation at constant lateral pressure, $M_{\eta,\perp} = \infty$ and $\eta_{\perp} = 0$ are necessary preconditions.

4.5 PBC and the Calculation of the Pressure

We have already mentioned in a comment on the formula (4.55) that this formula is not appropriate for calculating the pressure when periodic boundary conditions are supplied. The

same objection was made in commenting the expressions (4.111) and (4.112) for the lateral and transversal components of the pressure tensor in a planar system. We will now address this problem within the Hoover-Melchionna approach to the NpT -ensemble simulation. Applying the same ideas to the Nosé-Andersen method will lead to the same results. We further restrict ourselves to the case of a homogeneous system, the generalization to planar systems will be given at the end.

To obtain an expression for the pressure which takes into account the effects of periodic boundaries, it is necessary to extend H so that it includes also the effects of image particles. Let us consider a (real) system of N particles and its $N_{\text{sys}} - 1$ periodic images. If the number, $N_{\text{sys}} - 1$, of image systems is chosen large enough, the ratio of the surface of the composed system (containing the real and image systems) to its volume will tend to zero. We can therefore formulate the problem for a system composed of a real system and a sufficiently large but finite number of image systems. Without loss of generality, we will restrict ourselves to the case where the image systems are symmetrically ordered around the real one, so that the center of mass position of the composed system will be identical to that of the real system, i.e. $\mathbf{R}_{\text{cm}}^{\infty} = \mathbf{R}_{\text{cm}}$, where we used the superscript ‘ ∞ ’ to indicate the composed system. Further we obtain $V^{\infty} = N_{\text{sys}}V$ and $N^{\infty} = N_{\text{sys}}N$ where V^{∞} is the volume and N^{∞} the number of particles of the composed system (V still stands for the volume of the real system). For a homogeneous system, we now define [see Eq. (4.62)]

$$H^{\infty} = \sum_{i=1}^{N^{\infty}} \frac{\mathbf{p}_i^2}{2m_i} + U(\mathbf{r}^{N^{\infty}}) + \frac{1}{2}Q^{\infty}\xi^2 + \frac{1}{2}d M_{\eta}^{\infty}\eta^2 + P_{\text{ext}} V^{\infty}. \quad (4.135)$$

along with the equations of motion [see Eqs. (4.56)-(4.60)]

$$\dot{\mathbf{r}}_i = \frac{\mathbf{p}_i}{m_i} + \eta(\mathbf{r}_i - \mathbf{R}_{\text{cm}}) \quad (4.136)$$

$$\dot{\mathbf{p}}_i = \mathbf{F}_i - (\eta + \xi)\mathbf{p}_i \quad (4.137)$$

$$\dot{\xi} = \frac{1}{Q^{\infty}} \left(\sum_i^{N^{\infty}} \frac{\mathbf{p}_i^2}{m_i} - N^{\infty} k_{\text{B}} T_{\text{ext}} d \right) \quad (4.138)$$

$$\dot{\eta} = \frac{V^{\infty}}{M_{\eta}^{\infty}} (P(t) - P_{\text{ext}}) \quad (4.139)$$

$$\dot{V}^{\infty} = V^{\infty} \eta d. \quad (4.140)$$

As reader may have noticed, these equations are exactly analogous to Hoover-Melchionna Eqs. (4.75)-(4.79). The only difference is that, now, the particle index i runs over all particles including image particles, i.e. $i = 1, 2, \dots, N^{\infty}$ and that we have replaced the heat bath parameter Q by Q^{∞} and M_{η} by M_{η}^{∞} to indicate that ξ and η are now coupled to N^{∞} particles. Again, Eq. (4.65) can be used to show that

$$\frac{df}{dt} = N^{\infty} d \xi f, \quad (4.141)$$

where $f = f(\mathbf{r}^{N^{\infty}}, \mathbf{p}^{N^{\infty}}, \xi, V^{\infty}, \eta)$ is the probability distribution generated by Eqs. (4.136)-(4.140). The total time derivative of H^{∞} can be calculated in the same way as we did for dH/dt [see Eq. (4.68)]. The result is that the desired relation,

$$\frac{dH^{\infty}}{dt} = -\xi k_{\text{B}} T_{\text{ext}} N^{\infty} d, \quad (4.142)$$

is ensured by the following definition of the instantaneous pressure

$$P(t) = \frac{1}{dV^\infty} \left(\sum_i^{N^\infty} \frac{\mathbf{p}_i^2}{m_i} + \sum_{i=1}^{N^\infty} \mathbf{r}_i \cdot \mathbf{F}_i \right). \quad (4.143)$$

In the present definition, $P(t)$ is defined over the entire system, containing the real system and its $N_{\text{sys}} - 1$ images. The forces appearing in (4.143) thus contain also the contributions of the so called ghost particles (images of real particles).

When calculating dH^∞/dt and df/dt we have supposed that all variables appearing in H^∞ and f can be considered as independent of each other. Otherwise we could neither use Eq. (4.65) in calculating df/dt nor expand $dH^\infty/dt = \sum_\mu (\partial H^\infty / \partial x_\mu) \dot{x}_\mu$. This assumption, however, is *not* in contradiction to the obvious fact that the knowledge of the position and momentum of a real particle is sufficient to uniquely determine that of all its periodic images. To see this, we look at the time evolution of the system composed of real and image particles evolving according to the motion equations (4.136)-(4.140). Imagine a perfectly arranged periodic system at some initial time, $t = 0$ say. We suppose that the momentum of each image particle is equal to that of the corresponding real particle. As the surrounding of a given particle is identical to that of each of its periodic images, they will all move along parallel lines and will never cross each other. The whole system will thus keep its periodic structure. It means that the initial relation between the position and velocity of a particle and those of its periodic images remains unchanged under time evolution. Therefore, there is no fundamental necessity for explicit use of constraints to maintain the periodic structure. The absence of constraints in a problem is equivalent to saying that the corresponding variables are independent.

As an example, we recall the rigid body problem. It is clear that one could consider the positions and velocities of all particles of a rigid body as independent of each other, formulate the Hamiltonian of the system and then derive the appropriate equations of motion. However, for a rigid body, it is also clear that the knowledge of the positions and velocities of only two particles is sufficient to determine those of all others. This observation makes clear that the use of constraints is not based on some fundamental requirements, but in the very simple fact that it can simplify the problem by an appreciable amount. It is not very clever to solve $3N$ equations (where N is practically infinitely large) if one could achieve the same result by solving only 6.

Next, we try to express the redundant terms in the formula (4.143) for the pressure in terms of the momenta and positions of real particles. Let us suppose that we first start to label real particles and then the ghost particles so that $\sum_{i=1}^{N^\infty}$ will run over real particles only. Using the fact that the momentum of an image particle is equal to that of the corresponding real particle, the kinetic contribution to $P(t)$ can immediately be simplified to a sum containing the contribution of real particles only

$$\begin{aligned} P^K(t) &= \frac{1}{dN_{\text{sys}}V} \sum_i^{N_{\text{sys}}N} \frac{\mathbf{p}_i^2}{m_i} \\ &= \frac{1}{dV} \sum_{i=1}^N \frac{\mathbf{p}_i^2}{m_i}. \end{aligned} \quad (4.144)$$

One could think of applying the same procedure to the configurational part of the pressure. Indeed, like for the momenta, also the forces on a real particle and on its periodic images are equal. The position of a real particle, however, differs from that of its periodic images. Nevertheless, one can also obtain a well defined mapping of the configurational part of the

pressure into the real system and its boundaries. Recalling that the force \mathbf{F}_i on a particle i is in fact a sum over two particle forces, $\mathbf{F}_i = \sum_{j=1}^{N_{\text{sys}}N} \mathbf{F}_{ij}$, and using Newton's third law we write

$$\begin{aligned} P^U(t) &= \frac{1}{dN_{\text{sys}}V} \sum_{i=1}^{N_{\text{sys}}N} \mathbf{r}_i \cdot \mathbf{F}_i \\ &= \frac{-1}{dN_{\text{sys}}V} \sum_{i<j}^{N_{\text{sys}}N} \mathbf{r}_{ij} \cdot \mathbf{F}_{ij}, \end{aligned} \quad (4.145)$$

where $\mathbf{r}_{ij} = \mathbf{r}_j - \mathbf{r}_i$. Note that the sum in Eq. (4.145) runs over all pairs of particles regardless of whether they are real or images. Let us call a pair of particles as an *inner pair* if both particles lie inside the same (real or image) system. In contrast to an inner pair a *boundary crossing pair* is defined as a pair of particles belonging to two adjacent systems. In Fig. 4.4, for example, (i, j) , (i', j') and (i'', j'') are inner pairs whereas (i'', j) and (i, j') are boundary crossing pairs. We further assume that the forces \mathbf{F}_{ij} are sufficiently short-ranged and that the system size is large enough so that a particle does not interact with its own periodic images. In particular, particles of a system interact with those of the same system and of the adjacent systems only. The sum in (4.145) can therefore be split into two parts,

$$\begin{aligned} P^U(t) &= -\frac{1}{dN_{\text{sys}}V} \sum_{\text{all inner pairs}} \mathbf{r}_{ij} \cdot \mathbf{F}_{ij} \\ &\quad -\frac{1}{dN_{\text{sys}}V} \sum_{\substack{\text{all} \\ \text{boundary} \\ \text{crossing} \\ \text{pairs}}} \mathbf{r}_{ij} \cdot \mathbf{F}_{ij}. \end{aligned} \quad (4.146)$$

It is clear that, for a given inner pair (i, j) in the real system, its image pair in each of the image systems leads to the same contribution to the first sum on the rhs of Eq. (4.146). Hence, the

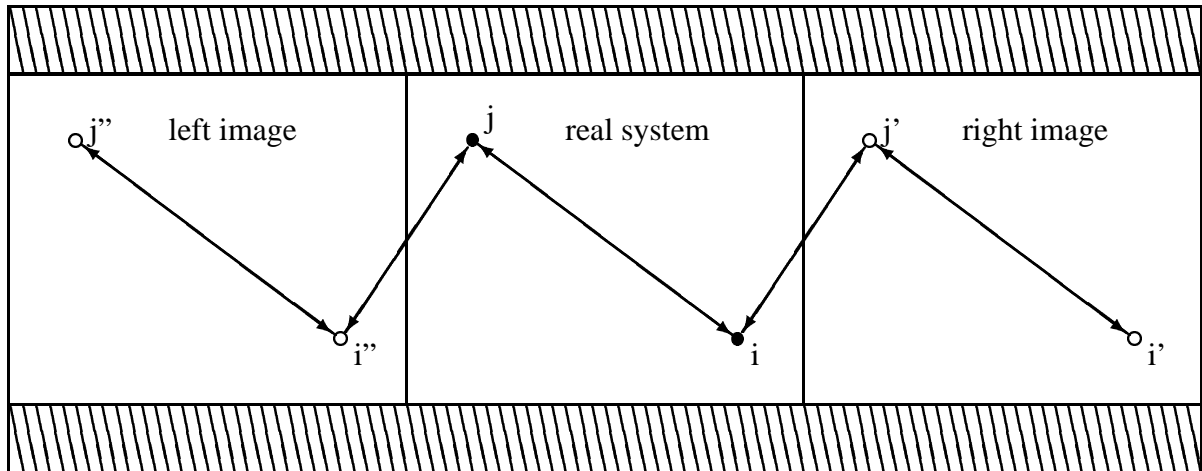


Figure 4.4: A system composed of a real system of $N = 2$ particles and two image systems symmetrically ordered around the real one. The *inner pairs* (i, j) , (i', j') and (i'', j'') are equivalent in the sense that $\mathbf{r}_{ij} \cdot \mathbf{F}_{ij} = \mathbf{r}_{i'j'} \cdot \mathbf{F}_{i'j'} = \mathbf{r}_{i''j''} \cdot \mathbf{F}_{i''j''}$. However, there are only $N_{\text{sys}} - 1 = 2$ equivalent *boundary crossing pairs*, namely (i'', j) and (i, j') .

sum over the inner pairs can be rewritten as

$$\frac{1}{dN_{\text{sys}}V} \sum_{\text{all inner pairs}} \mathbf{r}_{ij} \cdot \mathbf{F}_{ij} = \frac{1}{dV} \sum_{\text{real inner pairs}} \mathbf{r}_{ij} \cdot \mathbf{F}_{ij}, \quad (4.147)$$

where we used the fact that the composed system contains N_{sys} identical systems including the real one.

Now, we consider the sum over boundary terms in Eq. (4.146). It is illustrated in Fig. 4.4 that, for a finite number of image systems, a set of equivalent boundary crossing pairs has $N_{\text{sys}} - 1$ elements only. Note also that among the boundary crossing pairs of the same contribution, there are *two* pairs containing a real particle. In Fig. 4.4, for example, each of the boundary crossing pairs (i'', j) and (i, j') (whose contributions to the pressure are equal) contain a real particle. Let us denote by “boundary crossing pairs of the real system” all those pairs which are built up of a real particle and a particle stemming from one of the *adjacent* images of the real system. Now, we can write

$$\begin{aligned} \frac{1}{dN_{\text{sys}}V} \sum_{\substack{\text{all} \\ \text{boundary} \\ \text{crossing} \\ \text{pairs}}} \mathbf{r}_{ij} \cdot \mathbf{F}_{ij} &= \frac{N_{\text{sys}} - 1}{2 dN_{\text{sys}}V} \sum_{\substack{\text{boundary} \\ \text{crossing} \\ \text{pairs of the} \\ \text{real system}}} \mathbf{r}_{ij} \cdot \mathbf{F}_{ij} \\ &= \frac{1}{2dV} \sum_{\substack{\text{boundary} \\ \text{crossing} \\ \text{pairs of the} \\ \text{real system}}} \mathbf{r}_{ij} \cdot \mathbf{F}_{ij}, \end{aligned} \quad (4.148)$$

where we used the fact that $\lim_{N_{\text{sys}} \rightarrow \infty} (N_{\text{sys}} - 1)/N_{\text{sys}} = 1$. Summarizing Eqs. (4.147) and (4.148), we have shown that the appropriate expression for the configurational part of the pressure in a system with periodic boundaries is given by

$$P^U(t) = -\frac{1}{dV} \left(\sum_{\substack{\text{inner pairs} \\ \text{of the real} \\ \text{system}}} \mathbf{r}_{ij} \cdot \mathbf{F}_{ij} + \frac{1}{2} \sum_{\substack{\text{boundary} \\ \text{crossing} \\ \text{pairs of the} \\ \text{real system}}} \mathbf{r}_{ij} \cdot \mathbf{F}_{ij} \right). \quad (4.149)$$

Next we try to convince the reader that he has not been wasting his time following all the above arguments. For this purpose, we use the simple system of Fig. 4.4 to demonstrate that the correct result given in Eq. (4.149) is indeed different from the sum $\sum_i \mathbf{F}_i \cdot \mathbf{r}_i$, where \mathbf{F}_i is “generalized” to contain also the contribution of the image particles.

It is seen from Fig. 4.4 that $\mathbf{F}_{ji''} = -\mathbf{F}_{ij'}$ and $\mathbf{F}_{ij} = -\mathbf{F}_{ji}$. Therefore we can write

$$\begin{aligned} \sum_{i=1}^2 \mathbf{r}_i \cdot \mathbf{F}_i &= (\mathbf{r}_i - \mathbf{r}_j) \cdot \mathbf{F}_{ij} + (\mathbf{r}_i - \mathbf{r}_j) \cdot \mathbf{F}_{ij'} \\ &= -(\mathbf{r}_{ij} \cdot \mathbf{F}_{ij} + \mathbf{r}_{ij'} \cdot \mathbf{F}_{ij'}), \end{aligned} \quad (4.150)$$

where we further used $\mathbf{r}_{ij} = \mathbf{r}_j - \mathbf{r}_i$. On the other hand, evaluating the sums on the rhs of Eq. (4.149) for the system of two particles i and j in Fig. 4.4 yields

$$\begin{aligned} - \sum_{\substack{\text{rhs of} \\ \text{Eq. (4.149)}}} \mathbf{r}_{ij} \cdot \mathbf{F}_{ij} &= -(\mathbf{r}_{ij} \cdot \mathbf{F}_{ij} + \frac{1}{2} \mathbf{r}_{ji''} \cdot \mathbf{F}_{ji''} + \frac{1}{2} \mathbf{r}_{ij'} \cdot \mathbf{F}_{ij'}) \\ &= -(\mathbf{r}_{ij} \cdot \mathbf{F}_{ij} + \mathbf{r}_{ij'} \cdot \mathbf{F}_{ij'}). \end{aligned} \quad (4.151)$$

Here, we used $\mathbf{F}_{i'j} = \mathbf{F}_{ij'}$ and $\mathbf{r}_{ij'} = \mathbf{r}_{i'j}$. It follows from Eqs. (4.150) and (4.151) that

$$\sum_{i=1}^N \mathbf{r}_i \cdot \mathbf{F}_i + \sum_{\substack{\text{as on the} \\ \text{rhs of} \\ \text{Eq. (4.149)}}} \mathbf{r}_{ij} \cdot \mathbf{F}_{ij} = \mathbf{F}_{ij'} (\mathbf{r}_{ij'} - \mathbf{r}_{ij}) = \mathbf{F}_{ij'} \mathbf{r}_{jj'} \neq 0. \quad (4.152)$$

Hence, to obtain a correct formula for the instantaneous pressure, $P(t)$, in the presence of periodic boundaries, it is not sufficient to add the contribution of image particles to the forces appearing in Eq. (4.55).

We will close the argument by demonstrating that Eqs. (4.56)-(4.60) can be derived from Eqs. (4.136)-(4.140). It will be shown that the only necessary modification to Eqs. (4.56)-(4.60) is that of the definition of the instantaneous pressure, $P(t)$, which enters the time evolution of the variable ξ [see Eq. (4.59)]. Equations (4.56) and (4.136) have already the same form. Also Eqs. (4.57) and (4.137) are formally identical. We thus examine the time evolution of ξ , η and V^∞ . Using $V^\infty = N_{\text{sys}} V$ and dividing both sides of Eq. (4.140) by N_{sys} this equation becomes identical to Eq. (4.60). The identity between Eq. (4.138) and Eq. (4.58) is ensured by choosing $Q^\infty = N_{\text{sys}} Q$. This is in agreement with the optimum choice of the heat bath parameter given in Eq. (4.47), for Q^∞ couples to the momenta of N_{sys} times larger number of particles than Q . Finally, recalling Eq. (4.86), it is reasonable to set $M_\eta^\infty = N_{\text{sys}} M_\eta$. Plugging this choice in Eq. (4.139) leads to an equation which is very similar but *not* identical to Eq. (4.59). The difference lies in the new definition of the instantaneous pressure, $P(t)$. Therefore, in the presence of periodic boundaries, Eqs. (4.56)-(4.60) can still be used, if in Eq. (4.59) the configurational part of the instantaneous pressure, $P(t)$, is calculated via Eq. (4.149).

Applying the same procedure to the case of planar systems involves no difficulties. One generalizes H_{film} to H_{film}^∞ in a similar way as we did in going from H to H^∞ . Keeping Eqs. (4.98)-(4.102) in mind, one then writes down the equations of motion for N^∞ particles and finally simplifies the appropriate expressions for the parallel and normal components of the pressure. Noting that

$$\sum_i^{N^\infty} (\mathbf{r}_{i,\alpha} - \mathbf{R}_{\text{cm},\alpha}) \cdot \mathbf{F}_{i,\alpha} = - \sum_{i<j}^{N^\infty} \mathbf{r}_{ij,\alpha} \cdot \mathbf{F}_{ij,\alpha},$$

it is easy to see that the application of the above procedure leading to Eq. (4.149) will now give ($\alpha \in \{\parallel, \perp\}$, $d_\parallel = 2$ and $d_\perp = 1$)

$$P_\alpha^U(t) = -\frac{1}{d_\alpha V_\alpha} \left(\sum_{\substack{\text{inner pairs} \\ \text{of the real} \\ \text{system}}} \mathbf{r}_{ij,\alpha} \cdot \mathbf{F}_{ij,\alpha} + \frac{1}{2} \sum_{\substack{\text{boundary} \\ \text{crossing} \\ \text{pairs of the} \\ \text{real system}}} \mathbf{r}_{ij,\alpha} \cdot \mathbf{F}_{ij,\alpha} \right). \quad (4.153)$$

Finally, we describe a situation where the discrepancy mentioned in inequality (4.152) disappears: In a planar system confined between two unpenetrable walls, the transversal coordinates of a real particle and its periodic images are always equal. This is a consequence of the fact that, in this case, no particle has an image in the direction perpendicular to the walls. Hence, an argument similar to that which led to (4.152) can be used to show that

$$\sum_{i=1}^N \mathbf{r}_{i,\perp} \cdot \mathbf{F}_{i,\perp} = \sum_{\substack{\text{as on the} \\ \text{rhs of} \\ \text{Eq. (4.153)}}} \mathbf{r}_{ij,\perp} \cdot \mathbf{F}_{ij,\perp}. \quad (4.154)$$

For directions parallel to the walls, however, the discrepancy remains unchanged.

Chapter 5

$N P_N D T$ -Simulation of Thin Films

Real experiments on thin films are mostly done under the condition of constant normal pressure. This motivates us for simulations at constant normal pressure P_N . In addition, we are also interested in analyzing the temperature dependence of the static and dynamic properties of the system at a given film thickness D . However, a simulation at constant normal pressure requires the fluctuations of the conjugate length scale, D . Therefore, it is actually not possible to carry out a NpT -simulation, which directly fixes both the normal pressure and the thickness of the film.

Nevertheless, there is an indirect way of simulating a thin film at constant P_N and D . Let the number of particles N and the temperature T be constant. It is intuitively clear that, at constant film thickness, the normal pressure can be adjusted changing the density by a variation of the surface area, A . Moreover, fluctuations of the surface area (while $\dot{D} = 0$) suggest a simulation at constant *lateral* pressure \bar{P}_T . Actually, it immediately follows from the definition (3.31) of the surface tension that for a planar system containing two interfaces

$$\bar{P}_T = P_N - \frac{2\gamma}{D}, \quad (5.1)$$

where \bar{P}_T is the lateral pressure averaged over the transversal dimension, i.e.

$$\bar{P}_T = \frac{1}{D} \int_{-D/2}^{D/2} P_T(z) dz .$$

Note that for a given set of N , T and D the surface tension is a function of one remaining parameter, P_N or \bar{P}_T , only. Thus, $\bar{P}_T = P_N - 2\gamma(P_N)/D$ is uniquely defined by the value of P_N . A simulation at a constant *lateral* pressure $\bar{P}_T = P_{N,\text{ext}} - 2\gamma(P_{N,\text{ext}})/D$ is therefore in many aspects equivalent to a simulation at a constant normal pressure $P_N = P_{N,\text{ext}}$.

In studying the dynamic properties of physical systems along the isobaric curve, one is faced with the problem that the fluctuations of the volume disturb the dynamics of the system in a rather crude way [see chapter 6]. A NpT -simulation is thus not favorable. In such a situation, one resorts to a NVE or NVT simulation, where the volume V is chosen so that the corresponding pressure will fluctuate around the required value [91]. Adopting this approach for the simulation of a thin film at a given normal pressure $P_{N,\text{ext}}$ under the condition of $D = \text{const.}$, it is necessary to determine the surface area $A(P_{N,\text{ext}})$ for the specific value of the normal pressure. As seen from Eq. (5.1), this, in turn, requires a NpT -simulation at a lateral pressure $\bar{P}_T = P_{N,\text{ext}} - 2\gamma/D$. Hence, the knowledge of $\gamma(P_N)$ is equivalent to the solution of our problem.

5.1 Iterative Calculation of the Surface Tension, γ , While Keeping both P_N and D Constant

Let $\gamma_{\text{eq}} = \gamma(P_N = P_{N,\text{ext}})$ be the equilibrium value of the surface tension. If we consider the surface tension as a function of the lateral pressure we can write

$$\gamma_{\text{eq}} = \gamma\left(\bar{P}_T = P_{N,\text{ext}} - \frac{2\gamma_{\text{eq}}}{D}\right). \quad (5.2)$$

Thus, the surface tension γ , when considered as a function of the lateral component of the pressure, satisfies a self-consistent equation for a given value of $P_{N,\text{ext}}$. This self-consistency can be used to formulate an iterative procedure:

- (i) Choose for $n = 0$ a reasonable value for γ^n . If a better choice is unknown, set $\gamma^0 = 0$.
- (ii) Carry out a simulation at $P_{T,\text{ext}}^n \equiv P_{N,\text{ext}} - 2\gamma^n/D$ for a certain amount of time, τ , and calculate

$$\begin{aligned} \gamma_{\text{out}}^n &= \frac{1}{\tau} \int_{n\tau}^{(n+1)\tau} \gamma(t') dt' \\ &= \gamma_{\text{eq}}\left(P_{T,\text{ext}}^n = P_{N,\text{ext}} - \frac{2\gamma^n}{D}\right) \end{aligned} \quad (5.3)$$

and

$$P_{N,\text{out}}^n = \frac{1}{\tau} \int_{n\tau}^{(n+1)\tau} P_N(t') dt'. \quad (5.4)$$

- (iii) If $(P_{N,\text{out}}^n - P_{N,\text{ext}})/P_{N,\text{ext}} < \epsilon$ stop the iteration, if not, set $\gamma^{n+1} = \gamma_{\text{out}}^n$ and go to (ii).

The iteration can in principle be started with an arbitrary value of γ^0 . It will, however, converge faster if γ^0 is close to the equilibrium value γ_{eq} . The reason why we monitor the convergence of $P_{N,\text{out}}^n$ and not that of γ^n lies in the fact that we are interested in setting the normal pressure to the given external value $P_{N,\text{ext}}$. It is therefore reasonable to check for the convergence of $P_{N,\text{out}}^n$ already within the iteration procedure and use it as the exit-criterion.

5.2 Convergence of the Iterative Method

In this section, we will provide evidence for the convergence of the method described in section 5.1. First, we note that close to equilibrium

$$\begin{aligned} \gamma^{n+1} &= \gamma_{\text{out}}^n = \gamma\left(P_T = P_{N,\text{ext}} - \frac{2\gamma^n}{D}\right) \\ &\approx \gamma_{\text{eq}} + \frac{2}{D} (\gamma_{\text{eq}} - \gamma^n) \left(\frac{\partial\gamma}{\partial\bar{P}_T}\right)_{D,T}, \end{aligned} \quad (5.5)$$

where we used definition (5.2) of γ_{eq} and a first order Taylor expansion of γ at $\bar{P}_T = P_{N,\text{ext}} - 2\gamma_{\text{eq}}/D$. Note that we study a situation, where N , D and T are kept fixed. A change of the lateral pressure is therefore realized by a change of surface area, A , only. If we now assume that

$$\left(\frac{\partial\gamma}{\partial\bar{P}_T}\right)_{D,T} > 0 \quad (5.6)$$

we obtain from Eq. (5.5)

$$\begin{aligned} \gamma^n > \gamma_{\text{eq}} &\Rightarrow \gamma^{n+1} < \gamma_{\text{eq}}. \\ (<) & \qquad \qquad (>) \end{aligned} \quad (5.7)$$

It follows from Eq. (5.7) that the successive values of γ^n oscillate around the equilibrium value γ_{eq} . Using Eq. (5.7) we will use semi-analytic arguments to show that the series of γ^n , when calculated via Eq. (5.2), approaches the equilibrium value γ_{eq} , i.e.

$$|\gamma_{\text{eq}} - \gamma^{n+1}| < |\gamma_{\text{eq}} - \gamma^n|. \quad (5.8)$$

Let $\gamma^n < \gamma_{\text{eq}}$. It follows from Eq. (5.7) that $\gamma^{n+1} > \gamma^n$. Therefore, we have

$$\begin{aligned} & |\gamma_{\text{eq}} - \gamma^{n+1}| < |\gamma_{\text{eq}} - \gamma^n| \\ \Leftrightarrow & \gamma^{n+1} - \gamma_{\text{eq}} < \gamma_{\text{eq}} - \gamma^n \\ \Leftrightarrow & \frac{-2}{D} (\gamma_{\text{eq}} - \gamma^n) \left(\frac{\partial \gamma}{\partial \bar{P}_{\text{T}}} \right)_{D,T} < \gamma_{\text{eq}} - \gamma^n \\ \Leftrightarrow & \frac{2}{D} \left(\frac{\partial \gamma}{\partial \bar{P}_{\text{T}}} \right)_{D,T} < 1 \end{aligned} \quad (5.9)$$

Combining the last inequality in (5.9) with the assumption (5.6), it follows that the convergence of the method requires

$$0 < \frac{2}{D} \left(\frac{\partial \gamma}{\partial \bar{P}_{\text{T}}} \right)_{D,T} < 1. \quad (5.10)$$

A justification of the left inequality in (5.10) can be found as follows. Surface tension arises from imbalance between molecular forces on particles close to the interface [93]. Let the number of particles, film thickness and temperature be kept at some given values. Imagine that the average lateral pressure, \bar{P}_{T} is increased by a change of the surface area to a certain amount, $dA < 0$ say. As a result of this change of the surface area, the system volume decreases to an amount of DdA [recall that $D = \text{const.}$]. Consequently, the mean particle separation decreases leading to an enhancement of the imbalance between molecular forces at the surface and, thus, to an increase of the surface tension, γ . This explains the validity of the left inequality in (5.10).

There may be some similar argument for the validity of

$$\frac{2}{D} \left(\frac{\partial \gamma}{\partial \bar{P}_{\text{T}}} \right)_{D,T} < 1. \quad (5.11)$$

However, we have not found a general argument. Nevertheless, for sufficiently large D , it is clear that the inequality holds. To see this, we use $2\gamma = D(P_{\text{N}} - \bar{P}_{\text{T}})$ [see Eq.(5.1)], and rewrite inequality (5.11)

$$\left(\frac{\partial P_{\text{N}}}{\partial \bar{P}_{\text{T}}} \right)_{D,T} < 2. \quad (5.12)$$

For a sufficiently large film thickness, one can use the approximation $P_{\text{N}} \approx \bar{P}_{\text{T}}$ and thus obtain

$$\left(\frac{\partial P_{\text{N}}}{\partial \bar{P}_{\text{T}}} \right)_{D,T} \approx 1 < 2 \quad \text{for large } D. \quad (5.13)$$

Therefore, if there is a limit to the validity of the inequality (5.12), it must be at small film thicknesses. We implemented the method and carried out simulations at various film thicknesses. Even at the very thin film of thickness $D = 5$, whose results will be reported in the next section, the method converges. Recall that D stands for the wall-to-wall separation. The distance of the closest approach to a wall is approximately one atomic diameter. Therefore, a value of $D = 5$ corresponds to the extreme case of three monomer layers only. There is no region with bulk properties at this film thickness.

Therefore, at least for our model, the inequality (5.12) seems to hold at all relevant film thicknesses. Of course, we did *not* examine the case of a sole monomer layer. But, if one is interested in such a system, isn't it more efficient to start directly with a two dimensional system?

5.3 On the Choice of γ^0 and τ

It will be shown later in this chapter (see Figs. 5.6 and 5.7) that the method always converges towards the same limit independent of the specific value of γ^0 . However, it is obvious that a value of γ^0 close to γ_{eq} is favorable for the convergence of the iteration. Thus, if some estimate of γ_{eq} exists, for example if γ_{eq} is known for a different temperature and/or pressure, one should

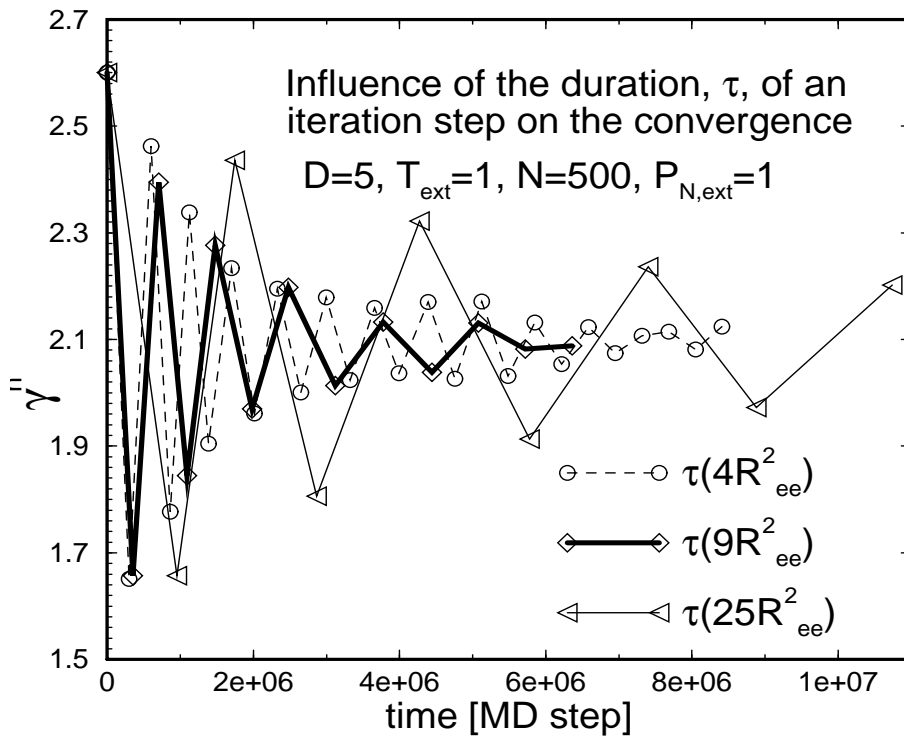


Figure 5.1: Dependence of the convergence rate of γ^n on the duration, τ , of an iteration step. The surface tension γ^n , computed within the iterative method [see Eq. (5.2)], is plotted for three choices of the duration of an iteration step: $\tau(4R_{ee}^2)$ (dashed line with circles), $\tau(9R_{ee}^2)$ (bold solid line with diamond) and $\tau(25R_{ee}^2)$ (solid line with triangles) [for the definition of $\tau(x)$, see definition (5.14)]. Rapid convergence is obtained only for the case of $\tau(9R_{ee}^2)$ [see also Fig. 5.2]. Note that, here, each γ^n is obtained as time average during the corresponding iteration step only, i.e. $\alpha = 1$ [see the combination rule (5.16)].

set γ^0 to this value.

In addition to γ^0 , the method described in section 5.1 contains a further parameter which must be well characterized before any concrete simulation can be done. It is the length, τ , of an iteration step. If τ is chosen too small, the time integrals in (5.2) and (5.4) will lead to inaccurate results for γ^n and $P_{N,\text{out}}^n$, respectively. On the contrary, if it is chosen too large, the method becomes inefficient.

It is generally known that the mean square displacements (MSD) and relaxation processes of position dependent physical quantities are closely related. Therefore, as the pressure tensor and thus the surface tension depend on intermolecular forces and distances, we expect the magnitude of MSD to be a natural measure of time for our purpose. Let us define $\tau(x)$ as the time needed by the mean square displacements of chains' centers of mass, g_3 , to satisfy $g_3(\tau(x)) = x$, i.e.

$$g_3(\tau(x)) \equiv x \quad (\text{defining equation for } \tau(x)). \quad (5.14)$$

We find empirically that $\tau(9R_{ee}^2)$ is a reasonable choice for the length of an iteration step, where R_{ee} is the average end-to-end distance of a chain. This leads to much faster convergence than the shorter time $\tau(4R_{ee}^2)$. Time integrals computed within an interval of length $\tau(4R_{ee}^2)$ are inaccurate so that the convergence of the series γ^n and/or $P_{N,\text{out}}^n$ is no longer warranted. On the other hand, the choice of a much larger time $\tau(25R_{ee}^2)$ does not improve the results very much. Therefore, $\tau(9R_{ee}^2)$ seems to be a good compromise between accuracy and computation time. This is demonstrated in Figs. 5.1 and 5.2 where simulation results on γ^n and $P_{N,\text{out}}^n$ are displayed as computed using Eqs. (5.2) and (5.4) for three choices of τ : $\tau(4R_{ee}^2)$, $\tau(9R_{ee}^2)$ and $\tau(25R_{ee}^2)$. The results correspond to a film of $D = 5$ containing $N = 500$ particles at $T_{\text{ext}} = 1$ (high temperature liquid state). The aim of the iteration was to find γ_{eq} corresponding to a normal pressure of $P_{N,\text{ext}} = 1$. As shown in Fig. 5.1, $\tau(9R_{ee}^2)$ leads to a rapidly converging series of γ^n thus satisfying the inequality (5.8). For the smaller τ , however, convergence is mainly limited to the beginning of the iteration only. After a few steps with well defined convergence towards the average value, statistical errors seem to dominate and results for γ^n improve much more slowly. There is even a region of more or less constant amplitude oscillations around the average value, in contradiction to the inequality (5.8). Finally, taking a much larger time $\tau(25R_{ee}^2)$ does not improve the results compared to those obtained from iteration steps of length $\tau(9R_{ee}^2)$. We recall that it is actually the convergence of $P_{N,\text{out}}^n$ towards the required value $P_{N,\text{ext}}$ which is used as the exit-condition of the iterative procedure:

$$\text{stop the iteration if } \frac{P_{N,\text{out}}^n - P_{N,\text{ext}}}{P_{N,\text{ext}}} < \epsilon \quad \text{for the required } \epsilon \quad (0 < \epsilon < 1). \quad (5.15)$$

A plot of $P_{N,\text{out}}^n$ is displayed in Fig. 5.2 for three choices of τ . The required relative accuracy was set to $\epsilon = 0.005$. As expected, the situation is similar to that of γ^n (see Fig. 5.1). Also in case of $P_{N,\text{out}}^n$, the best convergence is obtained for $\tau(9R_{ee}^2)$. It must be noted here, that for $\tau(4R_{ee}^2)$, the iteration actually did not satisfy the criterion (5.15) with $\epsilon = 0.005$. This run was therefore stopped manually, i.e. we did not wait long enough to observe a convergence (why should one waste computing time?).

Thus, when applying Eq. (5.2), the length of an iteration step must be chosen to $\tau(9R_{ee}^2)$ to ensure convergence. One should realize that $\tau(9R_{ee}^2)$ is approximately equal to the typical duration of a production run. To obtain an estimate of the time necessary for a whole iteration procedure, this time must further be multiplied by the number of iteration steps. From Fig. (5.2) we count 12 steps for a relative accuracy of $\epsilon = 0.005$. So, the iterative method introduced in section 5.2 seems to be very time consuming. The situation becomes even more crucial when

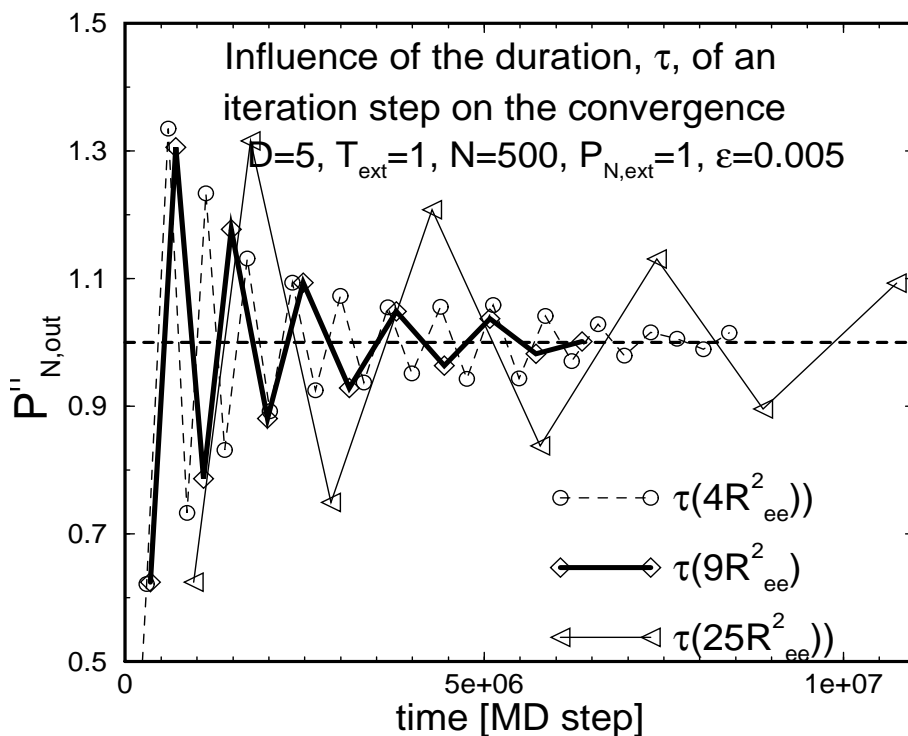


Figure 5.2: Dependence of the convergence rate of $P_{N,\text{out}}^n$ from the duration, τ , of an iteration step. $P_{N,\text{out}}^n$, as computed using Eq. (5.4), is plotted for three choices of the duration of an iteration step: $\tau(4R_{ee}^2)$ (dashed line with circles), $\tau(9R_{ee}^2)$ (bold solid line with diamonds) and $\tau(25R_{ee}^2)$ (solid line with triangles). [for the definition of $\tau(x)$, see definition (5.14)]. Rapid convergence is obtained only in the case of $\tau(9R_{ee}^2)$ [see also Fig. 5.1].

cooling down the system towards the glass transition temperature where the dynamics of the system starts to freeze and thus $\tau(9R_{ee}^2)$ tends to infinity. The lower the temperature, the higher the importance of reducing the number and length of necessary steps.

In fact, we will show in section 5.4 that a major improvement of the convergence can be achieved by introducing a kind of memory into the iteration procedure. This amounts to taking into account not only the actual iteration step, but also the previous ones in calculating the input of the next step.

5.4 An Improvement of the Iterative Method

Let us first summarize the results obtained so far. We have introduced an iterative method which permits the calculation of the surface tension, γ_{eq} , of a thin film at a given normal pressure, $P_{N,\text{ext}}$, without varying the film thickness D . The surface tension so obtained can be used to carry out a simulation in NpT -ensemble at the lateral pressure $P_{T,\text{ext}} = P_{N,\text{ext}} - 2\gamma/D$ which, in many aspects, is equivalent to a simulation at a constant normal pressure $P_{N,\text{ext}}$. We gave in section 5.2 semi-analytical evidence for the convergence of the method (see inequality (5.8)) and finally in section 5.3 we presented simulation results confirming this behavior if the length, τ , of a step is approximately chosen to $g_3(\tau) = 9R_{ee}^2$.

However, as mentioned at the end of section 5.3, repeating about 10 iteration steps of length $\tau(9R_{ee}^2)$ is very time consuming. It becomes even more unpractical at temperatures close to the

glass transition.

Fortunately, even at low temperatures, the method converges much faster than presented in section 5.3, if the results of previous iteration steps are taken into account when calculating γ^{n+1} which serves as the input of the next step. In fact, this idea has been already successful in iterative calculation of direct correlation function, $c(r)$ [94] and we were led to it by a remark in [64]. It is reported there that ‘‘To ensure convergence, it is generally necessary, to mix successive approximations to $c(r)$ before they are used as input at the next level of iteration (Boyles, 1960)’’ (see page 129 of [64], see also [94]).

We thus introduce an extra parameter, $0 < \alpha < 1$, and set

$$\gamma^{n+1}(\alpha) = \alpha\gamma_{\text{out}}^n + (1 - \alpha)\gamma^n. \quad (5.16)$$

It is easy to see that Eq. (5.16) is equivalent to

$$\gamma^{n+1}(\alpha) = \alpha \sum_{k=0}^n (1 - \alpha)^k \gamma_{\text{out}}^{n-k} + (1 - \alpha)^{n+1} \gamma^0. \quad (5.17)$$

The contribution of the k -th step before the most recent one is thus weakened by a factor of $(1 - \alpha)^k$. We have thus introduced a kind of memory into the iteration taking into account the information about previous steps. Actually, Eq. (5.17) is a weighted sum over γ_{out}^n which, due to inequality (5.7), oscillates around γ_{eq} . Therefore, the convergence of successive values of γ^n towards γ_{eq} is accelerated by the rule (5.17) as long as the length of an iteration step is long enough to yield the oscillating behavior (5.7). It is clear from the elementary analysis that the average of a converging series will converge to the same value, i.e. $\lim_{n \rightarrow \infty} \gamma^n(\alpha) = \lim_{n \rightarrow \infty} \gamma^n = \gamma_{\text{eq}}$. For finite n , however, there is a difference and therefore one should carry out some consistency checks on the output of the iteration procedure. In the situation presented here there is a well defined quantity which can be used to test the output of the method. It is the normal component of the pressure tensor. In taking the convergence of $P_{\text{N,out}}^n$ towards $P_{\text{N,ext}}$ as the exit-criterion, we already check the accuracy of the result, for an erroneous γ^n would manifest itself in $P_{\text{N,out}}^n$ as the former enters the time evolution of the system through $P_{\text{T,ext}}^n = P_{\text{N,ext}} - 2D/\gamma^n$. However, these simulations provide a further possibility to check the output of the iteration procedure: At the end of the iterative stage of the simulation, we set the volume of the system to the one calculated during the very last iteration step,

$$\langle V \rangle = \frac{1}{\tau} \int_{\text{last step}} dt' V(t'), \quad (5.18)$$

and then switch to the NVT -ensemble simulation. Within this ensemble, i.e. keeping both D and A constant, we carry out three successive equilibration steps monitoring the mean square displacements of chain centers. For the results presented here, for example, the duration of each equilibration step was chosen to $\tau(4R_{\text{ee}}^2)$. Finally, we carry out a production run (still in NVT -ensemble) of length 1×10^6 MD-steps for $D = 5$, $T_{\text{ext}} = 1$ and 1.6×10^7 MD-steps for $D = 5$, $T_{\text{ext}} = 0.55$. Now, if the normal pressure of the system is sampled during this production runs, one can examine whether the volume, computed within the iterative part of the simulation, does really correspond to the required external pressure $P_{\text{N,ext}} = 1$. Table 5.1 contains results obtained from the constant volume production runs, where V was computed using Eq. (5.18), i.e. as time average during the very last iteration step. It is seen from this table that the average volume, computed within the iterative method, corresponds to the given external normal pressure $P_{\text{N,ext}} = 1$ to a high degree of accuracy.

Table 5.1: Average normal pressure, $\langle P_N \rangle$, as obtained during NVT -production runs. The volume used in each run was computed within a preceding iterative approach with $P_{N,\text{ext}} = 1$. [see Eq. (5.18)] The film thickness was $D = 5$ and the number of particles $N = 500$.

T_{ext}	α	τ	γ^0	$\langle P_N \rangle_{NVT}$
1	0.5	$\tau(4R_{\text{ee}}^2)$	0	0.996 ± 0.009
1	0.5	$\tau(4R_{\text{ee}}^2)$	2.6	0.994 ± 0.009
1	0.6	$\tau(4R_{\text{ee}}^2)$	2.6	1.004 ± 0.010
1	0.7	$\tau(4R_{\text{ee}}^2)$	2.6	1.003 ± 0.010
0.55	0.7	$\tau(9R_{\text{ee}}^2)$	2.6	0.990 ± 0.002
0.55	0.7	$\tau(4R_{\text{ee}}^2)$	2.6	0.994 ± 0.002
0.55	0.5	$\tau(2R_{\text{ee}}^2)$	0	1.017 ± 0.015
0.55	0.5	$\tau(2R_{\text{ee}}^2)$	2.6	0.997 ± 0.002
0.55	0.5	$\tau(R_{\text{ee}}^2)$	2.6	1.004 ± 0.002

We will show in the following that the modification (5.16) does indeed speed up the convergence of the method and reduces the whole duration of the iterations by an order of magnitude or even more. This is clearly demonstrated in Figs. 5.3 and 5.4 where results are displayed on γ^n and $P_{N,\text{out}}^n$, respectively for $\alpha = 1$ (no mixing), 0.7, 0.6 and finally $\alpha = 0.5$. All other parameters (including the initial configuration) were the same for all runs, i.e. $D = 5$, $N = 500$, $T_{\text{ext}} = 1$ and $P_{N,\text{ext}} = 1$. Note that smaller values of the parameter α correspond to stronger memory effects, for the older steps are weighed by successive factors of $0 < 1 - \alpha < 1$. As shown in Figs. 5.3 and 5.4, the smaller α , the faster the method converges. However, there is not much difference between results obtained for $\alpha = 0.6$ and $\alpha = 0.5$. This may be related to the fact that, to some extent, $\alpha = 0.5$ is a lower bound, as the values below this limit, i.e. $\alpha < 0.5$, correspond to overemphasizing the past. One may also have noticed that oscillations of γ^n and $P_{N,\text{out}}^n$ are washed out or totally absent in Figs. 5.3 and 5.4. However, this is not in contradiction to inequality (5.7) since evidence for the validity of (5.7) was given in the absence of mixing only, i.e. for the case of $\alpha = 1$. For this specific value, oscillations of both γ^n and $P_{N,\text{out}}^n$ have been illustrated in Figs. 5.2 and 5.1.

Finally, we are interested in finding out to what extent the mixing rule accelerates the convergence of the method at low temperatures. Therefore, we have carried out simulations at $T_{\text{ext}} = 0.55$. At this temperature, the dynamics of the system is slowed down by an order of magnitude (see chapter 8). The question was how long the iteration procedure would take to achieve the same accuracy of $\epsilon = 0.005$ as used in previous high temperature examples. Again, the parameters of the system were $D = 5$, $N = 500$ and $P_N = 1$. Figure 5.5 compares results of two runs at $T_{\text{ext}} = 0.55$ for $\alpha = 0.7$ and $\alpha = 0.5$. As we already expected better convergence for smaller α , we went a step further and set the duration of an iteration step to $\tau(2R_{\text{ee}}^2)$ in the case of $\alpha = 0.5$, whereas for $\alpha = 0.7$ an approximately twice as large step length $\tau(4R_{\text{ee}}^2)$ was chosen. As seen from Fig. 5.5, for $\alpha = 0.5$, it takes only two steps to achieve the required relative accuracy of $\epsilon = 0.005$. In the case of $\alpha = 0.7$, however, it takes many more (actually 7) steps of larger length to satisfy the convergence criterion.

Now, we present simulation results proving that the method is independent of the chosen value of the initial parameter γ^0 . Figures 5.6 and 5.7 depict the surface tension $\gamma^n(\alpha)$ and the normal pressure $P_{N,\text{out}}^n$ as calculated by the iterative method, Eqs. (5.16) and (5.4) respectively. As expected, the method converges rapidly for $\gamma^0 = 2.6$ which is close to the equilibrium value $\gamma_{\text{eq}} = 2.53 \pm 0.005$. Nevertheless, the results obtained with $\gamma^0 = 0$, a value far from

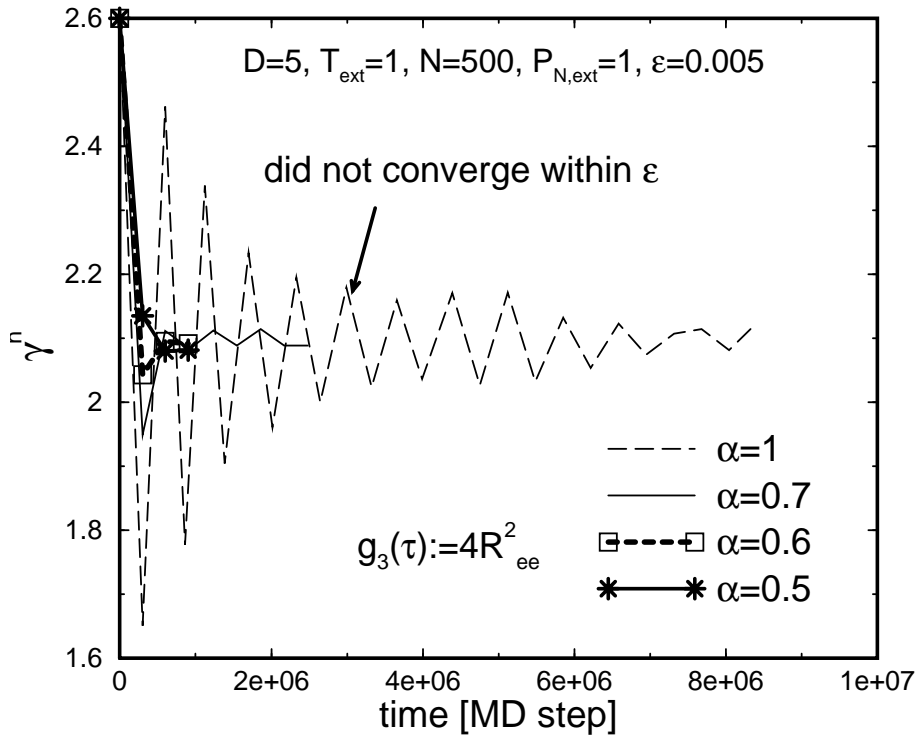


Figure 5.3: Effect of mixing successive iteration steps on the convergence of γ^n . Four values of the parameter α appearing in the mixing rule (5.16) are compared: $\alpha = 1$ (no mixing), 0.7, 0.6, 0.5. All other parameters including the initial configuration were identical for all runs. Combination rule (5.16) thus accelerates the rate of convergence by an appreciable amount. Smaller values of α (which correspond to stronger mixing) lead to faster convergence.

γ_{eq} , also converge towards the same limit. Thus, the method satisfies an important necessary condition, namely the convergence towards a well defined limit, regardless of the value of the initial parameter γ^0 . However, it is not surprising that the rate of convergence depends on the specific value of γ^0 . Note that there is no mixing in the calculation of $P_{N,\text{out}}^n$. For each iteration step, n , $P_{N,\text{out}}^n$ is calculated as the time average within *this* step only. However, as each $\gamma^n(\alpha)$ enters the time evolution of the system, there is an implicit memory effect in all physical quantities including $P_{N,\text{out}}^n$.

5.5 Again on the Choice of τ

The reader may have noticed that, for the case of $\gamma^0 = 0$, there are strong irregularities for $P_{N,\text{out}}^n$ shown in Fig. 5.7. Actually, for $\gamma^0 = 0$, some iteration steps follow the other in a much shorter time than the average distance between neighboring points. As a consequence, the time integral (5.4) becomes inaccurate. To see the origin of this irregularity in the length of an iteration step, we focus on what happens when going from the end of an iteration step to the beginning of the next one. There is actually a discrete jump in the value of the lateral pressure $P_{T,\text{ext}}$ which enters the equations of motion directly: It changes from $P_{N,\text{ext}} - 2\gamma^n/2D$ to $P_{N,\text{ext}} - 2\gamma^{n+1}/2D$. As γ^n and γ^{n+1} lie on opposite sides of γ_{eq} [see inequality 5.7] we can write $|\gamma^{n+1} - \gamma^n| = |\gamma^{n+1} - \gamma_{\text{eq}}| + |\gamma^n - \gamma_{\text{eq}}| \approx 2|\gamma_{\text{eq}} - \gamma^n|$. Therefore, the larger the difference

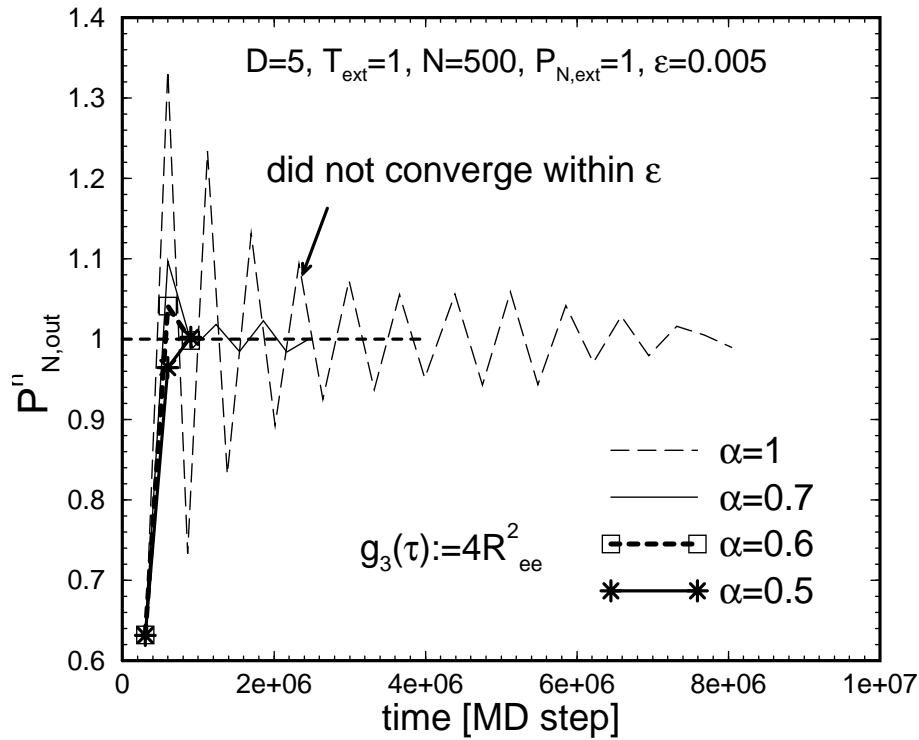


Figure 5.4: Effect of mixing successive iteration steps on the convergence of $P_{N,\text{out}}^n$. Four values of the parameter α appearing in the mixing rule (5.16) are compared: $\alpha = 1$ (no mixing), 0.7, 0.6, 0.5. All other parameters including the initial configuration were identical for all runs. Combination rule (5.16) thus accelerates the rate of convergence by an appreciable amount. Smaller values of α (which correspond to stronger mixing) lead to faster convergence.

$|\gamma_{\text{eq}} - \gamma^n|$, the stronger the discontinuity thus induced. The very first jump can be approximated by $|\gamma^1 - \gamma^0| \approx 2|\gamma_{\text{eq}} - \gamma^0|$. Values of γ^0 with a larger distance from γ_{eq} thus lead to more pronounced discontinuities between adjacent steps at the beginning of the iteration. These discrete jumps in $P_{T,\text{ext}}$ can accelerate the dynamics of the system. It may then happen that the mean square displacements, which serve as a kind of chronometer in the presented method (see comments on the choice of τ), will grow too fast and lead to an unexpectedly soon termination of the current iteration step. However, due to the convergence of the method, the strength of these discontinuities will tend towards zero during the iteration, which means that the irregularities should also disappear.

This explanation is confirmed in Fig. 5.7 where it is demonstrated that the behavior of the method becomes smoother at later iteration steps. Stronger evidence for this picture is, however, found by results obtained after introducing an empirical lower bound for τ . Actually, in all simulations at $T_{\text{ext}} = 1$ whose results have been presented here, a modified definition of τ was used. We defined τ as $\tau \equiv \max(\text{empirical lower bound}, \tau(xR_{\text{ee}}^2))$, where x is an adjustable dimensionless number (often set to 4). During the iteration, the value of the lower bound was corrected to the average length of a step. As shown in figures corresponding to $T_{\text{ext}} = 1$, no irregularities have been observed, using this modification.

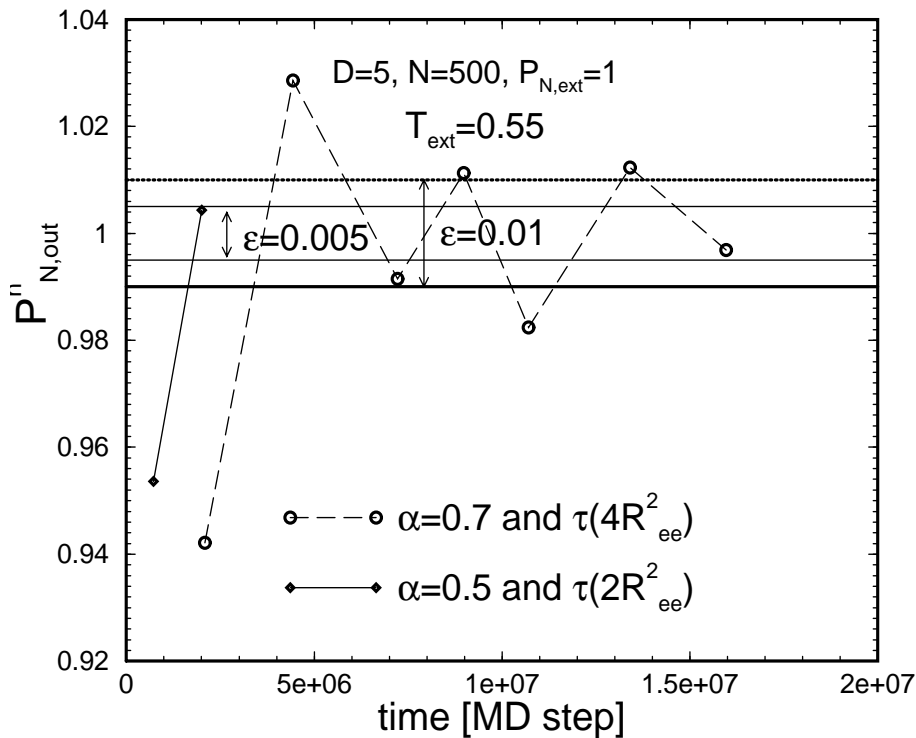


Figure 5.5: Effect of mixing successive iteration steps on the convergence of $P_{N,\text{out}}^n$ at a relatively low temperature $T_{\text{ext}} = 0.55$ for two values of the parameter α appearing in the mixing rule (5.16) $\alpha = 0.7$ and $\alpha = 0.5$. The duration of an iteration step was $\tau(2R_{\text{ee}}^2)$ for the case of $\alpha = 0.5$. This value is approximately twice as short as $\tau(4R_{\text{ee}}^2)$ which was chosen for $\alpha = 0.7$. For smaller α , the convergence criterion is satisfied within two steps, whereas for $\alpha = 0.7$ it takes 7 steps of double length to achieve the same accuracy.

5.6 How Small the Allowed Relative Error ϵ Can Be?

Some remarks are necessary concerning the choice of ϵ : It should not be chosen too small. One should realize that each independent run in a molecular dynamics simulation samples a certain portion of the phase space. Even for ergodic systems, it would take infinite time to sample the whole phase space. But this is neither feasible nor necessary. One is usually not interested in infinitely accurate results. Moreover, there is a better way for improving statistics than simply simulating longer and longer. We have made the experience that two fully independent runs of a given length give much better results than a sole run of double length. By the expression “fully independent runs” we mean simulation runs starting from independent random configurations. It seems that the typical duration of a simulation run is not sufficient to sample all relevant states for all relevant quantities. If one multiplies the length of a simulation by a factor of two, the system will still mostly visit neighboring states of the original region of the phase space during the second half of the simulation. Thus, the two halves of the simulation will have some correlations with each other which affect different quantities of interest in different ways. The problem is avoided, when starting from two different random configurations. Thus, it is not efficient to choose ϵ too small. (i.e. require too high an accuracy) as this would require longer and longer iteration steps. The length, τ , of an iteration step should be chosen such that the time integral (5.4) in combination with Eq. (5.16) is able to yield results on $P_{N,\text{out}}^n$ within the required relative accuracy determined by the parameter ϵ . It means that the smaller ϵ , the higher

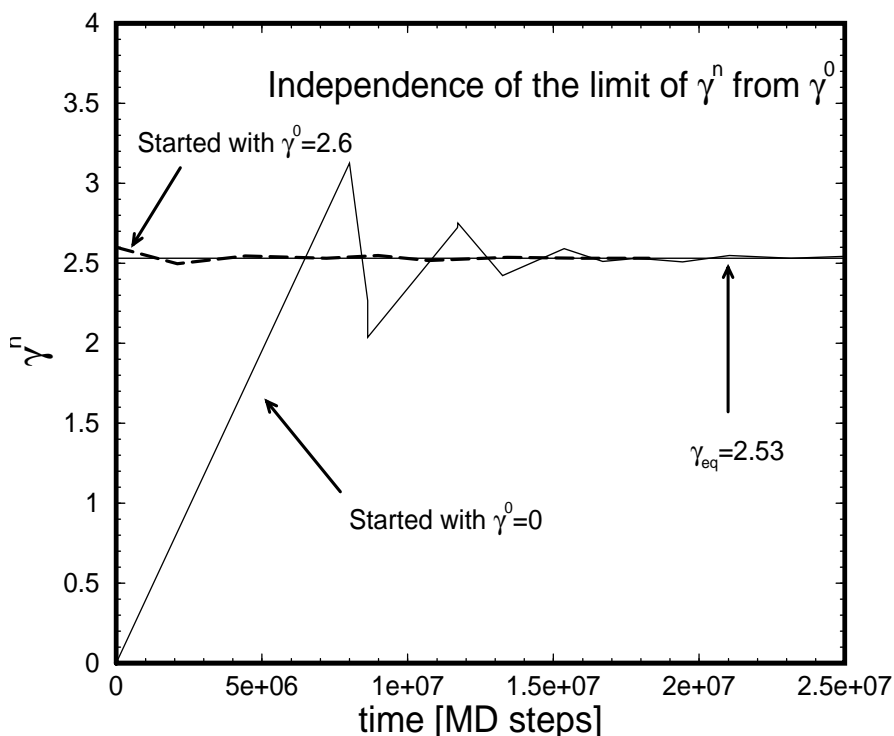


Figure 5.6: Independence of $\lim_{n \rightarrow \infty} \gamma^n$ of the initial value γ^0 . In computing the surface tension, γ^n , the mixing rule (5.16) was used with $\alpha = 0.7$ (not the optimum choice). The iterations should find $\gamma_{\text{eq}}(P_{N,\text{ext}} = 1)$. Results shown here correspond to $\gamma^0 = 0$ (far from γ_{eq}) and $\gamma^0 = 2.6$ (close to γ_{eq}). As expected, both series of γ^n converge towards the same limit, irrespective of the initial value γ^0 .

τ must be chosen. Results presented in this section suggest that $\epsilon = 0.01$ is a reasonable value leading to convergence after 2-5 iterations of length $\tau(2R_{\text{ee}}^2)$ (see for example Fig. 5.5). A further improvement of the accuracy could then be achieved by carrying out many independent runs.

We close this chapter by demonstrating in Fig. 5.8 the pressure profile of a film of thickness $D = 5$ at $T = 0.38$, the lowest simulated temperature for this film thickness. Five independent runs have been carried out and the pressure profiles have been sampled once in 10^3 MD steps. Length of each run was 4×10^7 . It is worth noting that due to the sharp raise of relaxation times at this temperature, a simulation run of the length $10^7 - 10^8$ MD steps is relative *short*. At the end of mentioned runs, for example, the mean square displacements of chain centers hardly reached R_{ee}^2 . Therefore, as a criterion for the length of an iteration step, we did *not* choose $\tau(4R_{\text{ee}}^2)$ but $\max(5 \times 10^6, \tau(0.5R_{\text{ee}}^2))$ for, otherwise, the simulation length would be inaccessible within our computation resources.

Despite this crude choice of τ , the iteration converged well. One could of course ask if the results thus obtained are accurate. Hence, we plot in Fig. 5.8 the obtained profile of the normal pressure, $P_N(z)$, as an average over all 5 independent runs. It is remarkable that not only the average value over the whole system is well reproduced, but also the local profile is in good agreement with the requirement $P_N(z) = P_{N,\text{ext}} = \text{const.}$ [see also subsection 3.3.4]. Thus, the iterative method works not only at small film thicknesses, but also at very low temperatures.

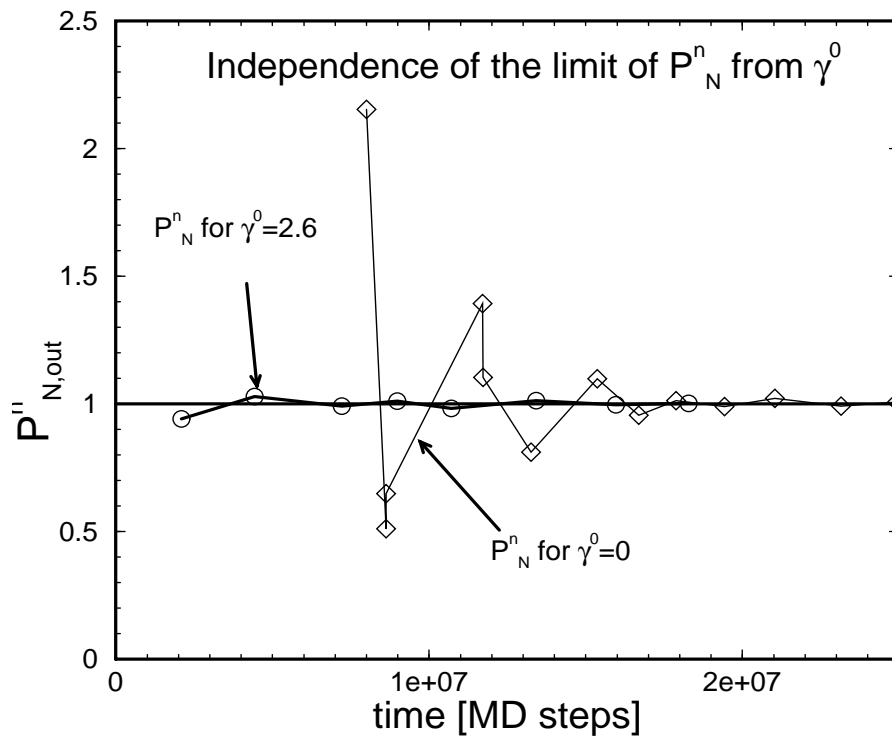


Figure 5.7: Independence of $\lim_{n \rightarrow \infty} P_{N,\text{out}}^n$ of the initial value γ^0 . In computing the surface tension, γ^n , the mixing rule (5.16) was used with $\alpha = 0.7$ (not the optimum choice). The iterations should find $\gamma_{\text{eq}} (P_{N,\text{ext}} = 1)$. Results shown here correspond to $\gamma^0 = 0$ (far from γ_{eq}) and $\gamma^0 = 2.6$ (close to γ_{eq}). As expected, both series of γ^n converge towards the same limit, irrespective of the initial value γ^0 . The irregularities in the case of $\gamma^0 = 0$ are due to large discrete jumps between two successive steps (see also the main text). Even in such a crude case, the method converges towards the required value of $P_{N,\text{ext}} = 1$.

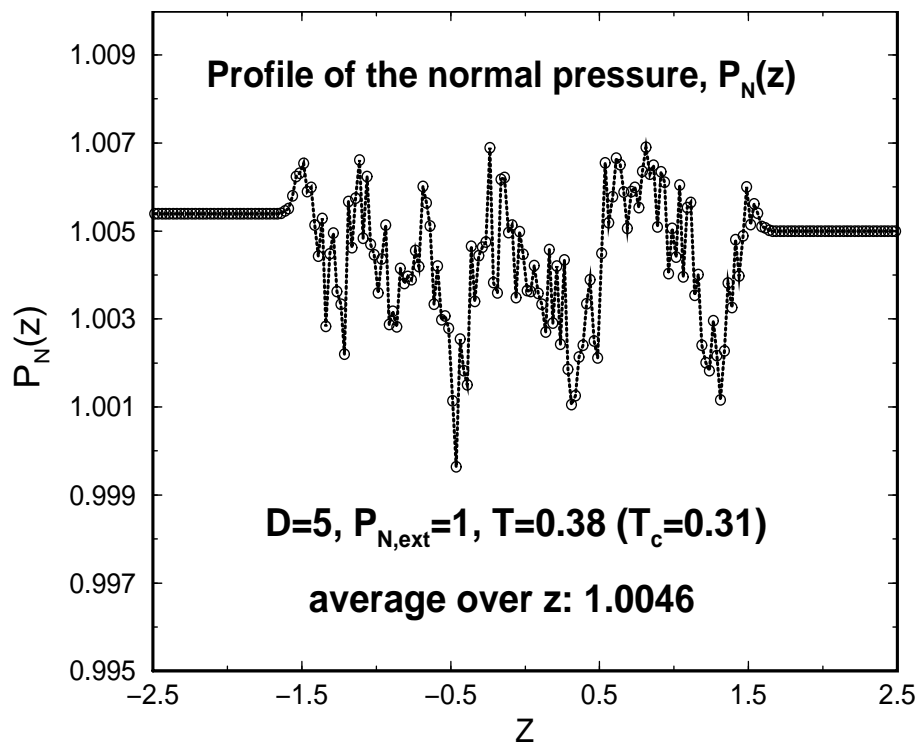


Figure 5.8: Profile of the normal pressure, P_N , as an average over 5 independent runs calculated within the NVT -ensemble. In each run, the volume of the system has been computed within the iterative method. Thus the volumes computed within the iterative method correspond very well to the given values of the temperature, T , and the external pressure, $P_{N,\text{ext}}$. Note that, compared to the lower temperature, $T = 0.55$, for which results have been discussed in this chapter, the system dynamics is slowed down by many orders of magnitude.

Chapter 6

NVE versus *NVT* and *NpT*

As described in chapter 4, in extended Lagrangian approach, a simulation at constant temperature and/or external pressure is realized by introducing extra degrees of freedom. A *NpT*-ensemble simulation requires a coupling between the appropriate extra variable, η say, on the one hand and both the particle positions and momenta on the other hand. As the force on a particle is a function of its position and that of all other particles, there is a direct coupling between η and interparticle forces. This is an essential difference to a pure *NVT*-ensemble simulation, where ξ couples to the particle momenta only. However, the physical properties of the system, should be, within the well-known $1/N$ -dependent deviations, independent of the appropriate statistical ensemble. In the ideal case, the properties calculated via *NVT*, or *NpT*-ensemble simulations must be identical to those obtained by solving the pure Newtonian motion equations (94.1), i.e. to a *NVE*-ensemble simulation. Therefore, if a difference is observed, *NVE*-results must be taken as a guiding reference.

In this chapter, we will examine if the requirement of ensemble independence is satisfied by a simulation at constant temperature and/or pressure. It will be shown that the static properties of the system are independent of the appropriate simulation ensemble. In the case of the coupling to a heat bath, also the dynamics of the system is unchanged, if the Nosé-Hoover approach is used. However, within a *NpT*-ensemble simulation, the perturbation of the dynamics of the system is not negligible.

To compare the *NVE*, *NVT* and *NpT* ensembles, we carried out, for each ensemble, 10 independent simulation runs for a film of thickness $D = 5$ at $P_{N,\text{ext}} = 1$ and $T = 0.55$. Note that, for this film thickness, this is a relative high temperature ($T_c(D = 5) = 0.31 \pm 0.02$).

6.1 Ensemble Independence of Static Properties

First, we focus on the dependence of static properties on the simulated ensemble. Figure 6.1 contains results on the density profile,

$$\rho(z) \equiv \frac{1}{A} \left\langle \sum_i^N \delta(z - z_i) \right\rangle, \quad (6.1)$$

for a film of thickness $D = 5$ at $T = 0.55$. In Eq. (6.1) A is the surface of a wall. The variable z can be taken as the distance from a wall or from the film center. Unless otherwise stated, we adopt the second choice, so that $-D/2 < z < D/2$. Three profiles are compared: that obtained from *NVE*-ensemble simulation, the density profile within the *NVT*-ensemble and

finally the same quantity computed from NpT -runs. As seen from this figure, the density profile is independent of the appropriate simulation ensemble.

Next, we consider the behavior of the pair distribution function within the mentioned simulation ensembles. For a planar system, this quantity can be defined through

$$g(z_1, z_2; r) = \frac{1}{A\rho(z_1)\rho(z_2)} \left\langle \sum_{i \neq j} \delta(z_1 - z_i) \delta(z_2 - z_j) \delta(r - r_{ij}) \right\rangle. \quad (6.2)$$

Here z_1 and z_2 denote the transversal coordinates within the system, $r_{ij} = (x_{ij}^2 + y_{ij}^2)^{1/2}$ is the distance between the particles parallel to the walls and the density $\rho(z)$ is defined by Eq. (6.1). Given a particle, in a layer at z_1 , $g(z_1, z_2; r)$ is then the probability to find another particle at distance r within a layer at z_2 . As we focus here on the case $z_1 = z_2$ which means that $z_{ij} = 0$, we give also the definition of the simplified version

$$g(z; r) = \frac{1}{A\rho^2(z)} \left\langle \sum_{i \neq j} \delta(z - z_i) \delta(z - z_j) \delta(r - r_{ij}) \right\rangle. \quad (6.3)$$

It follows from the above interpretation of $g(z_1, z_2; r)$ that, for a given particle within a layer at z , $g(z, r)$ is the probability of finding another particle in the same layer. Although the exact definition of $g(z_1 = z_2 = z; r)$ requires a layer of zero thickness, we are in practice forced to choose a finite thickness dz . In Fig. 6.2 $g(z_1 = z_2 = z; r)$ is displayed for a layer of thickness 0.25. The layer was centered at a distance $z = 1.125$ from the film center which is equivalent to a distance $z = 1.375$ from a wall. The independence of $g(z_1 = z_2 = z; r)$ from the chosen ensemble is clearly demonstrated in Fig. 6.2. As we find similar results for other static properties,

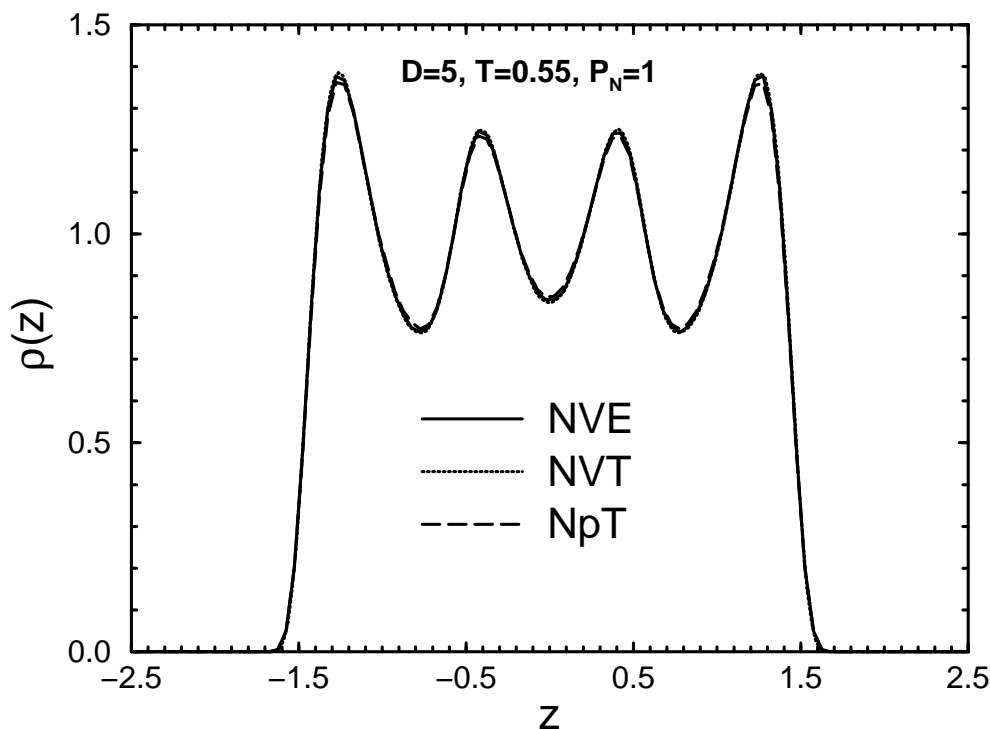


Figure 6.1: Density profile $\rho(z)$ as obtained from simulation runs within the microcanonical (solid line), canonical (dotted line) and the so called NpT (dashed line) ensembles. The number of particles was $N = 500$ in all three cases.

we conclude that, to the first approximation in the particle number N , at least a wide range of static properties are independent of the simulation ensemble. However, we will see in the next section that this is no longer the case for *dynamic* quantities.

6.2 *NpT*-Ensemble Simulation and the Dynamics

We are going to show that the dynamics of the system is practically unchanged if Nosé-Hoover thermostat is used. A simulation with fluctuating volume, however, seems not to be that harmless. First, we note that for time scales during which the volume is approximately unchanged, the dynamics of the system should behave similar to that of the *NVT*-case. For very long time scales, on the other hand, the amplitude of volume fluctuations will be small compared to the average displacement of the particles. This means that, also for long time scales *NpT* and *NVT* simulations should yield similar results. For intermediate times, however, a dynamical quantity obtained from a *NpT* run will in general be different from the same variable computed within a *NVT* simulation.

Let us first look at the short time case. With “short” we mean a time for which the mean square displacement of all particles is still much smaller than the square of chain’s radius of gyration, R_g^2 . A comparison of the short time dynamics within different ensembles, however,

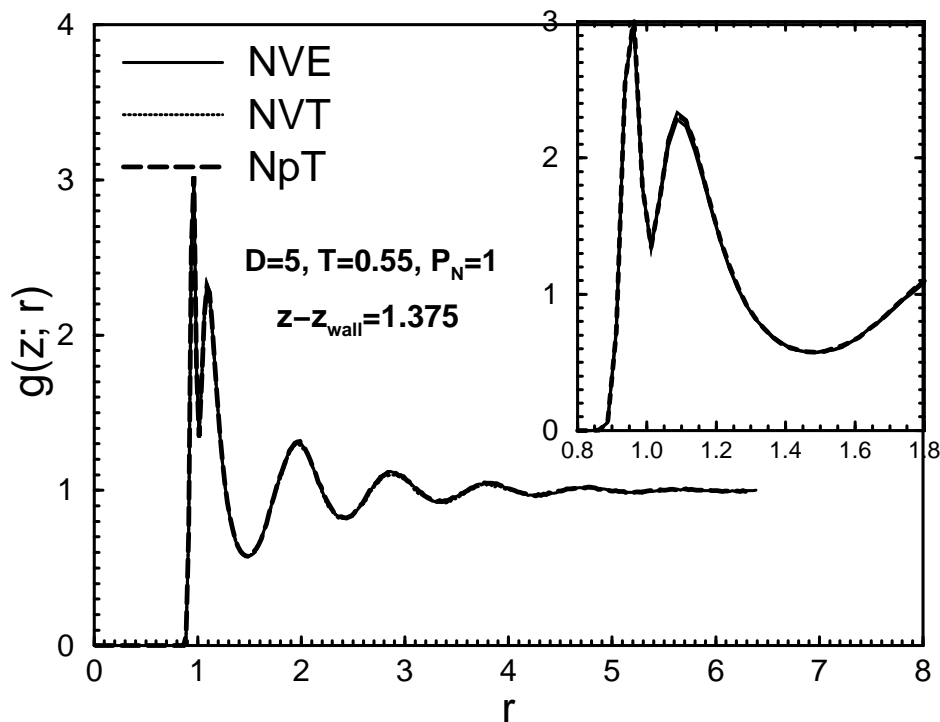


Figure 6.2: Pair distribution function $g(z_1 = z_2 = z; r)$ computed within a layer of thickness $dz = 0.25$ at a distance $z = 1.375$ from the left wall. Results presented here were obtained from simulation runs within the microcanonical (solid line), canonical (dotted line) and the so called *NpT* (dashed line) ensembles. The number of particles was $N = 500$ in all cases. As seen from the inset, the first peak occurs at an average distance < 1 . This approximately corresponds to the minimum position of the bond-potential ≈ 0.96 . The second peak arises from the preferred distance between non-connected monomers which interact via the Lennard-Jones potential only.

makes sense only if the test quantity varies fast enough over the time window of observation. Indeed, if we ignore the long time tails for this moment, the velocity autocorrelation function (VACF) is a good candidate for such a comparison. We expect a calculation of the VACF to yield the same results within *NVT* and *NpT*-ensemble simulations. This expectation is nicely borne out in Fig. 6.3 where results on the VACF are displayed for *NVE*, *NVT* and *NpT*-ensembles.

That the rate of volume change is really small, is shown in Fig. (6.4). From the inset of the same figure one can estimate a relative volume change of < 0.002 corresponding to the whole time window of Fig. (6.3).

Next, we consider the mean square displacement (MSD), again computed within the *NVE*, *NVT* and *NpT*-ensembles. For a polymeric system various kinds of MSD can be defined. For example, we can determine the displacements of a certain chain segment (monomer), that of the chain's center of mass or simply the displacements of all monomers regardless of their relative position along the chain. Furthermore, the displacements of a chain segment can be monitored in the coordinate system of the simulation box or in the chain's center of mass system. The number of possible choices is therefore quite large. Let $\alpha \in \{\parallel, \perp\}$ denote the specific direction (parallel or perpendicular to the walls) along which the particle displacements are monitored. Following common practice [91, 95], we pick up from the above set six “representatives” for

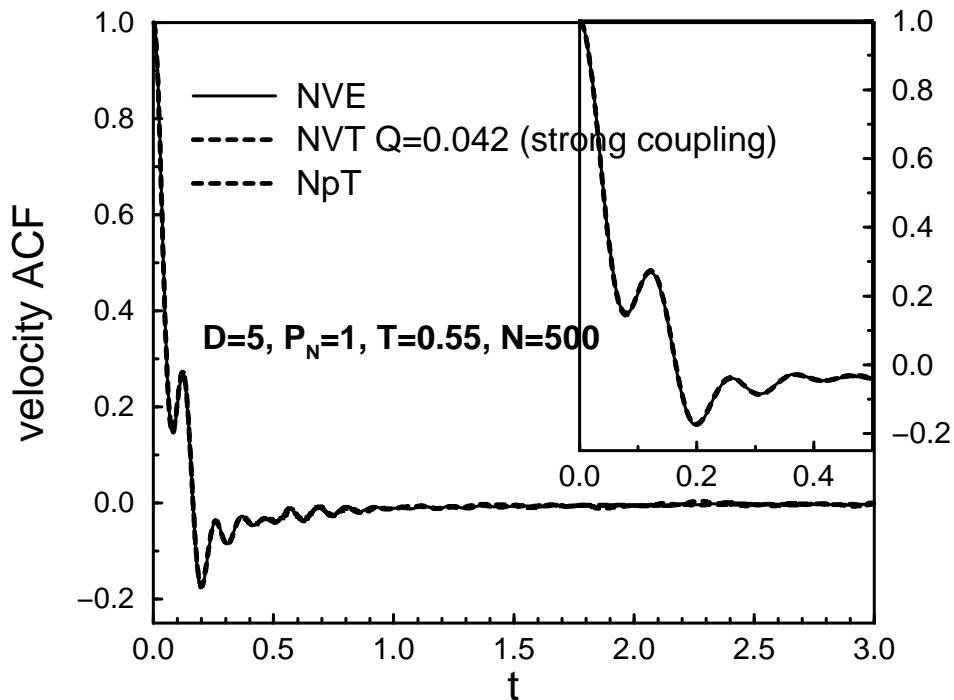


Figure 6.3: Velocity autocorrelation function as computed from simulation runs within the *NVE*, *NVT* and *NpT*-ensembles. In the *NVT*-case presented here, the “mass” Q of the heat bath was chosen to $0.01Q_{\text{opt}}$, where Q_{opt} is given by Eq. (4.117). The coupling to the heat bath was therefore much stronger than it is in a typical *NVT*-simulation. Nevertheless the VACF seems to be unaffected by such a coupling. Also the fluctuations of the volume do not affect the behavior of this quantity at short times.

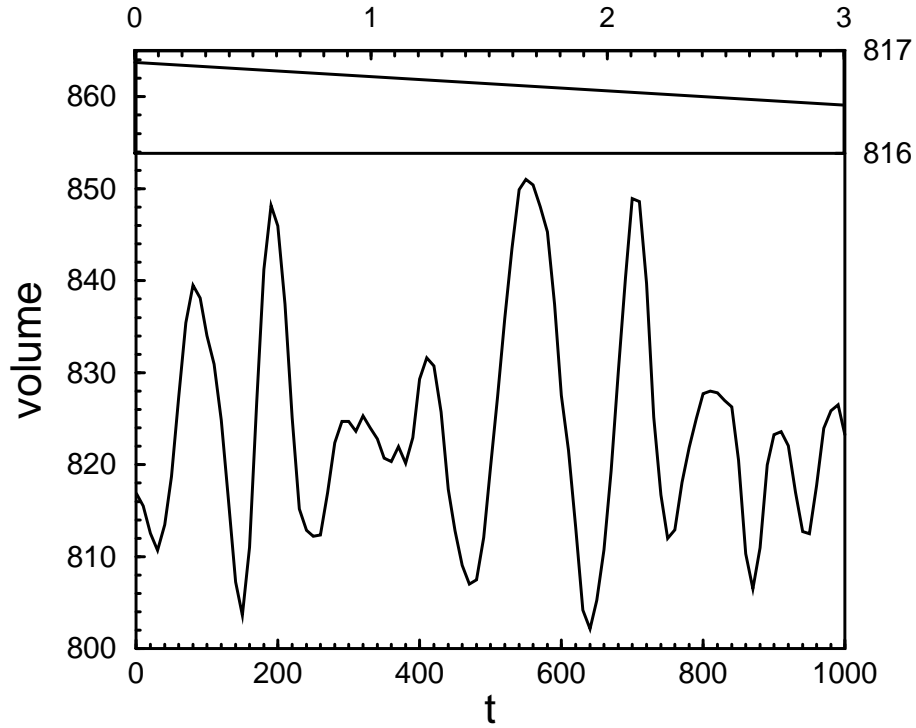


Figure 6.4: The volume of the system within a typical NpT -simulation. Some relevant parameters of this simulation run are: film thickness $D = 5$, number of particles $N = 500$ and the external pressure normal pressure $P_{N,\text{ext}} = 1$. $n_{\text{rt}} = 10$ was used in setting the “piston mass”, M_η [see Eq. (4.118)]. The inset demonstrates the volume variations during the time window for which the velocity autocorrelation function is computed [see Fig. 6.3]. The relative volume change during this time window is thus less than 0.002.

each direction. First, we give the (well-known) definition of the MSD of all monomers,

$$g_{0,\alpha}(t) = \frac{1}{N} \sum_{i=1}^N \left\langle [\mathbf{r}_{i,\alpha}(t) - \mathbf{r}_{i,\alpha}(0)]^2 \right\rangle, \quad (6.4)$$

where N is the total number of particles. The MSD of inner monomers is defined both in the coordinate system of the simulation box, $g_{1,\alpha}$, and in the chain’s center of mass frame, $g_{2,\alpha}$. These read

$$g_{1,\alpha}(t) = \frac{1}{M} \sum_{i=1}^M \left\langle [\mathbf{r}_{i,\alpha,\text{inner}}(t) - \mathbf{r}_{i,\alpha,\text{inner}}(0)]^2 \right\rangle, \quad (6.5)$$

$$g_{2,\alpha}(t) = \frac{1}{M} \sum_{i=1}^M \left\langle [\mathbf{r}_{i,\alpha,\text{inner}}(t) - \mathbf{R}_{\text{cm},i,\alpha}(t) - \mathbf{r}_{i,\alpha,\text{inner}}(0) + \mathbf{R}_{\text{cm},i,\alpha}(0)]^2 \right\rangle. \quad (6.6)$$

Here, M is the number of chains and $\mathbf{R}_{\text{cm},i}$ the center of mass vector of the i -th chain. The

corresponding MSD of end segments, $g_{4,\alpha}(t)$ and $g_{5,\alpha}(t)$, are defined in a similar fashion

$$g_{4,\alpha}(t) = \frac{1}{M} \sum_{i=1}^M \left\langle [\mathbf{r}_{i,\alpha,\text{end}}(t) - \mathbf{r}_{i,\alpha,\text{end}}(0)]^2 \right\rangle, \quad (6.7)$$

$$g_{5,\alpha}(t) = \frac{1}{M} \sum_{i=1}^M \left\langle [\mathbf{r}_{i,\alpha,\text{end}}(t) - \mathbf{R}_{\text{cm},i,\alpha}(t) - \mathbf{r}_{i,\alpha,\text{end}}(0) + \mathbf{R}_{\text{cm},i,\alpha}]^2 \right\rangle. \quad (6.8)$$

Note that, to simplify the notation, we considered in Eqs. (6.7) and (6.8) one end monomer per chain only. In practice, however, one takes into account the contribution of both ends and divides the sum by $2M$ (instead of M).

The reader may have missed the index 3 in the above set. This index is usually used to indicate the mean square displacement of the chains' center of mass

$$g_{3,\alpha}(t) = \frac{1}{M} \sum_{i=1}^M \left\langle [\mathbf{R}_{\text{cm},i,\alpha}(t) - \mathbf{R}_{\text{cm},i,\alpha}]^2 \right\rangle. \quad (6.9)$$

Results on the MSD of chain centers, $g_{3,\parallel}(t)$, is shown in Fig. 6.5. First, we note that, $g_{3,\parallel}(t)$ obtained from *NVE* and *NVT* runs agree well for all times. For *NpT* simulation runs, however, the agreement is limited to short and long time scales. For intermediate times, on the contrary, the deviation between *NpT* results on the one hand and *NVE* and *NVT* on the other hand is not negligible.

The enhancement of the MSD due to volume changes can be understood in the following way: When the system volume is increased to a certain amount, the particles must on average do work against the attractive forces to occupy the available volume. This necessary work has its origin in $1/r^6$ term of the LJ-potential. On the other hand, when the system volume is decreased, the external forces must do work against the much stronger $1/r^{12}$ forces. The expansion and the contraction of the system are thus not symmetric. On average, the expansion part of the volume fluctuations will lead to a larger enhancement of the mobility than the corresponding decrease of this quantity during the contraction phase. This explains the observed enhancement of the mobility within the *NpT*-simulation.

These deviations, however, are unphysical. To see this, we note that the relative volume fluctuations of a real system scale with $1/\sqrt{N}$ where $N \approx 10^{23}$. Therefore, these fluctuations and their effects on the dynamics are fully negligible in a real system. The enhancement of the mobility as a consequence of the volume fluctuations within a *NpT* simulation is thus an artificial finite size effect. Therefore, for small system sizes, *NpT* simulations will necessarily lead to unphysical results on the dynamics at intermediate times.

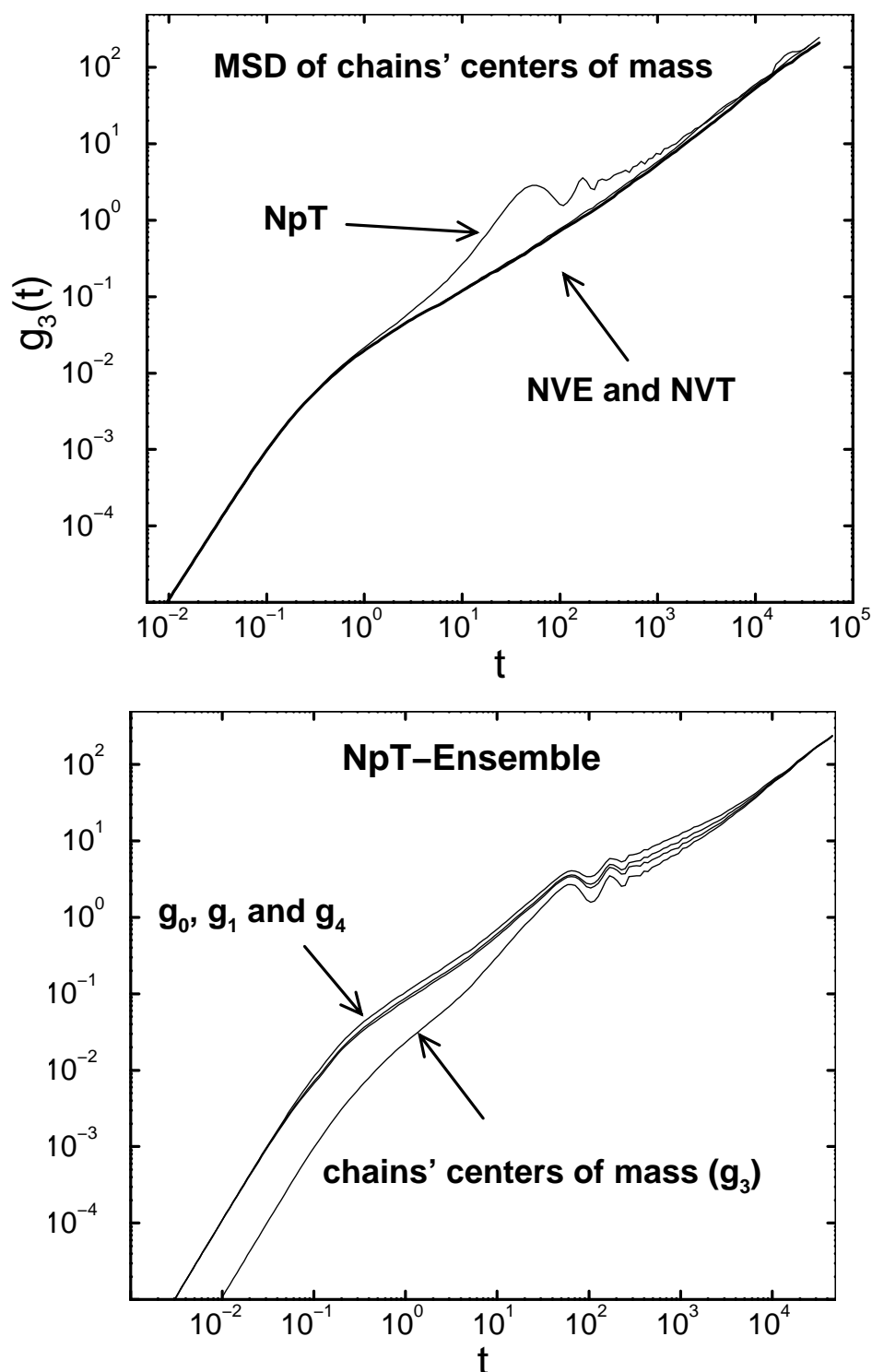


Figure 6.5: The panel on the top: The mean square displacement (MSD) of chain's centers, $g_3(t)$, obtained from *NVE*, *NVT* and *NpT* simulation runs. As described in the text, results for all ensemble coincide for short (ballistic) and long (diffusive) time scales. For intermediate times, however, *NpT*-ensemble method yields unphysical results. The panel at the bottom: MSD of all monomers, ($g_0(t)$), inner monomers, ($g_1(t)$), chain centers, ($g_3(t)$), and end monomers, ($g_4(t)$) within *NpT* runs. As described in the text, results for all ensemble coincide for short (ballistic) and long (diffusive) time scales. For intermediate times, however, *NpT*-ensemble method yields unphysical results.

Chapter 7

Statics

The static properties of the present model have already been studied for the bulk [91]. Therefore, we will focus our attention to the changes of these properties due to the presence of the walls.

7.1 A Brief Remark on Finite Size Effects

We have checked for finite size effects by varying the number of particles, N . For a film of thickness $D = 5$, for example, the particle number has been varied from $N = 100$ up to $N = 5000$ thus indirectly varying the system size by a factor of 7 (note that $L = \sqrt{N\rho/D} \propto N^{1/2}$). This was done both at a relative high temperature, $T = 1$, and at some lower temperatures, $T = 0.7, 0.55$ for example.

A test of possible N -dependence was also performed for thicker films. Even at the extremely small size of $L = 3.3$ ($D = 20, T = 1, 0.7$) hardly a size dependence could be observed for static properties. As there is nothing interesting in displaying identical results differing only in labels (“this was obtained at a particle number of $N = 100$ and that with $N = 5000$ ”, etc.), we restrict ourselves to this brief remark.

7.2 Density Profiles

Obviously, the presence of the walls induces an inhomogeneity in the system. The corresponding change of the system properties will also manifest itself in the particle distribution at different distances from a wall. The density, a unique number in a homogeneous system, now becomes a function of the distance from a wall, z say.

Let us first look at what happens to the density profile of all particles regardless of their connectivity, when keeping the temperature fixed, but varying the film thickness. Suppose that the wall-to-wall distance (film thickness), D , is sufficiently large in the sense that an approximately homogeneous region is formed in the film center. This implies that the effects of a wall are negligible there. Thus, they are not “felt” in the other half of the film. Consequently, the distribution of particles close to a wall is determined by the influence of *this* wall only. This means that, for “large” D , the density profile (and other local quantities) should be independent of the film thickness. However, as D gradually decreases, the particles in the film center “wake up” and realize that, actually, they live in a confined world. Now, the presence of a wall is also felt in the other half of the system. In such a situation, we expect changes in local quantities with respect to the variation of the wall-to-wall separation.

This idea is demonstrated in Fig. 7.1 (a), where density profiles are depicted for three different film thicknesses $D = 5, 10$ and 20 at $T = 0.55$. From this figure we see that for wall-to-wall separations smaller than 10 , no bulk region is present. As expected, this leads to a dependence of the density profile from the film thickness. This effect, however, is small even at the strongest confinement presented here ($D = 5$).

In Fig. 7.1 (b), we focus on the dependence of the density profiles from the temperature. For this purpose, the film thickness is kept constant ($D = 20$) and the temperature is varied. As seen from this figure, the density profile exhibits a strong temperature dependence. This can be related to pronounced packing effects. Note that we simulate at *constant normal pressure*. However, at constant density, the pressure is in general a decreasing function of the temperature. Therefore, as the temperature decreases, the system contracts to keep the pressure constant. In other words the average density increases with falling temperature [see Fig. 7.1 (b)]. In section 7.3, the change of the packing structure will be discussed in more detail.

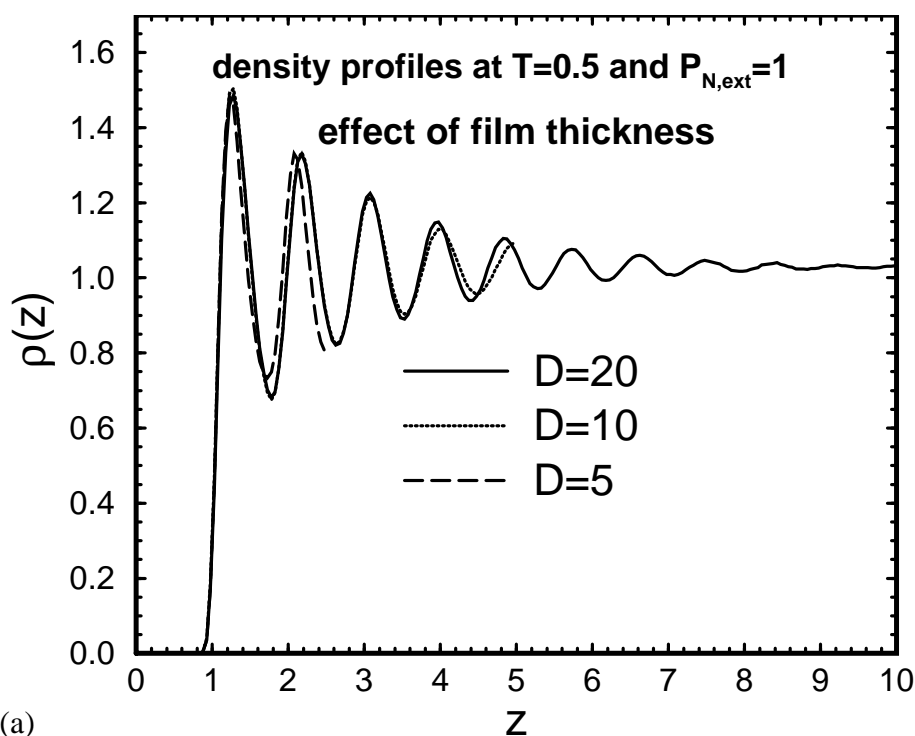
The observed density oscillations have an important consequence on the dynamics of the system. We will see in chapter 8 that, at low T , the particles prefer to move parallel to the walls. This can be related to the strong density oscillations observed here. Consider a particle at one of the minimums of the density profile. It is clear that if this particle tries to move in transversal direction, it will enter a region with higher density. Hence, the resulted displacement will be smaller compared to a step in a direction parallel to the walls.

7.3 Wall Effects on the Packing Structure

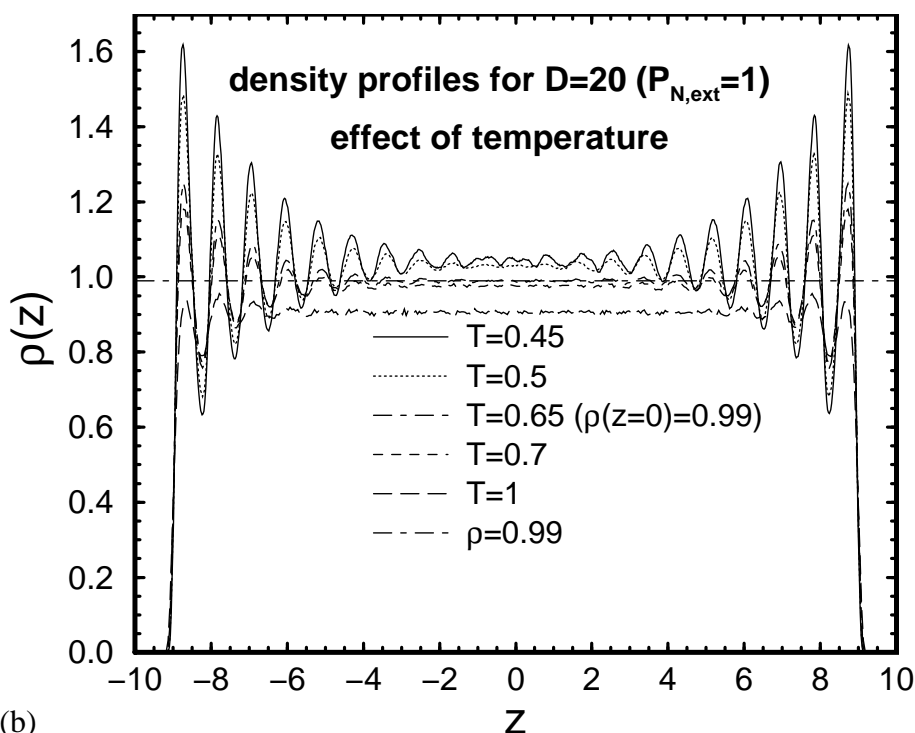
In section 7.2 we displayed density profiles at various film thicknesses and temperatures showing that, at high T , the effect of confinement on the density is rather small. However, it was also demonstrated that lowering the temperature enhanced the inhomogeneity in a significant way. These temperature effects were related to the increase of the average density as a consequence of constant pressure condition. However, parallel to the dependence of system properties on temperature, the local structure of a confined system varies strongly with distance from a wall. When averaged over the whole system, this will lead to a dependence from the wall-to-wall separation.

In Fig. 7.2 (a), the variation of the pair distribution function with respect to the temperature (left part) is compared to that caused by changing the distances from a wall (right part). When investigating the temperature dependence the same layer was considered. Similarly, in comparing $g(z, r)$ for different layers, the same temperature was chosen for all layers. As seen from this figure, the temperature has practically no effect on the first peak of $g(z, r)$. Nevertheless it has a strong impact on the second peak corresponding to the LJ-preferred distance: The lower the temperature, the more pronounced this peak. Note that, at low temperatures, the effect of the temperature is present also at relative large distances of 4 monomer diameter. It is seen from the left part of the same plot that the Lennard-Jones peak becomes also stronger, when the temperature is kept fixed, but the distance from the wall is increased. The similarity between the wall and temperature effects is more apparent in panel (b) where the temperature dependence of $g(z, r)$ within a layer at film center is compared to its z -dependence at a low temperature ($T = 0.44$).

At high temperatures, however, the presence of the walls is more striking when looking at the change of the first peak of $g(z, r)$. In the vicinity of the walls, the bond peak becomes dominant and grows when approaching the wall. This can be related to a change of the chain conformation close to the walls [68,96]. The chains become flat so that for a given monomer at



(a)



(b)

Figure 7.1: Top: Density profiles at $T = 0.5$ for $D = 5, 10$ and 20 . There is still a bulk-like region in the center of the largest film ($D = 20$). For the smaller films, however, this is no longer true. As a consequence, for $D \leq 10$, a slight dependence of the density profile on the film thickness develops. Bottom: Same quantity as above. Now the film thickness is kept constant ($D = 20$), but the temperature is varied. As the temperature decreases, the inhomogeneity, caused by the walls, propagates towards the inner part of the film. The horizontal line $\rho = 0.99$ is depicted to enable the comparison with the density at film center of isochoric simulations of shear stress [see chapter 9]. As seen here, this density corresponds to a temperature of $T = 0.65$.

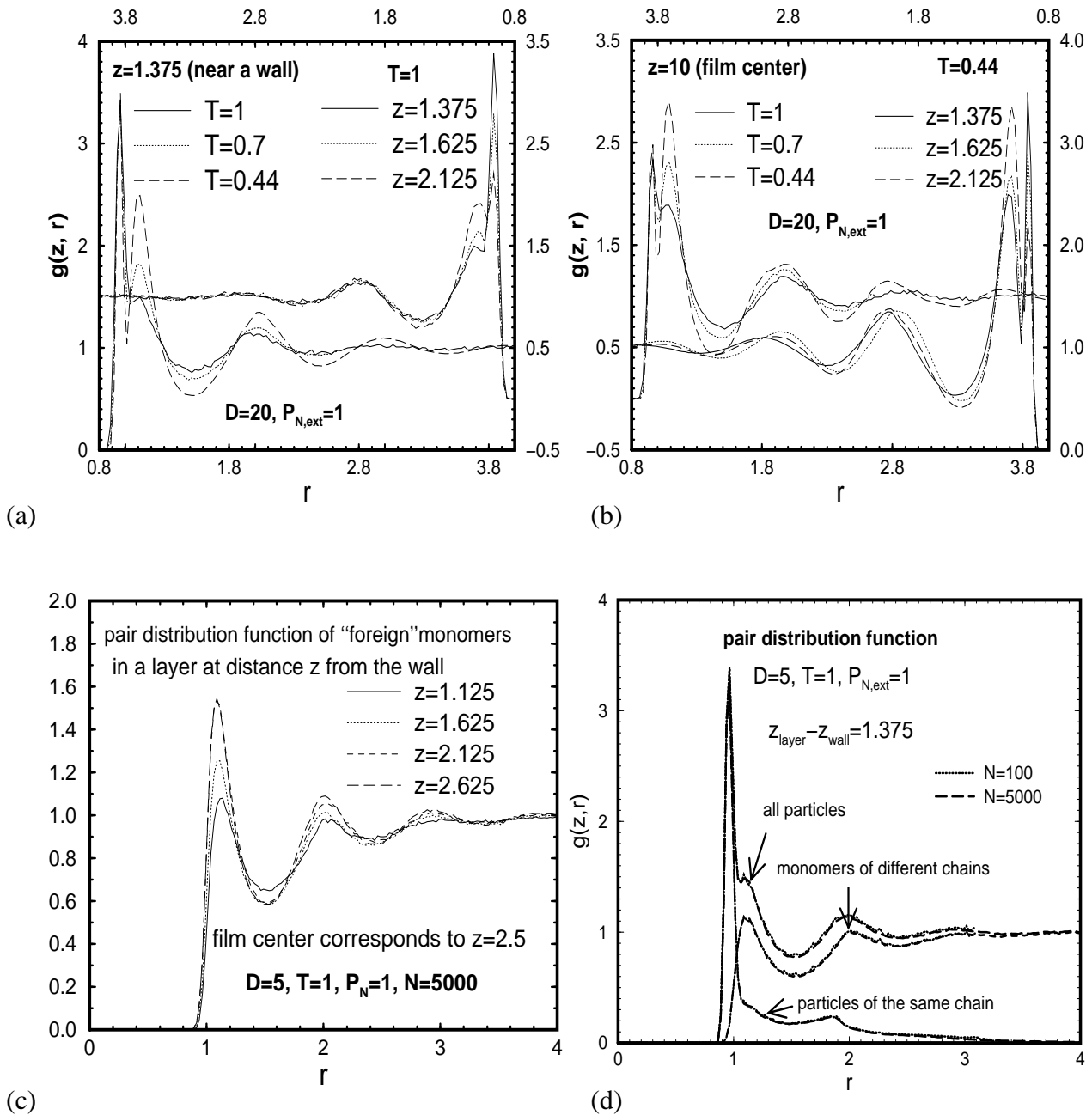


Figure 7.2: Panels (a) and (b): Effects of the temperature versus those of a wall on the pair distribution function, $g(z; r)$. Panel (c): Deepening of the “correlation hole” between monomers of different chains (called here “foreign” monomers). When approaching a wall, the position of the maximum is shifted towards larger r (Note that $r = |\mathbf{r}_{||}|$). Panel (d): Contribution to $g(z; r)$ of the correlations between monomers of the same chain and that between monomers of different chains obtained from simulations with particle numbers $N = 100$ and $N = 5000$ (Also the sum of these two contributions is plotted here). No size effect is observed for these very different particle numbers. The r -interval, for which $g(z; r)$ is computed, is shorter for the smaller system ($N = 100$).

the wall, the probability of finding a monomer of another chain at short distances is depressed compared to that of finding a monomer belonging to the same chain. To test this idea, we plot in panel (c) the contribution of the “foreign” monomers, i.e. of those monomers which belong to different chains, to the pair distribution function in various layers. As demonstrated in the panel, the position of the maximum of $g(z; r)$ is shifted towards larger r for layers closer to the wall. In addition, a small gap develops between curves corresponding to different layers, indicating that the so called “correlation hole” [97] becomes larger when a wall is approached.

Finally, we display in Fig. 7.2 (d) the two contributions to $g(z, r)$ and their sum. This panel also serves to stress our remark on the size-independence of the static properties. As shown here, the same results for $g(z, r)$ are obtained with $N = 100$ as well as with $N = 5000$ particles.

7.4 MD versus Self-Consistent-Field Theory

In this section we will compare MD results on the polymer specific profiles like the density of chain ends (end monomers), chains’ center of mass density, the profiles of end-to-end vector parallel and perpendicular to the walls etc. with the self-consistent field (SCF) calculations of Müller and Gonzalez MacDowell [68, 96].

A common feature of mean field theories is that they map the very complex many body problems onto the simpler problem of a particle in an external field. The “external field” thus introduced takes into account the presence of other particles in an average sense. Of course, the route from a many body problem to an appropriate mean field depends on the specific situation to capture and can be (and usually *is*) quite complicated.

For our polymer model, a discussion of the theory and of the underlying approximations is given in [68, 96].

Let $u(\mathbf{r})$ be the “effective field” at \mathbf{r} caused by all chains and let $\rho(\mathbf{r})$ be the average density measured at the same point. The system’s free energy is approximated by a functional of u and ρ . The self-consistent equations for u and ρ are then determined by the condition that they minimize this free energy functional. One obtains [68, 96]

$$u(\mathbf{r}) = g(\bar{\rho}(\mathbf{r})) + \int d^3\mathbf{r}' w(\mathbf{r} - \mathbf{r}') \rho(\mathbf{r}') \frac{dg}{d\rho}(\mathbf{r}') \quad (7.1)$$

$$\rho(\mathbf{r}) = \frac{\rho_{\text{av}} V \int \mathcal{D}_1[\mathbf{r}] \mathcal{P}_1[\mathbf{r}] \hat{\rho}_1(\mathbf{r}) \exp\left(-\int d^3\mathbf{r}' u(\mathbf{r}') \hat{\rho}_1(\mathbf{r}')\right)}{N_p \int \mathcal{D}_1[\mathbf{r}] \mathcal{P}_1[\mathbf{r}] \exp\left(-\int d^3\mathbf{r}' u(\mathbf{r}') \hat{\rho}_1(\mathbf{r}')\right)}, \quad (7.2)$$

$$\text{with } \bar{\rho}(\mathbf{r}) = \int d^3\mathbf{r}' w(\mathbf{r} - \mathbf{r}') \rho(\mathbf{r}') \quad (7.3)$$

$$\text{and } \int d^3\mathbf{r} w(\mathbf{r}) = 1. \quad (7.4)$$

In Eq. (7.1) g is the bulk free energy density and describes the thermodynamics of the homogeneous system, N_p is the number of segments of a chain (also called the degree of polymerization) and $\rho_{\text{av}} = N/V$ denotes the average density of all monomers. Obviously, w is a normalized smoothing function. The density $\hat{\rho}_1(\mathbf{r})$ is the (microscopic) density function of a chain,

$$\hat{\rho}_1(\mathbf{r}) = \sum_{i=1}^{N_p} \delta(\mathbf{r} - \mathbf{r}_i). \quad (7.5)$$

$\mathcal{D}_1[\mathbf{r}]$ sums over all conformations of a chain and $\mathcal{P}_1[\mathbf{r}]$ is the probability for the occurrence of a given conformation. The product $\mathcal{D}_1[\mathbf{r}]\mathcal{P}_1[\mathbf{r}]$ can therefore be approximated by a sum over chain conformation obtained from a MC or MD simulation of the corresponding homogeneous system [98–105]. Note that each configuration of a system of N_c chains simulated via MD or MC provides N_c single chain configurations.

Hence, the rhs of Eq. (7.2) is nothing but the Boltzmann average of the single chain density in the external field u . At this stage, the thermodynamic properties related to the presence of other chains are implicitly contained in u and ρ . In fact, it is only the bulk free energy density, g , which is relevant for the bulk thermodynamics of the system. This function enters the calculation of u and thus, indirectly, also that of ρ [see Eqs. (7.1) and (7.2)]. On the other hand, the smoothing function, w , describes packing effects [68].

As already mentioned, w is a kind of smoothing function. Choosing $w = 1/V$, for example, would lead to $\bar{\rho}(\mathbf{r}) = \rho_{av} = N/V$, whereas the other extreme, $w(\mathbf{r} - \mathbf{r}') = \delta(\mathbf{r} - \mathbf{r}')$, corresponds to the so called local-density approximation. The latter has been used by Sullivan in the framework of a density functional treatment of inhomogeneous (simple) fluids [64, 106–108]. This approximation, however, works well when no density oscillations occur or when the correlations are long-ranged [64]. The local-density approximation does not treat the short range correlations correctly and therefore becomes inaccurate when, for example, density oscillations are present. Without ignoring the differences between the density functional method used by Sullivan and the present SCF-approach, we should, however, keep in mind this important result on $w(\mathbf{r})$ when seeking a “guess” for this function.

It is commented in [68, 96] that $w(\mathbf{r})$ parametrizes the packing structure of the fluid on the monomer scale. Furthermore, a link was found between $w(\mathbf{r})$ and the direct correlation function, $c(\mathbf{r})$ [109–112]. Motivated by this observation, Müller and Gonzalez MacDowell set

$$w(\mathbf{r}) = \begin{cases} -K(\sigma - |\mathbf{r}|) & : |\mathbf{r}| < \sigma \\ -\frac{U_{LJ}(\mathbf{r})}{k_B T} & : |\mathbf{r}| > \sigma \end{cases} \quad (7.6)$$

where U_{LJ} denotes the Lennard-Jones potential [see Eq. 2.1]. Note that the case $|\mathbf{r}| > \sigma$, corresponds to the asymptotic (large \mathbf{r}) behavior of $c(\mathbf{r})$ [64]. The parameter K determines the relative weight of the attraction for $|\mathbf{r}| > \sigma$ and the repulsion for $|\mathbf{r}| < \sigma$. For $K = 10$ the best possible agreement with simulation data was observed at $T = 1.68$. Further SCF calculations have been carried out with this value of K . However, as the effect of attraction becomes more important at lower T , we expect stronger deviations between the SCF calculations and the MD-results when lowering the temperature.

Note that we are investigating a planar system. Thus, system properties do not depend on the lateral, say x and y , coordinates. Therefore, for each quantity of interest, we average over lateral coordinates. The density $\rho(\mathbf{r})$, for example, now becomes

$$\rho(z) = \frac{1}{A} \int dx dy \rho(x, y, z). \quad (7.7)$$

There are many routes for finding an approximate expression for g , the free energy density of the homogeneous system. Müller and Gonzalez MacDowell choose Wertheim’s thermodynamic perturbation theory (TPT1) [113]. Using the monomer fluid of Lennard-Jones particles as a reference system, the free energy of the (homogeneous) polymer system is determined by calculating the effects of the bonding potential U_{FENE} [see Eq. (2.3)] as a thermodynamic perturbation [96]. The free energy density ρg is then chosen such that the thermodynamics of the

homogeneous system in the SCF calculations coincides with TPT1 approximation

$$\rho g(\rho) = \frac{f_{\text{LJ}}^{\text{ex}}}{k_{\text{B}}T} - \rho \left(1 - \frac{1}{M}\right) \ln \delta, \quad (7.8)$$

where $f_{\text{LJ}}^{\text{ex}}$ is the excess free energy (i.e. free energy minus the ideal gas term) of the Lennard-Jones-reference system and [113–117]

$$\delta = \int d^3\mathbf{r}_{12} g(\mathbf{r}_{12}) \exp\left(-\frac{U_{\text{FENE}}(\mathbf{r}_{12})}{k_{\text{B}}T}\right), \quad (7.9)$$

where g is the pair distribution of the reference Lennard-Jones system. To avoid confusion with the free energy density, g , we have used a different character type for the pair distribution function, g .

It was shown in Fig. 7.1 (b) that, as the temperature falls, the density oscillations become stronger and that these oscillations propagate towards the film center. The presence of the walls is thus felt in a larger portion of the system. Therefore, it is instructive to start the investigation of the polymer specific profiles at a rather low temperature. Unfortunately, the self-consistent field (SCF) theory, whose results will be compared to the output of our MD-simulations, becomes inaccurate at lower temperatures. So at low T , we will present MD results only.

The reason for the failure of SCF-theory at low T is that this theory has some difficulties in properly taking into account the attractive forces (which act at longer distances compared to the repulsive forces) in an *inhomogeneous* system. Recall that SCF is a mean field theory. In a bulk system, it is not a crude approximation to suppose that the attractive contributions to the force on a particle cancel out each other. This is justified by the long range character of these forces. In an inhomogeneous system, however, the situation is different close to the interface. The sum over attractive forces on a particle close to the interface is definitely not negligible. In fact, on average, there will be a net attractive force decaying with distance from the interface. However, it seems not to be very easy to incorporate in a mean field theory such an effect [96]. As these attractive forces become more important with decreasing temperature, the theory becomes inaccurate at low T .

In panel (a) of Fig. 7.3 we plot the density profiles for end monomers, inner monomers, chains' centers of mass and finally all monomers regardless of their position within a chain. The data are extracted from a simulation of a film of thickness (wall-to-wall separation) $D = 10$ at $T = 0.5$ and $P_{\text{N,ext}} = 1$. Note that the mode-coupling critical temperature of the system is $T_{\text{c}}(D = 10) = 0.39$. The chosen temperature is thus relative low. The opposite trend of the inner and end monomers with respect to the walls is clearly demonstrated. The inner monomers avoid the very vicinity of the walls, whereas an enrichment of end monomers is observed in this region. Note that all presented profiles are rescaled to give the total monomer density in the isotropic and homogeneous case. The higher density of end monomers compared to the inner monomers can be related to their higher entropy. They are bonded only to one monomer instead of to two. Consequently, compared to an inner monomer, a move attempt of an end monomer towards the wall is hindered less strongly. Thus, end monomers can explore the region close to the walls more efficiently.

Reports on neutron reflectivity experiments do confirm the enrichment of the chain ends close to the interface [118]. Also simulations of hard chains at hard walls do show a higher relative density of end monomers in the vicinity of the walls [119, 120]. Therefore, the occurrence of end monomer enrichment seems not to depend on the details of the interaction. This observation is in favor of the above entropic argument.

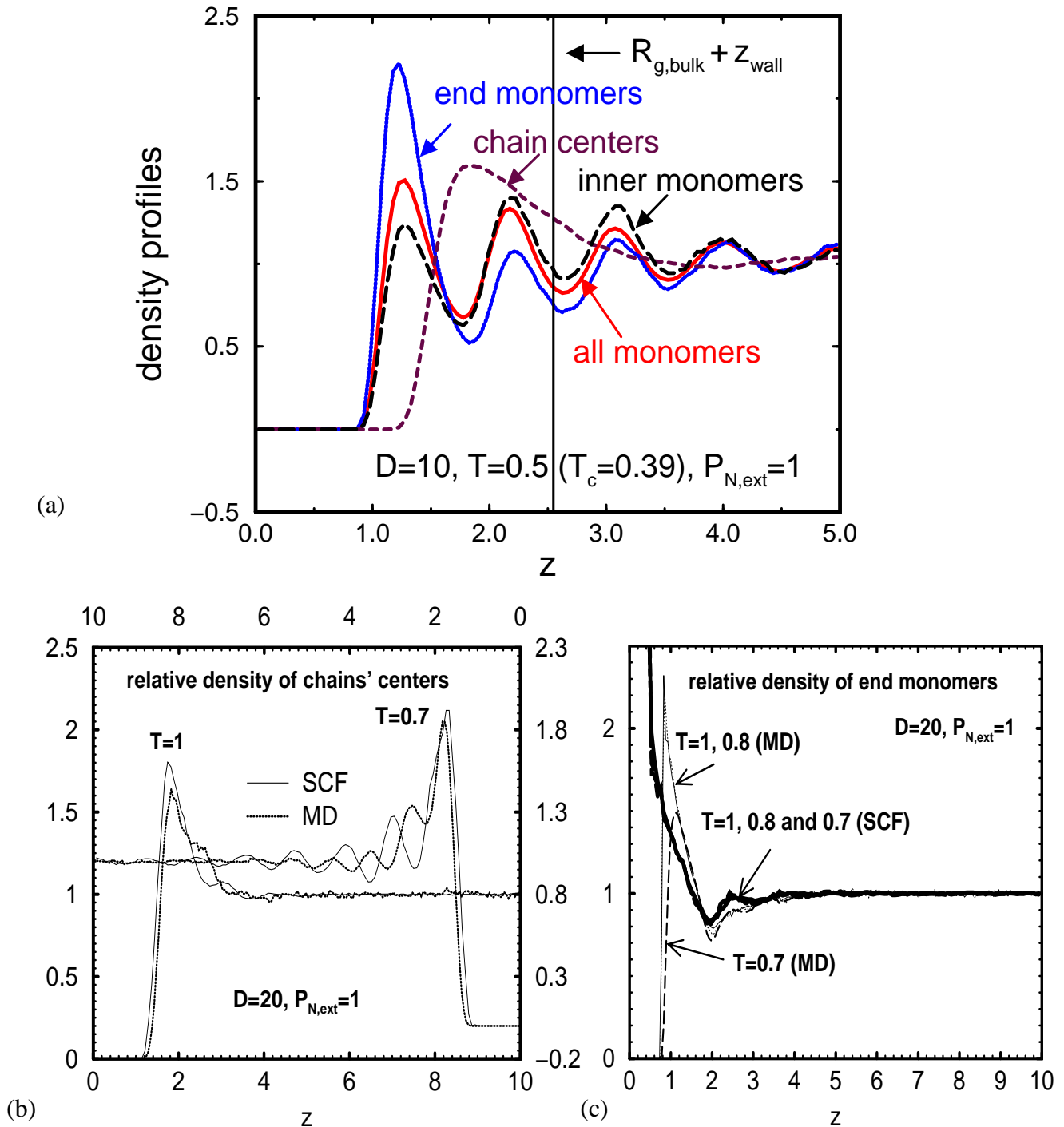


Figure 7.3: (a): Chain specific profiles: end segments, inner segments, chains' centers of mass and, finally, the density of all monomers regardless of their position within a chain ($D = 10$, $T = 0.5$ and $P_{N,ext} = 1$). Note that the mode-coupling critical temperature of the film is $T_c(D = 10) = 0.39 \pm 0.01$ [see chapter 8]. Obviously, sufficiently close to the walls, the end monomers prefer the vicinity of the walls whereas the inner part of the chains keep a larger distance from it. (b): Comparison of the relative density of chains' centers of mass, i.e. $\rho_{cm}(z)/\rho(z)$, at $T = 1$ and 0.7 as obtained from the molecular dynamics simulation (MD) and the self-consistent field calculation (SCF). Qualitative agreement is quite good. However, specially at low T , SCF fails on the quantitative level. (c): The same comparison as in panel (b), now for end monomers. Again, good qualitative agreement is observed. However, SCF overestimates the extra entropy of end monomers (compared to the inner ones) and leads to higher values of $\rho_{cm}(z)/\rho(z)$ than obtained via MD simulation.

It is also seen from panel (a) of Fig. 7.3 that the depletion of the monomer densities starts at a distance ≈ 1 , the monomer size, whereas that of the chains' centers of mass, $\rho_{\text{cm}}(z)$, starts at a distance of $\approx R_g$ from the walls. This indicates that R_g can indeed be interpreted as the average radius of a chain. The wave length of the monomer density oscillations is also very close to the monomer size. The oscillations of $\rho_{\text{cm}}(z)$, however, have very small amplitude. Nevertheless, one can see that the length scale of the variations of $\rho_{\text{cm}}(z)$ is fairly larger than the monomer size.

Let us start with a comparison of MD results from one side and the SCF calculations from the other side. In panel (b) of Fig. 7.3 we compare density profiles of chains' centers of mass, i.e. $\rho_{\text{cm}}(z)/\rho(z)$, at temperatures $T = 1$ and 0.7 as obtained from molecular dynamics simulation (MD) and self-consistent field calculation (SCF). The rescaling of $\rho_{\text{cm}}(z)$ by the inverse monomer density serves to separate packing effects on the monomer scale from the polymeric ones [96]. As seen from this figure, the SCF results are in good qualitative agreement with those obtained from MD simulations. The oscillatory nature of the profile, for example, is quite well reproduced by SCF calculations. However, at $T = 1$, the magnitude of the first peak close to the walls is overestimated by SCF calculations. As $\int_{-D/2}^{D/2} dz \rho_{\text{cm}}(z) = M$ (M being the number of chains), this overemphasis is then "compensated" by lower values of the ρ_{cm} compared to the corresponding MD-curve in the region just after the peak position.

As seen from the right side of the same figure, the discrepancy between SCF and MD data is enforced at lower temperature of $T = 0.7$. Now, the oscillations of SCF and MD curves are totally out of phase. This already explains why we did not try comparisons at still lower T .

The same comparison is repeated in panel (c) of Fig. 7.3 (now for three temperatures $T = 1, 0.8$ and 0.7) for the relative density of end profiles $\rho_e(z)/\rho(z)$. Again, we observe good qualitative agreements, but on the quantitative level the SCF overestimates the enrichment of end monomers. Furthermore, it is demonstrated in the same panel that, contrary to the rather strong temperature dependence of $\rho_{\text{cm}}(z)/\rho(z)$, a variation of the T from 1 to 0.7 seems not to have much impact on the relative density of end segments $\rho_e(z)/\rho(z)$.

In panel (a) of Fig. 7.4 the monomer density profile, $\rho(z)$, is plotted at $T = 1$ and 0.7 as output of SCF calculations and that obtained from MD simulation. First, we note that, for a given temperature, SCF yields a lower density in the film center. However, a comparison of the shape of density profiles reveals that a simple rescaling of the SCF result to bring in accord the values of MD and SCF results at film center, would not remove the observed discrepancy. Furthermore, at $T = 0.7$ the oscillations in SCF-density profile propagate much farther in the inner part of film than observed in MD simulations. These discrepancies show that SCF is not able to accurately take into account the effects of the long range attractive forces which come into play as a result of the confinement.

Now, we compare the orientational properties. In panel (b) of Fig. 7.4 MD and SCF results are compared for the parallel and perpendicular components of the end-to-end distance, i.e. $R_{\text{ee},\parallel}^2$ and $R_{\text{ee},\perp}^2$, at $T = 1$ and 0.7 .

Contrary to the monomer and chain density profiles, remarkable agreement is observed between SCF and MD. For the parallel component, the curves are nearly identical at both temperatures. A discrepancy, however, is observed for the transversal component. These deviations are enhanced at lower temperature. Note that $R_{\text{ee},\parallel}^2$ decays monotonically without any oscillations, whereas the variation of $R_{\text{ee},\perp}^2$ is a bit more complex. It increases up to a maximum value and then decreases towards the bulk average. The differences between the MD and SCF calculations at very short distances, however, must be related to statistical errors. It is shown in panel (c) of Fig. 7.4 that the radius of gyration exhibits very similar behavior to the end-to-end distance. All remarks made for $R_{\text{ee},\parallel}^2$ and $R_{\text{ee},\perp}^2$ are also valid for $R_{g,\parallel}^2$ and $R_{g,\perp}^2$.

Finally, panel (d) of Fig. 7.4 compares the average eigenvalues of the gyration tensor [see below], $\lambda_1 > \lambda_2 > \lambda_3$, for MD and SCF. Also here, the agreement is better when the quantity of interest is smooth enough.

From all that has been said and shown, we conclude that the self-consistent field approach of Müller and Gonzalez MacDowell captures well the qualitative features of our confined polymer model. For some of orientational quantities like $R_{ee,\parallel}^2$, $R_{g,\parallel}^2$ also quantitative agreement is observed. This quantitative agreement, however, is satisfactory for smoothly varying quantities, i.e. in cases where no oscillations are present. In the presence of oscillations, on the contrary significant deviations occur.

Note however that the derivation of the SCF equations (7.1) and (7.2) is not based on the assumption of a small external field [121]. In particular, no linear approximation is used for $\exp(-U_{\text{wall}}/k_B T)$. Therefore, in principle, it should work also at strong inhomogeneities.

Note that the input data in SCF-calculations was obtained from MD simulations of a bulk system at $T = 1$. These data have been then used for iterative calculation of the mean field u at other temperatures. However, we will see in section 7.5 that average chain shapes in the film center of a relative thick film ($D = 20$) where bulk-like behavior is observed, do not depend much on the temperature. Chain conformations in the bulk are therefore not expected to exhibit strong T -dependence and the use of bulk-data at $T = 1$ seems to be a reasonable choice. Much better results are therefore *not* expected when taking bulk-data at exactly the same temperature for which SCF is applied.

It has been shown in [68] that the density profile strongly depends on the specific choice of the weight function, $w(r)$ [see Fig. 7 in the same Ref.]. An improvement, therefore, should be possible when focusing on a better choice of this function. Also, taking into account $P_N = 1$ when searching for a suitable choice of the bulk free energy density, $g(z)$, could improve the results. These suggestions could be checked in further studies.

However, the quite good agreement of the SCF calculations with our MD data in all cases of smooth varying quantities demonstrates that the present SCF scheme, as it stands, is already accurate enough for systems with weak inhomogeneities like liquid-vapour interfaces. Further improvement, however, may expand the scope of its applications.

7.5 Average Chain Shape

We are going to close this chapter with a brief analysis of the so called shape factors. Aronovitz and Nelson [122] introduced rotationally invariant quantities, Δ and S (whose definition will be given below) to characterize the average asymmetry and degree of prolate- or oblateness of a polymer system.

Following [122] we first give the definition of the gyration tensor, \mathbf{Q} of a chain configuration

$$\mathbf{Q}_{\alpha\beta} = \frac{1}{N_p} \sum_{i=1}^{N_p} (\mathbf{r}_{i,\alpha} - \mathbf{R}_{\text{cm},\alpha})(\mathbf{r}_{i,\beta} - \mathbf{R}_{\text{cm},\beta}), \quad (7.10)$$

where $\alpha, \beta = x, y, z$. N_p is the number of chain segments ($N_p = 10$ in our model) and \mathbf{R}_{cm} stands for the chain's center of mass vector. It is easy to see that the statistical average of the sum over diagonal elements of \mathbf{Q} , i.e. $\langle \text{trace}(\mathbf{Q}) \rangle$, is equal to the square of the radius of gyration

$$\left\langle \sum_{\alpha} \mathbf{Q}_{\alpha\alpha} \right\rangle = \frac{1}{N_p} \sum_{i=1}^{N_p} \sum_{\alpha} \langle (\mathbf{r}_{i,\alpha} - \mathbf{R}_{\text{cm},\alpha})^2 \rangle = \mathbf{R}_g^2. \quad (7.11)$$

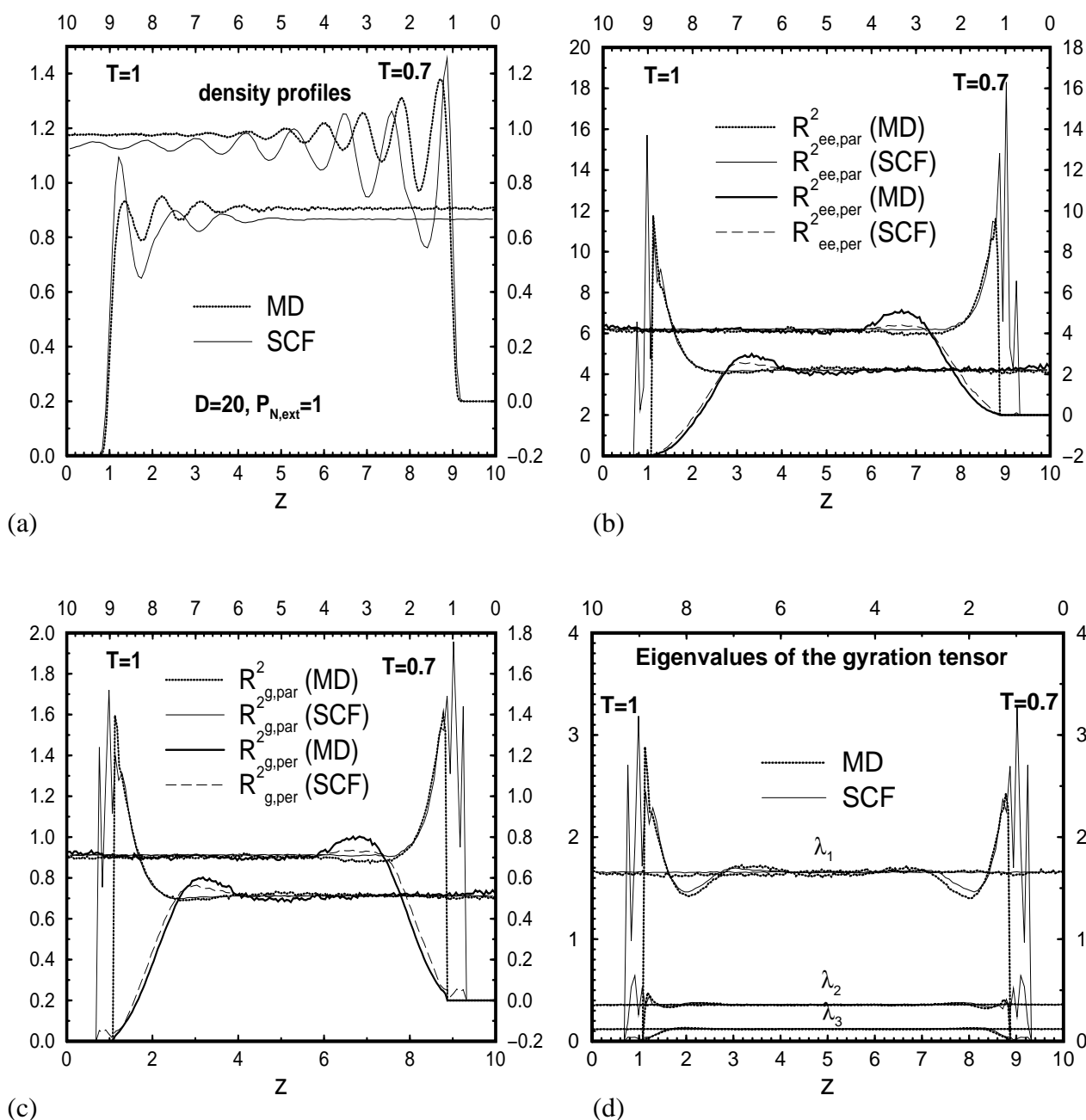


Figure 7.4: Panel (a): Density profiles at $T = 1$ and $T = 0.7$ as obtained from the molecular dynamics simulation (MD) and self-consistent field calculation (SCF). For both temperatures plotted here, SCF yields a lower density in the film center. However, it is also seen that a simple rescaling of the SCF result would not bring these in accord with MD data. Furthermore, at $T = 0.7$ the oscillations in SCF-density profile propagate much farther in the inner part of film than observed in MD simulations. Panel (b)-(c): SCF versus MD for profiles of $R_{ee,\parallel}^2$, $R_{ee,\perp}^2$, $R_{g,\parallel}^2$ and $R_{g,\perp}^2$. Qualitative agreement is quite remarkable. For monotonous quantities like $R_{ee,\parallel}^2$ and $R_{g,\parallel}^2$ for example, the agreement extends to a quantitative level. In cases where the z -dependence is a bit more complicated, however, small deviations occur. Panel (d): Same comparison for the eigenvalues of the gyration tensor \mathbf{Q} [see Eq. 7.10]. Within the mentioned (small) quantitative deviations, also here, SCF calculations reproduce the z -dependence of λ 's quite well.

Note that \mathbf{Q} is a symmetric matrix. It can thus be diagonalized. However, as the trace of a matrix is unchanged under an orthogonal transformation, it follows that the sum over the eigenvalues of \mathbf{Q} is also equal to R_g^2 ,

$$\sum_{i=1}^3 \lambda_i = R_g^2, \quad (7.12)$$

where $\lambda_1 \geq \lambda_2 \geq \lambda_3$ are the eigenvalues of \mathbf{Q} . Then, one defines a traceless matrix $\hat{\mathbf{Q}}$ via

$$\hat{\mathbf{Q}} = \mathbf{Q} - \bar{\lambda} \mathbf{I}_3, \quad (7.13)$$

where $\bar{\lambda} = \sum_{i=1}^3 \lambda_i / 3$ and \mathbf{I}_3 is the 3×3 unit matrix. Note that an orthogonal transformation which diagonalizes \mathbf{Q} will at the same time also diagonalize $\hat{\mathbf{Q}}$ and thus any function of it. Therefore, it is easy to see that

$$\text{trace}(\hat{\mathbf{Q}}^2) = \sum_i (\lambda_i - \bar{\lambda})^2. \quad (7.14)$$

The point is now that $\text{trace}(\hat{\mathbf{Q}}^2)$ is the variance of the eigenvalues of the gyration tensor, \mathbf{Q} , and thus a measure of how much a given polymer chain deviates from spherical symmetry [122]. In the spherical case, for example, $\lambda_1 = \lambda_2 = \lambda_3 = \bar{\lambda}$ and thus $\text{trace}(\hat{\mathbf{Q}}^2) = 0$.

On the other hand, it is easy to see that $\det \hat{\mathbf{Q}}$ provides useful information on the prolate- or oblateness of a given chain configuration. For, if a chain is prolate, i.e. if $\lambda_1 \gg \lambda_2 \approx \lambda_3$, then $\lambda_1 - \bar{\lambda} > 0$ while $\lambda_2 - \bar{\lambda} < 0$ and $\lambda_3 - \bar{\lambda} < 0$. Therefore $\det \hat{\mathbf{Q}} = \prod_{i=1}^3 (\lambda_i - \bar{\lambda}) > 0$ for a prolate chain. Similarly, one can see that in the oblate case, i.e. when $\lambda_1 \approx \lambda_2 \gg \lambda_3$, $\det \hat{\mathbf{Q}} < 0$. Thus, for a given chain configuration, the sign of $\det \hat{\mathbf{Q}}$ provides information on prolate- or oblateness of the chain and its magnitude “measures” how prolate or oblate the polymer is [122].

However, it follows from Eq. (7.12) that the eigenvalues of \mathbf{Q} scale with chain’s radius of gyration. As a consequence, $\det \hat{\mathbf{Q}}$ combines the shape information with that of the size. Therefore, $\det \hat{\mathbf{Q}}$ is not a suitable candidate for investigations of the chain shape. Nevertheless, with a slight modification, $\det \hat{\mathbf{Q}}$ can still be used to define a size independent quantity which “measures” the polymer shape only [see below].

It was shown in appendix A of [122] that

$$0 < \text{trace} \hat{\mathbf{Q}}^2 \leq 6\bar{\lambda}^2. \quad (7.15)$$

The argument is indeed very simple: $\text{trace} \hat{\mathbf{Q}}^2$ can be considered as the squared norm a vector \mathbf{v} defined as $\mathbf{v} \equiv (\lambda_1, \lambda_2, \lambda_3) - (\bar{\lambda}, \bar{\lambda}, \bar{\lambda})$. It is then clear that v^2 is maximized at one of the corners, $(\lambda_1, \lambda_2, \lambda_3) = (3\bar{\lambda}, 0, 0)$ say. In this case one obtains $v^2 = (2\bar{\lambda})^2 + (-\bar{\lambda})^2 + (-\bar{\lambda})^2 = 6\bar{\lambda}^2$. QED.

Inequality (7.15) motivates the definition of a normalized (and thus size independent) asphericity

$$0 \leq \Delta_0 \equiv \frac{\text{trace}(\hat{\mathbf{Q}}^2)}{6\bar{\lambda}^2} \leq 1. \quad (7.16)$$

Averaging inequality (7.16) over an statistical ensemble yields

$$0 \leq \langle \Delta_0 \rangle = \left\langle \frac{\text{trace}(\hat{\mathbf{Q}}^2)}{6\bar{\lambda}^2} \right\rangle \leq 1. \quad (7.17)$$

Unfortunately, $\langle \Delta_0 \rangle$ is not tractable analytically [122]. Therefore, Aranovitz and Nelsen introduced a separable version of $\langle \Delta_0 \rangle$, namely

$$\Delta \equiv \frac{\langle \text{trace}(\hat{\mathbf{Q}}^2) \rangle}{\langle 6\bar{\lambda}^2 \rangle}. \quad (7.18)$$

However, it is remarkable that the inequality (7.17) ‘‘survives’’ the separation ansatz. In fact, the situation is not that complicated. Applying the statistical averaging to the inequality (7.15) and dividing both sides by $\langle 6\bar{\lambda}^2 \rangle$ immediately leads to

$$0 \leq \Delta \leq 1. \quad (7.19)$$

Using similar arguments, it was further shown in Appendix A of [122] that

$$-\frac{1}{4} \leq S_0 \equiv \frac{\det \hat{\mathbf{Q}}}{\bar{\lambda}^3} = \frac{27 \det \hat{\mathbf{Q}}}{\text{trace}(\mathbf{Q})^3} \leq 2 \quad (7.20)$$

which after averaging reads

$$-\frac{1}{4} \leq \langle S_0 \rangle \leq 2. \quad (7.21)$$

The corresponding separable version of inequality (7.21) is

$$-\frac{1}{4} \leq S \equiv \frac{\langle \det \hat{\mathbf{Q}} \rangle}{\langle \bar{\lambda}^3 \rangle} = \frac{27 \langle \det \hat{\mathbf{Q}} \rangle}{\langle \text{trace}(\mathbf{Q})^3 \rangle} \leq 2. \quad (7.22)$$

As $\bar{\lambda} > 0$, it follows from the comments on $\det \hat{\mathbf{Q}}$ that S and $\langle S_0 \rangle$ are both measures of the average prolate- or oblateness of a polymer system. For positive values of S or $\langle S_0 \rangle$ the average shape is prolate whereas negative values indicate oblateness of the average shape.

A great advantage of defining quantities like Δ , $\langle \Delta_0 \rangle$, S and $\langle S_0 \rangle$ is that they separate the shape information from that of the orientation. Even if a polymer chain takes all possible orientations, the results obtained by these quantities will still yield the correct average shape of the chain.

Note, however, that the definition of Δ and S was mainly motivated by difficulties in analytical treatment of the more physical alternatives $\langle \Delta_0 \rangle$, and $\langle S_0 \rangle$ [122, 123].

Using MC-simulation results, a detailed comparison of the analytically tractable versions, i.e. Δ and S with the more natural alternatives $\langle \Delta_0 \rangle$ and $\langle S_0 \rangle$ has been done in [122, 123]. Simulations were done for a random walk (RW) on the one hand and a self avoiding walk (SAW) on the other hand. It was found that the insensitivity of S and Δ to the details of the interactions (which was known from the analytic calculations of Aranovitz and Nelson) are in fact artefacts of the separable ansatz underlying their definition. The more natural versions, i.e. $\langle \Delta_0 \rangle$ and $\langle S_0 \rangle$ do depend on the details of the model. For a random walk, for example, one obtains a smaller asphericity and degree of prolateness than for a self avoiding walk.

This has a simple physical interpretation. Adding intermolecular interactions to a random walk amounts effectively to reducing the probability of high energy configurations. Such situations, however, are more probable when a monomer is surrounded by other monomers. In other words, strong repulsive forces occur more frequently in isotropic configurations than in non-isotropic ones. Hence, the former are more efficiently suppressed compared to the latter.

If the above picture is not wrong, we should expect that the presence of attractive interactions should yield shapes between the random walk and the self avoiding walk results. Indeed, as shown in panel (a) of Fig. 7.5, our MD results do confirm this expectation. It is also shown in panel (b) of Fig. 7.5 that S and Δ are nearly equal to the values obtained for RW and SAW [123]. This demonstrates again that the effects of interactions are not properly taken into account in these quantities. Furthermore, they overestimate latter Very similar results to the MD data presented here have been also obtained from MC simulations of thin films within the Bond-Fluctuation-Model (BFM) [95]. A striking agreement is observed in qualitative features of $\langle \Delta_0(z) \rangle$ and $\langle S_0(z) \rangle$ for both MD and BFM. The bulk averages (values in the film center), however, differ slightly in both models. Tabel 7.1 compares bulk values of $\langle \Delta_0 \rangle$, $\langle S_0 \rangle$, Δ and S obtained for various models discussed in this section.

Next, we comment the shape profiles displayed in panel (a) of Fig. 7.5. It is seen from this figure that the average chain shape of the present polymer model is prolate both in the vicinity of the walls and in the film center. Close to the walls, however, this behavior is strongly pronounced. Now, a plot of $\rho_{\text{cm}}(z)$ in the same panel reveals that, in fact, there are only a few chains in the region of strong prolateness. These chains are quenched between the walls and a dense layer of chains indicated by the maximum of $\rho_{\text{cm}}(z)$. They thus align parallel to the walls and explore the space available in lateral direction. This explains not only the observed shape properties close to the walls but also the enhancement of $R_{\text{ee},\parallel}^2$ and $R_{\text{g},\parallel}^2$ discussed in section 7.4.

With increasing distance from the walls an opposite tendency appears, i.e. the chains become less prolate and less aspheric until a minimum is reached at a distance of ≈ 2 from the walls. This, again, can be related to the fact that the density of chain centers exhibits a maximum at approximately the same distance from the walls [see Fig. 7.5]. It is therefore not favorable for the chains at this distance to take a parallel orientation. Hence, they try to also explore regions in transversal directions thus becoming and less prolate and less aspheric.

	$\langle \Delta_{0,\text{bulk}} \rangle$	$\langle S_{0,\text{bulk}} \rangle$	Δ_{bulk}	S_{bulk}
RW ^{MC} [123]	0.396	0.481	0.529	0.895
RW ^{RG} [122]	-	-	0.526	0.887
BFM [95]	0.411	0.499	-	-
MD	0.432	0.541	0.539	0.89
SAW ^{MC} [123]	0.447	0.572	0.543	0.879
SAW ^{RG} [122]	-	-	0.534	0.893

Table 7.1: Bulk values of $\langle \Delta_0 \rangle$, $\langle S_0 \rangle$, Δ and S obtained from MC simulations of a random walk (RW^{MC}) and of a self avoiding walk (SAW^{MC}) [123], from MC simulations of a thin film within Bond-Fluctuation-Model (BFM) [95] and finally molecular dynamics results within the present work (MD). For RW and SAW we also show Δ and S obtained from a renormalization group calculation [122] (indicated by superscript ‘‘RG’’). MD data correspond to $T = 1$. At lower temperatures, however, no significant change is observed [see also Fig. 7.5].

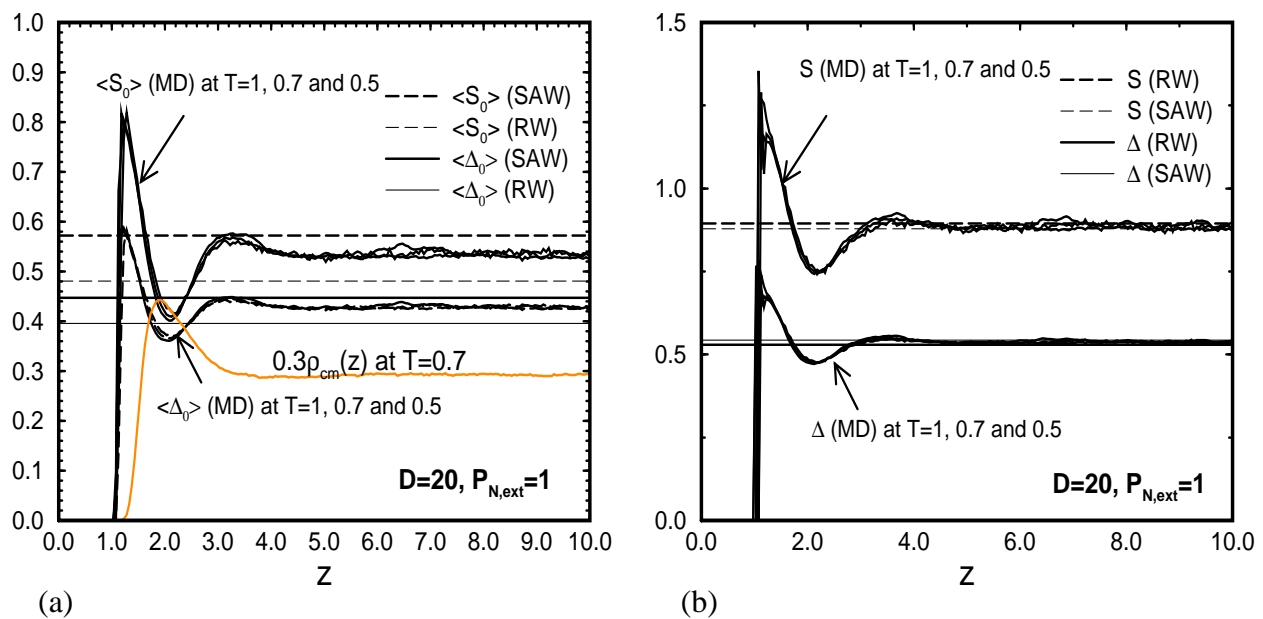


Figure 7.5: Panel (a): $\langle \Delta_0(z) \rangle$ and $\langle S_0(z) \rangle$ as obtained from molecular dynamics simulations (MD) at temperatures $T = 1, 0.7$ and 0.5 ($T_c(D = 20) = 0.41$). Horizontal lines indicate the corresponding MC bulk simulation results of a random walk (RW) and of a self avoiding walk (SAW) [123]. Finally the density profile of chains' centers is also depicted, whereby it is multiplied by a factor of 0.3 to be within the scale of the figure. The minimum values of the asphericity and of the prolateness are observed approximately at the maximum position of ρ_{cm} . Note that the position of the maximum of ρ_{cm} is insensitive to a change of temperature (not shown here). Panel (b): Same comparison, now for Δ and S . Note that, within the scales of the figure, the analytical results for RW and SAW obtained from a renormalization group calculation [122] can be hardly distinguished from the MC data and therefore are not presented here.

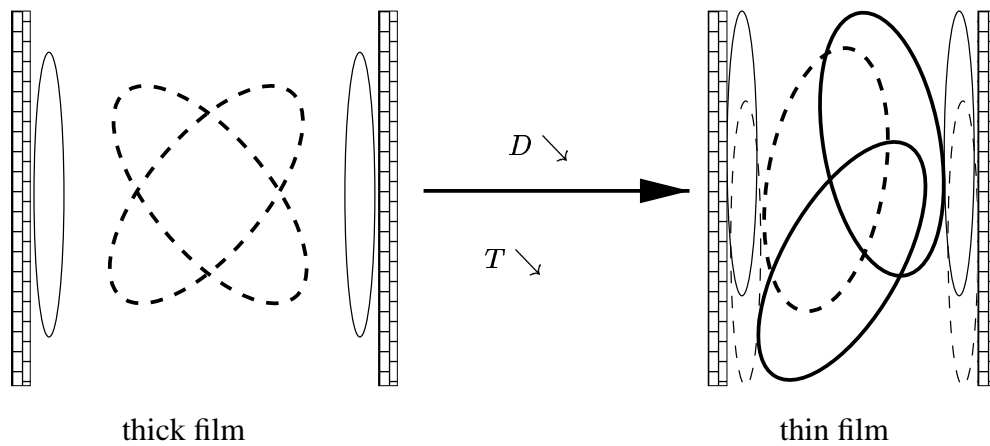


Figure 7.6: Schematic sketch of the influence of film thickness and temperature on static properties. A good approximation of the instantaneous structure of a chain is an ellipsoid. The chains are therefore represented by ellipsoids in the figure. Adjacent to a wall the two largest principal axes of the ellipsoid are aligned parallel to the wall, whereas the smallest axis points away from it in perpendicular direction. Furthermore, the chain is distorted (i.e., flattened). Both effects are entropically unfavorable so that the number of chains close to the wall is small at high temperature. If the film is sufficiently large, there is a bulk-like inner region, where the chains can freely reorient (indicated by dashed ellipsoids in the left sketch). With decreasing film thickness the bulk-like region shrinks more and more, leading finally to parallelly oriented chains also in the middle of the film if the thickness is $D \lesssim 4R_g$. At high temperature the walls are still avoided in such a thin film so that a high concentration of chains occurs in the middle (indicated by the three ellipsoids in the right sketch instead of two in the left) [from J. Baschnagel].

Chapter 8

Dynamics

In this chapter we are going to investigate some aspects of the dynamical properties of the system at high and low temperatures. However, contrary to the case of the static properties which are in a wide range independent of the specific number of particles, N , used within a simulation, the dynamics of the system can strongly depend on N . In fact the dependence on the number of particles is a consequence of the *size dependence* of the dynamic properties. Keeping the temperature at a constant value, it is clear that, for a given density and pressure, the system size is the smaller, the smaller the number of particles.

To reduce finite size effects, it is therefore important to check for the dependence of the quantity of interest on N , and choose N so that the size effects, at least to first order, are negligible. In practice, however, one must often choose a compromise between the reduction of the finite size effects and computing time.

8.1 Finite Size Effects

Motivated by the ideas just mentioned, we first carried out, for a film of thickness $D = 20$, simulation runs with various numbers of particles. The variation of the lateral system size was then a result of constant temperature-constant pressure condition.

We first show in Fig. 8.1 the mean square displacements of chain centers for a rather large film thickness, $D = 20$. Two temperatures are displayed: The left panel corresponds to a relatively high temperature $T = 1$ whereas the right panel to an intermediate one, namely $T = 0.7$ ($T_c = 0.41 \pm 0.01$ for $D = 20$). As seen from these figures, strong size dependence is limited to very small systems. Though not vanishing, the size dependence is very weak already for moderate system sizes $L \geq 10$ at both temperatures. Therefore, as a compromise between accuracy and computing time, we have chosen $N = 2000$ for this film thickness.

For $D = 20$, the observed acceleration of dynamics at smaller system sizes is in agreement with MC-simulation results of the two dimensional bond-fluctuation-model (BFM) [43]. In recent molecular dynamics simulations of Lennard-Jones [124] and hard core [125] systems, however, an opposite behavior is seen.

The size dependence of the dynamics for very small system sizes is often related to the concept of cooperative motion first introduced by Adam and Gibbs [32] to explain the sharp rise of the transport coefficients, such as viscosity, inverse diffusion constant or relaxation times in a narrow temperature range near the glass transition temperature, T_g .

According to Adam and Gibbs, near the glass transition, the system is divided into clusters of correlated molecules. The motion of a molecule inside a given cluster requires the cooperative

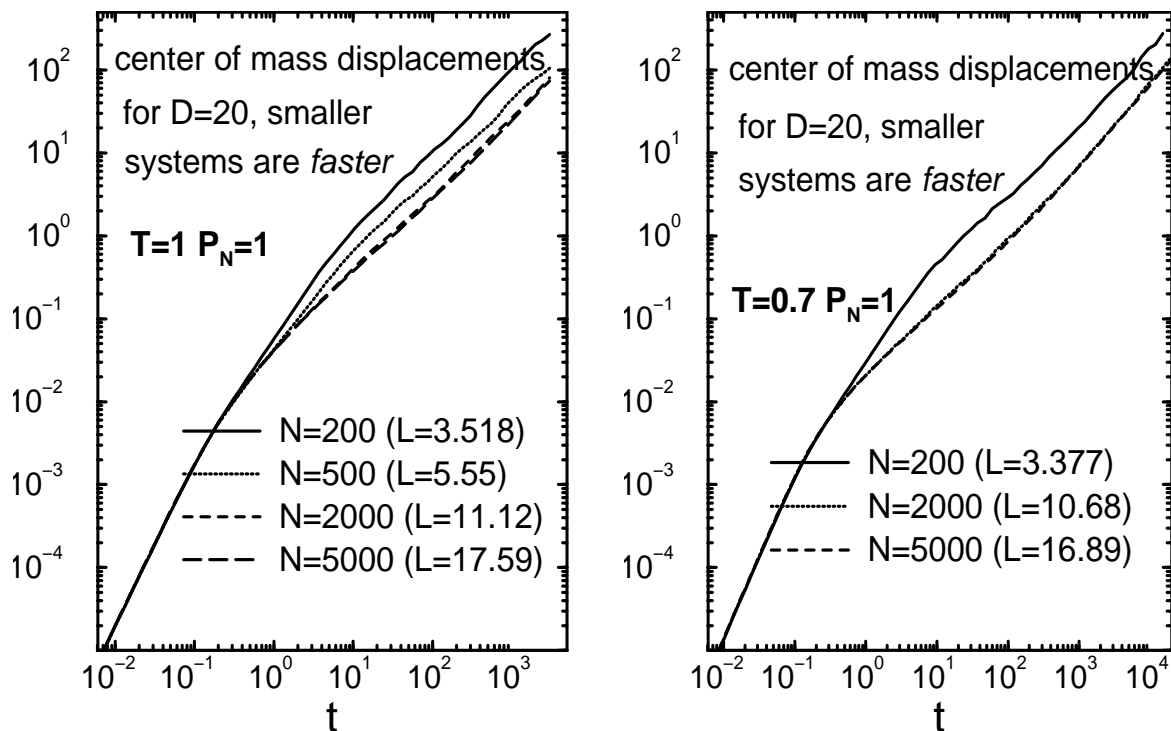


Figure 8.1: The mean square displacements of the chain centers parallel to the walls, $g_{3,||}$, for various particle numbers. For each particle number, the corresponding lateral system size, L , is indicated in brackets. The film thickness was $D = 20$ and the normal pressure was set to $P_{N,\text{ext}} = 1$. The left panel contains results at $T = 1$ and the right panel at $T = 0.7$. Both at high and low temperatures, the mobility increases for smaller system sizes. However, there is no appreciable size dependence for $L \geq 10$ ($N \geq 2000$).

motion of the other molecules (of the same cluster), hence the term “cooperatively rearranging regions”. It is easy to see that the probability for such a “cooperative motion” decreases with the size, ξ , of the cluster. However, as long as the system comprises many clusters, their relative motions (the so called collective flow) will contribute to the structural relaxation thus preventing the divergence of the transport coefficients.

On the other hand, if the typical size, ξ , of a cooperative region grows at lower temperatures, there will be a temperature at which the whole system builds up a sole cluster. The mobility of the system will then decrease drastically, for it will directly depend on the cooperative motion of all particles of the system. At the same time, for $L < \xi$, the relaxation time will exhibit a strong size dependence due to the mentioned argument that the larger the system size, the less probable a cooperative rearrangement. Thus, the diffusion constant will decrease with L for $L < \xi$. Obviously, when the system size L becomes larger than ξ , we get back to the situation where the system comprises many clusters and the alternative relaxation processes come into play thus leading to a weakening of the size dependence.

Thus, following the above arguments, one obtains an explanation of the acceleration of the dynamics for smaller systems. However, the same concept of cooperative motion is some times used in a different way to explain a slowing down of the dynamics for smaller systems (see for example [125]). It is indeed observed that the main contribution to the structural relaxation originates from the cooperatively rearranging regions [124]. Therefore, it is argued that the system dynamics is accelerated if the system contains larger clusters. Note that this argument is

exactly opposite to the one given above, namely that the *larger the cluster size, the less probable a cooperative motion and thus the slower the dynamics*.

One also finds that the linear size, ξ , of a cooperative region decreases for smaller L . Thus, one argues that the diffusion rate must decrease if the system becomes smaller. This result is in agreement with some recent simulation results. However, using the concrete numerical data given in [124] one can show that the same result can also be obtained starting from the opposite point of view, namely that the larger clusters are slower. Three system sizes are considered in [124]: $L = 5.13$ (10^2 particles), $L = 10.8$ (10^3 particles) and $L = 23.2$ (10^4 particles). The corresponding sizes of cooperative regions are $\xi = 3.38$, $\xi = 6.11$ and finally $\xi = 7.73$. So, this is really true that smaller systems contain smaller clusters. However, if one looks at the *relative* size of a cooperative region, one obtains: $\xi/L = 0.659$, 0.566 and 0.333 , respectively. The relative size of a cluster is obviously larger for smaller systems which means that there are less individual clusters. The possibility of alternative contributions to the structural relaxation is therefore decreased. The system relaxes more slowly, for the motion of a given particle requires the less probable cooperative motion of a large number of molecules.

We conclude from this discussion that the concept of cooperative motion must be handled with some care. Although the existence of regions of cooperative motion seems to be well accepted, there is still need for more quantitative investigations.

Next, we report on a kind of “cross over” in the size dependence of our system of study as a result of the variation of the film thickness, D . For the much thinner film of thickness $D = 5$, we found a size dependence of the mobility from the lateral size opposite to that seen for $D = 20$: the smaller systems are now *slower*. This finding is displayed in Fig. 8.2, where the mean square displacements of chain centers are compared for various particle numbers, i.e. for different lateral system sizes, L . In the left panel a film of thickness $D = 10$ is investigated and in the right panel a thinner film with $D = 5$. A change in the “sign of the size dependence” occurs when going from $D = 10$ to $D = 5$.

Note that, in a polymer system, the cooperativity of motion is pronounced by the chain connectivity. It is clear that a monomer can not go far without being accompanied by its adjacent “partner(s)”. Therefore, for a dense polymer liquid, the concept of cooperative motion has relevance even at very high temperatures. Recalling the importance of the *relative* cluster size, ξ/L , within the concept of cooperative motion, an explanation of the reported opposite size dependence for small D compared to the larger ones could be found assuming that ξ/L increases for smaller film thicknesses. This assumption, however, must be verified quantitatively.

8.2 High Temperatures

Consider two solid walls at rest and a fluid with a non zero center of mass velocity confined between these walls. It is well known from textbook hydrodynamics that the fluid velocity vanishes at contact with the solid. However, this argument is a macroscopic one. Nevertheless, as we will see in chapter 9 this can indeed occur also on a microscopic level: When averaged over sufficiently long times, the mean velocity of a fluid particle at the solid-liquid interface vanishes relative to the wall. This is the so called non-slip (or stick) boundary condition which is often used in hydrodynamic treatments of the flow. On the macroscopic level, the stick boundary condition is related to the roughness of the solid-liquid interface. The fluid particles lose energy due to the friction on this surface.

Obviously, perfect slip is the opposite to a stick boundary condition. Although not very usual in nature, it is very simple to achieve such a boundary condition in a molecular dynamics

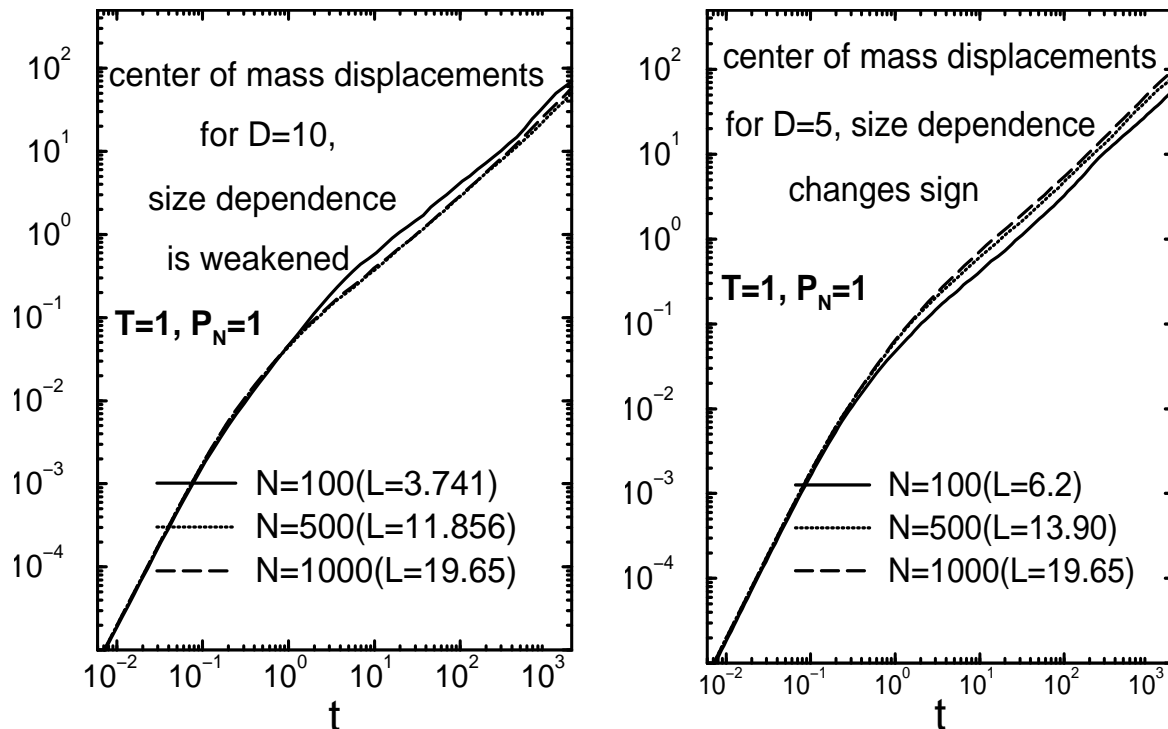


Figure 8.2: The mean square displacements of chain centers parallel to the walls, $g_{3,||}$, for various particle numbers. For each particle number, the corresponding lateral system size, L , is indicated in brackets. The temperature was $T = 1$ and the normal pressure $P_{N,\text{ext}} = 1$. The focus is now on the “change of the sign” of the size dependence when going from $D = 10$ (left panel) to the thinner film $D = 5$ (right panel).

simulation. The only thing to do is to choose a wall potential which does not depend on lateral coordinates. Hence, the $1/z^9$ walls used for equilibrium simulations within the present work correspond to the perfect slip limit.

Analyzing the mean square displacements, we find that the mobility of the confined system is enhanced compared to that of the bulk model. This increase in mobility is shown in Fig. 8.3 where the mean square displacements of chain centers, g_3 , are plotted for the bulk and for the film at various thicknesses. For a film, the components of the displacements parallel to the walls, x and y say, are taken into account whereas the bulk data contains all three directions. The latter is therefore multiplied with a factor $2/3$. Our result on the acceleration of the dynamics due to the presence of the soft walls may seem to be in contradiction to the observed *decrease* of mobility in [124] where also soft walls were considered. However, the system considered in this reference exhibits huge density oscillations [see figure 5.(a) of the same reference]. There, the outermost density peak (closest to the walls) has a value of approximately 5 (LJ units) decreasing towards unity near the film center. It is clear that at a density of 4-5 atoms per unit volume, the diffusive motion will be less efficient than at considerably smaller values. This may explain the observed decrease of the diffusion constant when approaching the walls.

Let us now have a look at density profiles of our model. It is shown in Fig. 8.4 that, with the exception of $D = 3$, the average density varies rather slowly with film thickness. In addition, the observed oscillations have small amplitude. This is a consequence of the fact that our simulations were carried out under the condition of *constant pressure*. The larger deviation of the density for $D = 3$ from the bulk value is related to the strong wall contributions to the normal

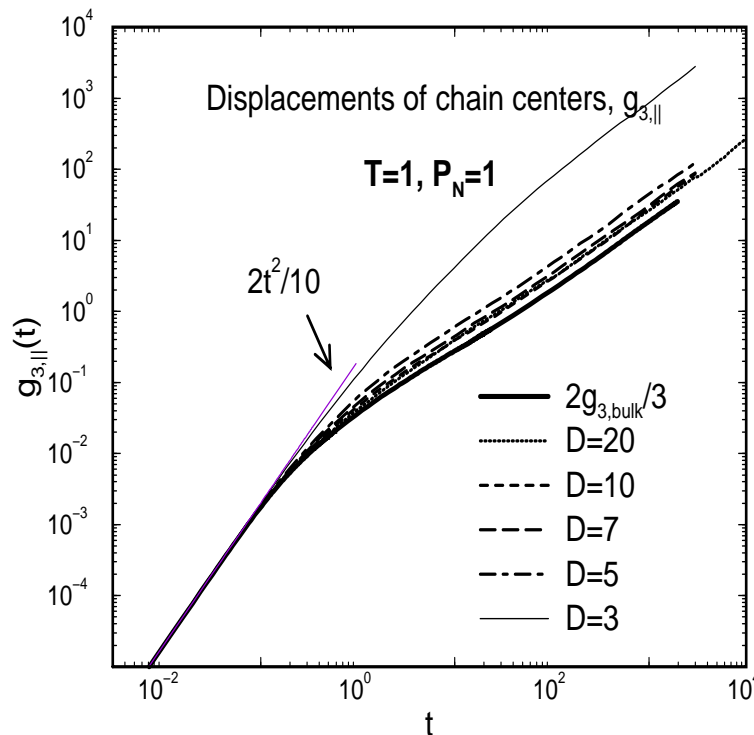


Figure 8.3: Mean-square displacement of the chains' center of mass parallel to the walls, $g_{3,||}(t)$, for films with various film thicknesses compared to the corresponding bulk quantity. The lateral dimension, L , is chosen such that the finite size effects discussed in section 8.1 are absent. The external pressure and temperature were set to unity in all cases, i.e. $p_{\text{bulk,ext}} = P_{\text{N,ext}} = 1$, and $T_{\text{ext}} = 1$. The smaller the film thickness, the stronger the mobility enhancement. The initial increase of $g_3(t)$ is ballistic, i.e., $g_{3,||}(t) \sim 2t^2/10$, the slope being determined by the thermal velocity and the chain length (here 10).

pressure [see Fig. 3.2]. The system expands to keep the sum of all contributions constant. Back to the discussion of the apparent discrepancy between the mobility enhancement in our model and its decrease in the model studied in [124] we note that these two systems are separated by a factor of 5 in density profile close to the walls. Hence, the results from the one cannot be directly extrapolated to the other.

As shown in Fig. 8.4, our study corresponds to a situation where, at least at high T , the static properties of the system are not strongly affected by the presence of the walls. Therefore, we can focus on the influence of geometric boundaries on the mobility. Following [126, 127] we first write the diffusion constant in terms of the velocity autocorrelation function (VACF)

$$D = \frac{1}{3} \int_0^\infty \langle \mathbf{v}(t) \mathbf{v}(0) \rangle dt. \quad (8.1)$$

It has been shown in [128] that the short time contributions to the integral in (8.1) can be well separated from the long time part which couples to the long wavelength, hydrodynamic motion of the fluid. The short time behavior of VACF is mainly determined by the interactions between a particle and its nearest neighbors. Therefore, for moderate confinements, i.e. for confinements which do not modify the static structure in a crucial way, it is reasonable to suppose that the short time part of VACF is not much affected by the boundaries. The long time part, however, can change if the long wavelength motion is hindered by some boundaries: The part of the

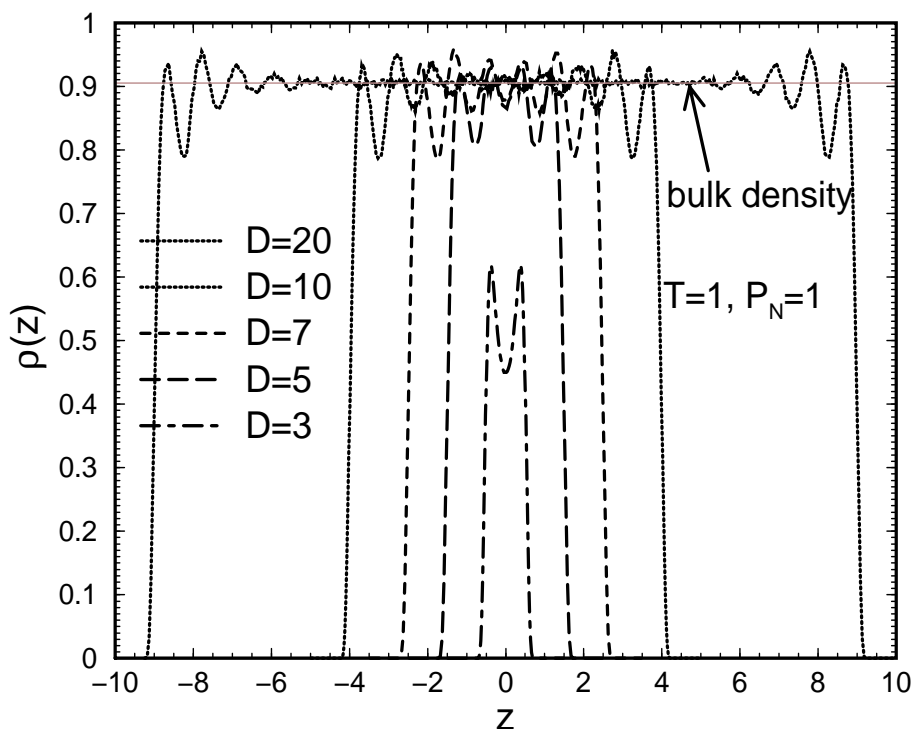


Figure 8.4: Density profiles at $T = 1$ and $P_{N,\text{ext}} = 1$ for films of thickness $D = 20, 10, 7, 5$ and 3. With the exception of $D = 3$ which has a much lower density, the average density is nearly equal to the corresponding bulk value for all thicknesses. The enhancement of mobility [see Fig. 8.3] is therefore not a simple consequence of density changes.

velocity of a tagged particle which is transferred to the hydrodynamic motion can, at later times, come back to the original particle and thus influence its velocity (“backflow” effect). Now, if reflecting walls are present (perfect slip), this effect will be enhanced, thus leading to an increase of mobility compared to the corresponding bulk system. On the other hand, if the walls are absorbing (non-slip case), the same argument will predict a decrease of the diffusion constant.

In addition to this “mode-coupling” approach, one can adopt a hydrodynamic point of view: Calculate the drag force \mathbf{F} on a particle moving with a given velocity \mathbf{v} through a fluid of viscosity η . Use $\mathbf{v} = \mu \mathbf{F}$ to compute the mobility, μ . Finally, apply the Einstein relation $D = k_B T \mu$ to obtain the diffusion constant. Of course, for a system confined between two parallel walls the component of the force parallel to the walls has to be computed. This leads to μ_{\parallel} and D_{\parallel} . The above procedure may seem very simple, but actually it requires a considerable amount of algebra. The problem lies in correctly treating the boundary conditions [128]. As we are interested in the case of the perfect slip boundary condition, we give here the corresponding result [128]

$$D_{\parallel}(h) = D_{\text{bulk}} \left(1 + \frac{9R}{8h} \right), \quad (8.2)$$

where R is the radius of a particle and h the wall-to-wall separation. As we have chains instead of spherical particles, we will approximate R by the radius of gyration R_g of a chain.

In Fig. 8.5 the mean-square displacement of the chain centers in direction parallel to the walls, $g_{3,\parallel}(t)$, divided by $4t$ are displayed versus $1/t$. From these curves, one can obtain the diffusion constant fitting a horizontal line to each curve for $1/t \rightarrow 0$. As shown in this figure, for

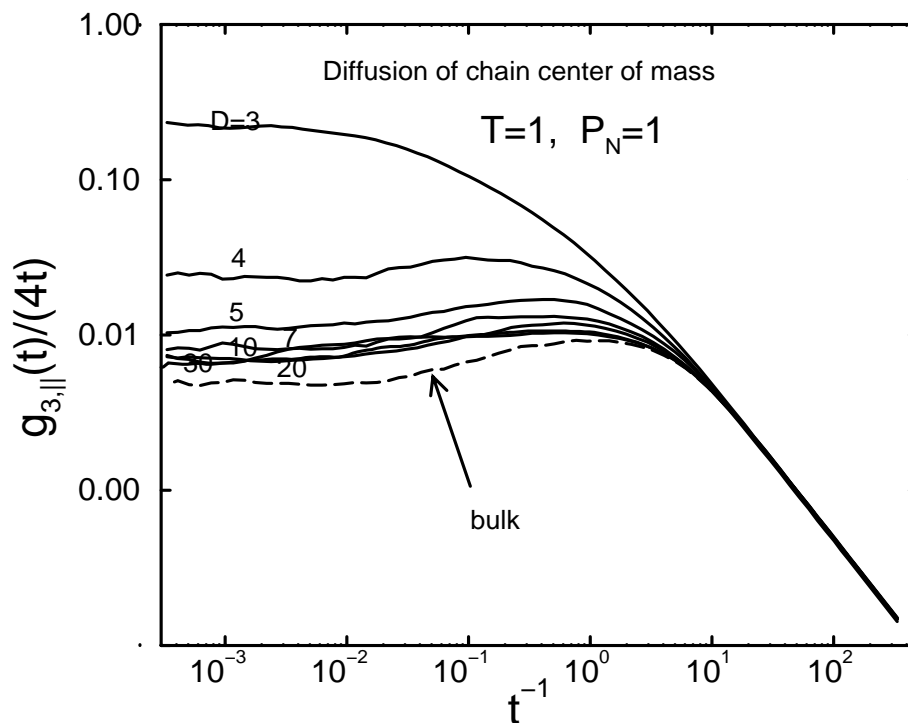


Figure 8.5: Mean-square displacement of chain centers in direction parallel to the walls, $g_{3,||}(t)$, divided by $4t$ versus $1/t$. The corresponding wall-to-wall separations, D , are indicated upon the curves. For $1/t \rightarrow 0$, each curve should converge towards the appropriate diffusion constant.

large film thicknesses, the error in determining the diffusion constant is comparable to its change due to the variation of the film thickness. This has two main reasons: First, the simulation length was rather short, so that only the beginning of the diffusive regime could be reached. Secondly, equidistant sampling of positions (and velocities) was done on a logarithmic scale. This is suitable for the analysis of dynamical correlation functions which usually decay exponentially. However, the disadvantage of such a sampling strategy is that later times are sampled less frequently than short and intermediate times. The present situation shows that, to obtain a good estimate of the diffusion constant, one should have enough samples also at large t . This would allow one to integrate out the oscillations of $D_{||}(t) := g_{3,||}/4t$ and thus, to a certain amount, to compensate the shortness of the simulation time span. Therefore, as long as it is feasible, one should adopt a linear sampling strategy with long distances (for example once in 10^4 MD steps for high T and once in 10^5 at lower temperatures) combined with a logarithmic one. The logarithmic part would take into account the need for more samples at short times and the linear part would allow for a better analysis of the diffusive processes.

Figure 8.6 compares the results obtained from MD simulations with Eq. (8.2). The left panel corresponds to a relative high temperature of $T = 1$ (recall that the bulk critical temperature of the same model is $T_c = 0.45$) whereas the right panel contains results at a rather intermediate temperature of $T = 0.7$. A qualitative agreement between the simulated data and Eq. (8.2) is observed. However, it was already noted in [126] that a quantitative agreement with simulation results cannot be expected. For the idea leading to Eq. (8.2) takes into account the “backflow” effect only. Other possible contributions to the mobility enhancement like that of the density depletion close to the walls is not considered here. From the right panel in Fig. 8.6 it is seen that the deviations from Eq. (8.2) become larger at lower temperatures. This can be related to the fact

that the derivation of Eq. (8.2) is based on a hydrodynamic argument. It is therefore applicable only if the system is in a well defined liquid state. At $T = 0.7$ however, the relaxation times of our system of study are already quite large. The system is in an intermediate state between the liquid and glassy states. Hence, the regime of validity of Eq. (8.2) is left.

8.3 Low Temperatures

As mentioned in chapter 2, the present polymer system contains two incompatible length scales whose competition prevents crystallization at low temperatures. As a consequence, the system exhibits an amorphous structure at low T . On the other hand, the chain length is chosen rather short so that entanglement effects are absent. These properties make our model a suitable candidate for studying a supercooled melt. The static and dynamic properties of this model were studied in the bulk when gradually supercooling towards the glass transition [37,46,48–50,129]. Not unexpectedly, it was found that the model begins to develop sluggish relaxation if the temperature drops below $T \approx 0.7$. This dramatic change in the dynamics was then successfully analyzed within the mode-coupling theory (MCT) [21,22,130,131]. As a result of this analysis, one obtained a corresponding critical temperature of $T_{c,\text{bulk}} \simeq 0.45$ [48].

The mode-coupling approach to the glass transition is mainly based on a closed set of differential equations for density fluctuations which must be solved in a self-consistent way. Actually, we will discuss some predictions of the *idealized* version of MCT only. One of the most impor-

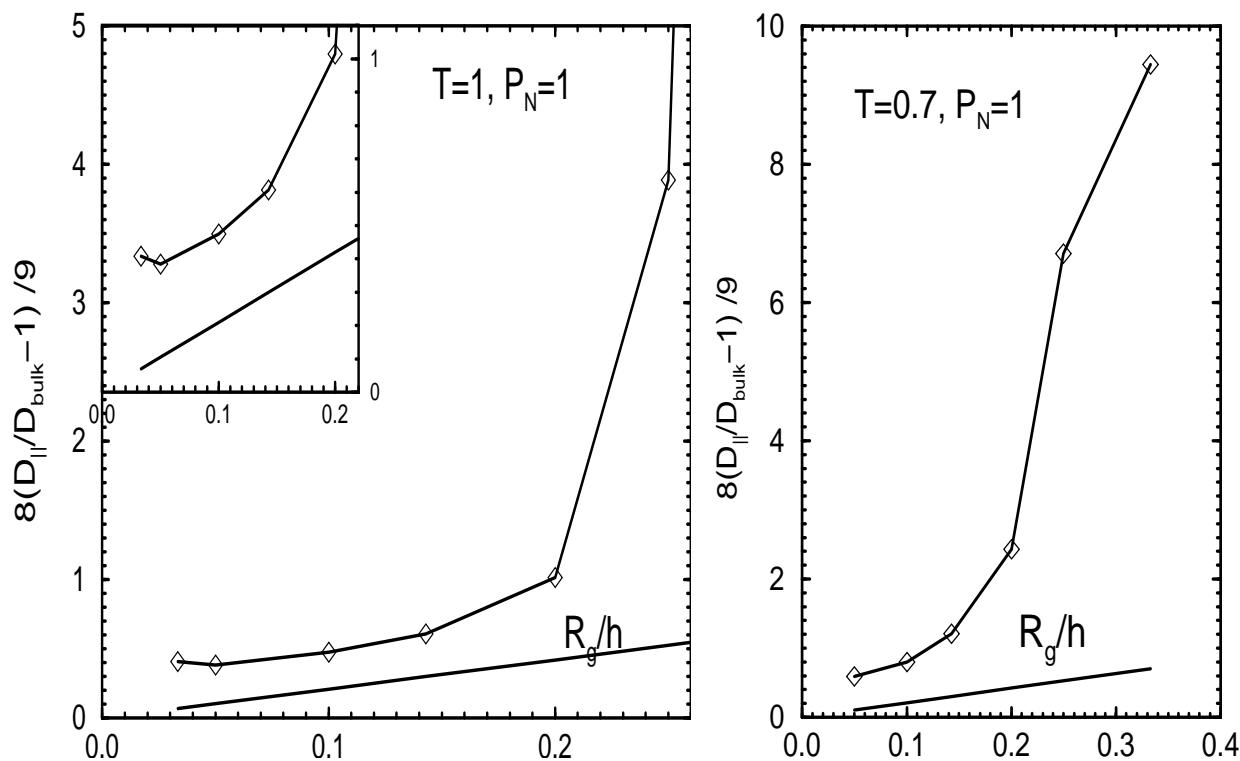


Figure 8.6: Left panel: Change in the Diffusion constant, $D_{||}$ relative to the bulk value versus $1/h$ (h is the wall-to-wall separation) at $T = 1$ and $P_{N,\text{ext}} = 1$. Right panel: The same quantity at a lower temperature of $T = 0.7$. The lines indicate the fit à la Eq. (8.2) where the particle radius R is set to the radius of gyration R_g .

tant predictions of the ideal MCT is the existence of a critical temperature $T_c > T_g$ (T_g is the glass transition temperature) below which the system becomes non-ergodic.

We recall that, in a mean field picture, as a point particle starts to move around through the fluid, after a very short period of free (ballistic) motion, it feels the presence of its neighbors. These neighbors build up a sort of cage, in which the particle has to spend a certain amount of time before being able to continue its “journey”. Within this picture, breaking of ergodicity can be understood as the divergence of the time which the particle spends in the cage constructed by its neighbors. In terms of the mean square displacements, one should therefore observe a plateau region extending to $t \rightarrow \infty$. Indeed, at low T , one does observe the formation of a plateau whose width expands when lowering the temperature.

Nevertheless, neither in real nor in computer experiments, a divergence of the relaxation time is ever observed. It means that the particle does in fact leave the cage of its neighbors after a long, but finite time. Thus, the idealized MCT overestimates the cage effect. In other words, there are mechanisms, like some kind of “hopping processes” which enhance the mobility of particles and thus “help” them to get rid of the cage. These processes are not taken into account in the idealized version of MCT. This must be kept in mind when verifying the ideal MCT predictions.

It was shown in chapter 7 that some static properties of the system like chains’ alignment and the distribution of chain ends change compared to the bulk if the system is confined within two smooth and purely repulsive walls. Close to the walls, the density of chain ends, for example, is much more pronounced than that of the inner monomers. Furthermore, parallel alignment is favored in the vicinity of the walls. As the dynamics of a physical system is related to its static properties, one should therefore expect corresponding changes in the dynamics.

However, as far as the idealized version of MCT is concerned, we should focus on the influence of the walls on the structure of the *cage* around a given particle. If the cage of neighbors is not strongly modified, one should be able to verify basic predictions of the idealized MCT in a similar way as done for the corresponding bulk system.

We have seen in chapter 7 (section 7.3) that the effect of the distance from a wall on the structure is very similar to that of the temperature [see panels (a) and (b) of Fig. 7.2]. To work out some consequences of this similarity, we are going to apply MCT fits on our data and calculate the critical temperatures for a few number of film thicknesses. We will see that, as far as the mean square displacements are concerned, the effect of the walls is mainly reduced to a shift of the temperature axis towards lower T . In other words, for films of different thicknesses, the mean square displacements exhibit similar time dependence when compared for the same *temperature difference*, $T - T_c(D)$ [see Fig. 8.11].

Let us first focus on the change of mobility due to the presence of the walls. Figure 8.7 compares $1.5 g_{3,\parallel}$ for the inner portion and the wall region of the film at $T = 0.45$ with g_3 of the bulk at $T = 0.46$. Note that the bulk critical temperature of mode-coupling theory is $T_c \simeq 0.45$ [48]. At very short times, the displacements increase ballistically ($g_3 \sim t^2$). The center of mass then behaves like a ‘free particle’. It neither feels the presence of other chains nor of the walls. Therefore, film and bulk data coincide. However, as time increases, the interaction with the surrounding polymers slows the dynamics down and a plateau develops: A chain is then blocked in a ‘cage’ formed by its neighbors, from which it can only escape gradually. This blocking is more effective in the bulk than in the film. Chains close to the walls are faster than those in the film center and these are in turn faster than those of the bulk.

When averaging displacements over the whole film, the resulting curves resemble corresponding bulk data at higher temperature. To quantify this effect we calculated relaxation times

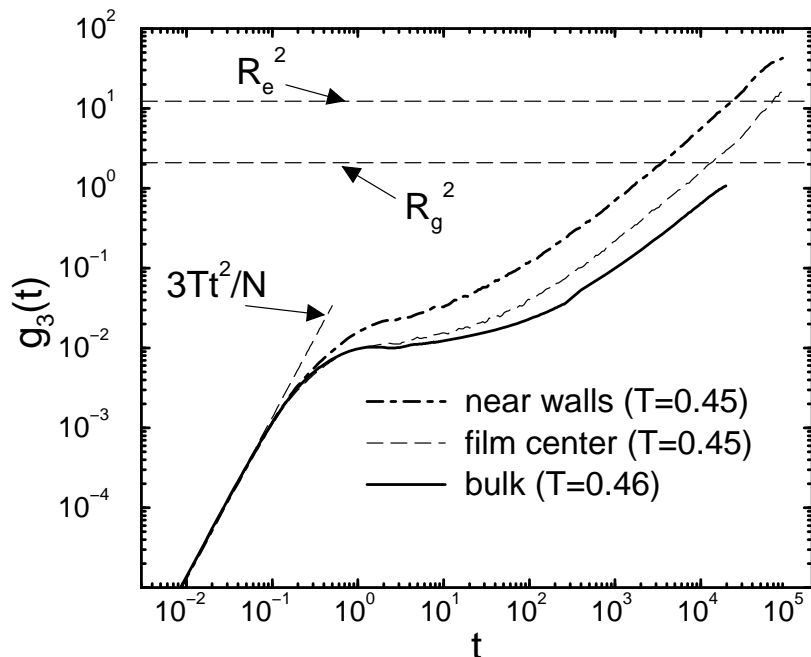


Figure 8.7: Mean-square displacement of the chains' center of mass, $g_3(t)$, for the bulk (at $T = 0.46$; note $T_c \simeq 0.45$) and in the film (at $T = 0.45$). For the film, the displacements parallel to the wall are shown, which were multiplied by $3/2$ to adjust them to the scale of the bulk. 'Near walls' and 'film center' mean averages over the regions close to the walls ($0 \leq z \leq 3.5$ and $6.5 \leq z \leq 10$) and the inner portion of the film ($3.5 \leq z \leq 6.5$). Only those chains which always remain in these regions were used for averaging. Two horizontal dashed lines indicate the bulk end-to-end distance ($R_e^2 \simeq 12.3$) and radius of gyration ($R_g^2 \simeq 2.09$). The initial increase of $g_3(t)$ is ballistic, i.e., $g_3(t) \sim t^2$, the slope being determined by the thermal velocity. This behavior is indicated for $T = 0.46$. Note also that the particles in the film at $T = 0.45$ are *faster* than bulk particles at the higher temperature of $T = 0.46$.

from g_0 , g_1 , g_3 and g_4 by

$$g_{i,\parallel}(\tau_{g,i}) := R_{g,\parallel}^2, \quad (8.3)$$

where $R_{g,\parallel}^2$ is the contribution of the parallel components (x and y , say) to R_g^2 . Next we tried to fit $\tau_{g,i}$ by

$$\tau_{g,i}(T) \propto |T - T_c(D)|^{-\gamma}. \quad (8.4)$$

The fits gave values for γ close to the bulk result $\gamma = 2.09$. Therefore, we fixed $\gamma = 2.09$ and determined $T_c(D)$. This yields $T_c(D = 10) \simeq 0.39$ (see Fig. 8.8), a value which is significantly smaller (about 14%) than $T_c(\infty) (\simeq 0.45)$ of the bulk. Contrary to T_c , γ seems not to be affected by the confinement. Since γ is directly related to other MCT-exponents which determine the time dependence of the displacements in the plateau region, it should be possible to superimpose the simulation data of the bulk and the film when using the same distance to the respective critical temperatures. Figure 8.8 supports this expectation. The dominant influence of completely smooth walls on the dynamics seems to be a reduction of T_c , i.e., a mere shift of the temperature axis. This observation will be further discussed below when analyzing other film thicknesses.

We saw in section 8.2 that, at high temperatures, the increase in the rate of diffusivity can be partly explained by saying that the long wavelength hydrodynamic modes are reflected at the

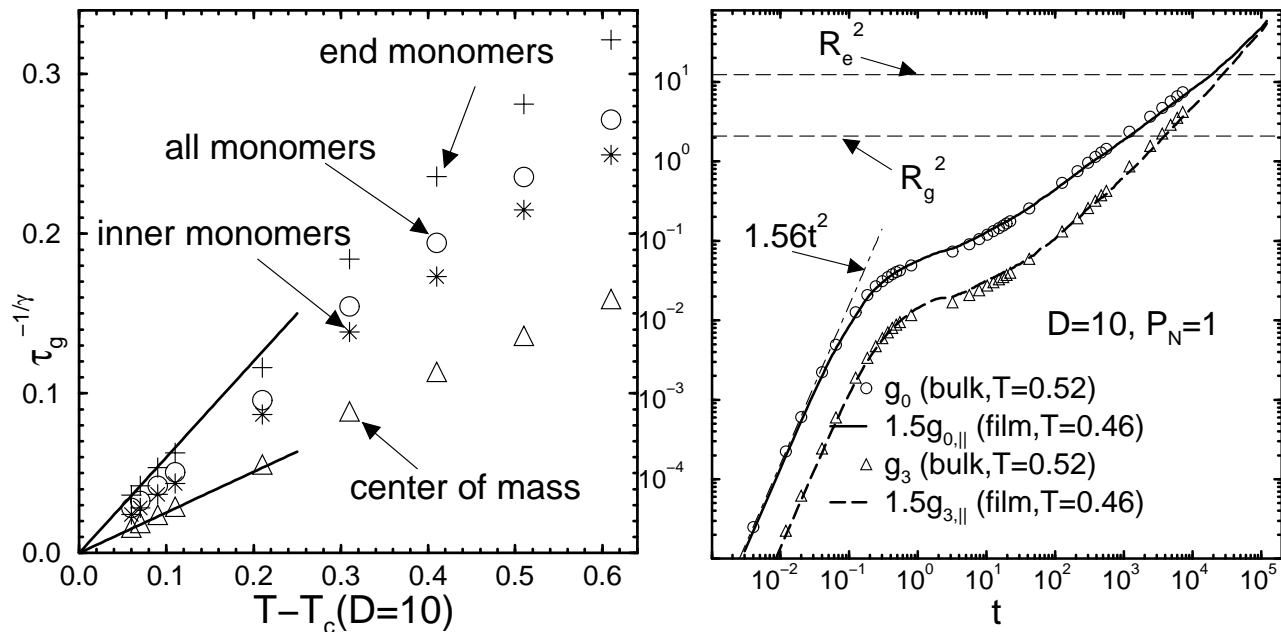


Figure 8.8: Left panel: Plot of $\tau_g^{-1/\gamma}$ versus $T - T_c(D = 10)$. The time τ_g was determined by Eq. (8.3) for the mean-square displacements of inner, end and all monomers and of the chains' center of mass. The mode-coupling exponent γ was taken from the bulk analysis ($\gamma = 2.09$ [48]). Holding $\gamma = 2.09$ fixed and fitting Eq. (8.4) to the last four data points (indicated by the solid lines) an average result of $T_c(D = 10) \simeq 0.39$ was obtained. This was used to rescale the temperature axis. Right panel: Mean-square displacements for all monomers, $g_0(t)$, and for the chains' center of mass $g_3(t)$ at the same $T - T_c = 0.07$ for the bulk ($T = 0.52$, $T_c = 0.45$) and for the film ($T = 0.46$, $T_c = 0.39$). The displacements of the film were calculated parallel to the wall and averaged over the whole system. They were multiplied by $3/2$ to match the scale of the bulk. The bulk end-to-end distance ($R_e^2 \simeq 12.3$) and radius of gyration ($R_g^2 \simeq 2.09$) are indicated by vertical dashed lines. The other dashed line shows the initial ballistic motion of the monomers, i.e., $g_0(t) \sim t^2$, whose slope is $3T$. The corresponding numerical values for $T = 0.46$ ($= 1.38$) and $T = 0.52$ ($= 1.56$) cannot be distinguished on the scale of the figure.

walls. It was also mentioned that for absorbing walls, a decrease of mobility is expected. At a qualitative level, this argument applies also to low temperatures. There is no reason to assume that the reflecting or absorbing property of the walls changes at lower T . However, adopting a still macroscopic but slightly different point of view, one can find an alternative explanation of the same phenomena. This involves the concept of friction. It is schematically shown in Fig. 8.9 that a particle in a bulk system is subject to the friction forces originating from all its neighbors, whereas in a system confined between perfectly smooth walls the friction force on a particle near a wall is due to its neighbors in the inner side of the system only and hence is smaller compared to the bulk case. However, if one replaces the smooth walls by rough ones the situation can change dramatically depending on the degree of roughness. Next we represent MCT-fits results for two further film thicknesses, namely a larger one, $D = 20$, and a smaller one, $D = 5$. Defining $\tau_{g,i}$, $i = 0, 1, 3, 4$, as in Eq. (8.3) and fitting the obtained data by Eq. (8.4) we obtain

$$\begin{aligned} T_c(D = 20) &= 0.41 \pm 0.01, \\ T_c(D = 5) &= 0.31 \pm 0.02. \end{aligned} \quad (8.5)$$

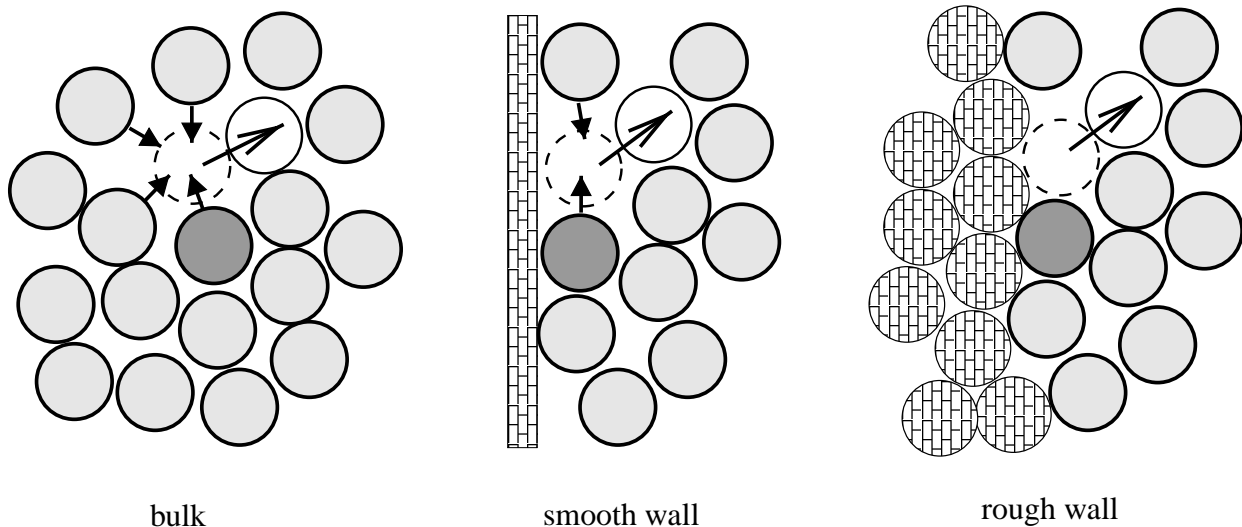


Figure 8.9: Illustration of a possible influence of confinement on the dynamics of a supercooled liquid. Two types of confinement are compared with the bulk: completely smooth walls and rough walls which are perfectly adapted to the liquid structure. Let us consider the bulk first and imagine that the particle \bigcirc moves from its dashed position in direction of the large arrow. It opens space which its neighbors try to occupy. The dark-shaded particle has to compete with all other neighbors which are simultaneously moving in the space formerly occupied by \bigcirc . This exerts a friction on the dark particle, which is partly absent if it sits next to a completely smooth wall (panel in the middle). On the other hand, the friction should be strongly enhanced if the particle is next to a rough wall exhibiting cavities, into which it perfectly fits (right panel). This constraint does not relax away contrary to the bulk. So, one can expect the mobility of the dark particle to decrease with respect to the bulk for such a rough wall (see [132], for instance), but to increase for a completely smooth wall which acts like a lubricant compared to the bulk [from J. Baschnagel].

The larger uncertainty in the critical temperature of the thinner film ($D = 5$) is due to the fact that, for this film thickness, the lowest investigated temperature, $T = 0.38$, is still far above the critical temperature. The extrapolation to lower T thus contains larger errors.

However, it is demonstrated in Fig. 8.8 that the relaxation time τ_g is less sensitive to the distance from T_c . The convergence of all data towards a well defined limit is already seen from the left panel where $\tau_g^{-1/\gamma}$ is displayed versus $T - T_c(D = 5)$ ($\gamma = 2.09$). The right panel, on the other hand, demonstrates the relaxation time, τ_g , in a slightly different way: It is displayed in a log-log plot showing that parallel straight lines can well be fitted to the data.

With the obtained results on the MCT-critical temperatures $T_c(D)$, we investigate again the question of the shifting property of the temperature axis. Recall that the idea was the following: As we saw essentially no dependence of the MCT-critical exponent γ on D , we expected that the time dependence of the dynamical functions should be similar for film and bulk, when compared for the same distance from the corresponding critical temperature, i.e. for the same $T - T_c(D)$. We checked this property by plotting for $T - T_c(D) = 0.07$ the mean square displacements of of a film of thickness $D = 10$ and that of the bulk [see the right panel in Fig. 8.8]. As the result of this comparison was rather confirmative, we repeat the same test comparing $g_{3,\parallel}$ of bulk and film for $T - T_c(D) = 0.03$, 0.05 and 0.07 . However, in the case of $D = 5$, the lowest simulated temperature is $T = 0.38$ which has a distance of 0.07 from the corresponding critical temperature, $T_c(D = 5) = 0.31$. Therefore for the first two values of $T - T_c(D)$ we can carry

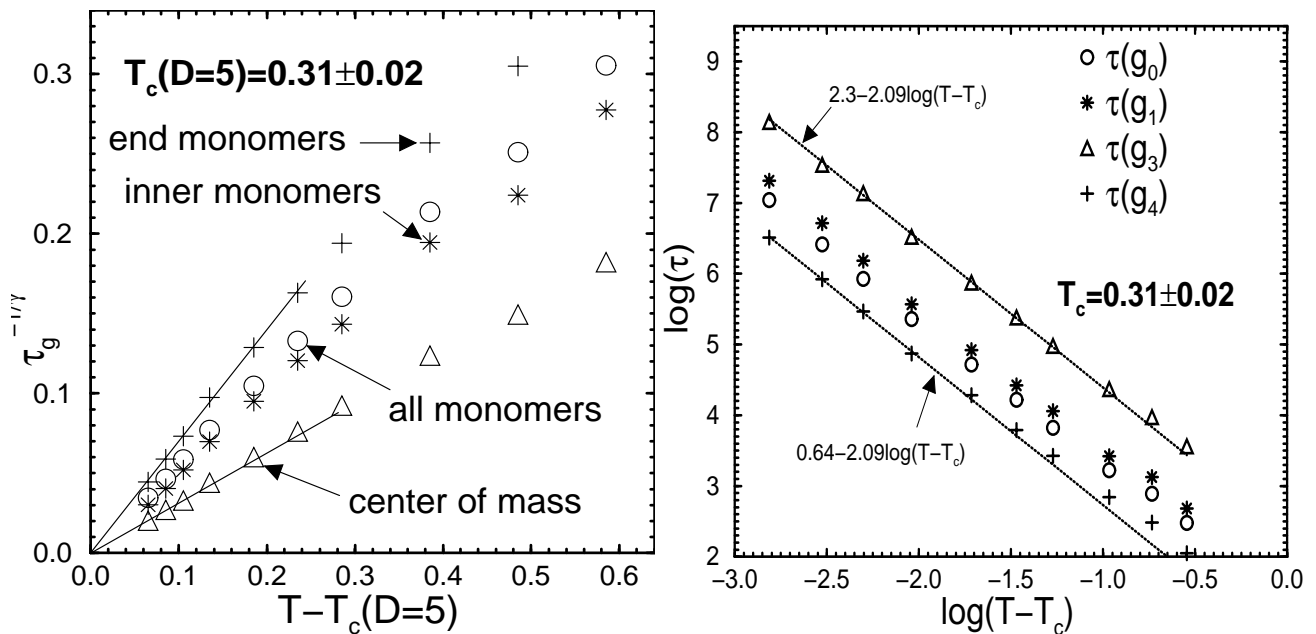


Figure 8.10: Left panel: Plot of $\tau_g^{-1/\gamma}$ versus $T - T_c(D = 5)$. The time τ_g was determined by Eq. (8.3) for the mean-square displacements of inner, end and all monomers and of the chains' center of mass. The mode-coupling exponent γ was taken from the bulk analysis ($\gamma = 2.09$ [48]). Holding $\gamma = 2.09$ fixed and fitting Eq. (8.4) to the last four data points (indicated by the solid lines) an average result of $T_c(D = 5) \simeq 0.31 \pm 0.02$ was obtained. Right panel: log-log plot of the relaxation times, τ_g , versus $T - T_c(D = 5)$. As demonstrated by dotted lines, parallel straight lines fit very well to this data.

out the comparison between the bulk system, and films of $D = 20$ and $D = 10$ only.

As seen from Fig. 8.11, the data coincide relatively well for all three temperature differences. Note that the curves are very sensitive to a temperature change. This means that the critical temperatures calculated for various film thicknesses have a certain physical relevance. Furthermore they are not inaccurate: A change of 0.02, for example, would fully destroy the agreement demonstrated in Fig. 8.11.

At the end, a remark must be made concerning the analysed quantity. It is reported that the diffusion constant at low T is sometimes well fitted both by a power law (as predicted by MCT) and by an Arrhenius law [133] and that it is sometimes not possible to decide which functional form best fits the data [134]. Therefore, it is desirable to look at a quantity which contains more detailed information on the microscopic dynamics of the system than is obtainable from the diffusion constant. The intermediate scattering function, for example, is a suitable choice and therefore is extensively investigated in the literature. In fact, we did *not* calculate $T_c(D)$ applying fits to the diffusion constant. We actually used the definition (8.3) because $2\pi/R_g$ corresponds to a wave vector slightly smaller than q_{\max} , the peak position of $S(q)$ [see Fig. 2.2]. As $2\pi/q_{\max}$ is a measure of the average cage size, it follows that R_g corresponds to a length scale slightly larger than the average size of a cage. If the mean square displacement of a particle reaches R_g^2 , it has most probably already left the neighbor cage. The definition (8.3) therefore corresponds to the idea that α -relaxation time is the time needed by a particle to leave the cage of its neighbors. Our study is thus based on one of the important ideas of the mode-coupling theory. Nevertheless, as a task for further investigations, it is still interesting to check the presented results via an extended analysis of the intermediate scattering function.

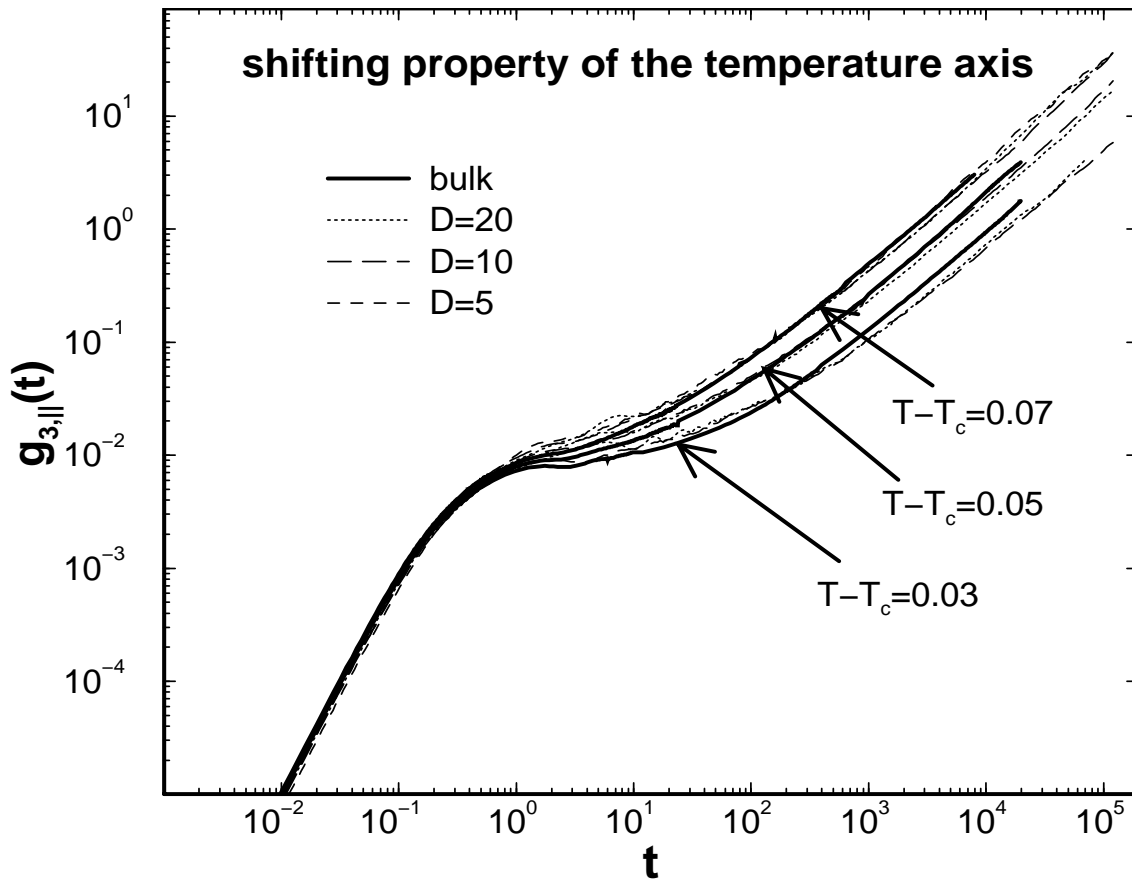


Figure 8.11: Demonstration of the shifting property of the temperature axis. For three values of the distance from the critical temperature, namely for $T - T_c(D) = 0.03, 0.05$ and 0.07 , the mean square displacements of chain centers are compared for films of thickness $D = 10, D = 20$ and bulk. In the case of $T - T_c(D) = 0.07$, also $D = 5$ is involved in the comparison. The corresponding absolute temperatures compared to each other are given below. $T - T_c(D) = 0.03$: $T = 0.48(\text{bulk}), T = 0.44(D = 20)$ and $T = 0.42(D = 10)$. $T - T_c(D) = 0.05$: $T = 0.50(\text{bulk}), T = 0.46(D = 20)$ and $T = 0.44(D = 10)$. $T - T_c(D) = 0.07$: $T = 0.52(\text{bulk}), T = 0.48(D = 20), T = 0.46(D = 10)$ and $T = 0.38(D = 5)$.

8.4 Scatter Plots

We will close the brief discussion of the system dynamics by showing some “scatter plots”. A “scatter plot” is a kind of visualization of the heterogeneity (if there is any) of the system dynamics [135]. Let us define a “scatter set” as the set of the displacement vectors $\Delta \mathbf{r}_i = \mathbf{r}_i(t) - \mathbf{r}_i(t_0)$ of all particles, i , whose position at the initial time, $\mathbf{r}_i(t_0)$, is within a certain region of space. A “scatter plot” is then obtained by simply displaying $\Delta \mathbf{r}_i$ as points in space.

For a thin film, we define “scatter sets” for two very different layers each of unit thickness: A layer in the vicinity of a wall, termed depletion layer, and a layer in the film center to which we will refer as central layer. The finite thickness of the layer introduces some averaging, which is, however, necessary to obtain a satisfactory number of particles and thus statistics. Let $S(t_0, z)$ be the set of all particles, contained in a layer at z at time t_0 . The corresponding scatter set at a later time t will be equivalent to the set of displacement vectors $\Delta \mathbf{r}_i$, where the index i runs over all particles of $S(t_0)$.

We further refine the definition of a scatter set, focusing on the motion of certain chain segments like chain ends or inner monomers. In chapter 7 we had already seen significant differences in density profiles of chain ends and inner monomers. Differences in dynamics are therefore not unexpected.

First, we look at the high temperature behavior. In Fig. 8.12 scatter plots are displayed for the end monomers (left panel) and the inner monomers (right panel). Each individual panel compares the mobility in the depletion layer (left clusters) with that in the film center (right ones). The film thickness was $D = 20$ and the temperature $T = 1$. The shortest time is beyond the end of ballistic motion in the regime where the presence of the neighbors becomes apparent. As the preferred bond length is smaller than that of the Lennard-Jones potential, a tagged particle first “recognizes” its connection to the adjacent monomer(s) of the same chain. Now, an inner monomer has two such bonds, whereas an end monomer is tied to the chain by a sole bond only. For intermediate times, end monomers are therefore more mobile compared to the inner segments of the chain. This is clearly seen both in scatterplot (Fig. 8.12) and in Fig. 8.13. For sufficiently long times, however, the diffusion is dominated by the displacement of the chain’s center of mass. The relatively small “tagging around” of various chain segments are therefore negligible. Hence, in the long time (or diffusive) limit, the difference in the mobility between inner and end monomers must disappear. This point is also nicely confirmed in Figs. 8.12 and 8.13.

The most interesting features of the scatter plots in Fig. 8.12, however, are perhaps the following two observations: First, they show the anisotropy in the motion of the *end monomers of the depletion layer*. This anisotropy is seen from the second largest cluster on the left side of the left panel which corresponds to the end monomers of the depletion layer at $t = 10^2$. The corresponding cluster of the right panel (inner monomers), however, does not exhibit such an anisotropy. This disparity is pronounced at lower temperatures [see Fig. 8.14]. Secondly, they clearly demonstrate the heterogeneity in the mobility of particles. Already for intermediate times, the dominance of the mobility of the particles within the depletion layer is obvious. To see this, we note that the size of the second largest cluster within the depletion layer (corresponding to $t = 10^2$) is comparable to the size of the cluster in the central layer at a much later time $t = 10^4$. A comparison of the cluster sizes reveals that the contribution of the central layer to the diffusion constant is less than 10% of that of the depletion layer.

Note, however, that in calculating the “scatter sets” for a layer close to a wall, we do *not* distinguish between the layer close to the left wall and that in the vicinity of the right wall. In plotting the data, however, we attribute all displacement vectors to a sole layer close to one of these walls, the left one say. The large negative z values seen in Fig. 8.12, therefore, originate from the motion of the particles close to the right wall, i.e. within the layer extending from $z = 8$ to $z = 10 = D/2$.

Now, we examine low temperatures. For this purpose, we choose the lowest simulated temperature $T = 0.44$ for $D = 20$ (recall that $T_c(D = 20) = 0.41$). At this temperature the system already exhibits some features of the glassy systems: The dynamics is slowed down by many orders of magnitude and the diffusion constant is quite small. We therefore first look at the behavior of the corresponding mean square displacements of chain centers to obtain an estimate of the appropriate time scales of the system at this temperature.

As plotted in panel (a) of Fig. 8.14 a plateau develops for $t_1 \approx 1$ after the ballistic motion. Again, for times comparable to t_1 , there is only a small difference between the mobility of the inner and end monomers. The chain ends are again faster. For later times this gap enlarges and the curves separate well, becoming almost parallel for intermediate times. However, due to the huge relaxation times at this temperature, the diffusive limit is not well established. Therefore

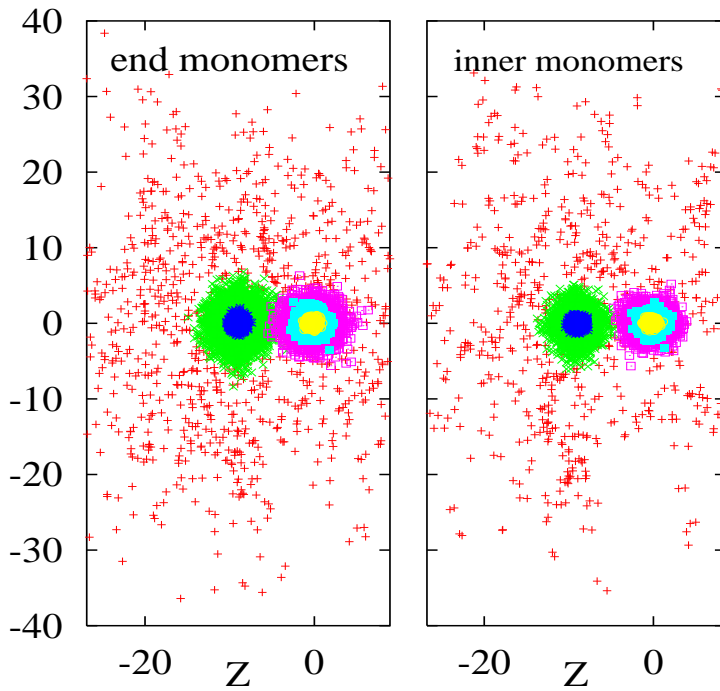


Figure 8.12: Left panel: Scatter-plot for end monomers in a film of thickness $D = 20$ at $T = 1$ ($\gg T_c(D = 20) = 0.41$). The left cluster visualizes $\Delta \mathbf{r}$ of chain ends within the layers closest to the left and right walls (whence the large negative z -values). The right one corresponds to the central layer. Each layer has a finite thickness of $\Delta z = 1$. Right panel: Same plots as in the left panel for inner monomers. In all displayed cases the innermost cluster corresponds to $t = 1$, the next cluster further outward to $t = 10^2$ and finally the outermost one contains displacement vectors at $t = 10^4$. Obviously, the mobility of particles within the depletion layers dominates the diffusion at large times.

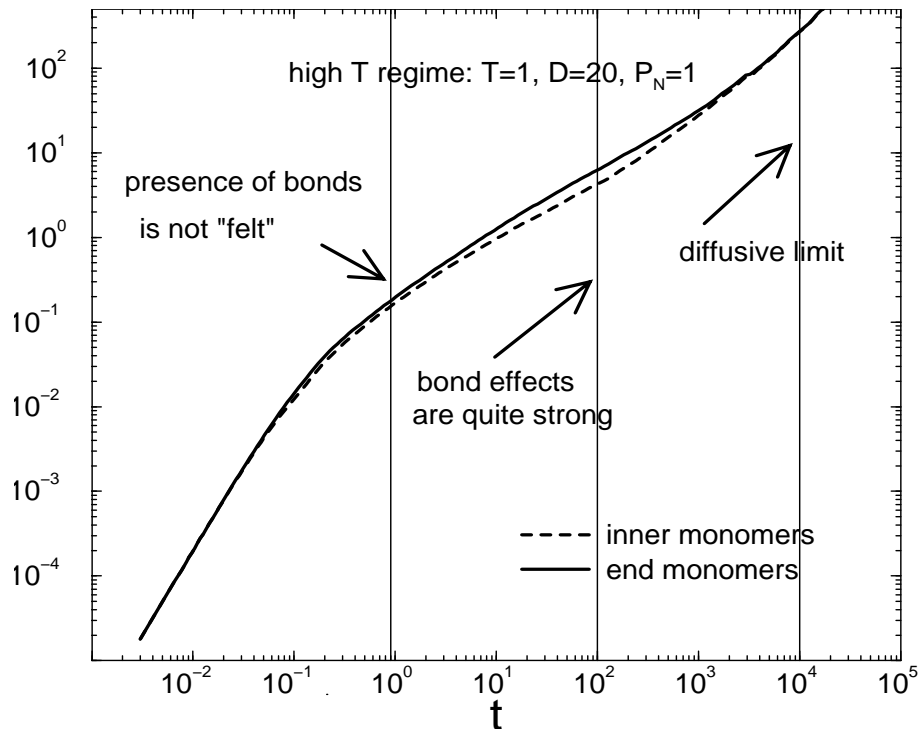


Figure 8.13: The mean square displacement of chain ends compared to that of the inner monomers. Three cuts in the time domain are considered: For short times the difference between the mobility of the inner and end monomers is small or absent at all (for $t \ll 1$). However, already for times $t \approx 1$, it is seen that the end monomers are faster. For later times, this gap enlarges and the curves separate well, becoming nearly parallel for intermediate times. In the long time (diffusive) limit, however, the main contribution to the mean square displacements comes from the motion of the chain's center of mass and the differences between the displacements of different segments vanish (note that $T_c(D = 20) \simeq 0.41$ at this pressure).

the curves do not coincide at the end of our simulation.

Examining the heterogeneity of the motion, we again observe in panels (b) and (c) of Fig. 8.14 that the main contribution to the mobility originates from the much faster particles within the layer close to the wall. This effect, however, is much more pronounced at this low temperature. The particles of the central layer seem to be still in the cage of their neighbors whereas those of the depletion layer have already left the cage. The anisotropy observed at the higher temperature of $T = 1$ has become also appreciably stronger. Although a small anisotropy can be observed also in the motion of the inner monomers, that of the chain ends is much more pronounced. Thus, we conclude that the end monomers prefer a movement parallel to the walls whereas the inner monomers do not much bother where to go.

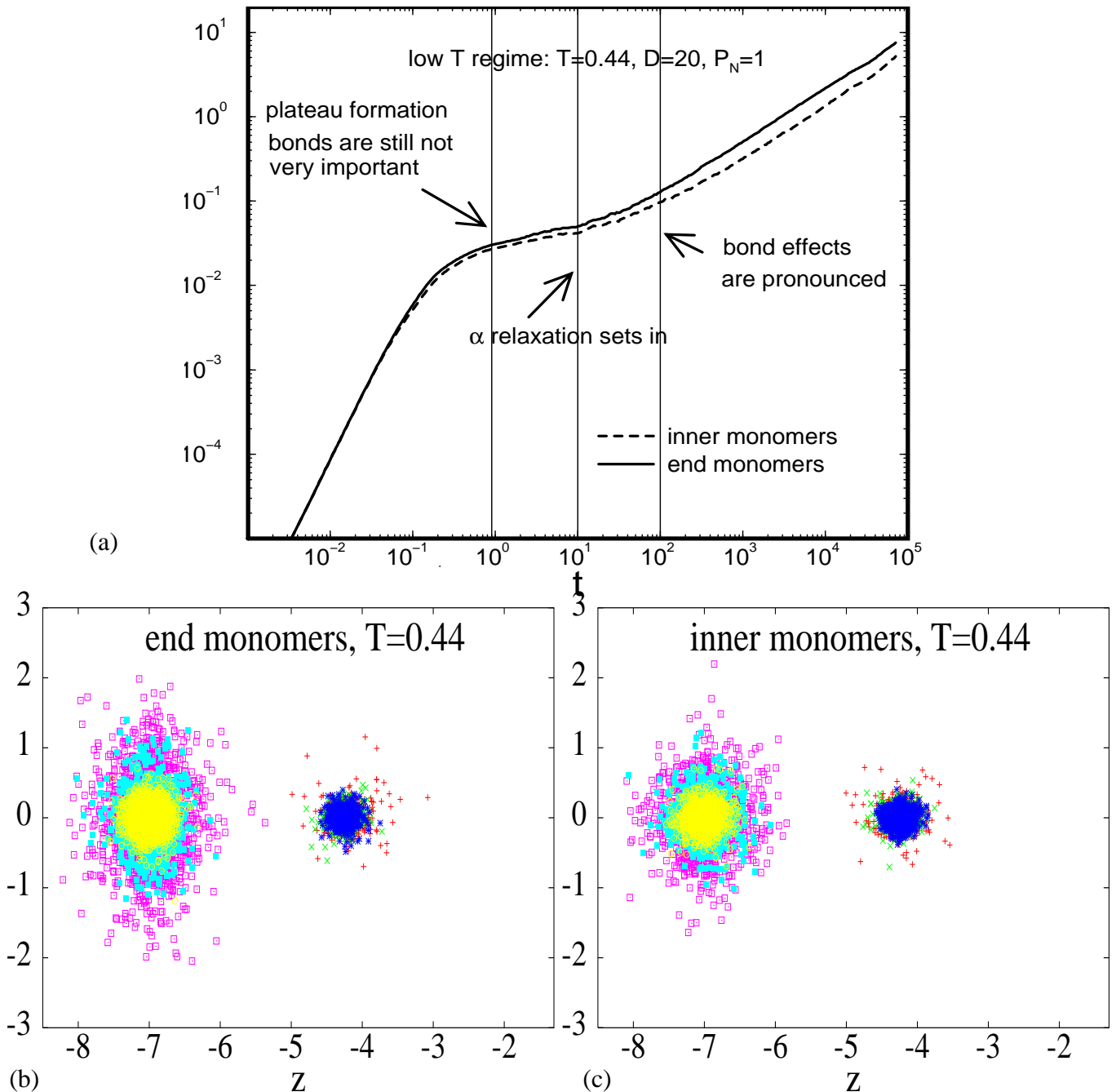


Figure 8.14: Panel (a): The mean square displacements of inner monomers compared to that of the end monomers. Three cuts in the time domain are considered: For short times (ballistic motion and the beginning of the plateau) there is only a weak difference between the mobility of the inner and end monomers. It is, however, seen that the end monomers are faster. For later times the curves separate well and become parallel. Note that even at longest simulated time, the system is far from the diffusive limit, where the curves should coincide [see Fig. 8.13]. Panel (b): Scatter plot for end monomers in a film of thickness $D = 20$ at $T = 0.44$ ($T_c(D = 20) = 0.41$). The left cluster visualizes the displacement vectors for end monomers within the layer closest to the wall (called depletion layer) and the right one that of the central layer. Each layer has a finite thickness of $\Delta z = 1$. Panel (c): The same plots as in the left panel for inner monomers. In all displayed cases the innermost clusters corresponds to $t = 1$, the next cluster further outward to $t = 10$ and finally the outermost one contains displacement vectors at $t = 10^2$. In both panels, the right and left clusters are shifted in z -direction. This serves to obtain an aspect ratio of 1 : 1 while keeping the size of the plot comparable to that of the largest cluster.

Chapter 9

System under Shear Stress

We saw in chapter 3 how the pressure tensor of an inhomogeneous system can be calculated. In particular, we obtained Eqs. (3.18) and (3.20) for the kinetic and configurational contributions, respectively, to the pressure tensor in planar systems. There, it has already been emphasized that these expressions are not restricted to systems at thermal equilibrium. Now, we are going to apply these equations to the present polymer model confined between two parallel walls in an external driving field and calculate an important transport coefficient, namely the shear viscosity.

9.1 The Pressure Tensor and the Shear Viscosity

For a fluid moving between flat parallel walls the knowledge of the off-diagonal component of the pressure tensor, $P_{xz}(z)$, on the one hand and that of the velocity profile, $u_x(z)$, on the other hand allows the calculation of the *local* viscosity [56, 57, 136]

$$\eta(z) = \lim_{F^e \rightarrow 0} -\frac{\langle P_{xz}(z) \rangle}{u'_x(z)}, \quad (9.1)$$

where $u'_x(z) = \partial u_x(z)/\partial z$ is the derivative of the velocity profile in the direction perpendicular to the walls and F^e is an external driving force (see below). As in previous chapters, $\langle \dots \rangle$ denote thermal averaging. Note that the velocity profile $u_x(z)$ is also obtained as a thermal average of one particle velocities,

$$u_x(z) \equiv \frac{\sum_{\{\text{Configurations}\}} \sum_{i=1}^N v_{x,i} \delta(z_i - z)}{\sum_{\{\text{Configurations}\}} \sum_{i=1}^N \delta(z_i - z)}. \quad (9.2)$$

It is well known that $P_{xz} = 0$ at thermal equilibrium. We thus need a mechanism to induce a non-vanishing off-diagonal pressure component. In real experiments a pressure gradient, ∇p , is often used. However, we will see that this is not the best choice for molecular dynamics simulation of a system under shear stress. Consider a fluid subject to a homogeneous field exerting the force $\mathbf{F}^e = F^e \mathbf{e}_x$ on each individual particle. The momentum conservation equation for

this system is [56, 57, 137]

$$\begin{aligned}\rho(\mathbf{r}, t) \frac{d\mathbf{u}(\mathbf{r}, t)}{dt} &= -\nabla \cdot \mathbf{P} + \rho(\mathbf{r}, t) \mathbf{F}^e \\ &= -\nabla \cdot \mathbf{\Pi} - \nabla p + \rho(\mathbf{r}, t) \mathbf{F}^e,\end{aligned}\quad (9.3)$$

where we introduced the *viscose pressure tensor* $\mathbf{\Pi} = \mathbf{P} - p\mathbf{I}_{3 \times 3}$ (p is the well-known hydrostatic pressure). Setting $\mathbf{F}^e = \mathbf{0}$ along with $\nabla p \neq 0$ in Eq. (9.3) corresponds to the case where the system is driven by a pressure gradient. On the other hand, the choice $\mathbf{F}^e \neq 0$ along with $\nabla p = \mathbf{0}$ is the situation we are going to study. The point is that the system cannot distinguish between these cases [56]. In addition to the simplicity of implementation in a MD-code, the use of an external field instead of a pressure gradient allows the system to remain longitudinally homogeneous [56]. In real experiments the fluid remains nearly incompressible under the applied pressure gradient. However, to obtain a satisfactory signal-to-noise ratio, pressure gradients used in MD simulations are considerably higher and lead to significant density variations. A combination of these density variations with periodic boundary conditions would then lead to discontinuities in the density at system boundaries, i.e. when going from the real system to one of its adjacent image systems.

9.2 Details of the Simulation

In all simulations whose results were discussed in the major part of this work, the confinement was achieved by placing two parallel walls acting on inner particles a repulsive force of z^{-9} , z being the distance of a given particle from the wall. Obviously, the inner particles can perfectly slide on the surface of these walls. Therefore, if we apply an external force acting in lateral direction, the system will simply accelerate endlessly.

However, a calculation of the shear viscosity via laminar flow requires a non-trivial velocity profile. Therefore, a certain degree of stick condition must be present at the vicinity of the walls. For this purpose, we introduced, on each side, a layer of wall atoms arranged in a triangular lattice. These atoms were bonded to their lattice sites via a harmonic potential

$$U_{\text{harm}}(\mathbf{r}_i) = \frac{1}{2} K_{\text{harm}} |\mathbf{r}_i - \mathbf{r}_{i,\text{eq}}|^2. \quad (9.4)$$

Here, the harmonic force constant, K_{harm} , is a measure of the stiffness of the spring, $\mathbf{r}_{i,\text{eq}}$ is the position of the i -th wall atom on the lattice (“equilibrium position”) and, obviously, \mathbf{r}_i stands for the actual position of the atom. The harmonic force constant was set to $K_{\text{harm}} = 100$. This value is close to 114.3 corresponding to the harmonic approximation on LJ-force in a linear chain, i.e. two times the (linear) force between two Lennard-Jones atoms at distances close to the potential minimum (the same value of 114.3 is obtained also for an fcc-lattice).

As we wanted to use the results of previous equilibrium simulations (with z^{-9} walls) as initial configuration, we placed the structured walls at a distance of $\approx 2^{1/6}$ from depletion layers (the layers closest to the walls) of a density profile corresponding to an equilibrium simulation at $T = 1$ and $D = 20$. This led to a separation of $\Delta z = 20.5$ between structured walls. To avoid strong rescaling of particle coordinates in x, y -directions, we set the lateral size to the average value computed from the lateral sizes of 10 independent initial configurations. So, $L_x = L_y \equiv L_S = 11.11$. The number of particles was $N = 2000$.

Note that all simulations reported in this chapter have been carried out at *constant volume*. However, after some simulations have been carried out, we had to decrease the lateral size to

avoid phase separation at low temperatures. Therefore, the results discussed here correspond to two different lateral system sizes, namely to $L_S = 11.11$ and to $L_S = 10.05$. At $T = 1$, the larger system size leads to a density at film center of $\rho(z = 0, L_S = 11.11) = 0.795$ whereas $\rho(z = 0, L_S = 10.05) = 0.99$. The latter remained unchanged also at all lower simulated temperatures.

In addition to the structured walls, we reintroduced the z^{-9} walls as a background at $z_{\text{botwall}} = -11.544$ and $z_{\text{topwall}} = 11.544$ [see Fig. 9.1]. This serves to prevent possible penetration of the structured walls by inner atoms. Such an additional wall potential has also been used by Jabbarzadeh, Atkinson and Tanner in MD studies of the wall slip in thin films of hexadecane [138]. Adopting the terminology of Jabbarzadeh *et al.* we call these walls “barrier walls”. Note, however, that the barrier walls used in [138] have a different functional dependence ($\propto z^{-10}$ compared to z^{-9} in our case) and act on the inner atoms only. The walls used in the present work, however, form an impenetrable background for *all* particles, i.e. for both inner and wall atoms.

For the interaction between the inner atoms from the one side and the wall particles from the other side we chose the truncated shifted Lennard-Jones potential from chapter 2 [see Eq. (2.1)], where we set $\sigma_{wi} = 1$ and $\epsilon_{wi} = 1$. Here, the index ‘w’ stands for a “wall atom” and ‘i’ for “inner atom”. The same potential was also used for the wall-wall interaction, again with $\sigma_{ww} = 1$ and $\epsilon_{ww} = 1$.

With this choice of interaction parameters we first carried out simulations at $T = 1$. As

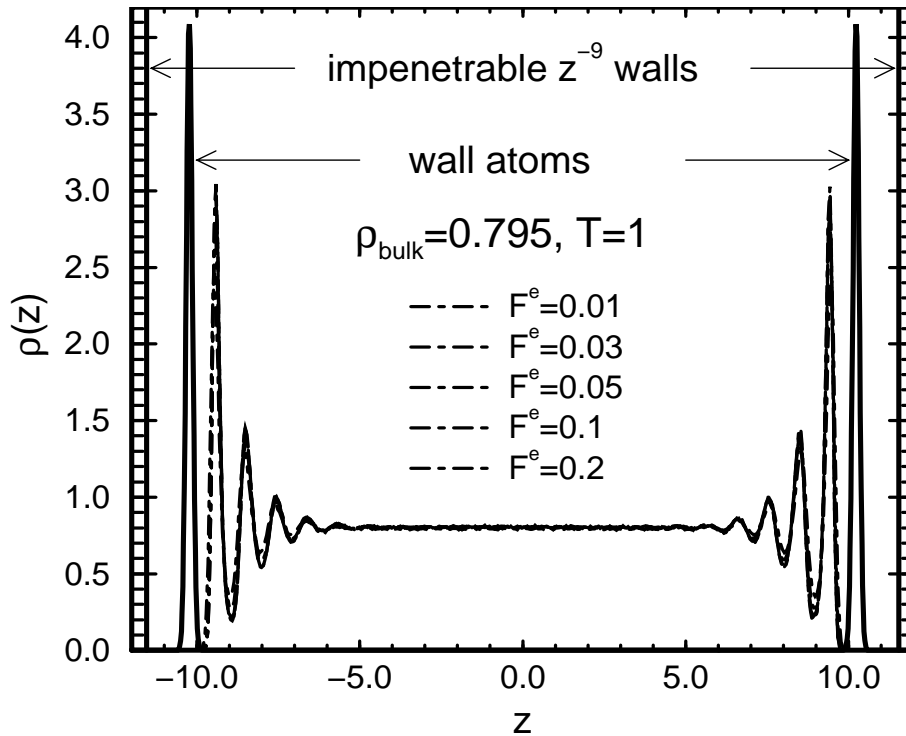


Figure 9.1: Density profile of inner and wall particles as obtained from MD-simulation for various values of the driving force, F^e . The positions of impenetrable backgrounds realized by z^{-9} walls are also indicated in the figure. Note that for $z \in [-5, 5]$ the system is homogeneous at all values of F^e . Results correspond to $\sigma_{ww} = \sigma_{ii} = 1$, $\epsilon_{ww} = \epsilon_{ii} = 1$, $\sigma_{wi} = 1/\sqrt{2} \approx 0.891$ and $\epsilon_{wi} = 2$.

demonstrated in Fig. 9.2, there is a large jump in the velocity profile very close to the walls. This indicates that the inner particles do not very well stick to the walls, but partially slide on them. However, it was mentioned in section 8.2 that hydrodynamic treatments of the flow usually assume a stick boundary condition. In particular, the use of this assumption in combination with continuum hydrodynamics leads to the following simple formula for the velocity profile $u_x(z)$ of the laminar flow of a fluid confined between parallel planar walls [56, 93]:

$$u_x(z) = -\frac{\rho_{\text{bulk}} F^e}{2\eta_{\text{bulk}}} \left(z^2 - \frac{D^2}{4} \right). \quad (9.5)$$

Here, ρ_{bulk} is the bulk density of the system, F^e the driving force per particle, η_{bulk} stands for the bulk viscosity and D is the wall-to-wall separation.

As we were interested in a calculation of η_{bulk} , we improved the stick boundary condition by favoring the inner-wall interaction compared to that between particles of the same type. This was achieved by setting $\sigma_{\text{wi}} = 1/\sqrt{2} \approx 0.891$ and $\epsilon_{\text{wi}} = 2$. Note that the inner-wall interactions are favored in two ways: First, as $\sigma_{\text{wi}} < \sigma_{\text{ww}} = \sigma_{\text{ii}}$, an inner atom can come closer to a wall atom than it is the case for two particles of the same type. Secondly, the energy cost to separate a wall atom from an inner atom is two times larger than the price one must pay to separate two particles of the same type. This explains why the inner atoms now better “stick” to the walls compared to the case where all parameters were set to 1 [see Fig. 9.2]. Therefore, unless otherwise stated, all simulations whose results are discussed here have been carried out with $\sigma_{\text{ww}} = \sigma_{\text{ii}} = 1$, $\epsilon_{\text{ww}} = \epsilon_{\text{ii}} = 1$, $\sigma_{\text{wi}} = 1/\sqrt{2} \approx 0.891$ and finally $\epsilon_{\text{wi}} = 2$.

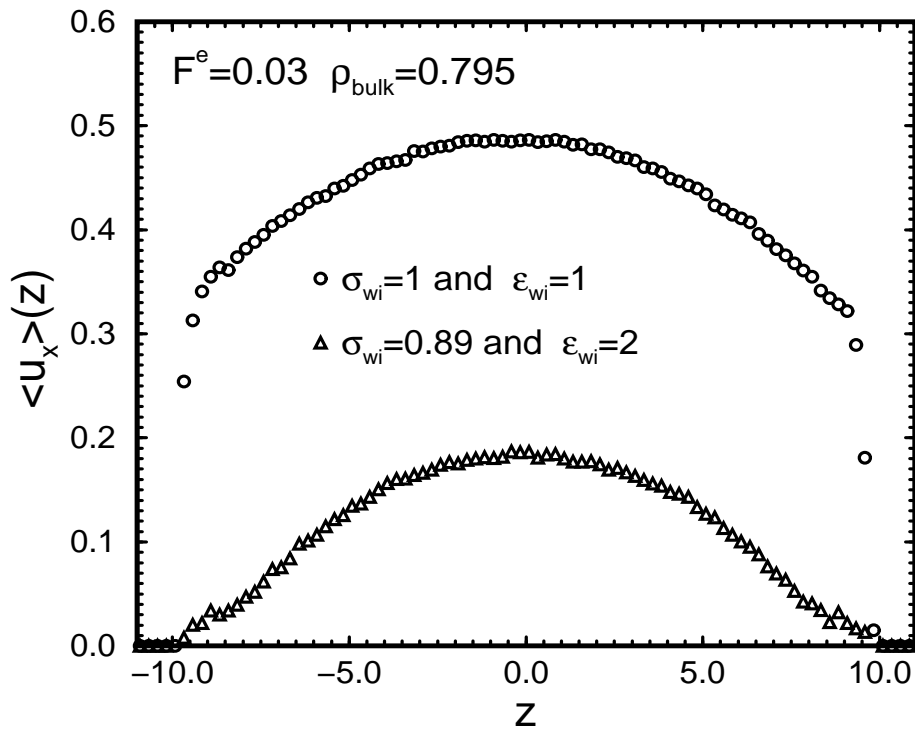


Figure 9.2: Velocity profile as obtained from MD-simulations for two choices of the parameters of wall-inner interactions.

9.3 Thermostating the System Through the Walls

We first show in Fig. 9.1 that the system's structure does not change much when varying the external driving force. This is an important precondition to check that we are not too far from the limit $F^e \rightarrow 0$. However, a satisfactory verification of this property requires the explicit check whether or not the quantity of interest, the bulk viscosity η_{bulk} for example, is independent of F^e . To verify this important point, we carried out simulations while varying F^e . For each value of F^e , the number of independent runs was 10 and the duration of each run was 10^6 MD steps. η_{bulk} was then computed using quadratic fits to the corresponding (average) velocity profiles [see Eq. (9.5)]. Note that to obtain a better estimate of the *bulk* viscosity, i.e. to suppress the contribution of the walls to this quantity, the fit range was restricted to $z \in [-5, 5]$ in all cases.

The velocity profiles (averaged over 10 independent runs) and the corresponding fits using Eq. (9.5) are shown in Fig. 9.3. As expected, deviations from a parabola increase with F^e . However, for the chosen fit range, a quadratic function is still a good approximation even at the highest applied force.

Results for η_{bulk} are depicted in Fig. 9.4. First, as expected, at small F^e , η_{bulk} is practically independent of the driving force. However, at larger values of F^e , significant change in η_{bulk} is observed. Recall that the system density is rather insensitive to F^e for all investigated cases [see Fig. 9.1]. In particular, the density remains homogeneous in the range where we fit the velocity profiles. Therefore, at least for the film center, we do not expect a significant change in the system properties, provided that the temperature is the same for all values of F^e (as it should be).

Indeed, as shown in Fig. 9.4, a check of the system temperature reveals that T strongly changes at higher shear stress. The larger F^e , the larger is the temperature. The rapid decrease of the bulk viscosity is therefore a consequence of increasing temperature.

It is easy to see where the mentioned heating comes from. The driving force accelerates the inner particles. If the walls were not present or if they had no structure (as in the case of z^{-9} walls) this acceleration would lead to a continuous increase of the system velocity. However, for particles in contact with wall atoms, an important amount of this kinetic energy is transferred into thermal motion. As a consequence, the streaming velocity of a layer in the very vicinity of the walls is decreased compared to that of a neighboring layer in the inner side. The particles of the slower layer now hinder their faster neighbors and, again, a part of lateral motion is transferred into heat. Hence, a velocity profile accompanied by heat creation develops.

Obviously, to keep the system temperature constant, the extra heat must be removed in some way. At this place, it is interesting to note that, historically, the introduction of some of the common thermostating algorithms was motivated by the need to remove the extra heat created within a non-equilibrium simulation. An example is the so called Gaussian isokinetic thermostat, developed by Hoover [139] and, independently, by Evans [140]. Well, it is time to look at the way the system is thermostated. In fact, no thermostating was applied for inner particles. They were thus propagated within the NVE -ensemble, i.e. integrating the Newtonian motion equations (4.1). The wall particles, however, were coupled to a heat bath using the Nosé-Hoover algorithm [see Eqs (4.36)-(4.39)].

This approach is similar to (and was in fact motivated by) that described in [56]. Both in [56] and in the present case, the inner part of the system was thermostated indirectly, i.e. via interactions with wall atoms the temperature of which was controlled by some thermostating algorithm. This is an attractive way as it does not require the knowledge of the velocity profile, which should be taken into account if the moving fluid was to be directly coupled to a heat bath. Furthermore, one has not to deal with possible influence on the system properties of some

additional degrees of freedom which are typical of thermostating algorithms [see chapter 4]. The latter point, however, is less important because, as demonstrated in chapter 6, both for static and for dynamic properties, a NVT -simulation using Nosé-Hoover thermostat leads to results in agreement with those obtained from microcanonical-ensemble simulations.

However, the drawback of this approach is that heat conduction towards the walls is the only mechanism to regulate the temperature of the inner part of the system. A heat current, on the other hand, is driven by a temperature gradient. So, for moderate heat conductivities, or for large rates of heat creation, the temperature of the fluid will significantly differ from that of the walls.

Next, we give an estimate of the increase of the system temperature. Consider a plane at $z > 0$. As the inner part of the system is not thermostated, it follows that all the heat created between this plane and the film center must pass through this plane towards the wall at $z = D/2$ if the steady state is reached. This heat current is, of course, driven by a temperature gradient at this plane. To first order, we can write

$$\begin{aligned} \frac{\partial T(z)}{\partial z} &= -\frac{1}{A\lambda(z)} \int_0^z d\dot{Q}(z') \\ &= -\frac{F^e}{\lambda(z)} \int_0^z u_x(z')\rho(z')dz' . \end{aligned} \quad (9.6)$$

for a plane at $0 < z < D/2$. Here, A is the surface area of a wall (to which the heat current is perpendicular), $d\dot{Q}(z') = F^e A u_x(z')\rho(z')dz'$ is the amount of heat created per unit time within the region $[z' \ z' + dz']$ and $\lambda(z)$ is the heat conductivity at z .

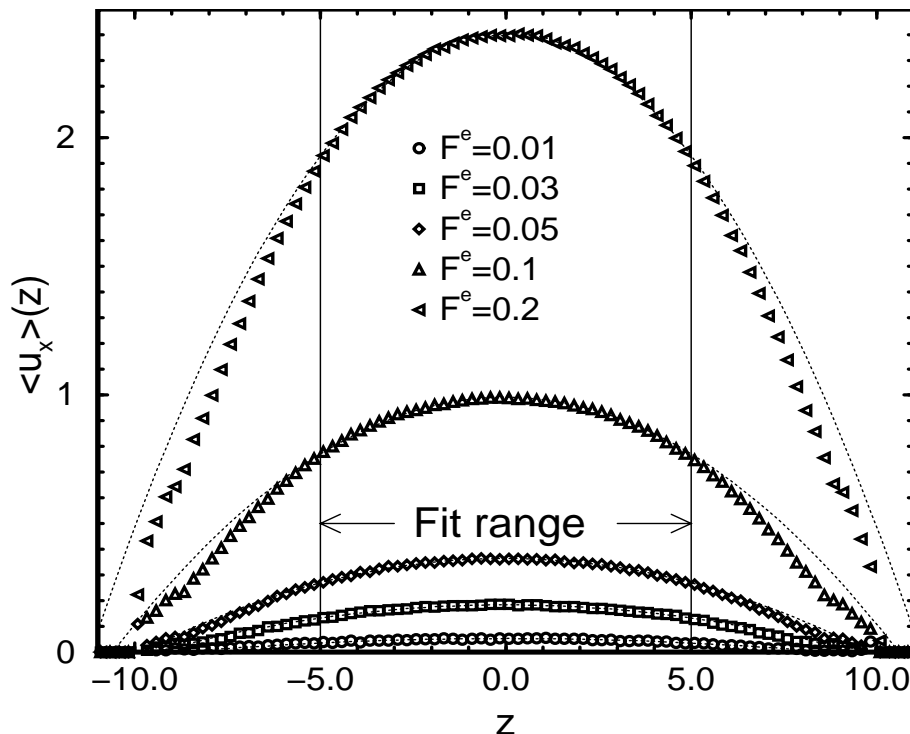


Figure 9.3: Profiles of the streaming velocity, $u_x(z)$, for various values of the driving force and the corresponding fits à la Eq. (9.5). As indicated in the panel, only values with $z \in [-5, 5]$ are taken into account during the fit. This reduces the effects of the walls and thus leads to a better estimate of the *bulk* viscosity, η_{bulk} .

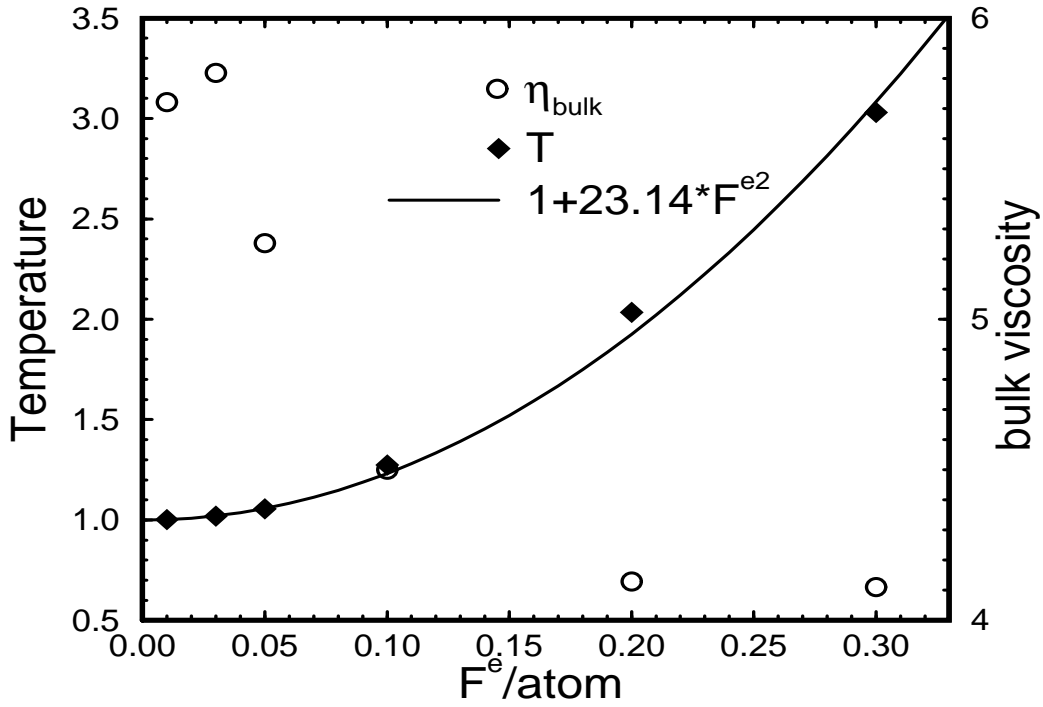


Figure 9.4: Resulting Temperature of the inner part of the system during NVE simulation versus the driving force per atom (diamonds). The solid line represents a best fit using Eq. (9.7), where $\eta_{\text{bulk}}\lambda$ was taken as a fit parameter. The open circles show the bulk viscosity obtained from fits on the streaming velocity profile, $u_x(z)$, à la Eq. (9.5).

Let us assume that the system can be approximated by a homogeneous continuum fluid. This might seem to be a crude approximation. However, for non-local properties (i.e. for properties defined as averages over the whole system like the average temperature) such an approximation may be justified by saying that the inhomogeneous part of the system is relatively thin compared to the wide homogeneous region around the film center. With this assumption we can insert the rhs of Eq. (9.5) in Eq. (9.6) and obtain the temperature gradient at the wall,

$$\left. \frac{\partial T(z)}{\partial z} \right|_{z=D/2} = -\frac{\rho_{\text{bulk}}^2 D^3}{12\eta_{\text{bulk}}\lambda(z=D/2)} F^{e2}. \quad (9.7)$$

In general, system properties and thus λ and η_{bulk} change with a variation of the driving force. However, it is demonstrated in Fig. 9.4 that η_{bulk} changes rather slowly with F^e . The driving force per atom varies by a factor of 30, whereas the relative variations of η_{bulk} are less than 50%. So, to first order, the F^e -dependence of η_{bulk} can be ignored in Eq. (9.7). Assuming a similar behavior for the F^e -dependence of λ , we examine the quadratic dependence of $\lambda(z=D/2)\left.\frac{\partial T}{\partial z}\right|_{z=D/2} \approx 2\bar{\lambda}(T_{\text{walls}} - T_{\text{inner}})/D$ from the driving force F^e by setting

$$T_{\text{inner}} = T_{\text{walls}} + aF^{e2}, \quad (9.8)$$

where a is the fit parameter. This leads to

$$\frac{\rho_{\text{bulk}}^2 D^4}{24\lambda\eta_{\text{bulk}}} = a = 23.14 \pm 0.5789, \quad (9.9)$$

where $\bar{\lambda}$ is the average heat conductivity.

It can also be seen from Fig. 9.4 that, in the observed temperature range, η_{bulk} does not change much with temperature. The temperature varies by a factor of 3 whereas the relative variations of η_{bulk} is less than 50%. Thus, we set the average value of $\bar{\eta}_{\text{bulk}} \approx 5$ in Eq. (9.9) along with $\rho_{\text{bulk}} = 0.795$ and $D = 20$ and obtain a (rather crude) estimate of the system's heat conductivity

$$\bar{\lambda}(T = 1; \rho_{\text{bulk}} = 0.795) \approx 36.8 . \quad (9.10)$$

The huge temperature changes demonstrated in Fig. 9.4 may hide, to some extent, the variation of T at smaller F^e . Therefore, we note that a temperature change of 2% was observed at a relative small driving force of $F^e = 0.03$. Note that, using the Nosé-Hoover algorithm, we have usually been able to set the average system temperature within a relative error of 0.1% during a single run. Averaging over many runs yields still better results. Thus, a change of 2% in T is far outside the typical statistical uncertainty.

Now, we are in fact interested in system properties at low temperatures, where a strong T -dependence in system properties is expected. From our previous equilibrium simulations [see chapter 8, for example] we know that, at low T , a temperature change of 1% can have a dramatic impact on the system properties. We therefore need a better control of the system temperature than provided by just thermostating the walls.

Finally, we show in panel (a) of Fig. 9.5 temperature profiles obtained within this part of the simulation. As seen from this figure, the higher the applied force, the faster the temperature rises, i.e. the larger is $\partial T/\partial z$. This is intuitively clear because the rate of heat creation increases with F^e . It is also seen from this figure that, for a given value of F^e , the temperature gradient is quite small in the film center increasing towards the walls. Recall that the temperature gradient at z is proportional to the amount of heat created per time unit between the film center and a plane at z [see Eq. (9.6)]. Assuming that the increase in heat conductivity with temperature is not fast enough to compensate the growth of the heat current with distance from the film center, one can conclude that the temperature gradient should indeed increase with z , i.e. when approaching the walls.

Note that in Eq. (9.6) the heat conductivity appears *outside* the integral. Therefore, the knowledge of the temperature profile, $T(z)$, density profile, $\rho(z)$, and that of the velocity profile, $u_x(z)$, allows a calculation of the heat conductivity profile

$$\lambda(z) = -F^e \left(\frac{\partial T(z)}{\partial z} \right)^{-1} \int_0^z u_x(z') \rho(z') dz' . \quad (9.11)$$

It must be emphasized that Eq. (9.11) provides a way of calculating the heat conductivity not at a single temperature, but over a *temperature range*. This comes from the fact that, as the inner part of the system is thermostated through interaction with the walls only, the temperature is necessarily a decreasing function of z . For, otherwise, an heat current towards the film center would exist. Panel (a) of Fig. 9.5 provides some examples of temperature profiles where one can also observe this decreasing property. Therefore, $T(z)$ can be inverted to yield $\lambda(T) \equiv \lambda(z(T))$.

Note, however, that the temperature gradient is quite small close to the film center. In fact, due to symmetry, it must vanish at $z = 0$. As the inverse temperature gradient enters the calculation of the heat conductivity, it follows that a small error in T will lead to a large uncertainty in $\lambda(z)$. Therefore, the application of Eq. (9.11) requires a much more accurate determination of the temperature profile than is usually achieved in a typical MD simulation.

As an example we show in panel (b) of Fig. 9.5 results on the heat conductivity $\lambda(T)$ computed using the data corresponding to $F^e = 0.3$. Note that we have chosen quite a large value

of the driving force to create an appreciable temperature difference between the (thermostated) walls and the film center so that the computed $\lambda(z)$ covers a sufficiently large temperature range. The data was first smoothed (by a sort of spline interpolation known as “spline under tension”) before differentiating numerically. The derivative obtained from the smoothed curve is also shown in this panel. Note that the sharp rise of heat conductivity at high T is an artefact of large relative errors in calculating the derivative of T with respect to z . We have also tried to fit $T(z)$ by symmetric polynomials of 6-th or 8-th order and then use the corresponding coefficients to compute the derivative. The relative errors in fit coefficients, however, were larger than 100% indicating again that an accurate calculation of $\partial T/\partial z$ does require a still more precise determination of the temperature profile. Nevertheless, our numerical result is, at least, in qualitative agreement with the general observation that the heat conductivity is an increasing function of the temperature in amorphous, glassy systems (see for example page 788 of [93]).

9.4 Thermostating a Flow via Nosé-Hoover

The considerations of section 9.3 make clear that a certain amount of heating will always occur if the inner part of the system is to be thermostated indirectly through the heat transport towards the (thermostated) walls. A zero temperature gradient between the inner part (which acts as a heat source) and the walls (which play the role of a heat absorbing medium) requires an infinitely large heat conductivity.

The study of the temperature dependence of the viscosity, however, is one of the major goals of the present non-equilibrium simulations. It is therefore desirable to have a safe control of the system temperature. The simplest way, of course, would be to apply the same thermostating algorithm, i.e. the Nosé-Hoover Eqs (4.36)-(4.39), not only to the wall atoms, but also to the polymer chains. Recalling the definition of the temperature in a flow, $T \equiv m\langle(\mathbf{v} - \langle\mathbf{v}\rangle)^2\rangle/3k_B$, we see that a direct thermostating of the inner part of the system requires the knowledge of the velocity profile $u_x(z) \equiv \langle v_x \rangle(z)$ (note that $\langle v_y \rangle = \langle v_z \rangle = 0$).

This problem was solved in a simple way. For each run, the corresponding velocity profile was calculated as statistical average of particle velocities during the preceding equilibration period. Note that, in general, the equilibration is a necessary part of a MD simulation. So, we do not spend extra computation power to compute $u_x(z)$ (compared to the computation of forces, the time needed for averaging over velocities is negligible in a MD-run). The equilibration itself starts with $u_x(z) \equiv 0$ and improves this initial “guess” by sampling velocities. That this procedure does indeed lead to a reliable information on the velocity profile is demonstrated in Fig. 9.2. As shown in this figure, the velocity profile computed within the equilibration period (which starts with a vanishing velocity profile) is of comparable accuracy as the profile obtained during the subsequent production.

Combined with the above approach for the calculation of the velocity profile, we applied the Nosé-Hoover thermostat for the propagation of both the inner and the wall atoms. Simulations at various values of the driving force F^e showed that, even at the largest applied force, i.e. $F^e = 0.3$, the average system temperature could be set, to a high accuracy, to the given value of T_{ext} . Therefore, all subsequent simulations, have been carried out using Nosé-Hoover thermostat both for the wall and for the inner particles.

The reader may have noticed that, contrary to the data presented so far, Fig. 9.2 shows results obtained at a higher bulk density of $\rho_{\text{bulk}} \equiv \rho(z=0) = 0.99$ and not at $\rho_{\text{bulk}} = 0.795$. In fact, all simulations whose results we are going to discuss in the next section have been carried out at this density. The reason for the choice of a higher density was that, at $T < 0.9$, anomalous

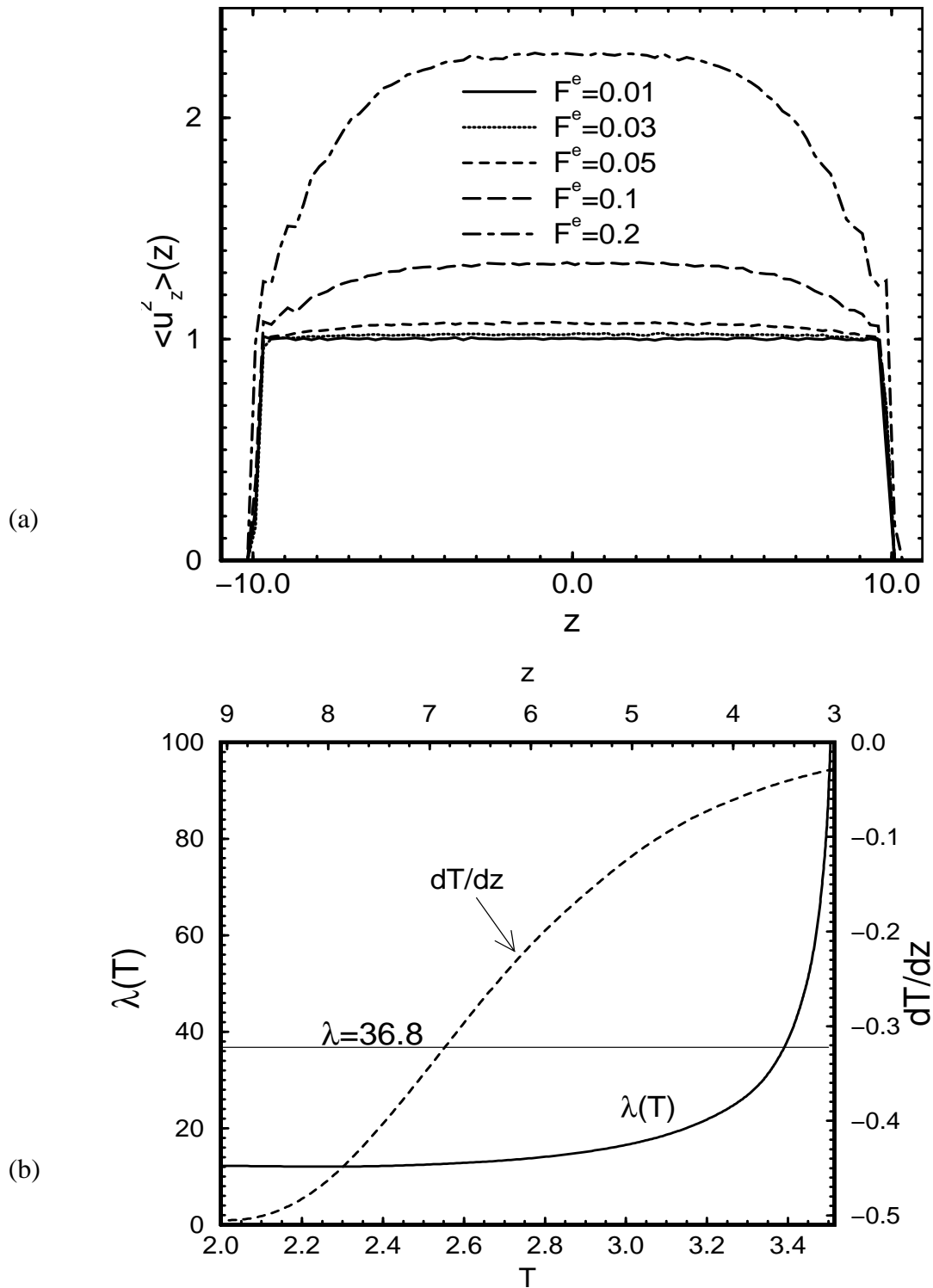


Figure 9.5: Panel (a): Temperature profiles resulting from *NVE* simulation for various values of F^e . The region of nearly constant $T(z)$ in the film center can be ascribed to the fact that the amount of the heat to be transmitted through a plane at the film center is zero and grows when approaching the walls. This implies that ∇T must be larger close to the walls provided that $\lambda(z)$ is constant or does not increase faster than heat current, $\dot{Q}(z)/A$, with distance from the film center. Panel (b): Heat conductivity as computed using Eq. (9.11). The corresponding temperature gradient is also shown in this panel. An increase with temperature is clearly observed from this results. However, the strong increase in λ at higher temperatures is probably an artefact of large errors in computing $\partial T / \partial z$.

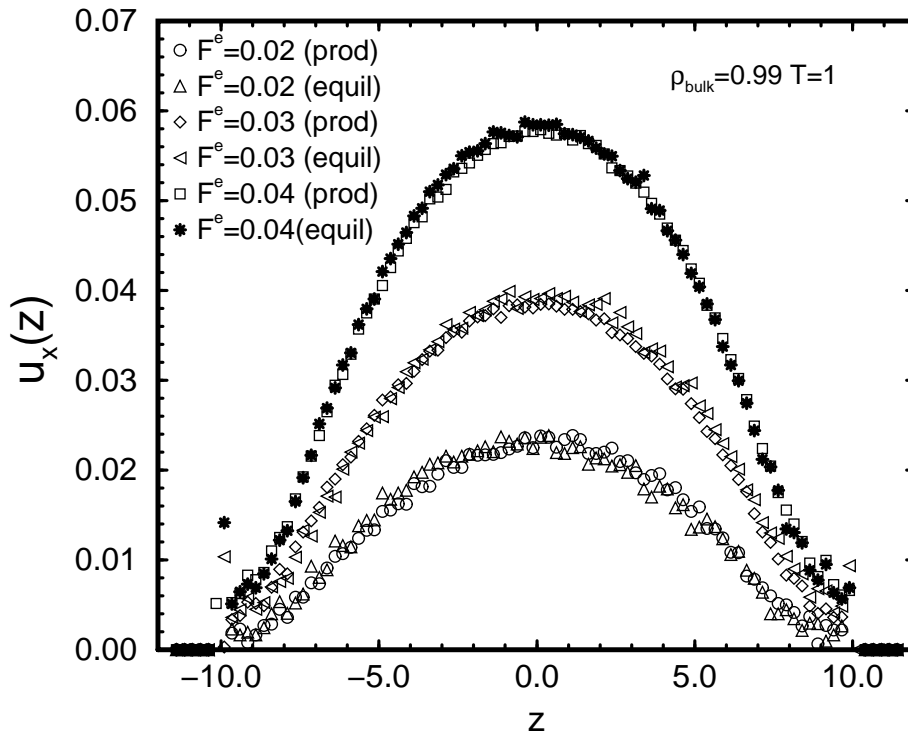


Figure 9.6: Velocity profile, $u_x(z)$, as obtained during the equilibration phase (equil) and that obtained from the subsequent production run (prod) for three values of the driving force, F^e . Within the statistical uncertainty, the accuracy of the profile obtained within the equilibration run, is comparable to that of the production period. The former was therefore used as an initial guess of $u_x(z)$ in calculating the temperature via $k_B T \equiv m_i \langle (\mathbf{v}_i - \mathbf{u})^2 \rangle / 3$, where i denotes a tagged particle and $u_y = u_z = 0$.

behavior was observed in system properties. In particular, the density profile was no longer symmetric.

This situation is depicted in Fig. 9.7 for $T = 0.8$. As shown in this figure, from 10 independent runs, in 4 cases a sort of “drying” occurs at the left wall and in the remaining 6 ones at the right wall. Due to the increase of the bulk density at lower temperatures, the system tries to contract. However, a volume change is not feasible in a NVT -ensemble simulation. The higher density in the film center (which exhibits bulk-like properties) is therefore achieved by particle transport from the walls towards the inner part. Obviously, such a transport does in general not set in simultaneously at both walls. Therefore, the asymmetry first develops at one of the walls. Suppose that a particle current towards the film center first sets in at the left wall. As a consequence, the system density close to this wall decreases and, at the same time, increases in the remaining part of the film approaching the value consistent with the actual temperature. Thus, the new particle distribution is stable from a thermodynamic point of view and the asymmetry will not vanish at later times.

Formation of the regions of very low density as a result of cooling down the system at constant volume has also been observed in MD-simulations of the present model in bulk [91]. Such a situation would of course not occur in a simulation at *constant pressure*.

However, due to the presence of the structured walls, we could not use the same program code that has been developed for (equilibrium) simulations of a system confined between z^{-9}

walls to regulate the normal pressure in the present situation. As we wanted to focus our attention on the new aspects of a non-equilibrium simulation, we postponed the generation of a NpT -program code to further studies. The observed problem of the phase separation near the walls has been simply solved by choosing a higher bulk density [see section 9.5].

Note that the observation of the mentioned phase separation was greatly simplified by an analysis of the density profiles computed during each independent run. An averaging over these runs, for example, would have led to a symmetric profile and thus would have, at least by part, hidden the effect. This demonstrates one of the advantages of what is usually called “on the fly analysis” or, simply, online analysis. Monitoring system properties during the simulation yields direct information about what is going on in the system. An information which would probably be washed out in the case of averaging over independent runs.

Recall also, that in a usual MD simulation of glassy systems the system configuration is sampled in regular distances and is saved on the disk. This results from the fact that such simulations are very time consuming and, therefore, not so easy to repeat. However, due to finite disk space, the number of samples which can be saved are moderate. Therefore, an online analysis does usually yield much better statistics.

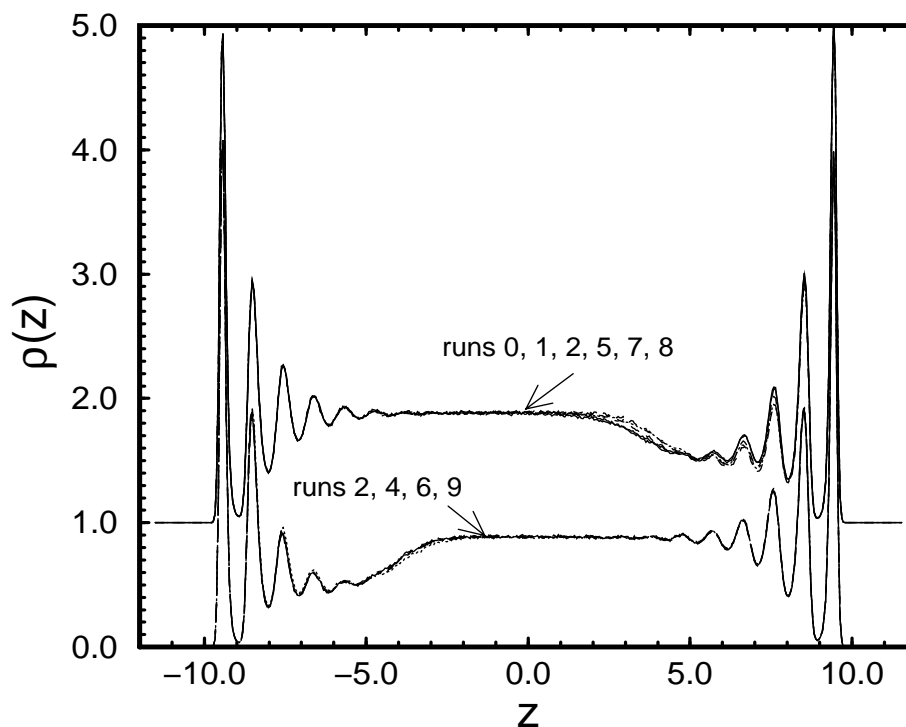


Figure 9.7: Density profiles for 10 independent runs at $T = 0.8$ for a bulk density of $\rho_{\text{bulk}} = 0.795$. As the volume is kept constant, the system separates into two phases at this low temperature. A low density region close to one of the walls and a high density one in the other part of the film.

9.5 Bulk Viscosity

We saw that a density of $\rho_{\text{bulk}} \equiv \rho(z=0) = 0.795$ at the film center leads to phase separation at lower temperatures. A region of low density develops close to one of the walls, whereas ρ increases in the remaining part of the system. We therefore reduced the lateral system size from $L_S = 11.11$ to $L_S = 10.05$ which led to $\rho_{\text{bulk}} = 0.99$. It is shown in panel (a) of Fig. 9.8 that the problem of phase separation is indeed avoided at this density. Furthermore, we observe that the bulk viscosity does not depend much on temperature. The system thus approaches the limit of an incompressible liquid. Compared to the previous lower density case [see Fig. 9.1], the presence of the walls is now “felt” farther inside the system. However, a look at panel (b) of the same figure reveals that, for $z \in [-5, 5]$, a quadratic function very well describes the velocity profile. Therefore, we used the coefficient of z^2 obtained from a fit of the form

$$u_x(z) = a - bz^2 \quad (9.12)$$

to compute the bulk viscosity [see (Eq. 9.5)]

$$\begin{aligned} \eta_{\text{bulk}} &= \frac{\rho_{\text{bulk}} F^e}{2b}, \\ \Delta\eta_{\text{bulk}} &= \frac{\rho_{\text{bulk}} F^e}{2b^2} \Delta b. \end{aligned} \quad (9.13)$$

In Eq. 9.13 $\Delta\eta_{\text{bulk}}$, the error in bulk viscosity, is simply estimated from that of corresponding fit coefficient. The accuracy of the fit manifested itself in small relative errors in b and thus in η_{bulk} .

Next, we plot in Fig. 9.9 the bulk viscosity at $\rho_{\text{bulk}} = 0.99$ obtained from Eq. (9.13). The temperature was varied (along an isochoric line) from 0.9 down to 0.46 at a constant driving force of $F^e = 0.05$. This value of F^e was necessary in order to obtain satisfactory signal to noise ratio not only at high but also at low temperatures.

First, we note that the change in viscosity is unexpectedly small for the investigated temperature range. From equilibrium studies of the present polymer model in bulk, we know that the relaxation times of the system increase by many orders of magnitude within this temperature interval [46, 91]. As we saw in chapter 8, similar slowing down was also observed for the confined model. The observed difference compared to the bulk was a change in the critical temperature towards lower T . This decrease of T_c , however, has been ascribed, at least by part, to the perfect slip boundary condition at smooth walls. Following the argument given in section 8.2, an *increase* of T_c should be expected when replacing the smooth walls by structured ones or, more precisely, when particles “stick” to the walls. In other words, a dramatic increase in transport coefficients like viscosity or inverse diffusion constant should be expected at still higher temperatures than was the case in equilibrium bulk simulations.

However, recall that the relaxation times not only depend on the temperature but also on *density*. Within a NpT -ensemble simulation the density increases when the temperature is lowered. In the present case, however, it is kept constant at all temperatures. Indeed, an examination of the density profiles of equilibrium simulations reveals that, at a normal pressure of $P_{\text{N,ext}} = 1$, a density of 0.99 in the film center corresponds to a relative high temperature of $T \approx 0.65$ [see Fig. 7.1].

The same argument can be formulated in a slightly different way. In [91], the bulk density of the present model at the critical temperature of $T_c = 0.45$ (corresponding to a pressure $p = 1$) has been estimated to $\rho = 1.042$. Then, in the same reference, the system has been cooled down

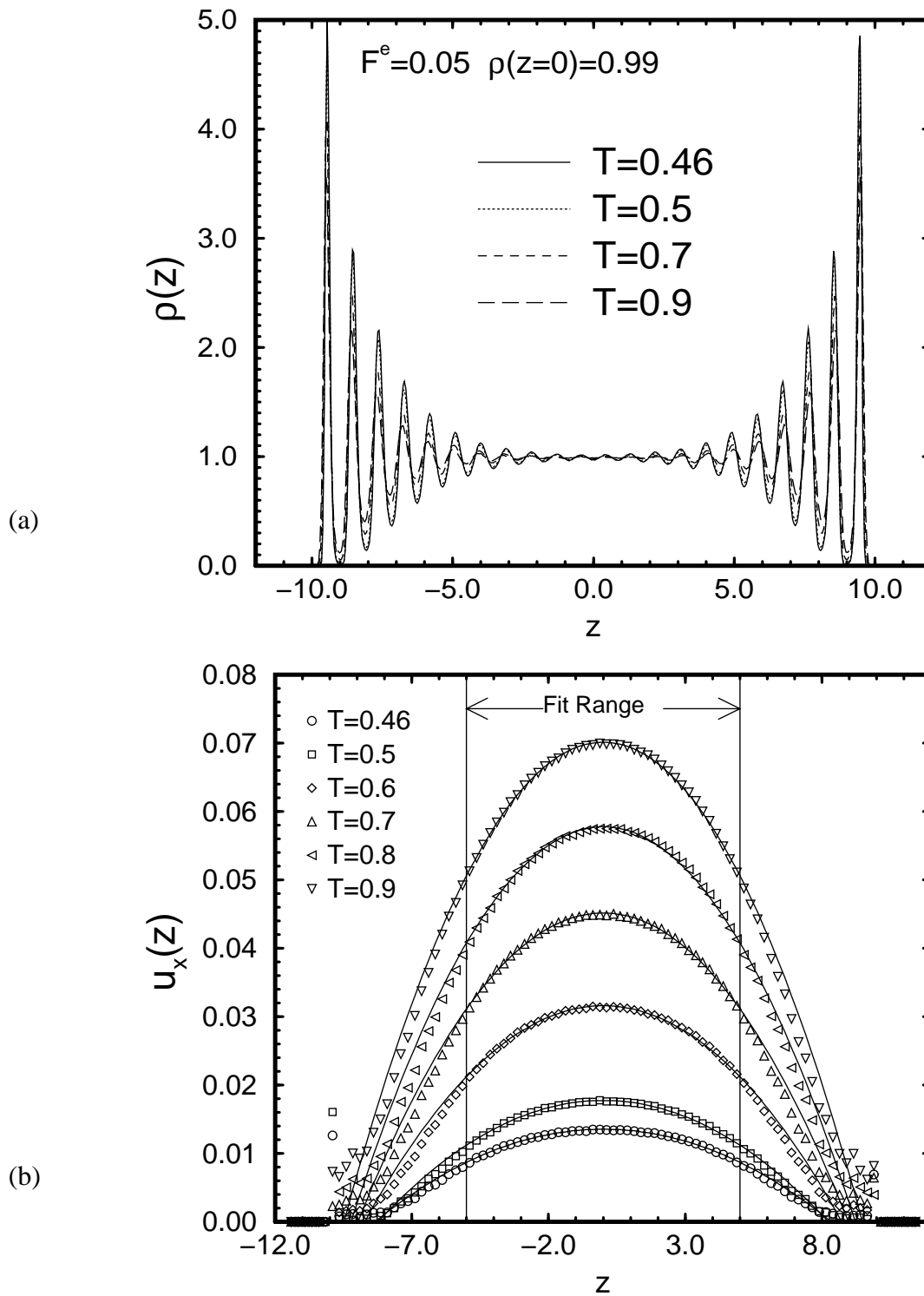


Figure 9.8: Panel (a): Density profile of inner particles as obtained from MD-simulation for various temperatures. Contrary to the case of $\rho_{\text{bulk}} = 0.795$, where a relative wide range of homogeneous region could be observed [see Fig. 9.1], now oscillations occur even in the film center. The magnitude of these density variations is, however, much smaller around $z = 0$. Panel (b): Velocity profile at various temperatures. Solid lines are results of a fit using $u_x(z) = a - bz^2$. Note that the coefficient b is directly related to the bulk viscosity, via $\eta_{\text{bulk}} = \rho_{\text{bulk}} F^e / (2b)$ [see Eq. 9.5].

towards the glass transition point along an isochoric curve at this density and, finally, the corresponding MC critical temperature has been computed to $T_c(\rho = 1.042) = 0.445$. Obviously, if cooling had been carried out at an isochoric of a higher density, critical slowing down would have set in at a higher temperature. Similarly, an isochoric of a lower density would have intersect the mode coupling critical line at a lower temperature. Therefore, to observe the sharp rise of the transport coefficients at a density of 0.99, the system should be further cooled down beyond our lowest simulated temperature of $T = 0.46$.

It is also shown in Fig. 9.9 that, in the observed temperature range, the T -dependence of the shear viscosity is *not* well described by an Arrhenius law.

Therefore, we tried to fit the data with the (empirical) Vogel-Fulcher-Tammann (VFT)-formula,

$$\eta_{\text{bulk}}(T) = \eta_{\text{bulk}}(\infty) \exp\left(\frac{B}{T - T_0}\right). \quad (9.14)$$

The result of this fit is shown in panel (a) of Fig. 9.10. As seen from this panel, the simulated temperature range seems to be close enough to the glassy region to verify an important property of *fragile* glass formers [141], namely the validity of the (VFT)-law. Fitting Eq. (9.14) to our data, we obtained for the fit parameters: $\eta_{\text{bulk}}(\infty) = 13.8 \pm 0.05$, $B = 0.592 \pm 0.036$ and $T_0 = 0.194 \pm 0.012$. As seen from panel (a) of Fig. 9.10, the “goodness” of the fit is remarkable.

Next, we discuss what is behind an Arrhenius law. Suppose that the particles of a system are effectively surrounded by more or less rigid potential barriers. In such an environment, a particle can only move around if it has enough energy to jump from one potential minimum to another one. Obviously, the probability of such a jump scales with $\exp(-E_A/T)$, where E_A is the average activation energy. This gives rise to a similar temperature dependence of transport coefficients. The observed non-Arrhenius behavior thus indicates that the picture of an effective “potential landscape” is not appropriate for the observed temperature range.

As the driving force acts in x -direction only, we were able to use the y -component of the mean square displacements to determine the diffusion constant, D . This allowed us to examine the validity of the Stokes-Einstein relation between the viscosity and the diffusion constant,

$$\frac{k_B T}{D \eta_{\text{bulk}}} = \lambda = \text{const.}, \quad (9.15)$$

where λ characterizes the length of an elementary diffusive process [142].

It is shown in panel (b) of Fig. 9.10 that λ is not a constant but decreases with the inverse temperature. A decrease of λ with T^{-1} has been also observed in MD simulations of SiO_2 [71] and in experiments on fragile glass formers below the critical temperature, T_c [143–148]. However, an accurate calculation of the diffusion constant is always a difficult problem at low temperatures. Therefore, errors in D are quite large. This, of course, leads to corresponding errors in λ . Nevertheless, the general decrease of λ with the inverse temperature cannot be explained by statistical errors, it is a physical effect. We close this section by noting that, instead of a VFT-law, $\eta_{\text{bulk}}(T)$ can be also well described by assuming a power law as predicted by MCT,

$$\eta_{\text{bulk}}(T) = c |T - T_c|^{-\gamma}, \quad (9.16)$$

where c , T_c and γ are fit parameters. A fit using Eq. (9.16) yields $c = 18.7 \pm 0.6$, $\gamma = 0.78 \pm 0.04$ and $T_c = 0.376 \pm 0.009$. The result of this fit is shown in Fig. 9.11. However, a comparison with Fig. 9.11 reveals that the VFT-formula (9.14) is in better agreement with the MD-data than the power law (9.16).

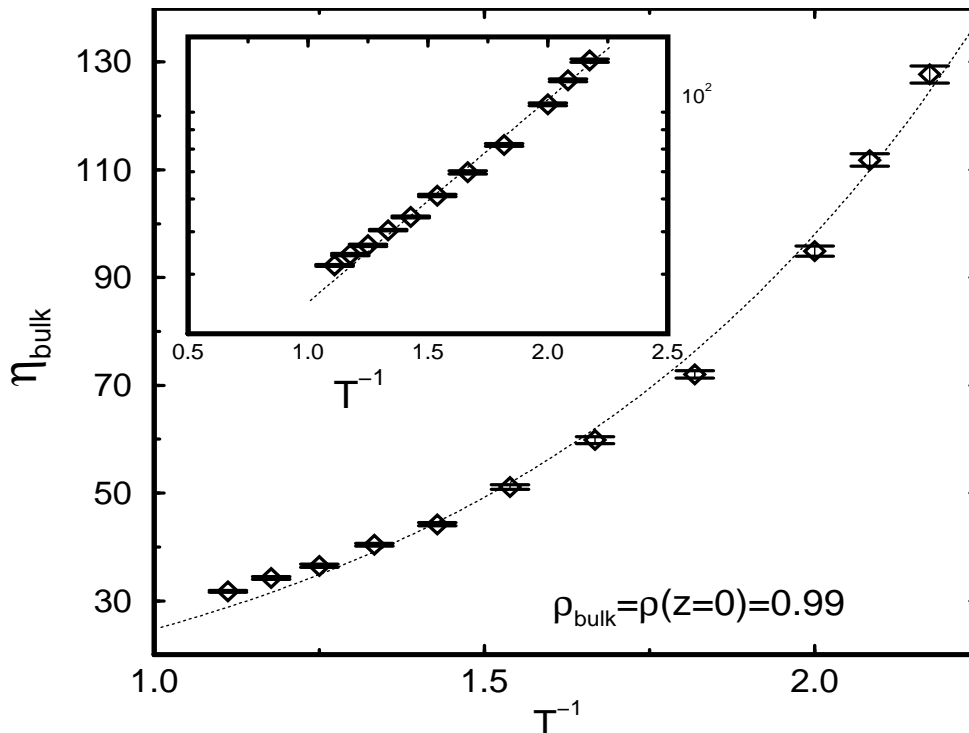


Figure 9.9: The shear viscosity in bulk, η_{bulk} , versus $1/T$. The dashed line corresponds to the best fit assuming the Arrhenius law. The inset contains the same data in a linear-log plot. The MD-data is obviously not well described by the fit.

9.6 Local Viscosity

So far, we have focused our attention on an analysis of the shear viscosity in bulk. However, it is also interesting to look at what happens close to the walls.

Evaluating Eq. (3.18) we have computed the local pressure tensor $\mathbf{P}(z)$. Of particular interest to us, is, of course, the off diagonal component $P_{xy}(z)$. This quantity is depicted in panel (a) of Fig. 9.12. As seen from this panel, within the simulated temperature range, $P_{xy}(z)$ is rather insensitive to a change of T . Contrary to that, a strong variation is observed in the local viscosity $\eta(z)$ as the temperature is lowered. In particular, the effect of the walls is enhanced. This enhancement is manifested by a strong z -dependence of $\eta(z)$ at lower T . $\eta(z)$ increases rapidly when approaching the walls. As seen from panel (b) of Fig. 9.8, the streaming velocity vanishes in the very vicinity of the walls. This means that the particles in the very vicinity of the walls do at least partially stick on the latter. Therefore, the mobility decreases and as a consequence the viscosity grows. Although not as dramatic as in the present case, an increase in shear viscosity at smaller x has been also reported in [56] for a system with WCA interaction at an average density of $\bar{\rho} = 0$.

In the same panel, we have plotted horizontal lines indicating the bulk viscosity at corresponding temperatures. For $T = 0.5$ the bulk viscosity is approximately equal to the average over the range $z \in [-5, 5]$. Recall that η_{bulk} has been computed applying quadratic fit to the velocity profile within this interval.

The determination of the local viscosity profile thus provides an independent check of the reliability of the computed results.

The deviations from the bulk viscosity observed at a higher temperature of $T = 0.9$ are

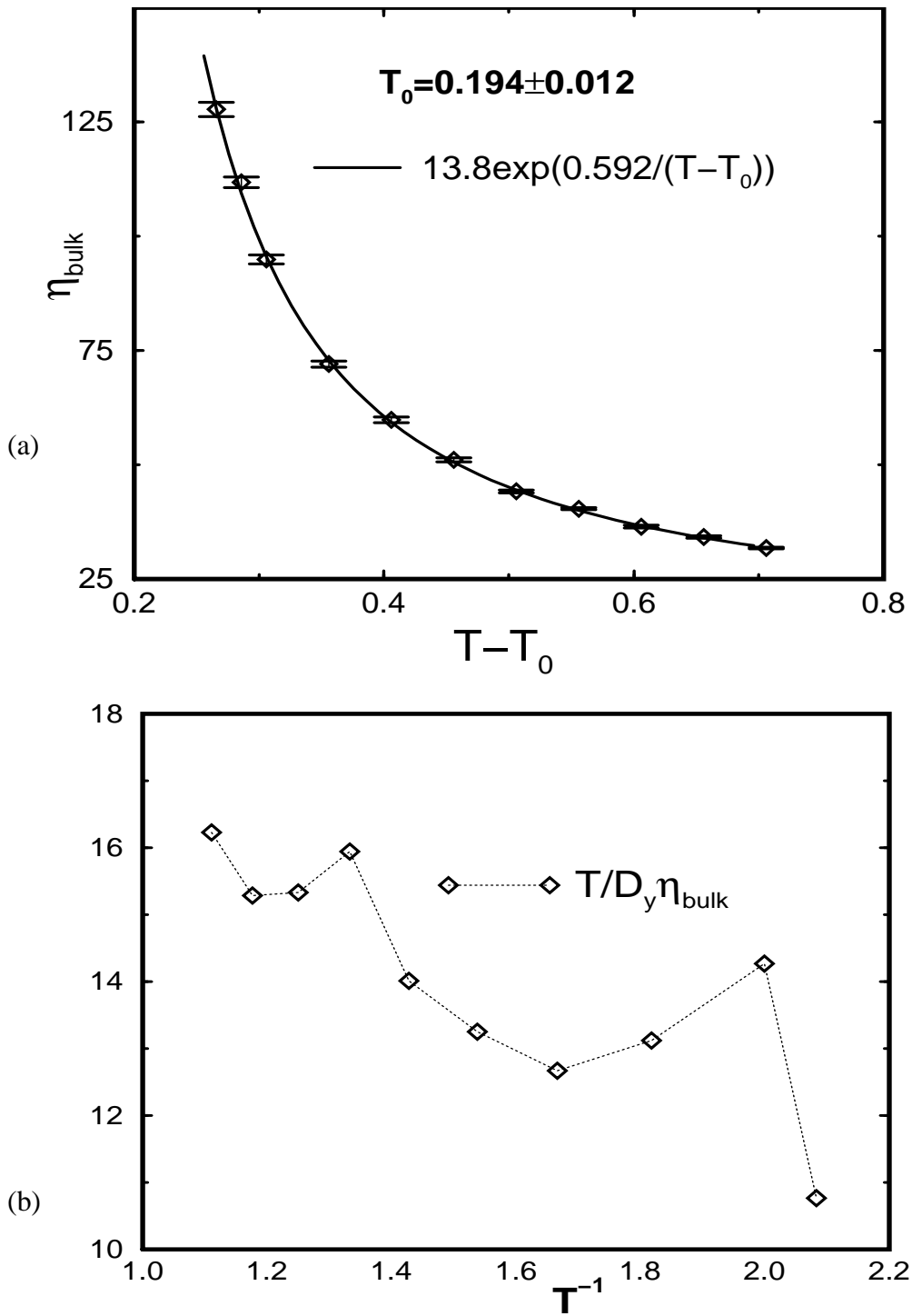


Figure 9.10: Panel (a): Temperature dependence of the bulk viscosity, η_{bulk} (diamonds) and the corresponding VFT-fit. Our polymer model is, obviously, a *fragile* glass former. Panel (b): Diffusion constant in y -direction (circles) and the ratio $T/D_y \eta_{\text{bulk}}$ (diamonds). The latter should be a constant provided that the Stokes-Einstein relation holds. This, obviously, is not the case.

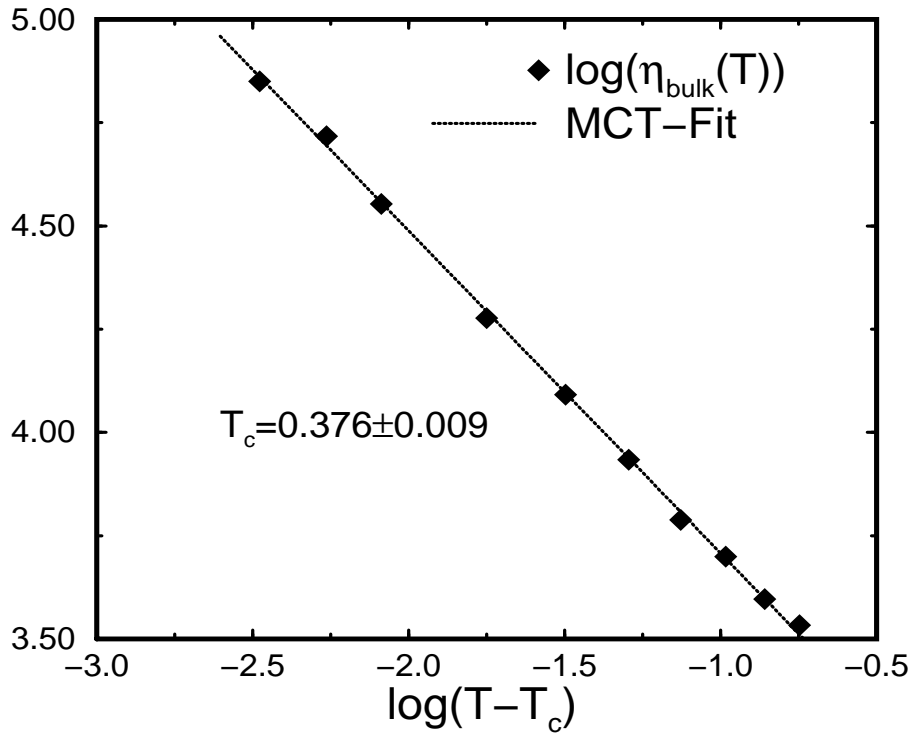


Figure 9.11: Temperature dependence of the bulk viscosity, η_{bulk} (diamonds) and the corresponding mode-coupling fit [see Eq. (9.16)].

most probably due to the error in computing $\partial u_x(z)/\partial z$, the derivative with respect to z of the velocity profile. The magnitude of the error, however is smaller than 5% and therefore relatively small.

Note also that $\eta(z)$ is susceptible to large numerical errors when evaluated in the film center, i.e. for $z = 0$. This comes from the fact that the streaming velocity is a symmetric function of z , the distance from the film center. Therefore, $\partial u_x(z)/\partial z = 0$ for $z = 0$. Inserting this result in Eq. (9.1) would lead to infinitely large values. The large deviations in the region around the film center are therefore an artefacts of this numerical instability [56].

However, it has also to be said that the mentioned objection is *not* a physical, but a numerical problem. Let us recall here the trivial example from elementary analysis that although $\sin(x) = 0$ at $x = 0$, $\lim_{x \rightarrow 0} x/\sin(x)$ is not infinity, but 1.

Finally, to be sure that the change in the viscosity profile is not caused by some temperature gradients like what has been observed in section 9.3, we plot in Fig. 9.13 the density profiles at a few temperatures ranging from $T = 0.9$, the highest temperature discussed here, to $T = 0.5$, the lowest one. As a guidance for the eye, a horizontal line is drawn for each examined temperature profile. As seen from these temperature profiles, our applied method was indeed able to generate a homogeneous temperature profile even at the lowest value of $T = 0.46$.

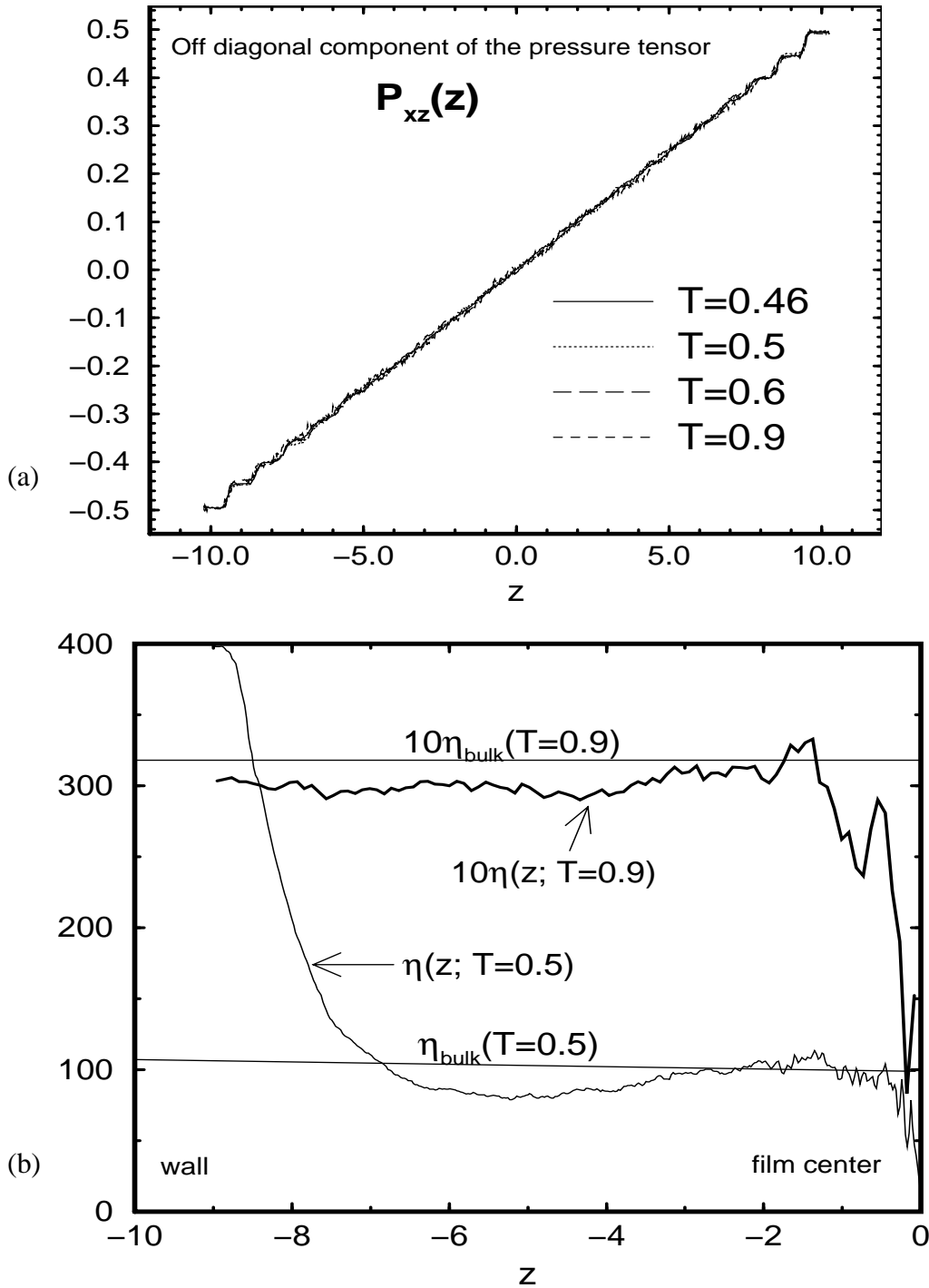


Figure 9.12: Panel (a): Off diagonal component of the pressure tensor, $P_{xy}(z)$, as obtained from MD simulations at various temperatures. Apparently, $P_{xy}(z)$ does not depend much on temperature. Panel (b): Local viscosity, $\eta(z)$, computed using Eq. (3.18) from chapter 3. At low temperatures, a significant increase in $\eta(z)$ is observed when approaching the wall. Horizontal lines indicate the corresponding bulk values computed in section 9.5. The data corresponding to $T = 0.9$ is multiplied by a factor of 10 to match in the scale of the figure.

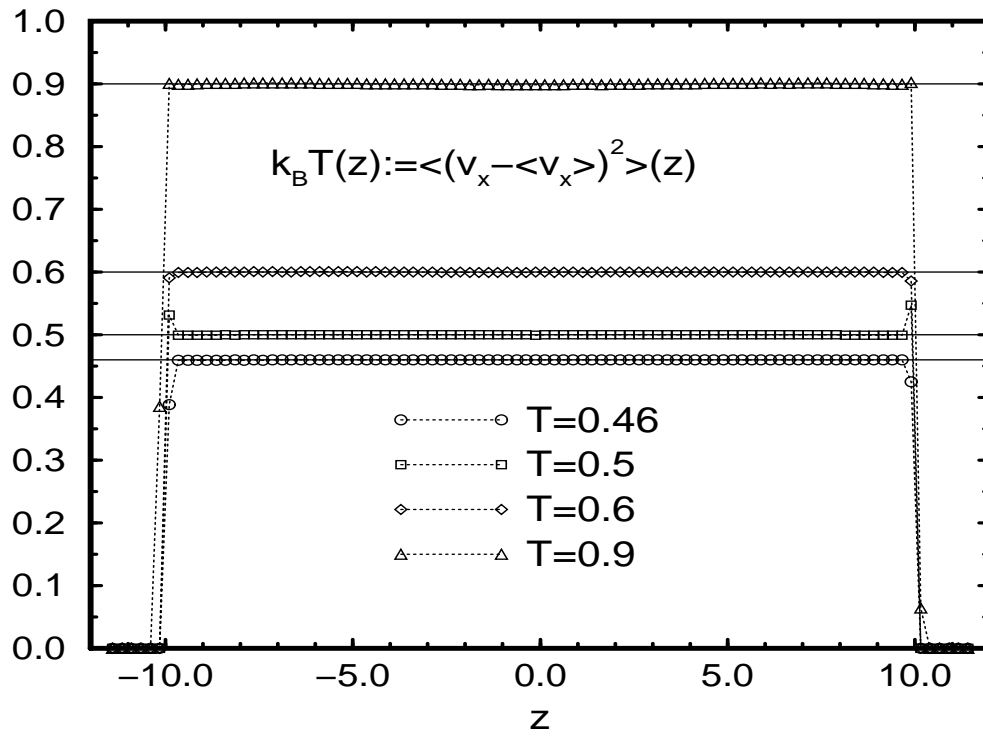


Figure 9.13: Profiles of the thermal energy per particle in the flow direction, i.e. $(v_x - \langle v_x \rangle)^2(z)$ ($m = 1$ and $k_B = 1$). As seen here, all profiles coincide with horizontal lines indicating the corresponding external temperature T_{ext} .

Chapter 10

Conclusion

The present work was, in some sense, the natural extension of the previous studies of a polymer melt in the bulk [91] the main focus of which was the study of the relaxation dynamics of the model system at temperatures close to the glass transition. This analysis of the bulk data has led to an understanding of some important aspects of the glassy behavior of the present model at low T . One of the main goals of the present work was to further improve this knowledge. An important question related to the glass transition is whether or not a diverging length scale is the origin of the transition. In recent times, there have been hints for the existence of such a length scale [34–38, 42, 43].

The study of confined systems yields an important approach to the question of a diverging length scale, ξ say. If such a length scale exists, system properties should show strong size dependence if the system size, L , is smaller than ξ . One can carry out simulations varying the length of the simulation box. In a real experiment, however, periodic boundary conditions do not exist. One resorts to confinements in one or two directions like film or nano-pores. Our choice was to start with thin films.

“Aller Anfang ist schwer”. The first problem to solve was that of the pressure. Motivated by real experiments on thin films, we wanted to carry out simulations at constant external pressure. What is the pressure in an inhomogeneous system? Isn’t it a complicated function of the position? Therefore, we investigated this problem ending up with the result that:

- In an inhomogeneous liquid the pressure is no longer a simple number, but a *tensor*, $\mathbf{P}(\mathbf{r})$, which, in general, depends on the position where it is measured.
- In planar systems *at equilibrium* only two components of $\mathbf{P}(\mathbf{r})$ “survive”, namely the component normal to the interface (surface), P_N , and the tangential one, P_T . All other components vanish provided that the system is in thermal equilibrium.
- In all situations where a steady state condition is satisfied (equilibrium systems being regarded as a special case), P_N is a unique number constant throughout the system. Other component(s), however, do depend on z , the distance from the film center.

Although all these conclusions can already be found in some previous papers in the literature, other papers have reached different conclusions, and thus we felt that a thorough new analysis of the problem was warranted.

Chapter 3 has been devoted to this important topic, where we also presented MD-results on the surface tension of the present confined model.

In chapter 4 we investigated some common simulation techniques and, have generalized the so called Hoover-Melchionna equations of motion [see Eqs. (4.75)-(4.79)] to planar systems.

At the end of this chapter, a subtle point has been addressed. This concerns the contribution of the interparticle forces to the pressure in the presence of periodic boundary conditions (pbc). We have shown that the appropriate expression for the system pressure should be written in terms of *relative distances* (\mathbf{r}_{ij}) and *pairwise forces* (\mathbf{F}_{ij}). The well-known expression of the form $\sum_i \mathbf{r}_i \mathbf{F}_i$ is *not* valid when pbc is applied.

Within the present work, an iterative method has been developed and successfully implemented which effectively allows a simulation at a given normal pressure *without varying the film thickness*, the latter being conjugate to P_N [see chapter 5]

Studying the influence of the NVE , NVT and NpT -ensemble simulations on the system properties we have found that [see chapter 6]:

- Static properties are independent of the specific ensemble within the simulation.
- For the dynamics, Nosé-Hoover algorithm yields results in agreement with the micro-canonical one (NVE), whereas a simulation with fluctuating volume (NpT -ensemble simulation) disturbs the system dynamics at intermediate times. For short and long times, however, results obtained from a NpT run are in agreement with those computed within NVE or NVT -runs.

Concerning the influence of the walls on the static properties we find that:

- Density oscillations occur close to the walls and become stronger when the temperature is lowered.
- Influence of the walls on the packing structure is similar to that of the temperature. In particular, when approaching the walls, the pair distribution function (measured within a plane parallel to the walls) varies (qualitatively) in a similar way as if the temperature was increased.
- Parallel alignment of the chains is favored by the walls.
- Within the depletion layer (layer of closest approach), inner monomers tend to avoid the walls, whereas end monomers exhibit a higher density close to the walls.
- Chains are in general prolate (rod-like), the degree of prolateness being a function of the distance from the walls. At very short distances a maximum prolateness occurs indicating that the chains align parallel to the walls and are flattened. The latter point is supported by the observation of an enhanced bond-peak of the pair distribution function close to the walls.

Furthermore we have compared our MD-results on chain specific profiles with self-consistent-field (SCF) calculations of Müller and Gonzalez MacDowell [68,96] [see chapter 5]. The result is:

- Qualitative agreement is observed in all compared cases.
- Very good quantitative agreement is achieved for non-oscillating quantities, like $R_{g,\parallel}^2(z)$, $R_{ee,\parallel}^2(z)$.
- Discrepancies on a quantitative level have been observed for more complex functions of the distance from the walls.

We have suggested in chapter 5 that a better choice of the weight function, $w(r)$, which enters the SCF equations, along with consideration on the constancy of the normal pressure to obtain a better guess of the bulk free energy density $g(z)$ should improve the agreement. It remains a task for the future studies to examine whether or not these suggestions do yield the expected improvement.

The following results have been obtained from a finite size analysis. First, the static properties do not depend much on the system size. Results for pair distribution function, for example, did not change when going from $L = 17$ to $L = 3.3$. Contrary to the static properties, the system dynamics exhibits a strong size dependence when $L < 5$.

The important point is that the size dependence which occurs at very small lateral system sizes, L , “changes sign”:

- For $D = 20$ the dynamics slows down as L increases, i.e. systems with smaller L are faster.
- For $D = 5$ the opposite behavior occurs. Systems with smaller L are now slower.

An explanation of this behavior could be found in terms of cooperative motion, if one could show that the relative size, ξ/L , of a cooperatively rearranging region becomes smaller with smaller D .

For system sizes much larger than values typical of finite size effects, the dynamic properties of the confined polymer model have been investigated both at high and at low temperatures. At high T a hydrodynamic treatment has been adopted with the result that the so called “back flow” effect plays an important role in the acceleration of the dynamics in our model [see section 8.1].

At low T we computed the mode-coupling critical temperature, T_c , for film thicknesses of $D = 20$, $D = 10$ and $D = 5$ showing a significant decrease of T_c at smaller D . This result is consistent with the observed acceleration of the system dynamics due to the confinement. Furthermore it was shown that the time dependence of mean square displacements at various film thicknesses is approximately the same when compared for the same difference from the critical temperature of the corresponding film thickness. This finding, however, must be further examined. A more precise analysis could reveal more complex behavior. An analysis of the intermediate scattering function, for example, would deepen the insight of the problem.

“Scatter plots” have been used in the same chapter to visualize the heterogeneity in the dynamics. We could demonstrate that the motion of end monomers is more heterogeneous than that of inner monomers in the sense that the former do preferably move parallel to the walls whereas the motion of inner monomers is nearly isotropic. A direct improvement of the ideas underlying the “scatter plots” would be to quantify the heterogeneity in motion.

We also reported simulation results of our polymer model confined between structured walls and subject to a constant driving force.

First, we investigated some technical aspects of the new situation. An important result of these studies was that the system will necessarily heat up if the inner particles are to be thermostated indirectly through interactions with thermostated wall atoms. Obviously, the amount of heating will depend on the magnitude of the driving force and also on the *heat conductivity*. Searching for an expression for the local temperature gradient we found that, in fact, one can use the knowledge of the temperature profile obtained from a simulation along with that of the density and (streaming) velocity profiles to compute the heat conductivity, $\lambda(T)$, within the observed temperature range.

Using the knowledge of the velocity profiles, we could also determine the temperature dependence of the bulk viscosity of the model along an isochoric curve of density $\rho_{\text{bulk}} = 0.99$.

The temperature dependence of $\eta_{\text{bulk}}(T)$ could be fitted by a VFT-law. Furthermore, computing the diffusion constant we could show that the Stokes-Einstein relation does not hold in the investigated temperature range.

Finally, using the knowledge obtained during this work on the calculation of the pressure tensor, the local viscosity profile $\eta(z)$ could be computed. This quantity exhibits strong z -dependence at lower temperature and grows rapidly when approaching the walls. This is in agreement with the fact that particles in the very vicinity of the walls do stick to them. The mobility thus decreases when approaching the walls and, consequently, the viscosity should raise. Thus, being able to calculate the local viscosity profile, we have a further important tool for analyzing the local dynamics.

Appendix A

A.1 Properties of the Liouville operator \mathcal{L}

Let $\Gamma = (\mathbf{r}_1, \dots, \mathbf{r}_N; \mathbf{p}_1, \dots, \mathbf{p}_N)$ denotes a point in phase space. Let f and g be square integrable functions of the phase space variables. We define a scalar product between such functions as

$$\langle f|g \rangle \equiv \int d\Gamma f^*(\Gamma)g(\Gamma). \quad (\text{A.1})$$

We recall that the adjunct operator \mathcal{A}^\dagger of an operator, \mathcal{A} , is defined as

$$\langle f|\mathcal{A}^\dagger|g \rangle \equiv \langle g|\mathcal{A}|f \rangle^* \quad (\text{A.2})$$

for all pairs of vectors (f, g) . An operator \mathcal{A} is said to be Hermitian if it is adjunct to itself, i.e. if $\mathcal{A}^\dagger = \mathcal{A}$. To demonstrate the Hermitian property of the Liouville operator \mathcal{L} it is thus sufficient to show

$$\langle f|\mathcal{L}|g \rangle = \langle g|\mathcal{L}|f \rangle^* \quad (\text{A.3})$$

for all pairs of quadratic integrable functions (f, g) . Using the definition (4.4) of the Liouville operator we can write

$$\langle f|\mathcal{L}|g \rangle = -i \int d\mathbf{r}^{3N} d\mathbf{p}^{3N} f^* \left\{ \sum_i \frac{\partial g}{\partial \mathbf{r}_i} \frac{\partial H}{\partial \mathbf{p}_i} - \frac{\partial g}{\partial \mathbf{p}_i} \frac{\partial H}{\partial \mathbf{r}_i} \right\} \quad (\text{A.4})$$

$$= -i \int d\mathbf{r}^{3N} d\mathbf{p}^{3N} f^* \left\{ \sum_i \frac{\partial}{\partial \mathbf{r}_i} \left(g \frac{\partial H}{\partial \mathbf{p}_i} \right) - \frac{\partial}{\partial \mathbf{p}_i} \left(g \frac{\partial H}{\partial \mathbf{r}_i} \right) \right\} \quad (\text{A.5})$$

$$\begin{aligned} &= -i \sum_i \int d\mathbf{p}^{3N} d\mathbf{r}_1 \cdots d\mathbf{r}_{i-1} d\mathbf{r}_{i+1} \cdots d\mathbf{r}_N \\ &\quad \times \left(f^* g \frac{\partial H}{\partial \mathbf{p}_i} \Big|_{+\infty}^{-\infty} - \int d\mathbf{r}_i g \frac{\partial H}{\partial \mathbf{p}_i} \frac{\partial f^*}{\partial \mathbf{r}_i} \right) \\ &\quad -i \sum_i \int d\mathbf{r}^{3N} d\mathbf{p}_1 \cdots d\mathbf{p}_{i-1} d\mathbf{p}_{i+1} \cdots d\mathbf{p}_N \\ &\quad \times \left(f^* g \frac{\partial H}{\partial \mathbf{r}_i} \Big|_{+\infty}^{-\infty} - \int d\mathbf{p}_i g \frac{\partial H}{\partial \mathbf{r}_i} \frac{\partial f^*}{\partial \mathbf{p}_i} \right) \end{aligned} \quad (\text{A.6})$$

$$= i \int d\mathbf{r}^{3N} d\mathbf{p}^{3N} g \left\{ \sum_i \frac{\partial f^*}{\partial \mathbf{r}_i} \frac{\partial H}{\partial \mathbf{p}_i} - \frac{\partial f^*}{\partial \mathbf{p}_i} \frac{\partial H}{\partial \mathbf{r}_i} \right\} \quad (\text{A.7})$$

$$= \left[-i \int d\mathbf{r}^{3N} d\mathbf{p}^{3N} g^* \left\{ \sum_i \frac{\partial f}{\partial \mathbf{r}_i} \frac{\partial H}{\partial \mathbf{p}_i} - \frac{\partial f}{\partial \mathbf{p}_i} \frac{\partial H}{\partial \mathbf{r}_i} \right\} \right]^* \quad (\text{A.8})$$

$$= \langle g|\mathcal{L}|f \rangle^*. \quad (\text{A.9})$$

In the above derivation, (A.5) was obtained from (A.4) by adding $(\partial^2 H / \partial \mathbf{r}_i \partial \mathbf{p}_i - \partial^2 H / \partial \mathbf{p}_i \partial \mathbf{r}_i) = 0$. The step leading to (A.6) makes use of partial integration in many dimensions. Finally, (A.7) was obtained by assuming that the functions f and g vanish at infinity.

It follows from the unitary property of \mathcal{U} , Eq. (4.6), that the norm of a quadratic integrable function $f(\Gamma)$ is conserved under time evolution

$$\langle f(t) | f(t) \rangle = \langle f(0) | \mathcal{U}^\dagger \mathcal{U} | f(0) \rangle = \langle f(0) | f(0) \rangle \Rightarrow \int d\Gamma |f(t)|^2 = \int d\Gamma |f(0)|^2. \quad (\text{A.10})$$

We use this property to demonstrate the conservation of the phase space volume under the action of $\mathcal{U}(t)$. Let $\mathcal{C}(0)$ denote the set of all points which, at time $t = 0$, are contained in a given region of phase space and let $\mathcal{C}(t)$ be the set of the *same* points at a later time t . At later times, the phase points in \mathcal{C} will probably move apart and thus the shape of \mathcal{C} may change. However, using Eq. (A.10) one can show that the *volume* of \mathcal{C} remains unchanged under time evolution. The only thing to do is to define $f(t)$ as the characteristic function of the set of phase points $\mathcal{C}(t)$, i.e.

$$f(\Gamma) \equiv \begin{cases} 1 & : \Gamma \in \mathcal{C}(t) \\ 0 & : \text{else.} \end{cases} \quad (\text{A.11})$$

Plugging this definition in Eq. (A.10) yields

$$\int_{\mathcal{C}(t)} d\Gamma = \int_{\mathcal{C}(0)} d\Gamma. \quad (\text{A.12})$$

A.2 Hoover- NpT Equations versus Nosé-Andersen

We start from the Nosé-Andersen Lagrangian (4.17)

$$\begin{aligned} L_{\text{NA}} &= s^2 V^{2/d} \sum_i \frac{m_i \dot{\boldsymbol{\rho}}_i^2}{2} - U(V^{1/d} \boldsymbol{\rho}^N) + \frac{M_V}{2} \dot{V}^2 - P_{\text{ext}} V \\ &\quad + \frac{Q}{2} \dot{s}^2 - \frac{g}{\beta} \ln(s). \end{aligned} \quad (\text{A.13})$$

The corresponding conjugate momenta are

$$\boldsymbol{\pi}_i = \frac{\partial L_{\text{NA}}}{\partial \dot{\boldsymbol{\rho}}_i} = m_i s^2 V^{2/d} \dot{\boldsymbol{\rho}}_i \quad (\text{A.14})$$

$$\pi_s = \frac{\partial L_{\text{NA}}}{\partial \dot{s}} = Q \dot{s} \quad (\text{A.15})$$

$$\pi_V = \frac{\partial L_{\text{NA}}}{\partial \dot{V}} = M_V \dot{V}. \quad (\text{A.16})$$

The Hamiltonian of the system is thus found to be

$$\begin{aligned} H_{\text{NA}} &= s^{-2} V^{-2/d} \sum_i \frac{\boldsymbol{\pi}_i^2}{2m_i} + U(V^{1/d} \boldsymbol{\rho}^N) + \frac{\pi_V^2}{2M_V} + P_{\text{ext}} V \\ &\quad + \frac{1}{2Q} \pi_s^2 + \frac{g}{\beta} \ln(s). \end{aligned} \quad (\text{A.17})$$

The canonical equations of motion derived from H_{NA} are

$$\dot{\boldsymbol{\rho}}_i = \frac{\partial H_{\text{NA}}}{\partial \boldsymbol{\pi}_i} = \frac{\boldsymbol{\pi}_i}{m_i s^2 V^{2/d}} \quad (\text{A.18})$$

$$\dot{\boldsymbol{\pi}}_i = -\frac{\partial H_{\text{NA}}}{\partial \boldsymbol{\rho}_i} = V^{1/d} \mathbf{F}_i \quad (\text{A.19})$$

$$\dot{s} = \frac{\pi_s}{Q} \quad (\text{A.20})$$

$$\dot{\pi}_s = \frac{1}{s} \left\{ \sum_i \frac{\boldsymbol{\pi}_i^2}{m_i s^2 V^{2/d}} - g k_{\text{B}} T_{\text{ext}} \right\} \quad (\text{A.21})$$

$$\dot{V} = \frac{\pi_V}{M_V} \quad (\text{A.22})$$

$$\dot{\pi}_V = \frac{1}{dV} \sum_i \left(\frac{\boldsymbol{\pi}_i^2}{m_i s^2 V^{2/d}} + V^{1/d} \boldsymbol{\rho}_i \cdot \mathbf{F}_i \right) - P_{\text{ext}}. \quad (\text{A.23})$$

If we now introduce the real time $dt' \equiv dt/s$ while keeping the superior dot notation for derivatives with respect to the new time, (i.e. $\dot{s} = ds/dt'$ etc.) we obtain

$$\dot{\boldsymbol{\rho}}_i = \frac{\boldsymbol{\pi}_i}{m_i s V^{2/d}} \quad (\text{A.24})$$

$$\dot{\boldsymbol{\pi}}_i = s V^{1/d} \mathbf{F}_i \quad (\text{A.25})$$

$$\dot{s}/s = \frac{\pi_s}{Q} \quad (\text{A.26})$$

$$\dot{\pi}_s = \sum_i \frac{\boldsymbol{\pi}_i^2}{m_i s^2 V^{2/d}} - g k_{\text{B}} T_{\text{ext}} \quad (\text{A.27})$$

$$\dot{V} = s \frac{\pi_V}{M_V} \quad (\text{A.28})$$

$$\dot{\pi}_V = s \frac{1}{dV} \sum_i \left(\frac{\boldsymbol{\pi}_i^2}{m_i s^2 V^{2/d}} + V^{1/d} \boldsymbol{\rho}_i \cdot \mathbf{F}_i \right) - s P_{\text{ext}} \quad (\text{A.29})$$

The next step is to introduce real variables $\mathbf{p}_i \equiv \boldsymbol{\pi}_i/(sV^{1/d})$, $p_s \equiv \pi_s/s$, $p_V \equiv \pi_V/s$ and finally $\mathbf{r}_i = V^{1/d} \boldsymbol{\rho}_i$. After tedious but simple algebraic manipulations, one obtains the Nosé-Andersen

equations of motion for real variables in real time

$$\dot{\mathbf{r}}_i = \frac{\mathbf{p}_i}{m_i} + \frac{\dot{V}}{dV} \mathbf{r}_i \quad (\text{A.30})$$

$$\begin{aligned} \dot{\mathbf{p}}_i &= \frac{\dot{\boldsymbol{\pi}}_i}{sV^{1/d}} - \left(\frac{\dot{s}}{s} + \frac{\dot{V}}{dV} \right) \frac{\boldsymbol{\pi}_i}{sV^{1/d}} \\ &= \mathbf{F}_i - \left(\frac{\dot{s}}{s} + \frac{\dot{V}}{dV} \right) \mathbf{p}_i \end{aligned} \quad (\text{A.31})$$

$$\dot{s}/s = s \frac{p_s}{Q} \quad (\text{A.32})$$

$$\dot{p}_s = \frac{1}{s} \left(\sum_i \frac{\mathbf{p}_i^2}{m_i} - gk_B T_{\text{ext}} \right) - \frac{\dot{s}}{s} p_s \quad (\text{A.33})$$

$$\dot{V} = s^2 \frac{p_V}{M_V} \quad (\text{A.34})$$

$$\begin{aligned} \dot{p}_V &= \sum_i \left(\frac{\mathbf{p}_i^2}{m_i} + \mathbf{r}_i \cdot \mathbf{F}_i \right) - P_{\text{ext}} - \frac{\dot{s}}{s} p_V \\ &= (P(t) - P_{\text{ext}}) - \frac{\dot{s}}{s} p_V \end{aligned} \quad (\text{A.35})$$

where we used the definition (4.55) of the instantaneous pressure. The reader may verify that, if derived with respect to the time, these equations, directly lead to the set of Eqs. (4.52)-(4.54). The last step to derive a set of equations comparable to Hoover NpT -equations (4.56)-(4.60) is the introduction of the friction coefficient $\xi = \dot{s}/s$ and the strain rate $\eta = \dot{V}/(dV)$. Eqs. (A.30)-(A.35) now read

$$\dot{\mathbf{r}}_i = \frac{\mathbf{p}_i}{m_i} + \eta \mathbf{r}_i \quad (\text{A.36})$$

$$\dot{\mathbf{p}}_i = \mathbf{F}_i - (\eta + \xi) \mathbf{p}_i \quad (\text{A.37})$$

$$\dot{\xi} = \frac{1}{Q} \left\{ \sum_i \frac{\mathbf{p}_i^2}{m_i} - gk_B T_{\text{ext}} \right\} \quad (\text{A.38})$$

$$\dot{\eta} = \eta (\xi - d\eta) + \frac{s^2}{dV M_V} (P(t) - P_{\text{ext}}) \quad (\text{A.39})$$

$$\dot{V} = V \eta d. \quad (\text{A.40})$$

Note that the Eq. (A.39) still contains the Nosé-time scale variable s . Actually, within the NpT -ensemble, it is not possible to eliminate all three variables s , \dot{s} and \dot{V} by the introduction of new variables ξ and η . The origin of this problem lies in the fact that the time scale parameter s influences the time evolution of the volume by rescaling the kinetic part of the pressure. Hoover's Eq. (4.59) for $\dot{\eta}$ is thus heuristic in the sense that it cannot be obtained within the framework of an extended Lagrangian approach. However, as we have shown in chapter 4, the Hoover equations (4.56)-(4.60), along with a slight modification,

$$\dot{\mathbf{r}}_i = \frac{\mathbf{p}_i}{m_i} + \eta (\mathbf{r}_i - \mathbf{R}_{\text{cm}}),$$

generate the exact NpT -probability distribution.

Bibliography

- [1] <http://www.psrc.usm.edu/macrog/floor1.htm>.
- [2] <http://www.ixi.net/~wubbaldo/PolymerHistory.htm>.
- [3] W. Kob, in *Annual Review of Computational Physics*, edited by D. Stauffer (World Scientific, Singapore, 1995).
- [4] K. Vollmayr, W. Kob, and K. Binder, *Phys. Rev. B* **54**, 15808 (1996).
- [5] K. Vollmayr, Ph.D. thesis, Johannes Gutenberg-Universität, Mainz, 1995.
- [6] K. Vollmayr, W. Kob, and K. Binder, *J. Chem. Phys.* **105**, (1999).
- [7] G. B. McKenna, in *Comprehensive Polymer Science*, edited by C. Booth and C. Price (Pergamon Press, New York, 1989), Vol. II.
- [8] J. Baschnagel, Ph.D. thesis, Mainz, 1993.
- [9] J. Jäckle, *Rep. Prog. Phys.* **49**, (1986).
- [10] R. Zallen, *The Physics of Amorphous Solids* (Wiley, New York, 1983).
- [11] W. D. Kristensen, *J. Non-Cryst. Solids* **21**, 303 (1976).
- [12] A. Rahman, M. J. Mandell, and J. P. McTague, *J. Chem. Phys.* **64**, 1564 (1976).
- [13] F. F. Abraham, *J. Chem. Phys.* **72**, 359 (1980).
- [14] J. R. Fox and H. C. Andersen, *J. Chem. Phys.* **88**, 4019 (1984).
- [15] M. H. Cohen and D. Turnbull, *J. Chem. Phys.* **31**, 1164 (1959).
- [16] M. H. Cohen and D. Turnbull, *J. Chem. Phys.* **34**, 120 (1961).
- [17] M. H. Cohen and D. Turnbull, *J. Chem. Phys.* **52**, 3038 (1970).
- [18] U. Bengtzelius, W. Götze, and A. Sjölander, *J. Phys. C* **17**, 59115 (1984).
- [19] E. Leutheusser, *Phys. Rev. A* **29**, (1984).
- [20] W. Götze, in *Liquids*, edited by J. P. Hansen, D. Levesque, and Zinn-Justin (North-Holland, Amsterdam, 1991), p. 287.
- [21] W. Götze and L. Sjögren, *Rep. Prog. Phys.* **55**, 241 (1992).

- [22] W. Götze and L. Sjögren, *Transport Theory and Statistical Physics* **24**, 801 (1995).
- [23] R. Schilling, in *Disorder Effects on Relaxational Processes*, edited by R. Richter and A. Blumen (Springer, Berlin, 1994), p. 193.
- [24] G. Li *et al.*, *Phys. Rev. A* **45**, (1992).
- [25] W. van Megen and S. M. Underwood, *Phys. Rev. E* **47**, 248 (1993).
- [26] H. Z. Cummins, G. Li, W. M. Du, and J. Hernandez, *Physica A* **204**, 169 (1994).
- [27] J. Baschnagel, *Phys. Rev. B* **49**, 135 (1994).
- [28] J. Baschnagel and M. Fuchs, *J. Phys.: Condens. Matter* **7**, 6761 (1995).
- [29] W. Kob and H. C. Andersen, *Phys. Rev. E* **51**, 4626 (1995).
- [30] W. Kob and H. C. Andersen, *Phys. Rev. E* **52**, 4134 (1995).
- [31] M. Nauroth and W. Kob, *Phys. Rev. E* **55**, 657 (1997).
- [32] G. Adam and J. Gibbs, *J. Chem. Phys.* **43**, 139 (1965).
- [33] P. M. Chaikin and T. C. Lubensky, *Principles of condensed matter physics* (Cambridge University Press, Cambridge, 1995).
- [34] S. Edwards and T. Vilgis, *Physica Scripta* **T13**, 7 (1986).
- [35] W. Kob *et al.*, *Phys. Rev. Lett.* **79**, 2827 (1997).
- [36] C. Donati *et al.*, *Phys. Rev. E* **60**, 3107 (1999).
- [37] C. Bennemann, C. Donati, J. Baschnagel, and S. Glotzer, *Nature* **399**, 246 (1999).
- [38] R. Yamamoto and A. Onuki, *Phys. Rev. E* **58**, (1998).
- [39] R. Yamamoto and A. Onuki, *J. Phys. Soc. Jpn.* **66**, (1997).
- [40] R. Yamamoto and A. Onuki, *Europhys. Lett.* **40**, (1997).
- [41] A. Onuki and R. Yamamoto, *J. Non-Cryst. Solids* **235-237**, (1998).
- [42] J. A. Forrest and K. Dalnoki-Veress, in press (2000).
- [43] P. Ray and K. Binder, *Europhysics Letters* **27**, 53 (1994).
- [44] J. L. Keddie, R. A. L. Jones, and R. A. Cory, *Faraday Discuss.* **98**, (1994).
- [45] J. A. Forrest, K. Dalnoki-Veress, and J. R. Dutcher, *Phys. Rev. E* **56**, 5705 (1997).
- [46] C. Bennemann, W. Paul, K. Binder, and B. Dünweg, *Phys. Rev. E* **57**, 843 (1998).
- [47] K. Kremer and G. Grest, *J. Chem. Phys.* **92**, 5057 (1990).
- [48] C. Bennemann, J. Baschnagel, and W. Paul, *Eur. Phys. J B* **10**, 323 (1999).

- [49] C. Bennemann, W. Paul, J. Baschnagel, and K. Binder, *J. Phys.: Condens. Matter* **11**, 2179 (1999).
- [50] C. Bennemann, J. Baschnagel, W. Paul, and K. Binder, *Comp. Theo. Poly. Sci.* **9**, 217 (1999).
- [51] R. Feynman, R. Leighton, and M. Sands, *The Feynman Lectures on Physics* (Addison-Wesley, Massachusetts, 1963).
- [52] C. Garrod, *Statistical Mechanics and Thermodynamics* (Oxford University Press, Oxford, 1995).
- [53] J. Rowlinson and B. Widom, *Molecular Theory of Capillarity* (Clarendon Press, Oxford, 1982).
- [54] J. Haile, *Molecular Dynamics Simulation* (John Wiley & Sons, New York, 1992).
- [55] J. Irving and J. Kirkwood, *J. Chem. Phys.* **18**, 817 (1950).
- [56] B. Todd, D. Evans, and P. Daivis, *Phys. Rev. E* **52**, 1627 (1995).
- [57] D. Evans and G. Morriss, *Statistical Mechanics of Non Equilibrium Liquids* (Academic Press, London, 1990).
- [58] R. Lovett and M. Baus, *Adv. Chem. Phys.* **102**, (1997).
- [59] P. Schofield and J. Hendersen, **379**, 231 (1982).
- [60] M. Rao and B. Berne, *Mol. Phys.* **37**, 455 (1979).
- [61] A. Harasima, *Adv. Chem. Phys.* **1**, 203 (1958).
- [62] J. Walton, D. Tildesly, J. Rowlinson, and J. Henderson, *Mol. Phys.* **48**, 1357 (1983).
- [63] B. Todd and D. Evans, *Mol. Sim.* **17**, 317 (1996).
- [64] J.-P. Hansen and I. McDonald, *Theory of Simple Liquids* (Academic Press, London, 1990).
- [65] D. Yoon, M. Vacatello, and G. Smith, in *Monte Carlo and Molecular Dynamics Simulations in Polymer Science*, edited by K. Binder (Oxford University Press, New York, 1995), pp. 433–475.
- [66] M. Nijmeijer, C. Bruin, and A. Bakker, *Phys. Rev. A* **42**, 6052 (1990).
- [67] R. Pandey, A. Milchev, and K. Binder, *Macromolecules* **30**, 1194 (1997).
- [68] M. Müller and L. G. MacDowell, *Macromolecules* **33**, 3902 (2000).
- [69] F. Varnik, J. Baschnagel, and K. Binder, *J. Phys. IV* **10**, (2000).
- [70] D. Frenkel and B. Smith, *Understanding Molecular Dynamics Simulation* (Academic Press, San Diego, 1996).
- [71] J. Horbach, Ph.D. thesis, Johannes-Gutenberg-Universität Mainz, 1998.

- [72] H. Trotter, Proc. Am. Math. Soc. **10**, 545 (1959).
- [73] H. Andersen, J. Chem. Phys. **72**, 2384 (1980).
- [74] M. Parinello and A. Rahman, J. Appl. Phys. **52**, 7182 (1981).
- [75] M. Parinello and A. Rahman, J. Chem. Phys. **76**, 2662 (1982).
- [76] A. Branka and M. Parinello, Mol. Phys. **58**, 989 (1986).
- [77] S. Nosé and M. Klein, Mol. Phys. **50**, 1055 (1983).
- [78] S. Nosé, J. Chem. Phys. **81**, 511 (1984).
- [79] S. Nosé, Mol. Phys. **52**, 255 (1984).
- [80] S. Nosé, Mol. Phys. **57**, 187 (1986).
- [81] D. Evans and J. Morriss, J. Chem. Phys. **77**, 63 (1983).
- [82] D. Evans and J. Morriss, Comp. Phys. Rep. **1**, 297 (1984).
- [83] W. Hoover, Phys. Rev. A **31**, 1695 (1985).
- [84] W. Hoover, Phys. Rev. A **34**, 2499 (1986).
- [85] J. Ryckaert and G. Ciccotti, J. Chem. Phys. **87**, 7368 (1983).
- [86] G. Ciccotti and J. Ryckaert, Comp. Phys. Rep. **4**, 345 (1986).
- [87] S. Melchionna, G. Ciccotti, and B. Holian, Mol. Phys. **78**, 533 (1993).
- [88] S. Nosé, Prog. Theor. Phys. **103**, 1 (1991).
- [89] C. Cohen-Tannoudji, *Quantum Mechanics* (Wiley-Interscience, New York, 1977).
- [90] B. Buttler, G. Ayton, O. Jepps, and D. Evans, Chem. Phys. **109**, 6519 (1998).
- [91] C. Bennemann, *Untersuchung des thermischen Glassübergangs von Polymerschmelzen mittels Molecular Dynamik Simulation* (Dissertation, Mainz, 1998).
- [92] N. W. Ashcroft and N. D. Mermin, *Solid State Physics* (Saunders College, Orlando, 1976).
- [93] H. Vogel, *Gerthsen Physik* (Springer, Berlin, 1999).
- [94] A. A. Broyles, J. Chem. Phys. **33**, 456 (1960).
- [95] K. Mischler, Master's thesis, Universität Mainz, 1999.
- [96] L. G. MacDowell, M. Müller, C. Vega, and K. Binder, J. Chem. Phys. **109**, 419 (2000).
- [97] P. G. de Gennes, *Scaling Concepts in Polymer Physics* (Cornell University Press, Ithaca, USA, 1979).
- [98] M. Müller and M. Schick, Macromolecules **29**, 8900 (1996).

- [99] M. Müller and M. Schick, *Phys. Rev. E* **57**, 6973 (1998).
- [100] M. Müller and A. Werner, *J. Chem. Phys.* **107**, 10764 (1997).
- [101] M. Müller and K. Binder, *Macromolecules* **31**, 8323 (1998).
- [102] M. Müller, *Macromolecules* **31**, 9044 (1998).
- [103] I. Szleifer, A. Ben-Shaul, and W. M. Gelbhart, *J. Chem. Phys.* **85**, 5345 (1986).
- [104] I. Szleifer and M. A. Carignano, *Adv. Chem. Phys.* **94**, 742 (1996).
- [105] I. Szleifer, A. Ben-Shaul, and W. M. Gelbhart, *J. Chem. Phys.* **86**, 7094 (1987).
- [106] D. E. Sullivan, *Phys. Rev. B* **20**, 3991 (1979).
- [107] D. E. Sullivan, *J. Chem. Phys.* **74**, 2604 (1981).
- [108] R. Evans and P. Tarazona, *Phys. Rev. A* **28**, 1864 (1983).
- [109] C. Woodward, *J. Chem. Phys.* **94**, 3183 (1991).
- [110] C. Woodward, *J. Chem. Phys.* **97**, 695 (1992).
- [111] C. Woodward and A. Yethiraj, *J. Chem. Phys.* **100**, 3181 (1994).
- [112] A. Yethiraj and C. Woodward, *J. Chem. Phys.* **102**, 5499 (1995).
- [113] M. S. Wertheim, *J. Chem. Phys.* **87**, 7323 (1987).
- [114] G. Stell and Y. Zhou, *J. Chem. Phys.* **91**, 3618 (1989).
- [115] G. Stell and Y. Zhou, *J. Chem. Phys.* **96**, 1504 and 1507 (1989).
- [116] W. G. Chapman, G. Jackson, and K. E. Gubbins, *Mol. Phys.* **65**, 1057 (1988).
- [117] J. K. Johnson, J. A. Zollweg, and K. E. Gubbins, *Mol. Phys.* **3**, 591 (1993).
- [118] W. Zhao *et al.*, *Macromolecules* **26**, (1993).
- [119] J. P. Donley, J. J. Rajasekaran, J. D. McCoy, and J. G. Curro, *J. Chem. Phys.* **103**, 5061 (1995).
- [120] E. Kierlik and M. L. Rosinberg, *J. Chem. Phys.* **100**, 1716 (1993).
- [121] M. Müller, private communication, Mainz, Septembre 2000.
- [122] J. A. Aronovitz and D. R. Nelson, *J. Phys. France* **47**, 1445 (1986).
- [123] J. W. Cannon, J. A. Aronovitz, and P. Goldbart, *J. Phys. I* **1**, 629 (1991).
- [124] R. Yamamoto and K. Kim, *J. Phys. IV* **10**, (2000).
- [125] J. Jäckle, *J. Phys. IV* **10**, (2000).
- [126] Y. Alméras, J.-L. Barrat, and L. Bocquet, *J. Phys. IV* **10**, (2000).

- [127] Y. Alm eras, calcul du coefficient de diffusion d'un fluid confin , 1999, available from lyderic.bocquet@ens-lyon.fr.
- [128] L. Bocquet and J.-L. Barrat, *Europhysics Letters* **131**, (1995).
- [129] M. Aichele, Master's thesis, Universit t Mainz, 2000.
- [130] W. Kob, *Experimental and Theoretical Approaches to Supercooled Liquids: Advances and Novel Application* (ACS Books, Washington, 1997).
- [131] R. Schilling, in *Disorder Effects on Relaxation Processes*, edited by Richert and Blumen (Springer, Berlin, 1994).
- [132] P. Scheidler, W. Kob, and K. Binder, *J. Phys. IV* **10**, (2000).
- [133] D. Thirumalai and R. D. Mountain, *Phys. Rev. E* **47**, 479 (1993).
- [134] B. Bernu, J. P. Hansen, Y. Hiwatari, and G. Pastore, *Phys. Rev. A* **36**, 4891 (1987).
- [135] B. Doliwa and A. Heuer, *Phys. Rev. Lett.* **80**, 4915 (1998).
- [136] L. D. Landau and E. M. Lifschitz, *Hydrodynamik* (Akademie Verlag, Berlin, 1991), Vol. VI.
- [137] R. Evans and P. Tarazona, *Phys. Rev. A* **23**, 2622 (1981).
- [138] A. Jabbarzadeh, J. Atkinson, and R. Tanner, *J. Chem. Phys.* **110**, 2612 (1999).
- [139] W. Hoover, A. Ladd, and B. Moran, *Phys. Rev. Lett.* **48**, 1818 (1982).
- [140] D. Evans, *J. Chem. Phys.* **78**, 3297 (1983).
- [141] J. Wong and C. A. Angell, *Glass: Structure by Spectroscopy* (Marcel Dekker, Basel, 1976).
- [142] S. Glasstone, K. Laidler, and H. Eyring, *The Theory of Rate Processes* (McGraw-Hill, New York, 1941).
- [143] F. Fujara, B. Geil, H. Silesku, and G. Fleischer, *Z. Phys. B* **88**, 195 (1992).
- [144] I. Chang *et al.*, *J. Non-Cryst. Sol.* **172-174**, 248 (1994).
- [145] M. Cicerone, F. Blackburn, and M. Ediger, *Macromolecules* **28**, 8224 (1995).
- [146] M. Cicerone and M. Ediger, *J. Chem. Phys.* **104**, 7210 (1996).
- [147] M. Ediger, C. Angell, and S. Nagel, *J. Phys. Chem.* **100**, 13200 (1996).
- [148] F. Stillinger and A. Hodgdon, *Phys. Rev. E* **50**, 2064 (1994).

Acknowledgements

I would like to thank Höchstleistungsrechenzentrum (HLRZ) in Jülich, Hochschulrechenzentrum Kaiserslautern (RHRK), Rechenzentrum für Datenverarbeitung (ZDV) of the University of Mainz and Koma support team for providing me with computing power.

Financial support of the Deutsche Forschungsgemeinschaft DFG in the framework of SFB 262 are also acknowledged.

CURRICULUM VITAE

Personal Data

Name	Fathollah Varnik
Date of birth	26.04.1965
Place of birth	Bandar-Shah (Iran)
Marital status	married
Nationality	Iranian and French
Address	Hintere Bleiche 12a, 55116 Mainz, Germany

Professional History

Sep. 1985	School leaving examination in Gorgan (Iran)
Sep. 1988 - June 1989	Visit of the “Deutsches Studienkolleg für ausländische Studierende” (final examination qualifying for further studies at German Universities)
Oct. 1989 - July 1995	Study of physics at the University of Cologne. Obtained title: Diplom Physiker (Master of Science in Physics) Subject of the Diploma Thesis: Density Matrix Theory of Binary Bose Mixtures
Dec. 1995 - May 1998	Laser development in the “Institut für Strahlwerkzeuge”, University of Stuttgart
Since June 1998	Dissertation in Theoretical Physics supervised by Prof. Dr. K. Binder in the framework of SFB 262 (Sonderforschungsbereich): “Glaszustand und Glasübergang nichtmetallischer amorpher Materialien” (Glassy state and glass transition in non-metallic amorphous materials)